

# Interaction of Cosmic Rays with the Earth's Magnetosphere and Atmosphere

Modeling the Cosmic Ray Induced Ionization and the Production of  
Cosmogenic Radionuclides

Dissertation

zur Erlangung des Doktorgrades

der Mathematisch-Naturwissenschaftlichen Fakultät

der Christian-Albrechts-Universität

zu Kiel

vorgelegt von  
Klaudia Herbst

Kiel, 2012

*Referent:* \_\_\_\_\_ Prof. Dr. Bernd Heber

*Korreferent :* \_\_\_\_\_ Prof. Dr. Jürg Beer

*Tag der mündlichen Prüfung:* \_\_\_\_\_ 23.10.2012

*Zum Druck genehmigt :* \_\_\_\_\_ 23.10.2012

\_\_\_\_\_  
**gez. Prof. Dr. Wolfgang J. Duschl, Dekan**

---

**Abstract:**

Cosmogenic radionuclides like  $^{10}\text{Be}$  and  $^{14}\text{C}$  are produced by reactions of primary cosmic rays (CR) and secondary particles with atmospheric nuclei, are then mixed in the atmosphere and finally deposited in natural archives like ice sheets, tree rings or sediments. Because the flux of CRs strongly depends on solar activity the production rate of cosmogenic radionuclides being stored in these archives have recorded the solar activity over thousands of years. Although cosmogenic radionuclide measurements can, thus, in principle be used to reconstruct solar activity back in time, the problem arises that reconstructions based on  $^{10}\text{Be}$  and  $^{14}\text{C}$  differ significantly. This work provides a reconstruction which for the first time is consistent with both  $^{10}\text{Be}$  and  $^{14}\text{C}$  archive data. In order to do so, the full simulation chain — starting with the local interstellar medium beyond the heliosphere and ending with the deposition of the radionuclides in natural archives — determining the generation of cosmogenic radionuclides has to be taken into account. For the reconstruction of the solar activity over thousands of years in this work the activity is reflected by the solar modulation parameter  $\phi$ . Investigating first the different local interstellar spectrum (LIS) models this work provides a method to convert them into each other, models the CR modulation within the heliosphere and studies their consistency with terrestrial and space data. Secondly, the particle transport within the Earth's magnetosphere is described, stressing the importance of the field geometry for the vertical cutoff rigidity, complemented by investigations of the direction of incidence. In a third step the secondary particle environment and its dependence on the respective LIS model as well as hadronic interaction models is studied. Using LIS-dependent solar modulation parameters all LIS models are shown to be able to represent the measurements. In order to decide which hadronic interaction model is the more suitable one, fourth, the CR-induced ionization of the atmosphere is investigated, favoring the Bertini model rather than the BIC model. After having successfully validated the local and global production rates of  $^{10}\text{Be}$ ,  $^7\text{Be}$ ,  $^{36}\text{Cl}$ ,  $^3\text{H}$ ,  $^{26}\text{Al}$  and  $^{14}\text{C}$  in a fifth issue, on the basis of modeled and measured production rates and taking into account temporal variations of the Earth's magnetic field strengths, this work provides a new solar modulation parameter being able to represent  $^{10}\text{Be}$  as well as  $^{14}\text{C}$  data over the entire Holocene.

---

---

## Zusammenfassung:

Kosmogene Radionuklide, wie  $^{10}\text{Be}$  und  $^{14}\text{C}$ , werden überwiegend durch Reaktionen der Kosmischen Strahlung sowie der sekundären Teilchen mit den Bestandteilen der Atmosphäre produziert, dort gemischt und anschließend in natürlichen Archiven wie Baumringen, Eisschichten und Sedimenten abgelagert. Aufgrund der Tatsache, dass der Fluss der kosmischen Strahlung stark von der solaren Aktivität abhängt, haben die in den Archiven gespeicherten Produktionsraten der kosmogenen Radionuklide die Aktivität über tausende von Jahren aufgezeichnet. Doch obwohl die Messungen zur Rekonstruktion der solaren Aktivität genutzt werden können, zeigt sich, dass die Ergebnisse unter Benutzung der beiden Radionuklide stark voneinander abweichen. Die vorliegende Arbeit unternimmt den Versuch, eine Rekonstruktion der solaren Aktivität bereitzustellen, welche erstmals sowohl mit  $^{10}\text{Be}$ , als auch  $^{14}\text{C}$  Messungen konsistent ist. Um dies zu erreichen wird die vollständige Simulationskette, welche für die Produktion der kosmogenen Radionuklide verantwortlich ist, beginnend mit dem lokalen interstellaren Medium jenseits der Heliosphäre und endend mit der Einlagerung der kosmogenen Radionuklide in natürlichen Archiven, berücksichtigt. Dabei wird die solare Aktivität durch den solaren Modulationsparameter  $\phi$  beschrieben. In der Untersuchung der verschiedenen Modelle des lokalen interstellaren Spektrums (LIS) wird zunächst eine Methode vorgestellt, mit der die verschiedenen Modellspektren ineinander umgerechnet werden können, sowie ihre Modulation innerhalb der Heliosphäre simuliert. Des Weiteren wird ihre Konformität mit terrestrischen und extraterrestrischen Messungen geprüft. In einem zweiten Schritt wird der Teilchentransport innerhalb der Erdmagnetosphäre beschrieben, wobei insbesondere die Bedeutung der Magnetfeldgeometrie für die vertikale Cutoff-Steifigkeit betont, und zusätzlich der Einfluss der Einfallrichtung Kosmischer Strahlung untersucht wird. Die dritte Untersuchung beschäftigt sich mit der Simulation der sekundären Teilchenkomponenten sowie der Untersuchung ihrer Abhängigkeit vom LIS-Modell und des hadronischen Wechselwirkungsmodells. Mit Hilfe der LIS-abhängigen solaren Modulationsparameter wird gezeigt, dass alle LIS-Modelle in der Lage sind die Messungen widerzuspiegeln. Um dagegen zu entscheiden, welches der hadronischen Wechselwirkungsmodelle für die Zwecke dieser Arbeit besser geeignet ist, wird in einem vierten Schritt die Ionisation der Atmosphäre untersucht. Wie gezeigt wird, begünstigen diese Untersuchung das Bertini-Modell gegenüber dem BIC-Modell. Nach erfolgreicher Validierung der simulierten lokalen und globalen Produktionsraten der kosmogenen Radionuklide  $^{10}\text{Be}$ ,  $^7\text{Be}$ ,  $^{36}\text{Cl}$ ,  $^3\text{H}$ ,  $^{26}\text{Al}$  und  $^{14}\text{C}$  wird, unter Benutzung gemessener und modulierter  $^{10}\text{Be}$  und  $^{14}\text{C}$  Produktionsraten sowie unter Berücksichtigung der zeitlichen Variation der Stärke des Erdmagnetfeldes, in einem fünften Punkt, ein solarer Modulationsparameter, welcher in der Lage ist, sowohl die  $^{10}\text{Be}$  als auch die  $^{14}\text{C}$  Messungen während des Holozäns widerzuspiegeln, bestimmt.

# Contents

<b>1</b>	<b>Introduction</b>	<b>3</b>
<b>2</b>	<b>The Sun-Earth Environment</b>	<b>7</b>
2.1	Cosmic Radiation Environment . . . . .	8
2.2	Galactic Cosmic Rays (GCRs) . . . . .	10
2.3	The Terrestrial Magnetosphere . . . . .	14
2.4	The Earth's Atmosphere . . . . .	18
<b>3</b>	<b>The Solar Modulation</b>	<b>27</b>
3.1	The Local Interstellar Spectrum . . . . .	28
3.2	The Local Interstellar Spectrum Beyond the Heliopause: . . . . .	33
3.3	Parker Equation Versus Solar Modulation Parameter . . . . .	41
3.4	Conversion of the Solar Modulation Parameter . . . . .	42
3.5	Application to a Long-Term Record of $\phi$ . . . . .	50
<b>4</b>	<b>Computation of the Particle Transport</b>	<b>55</b>
4.1	Magnetospheric Transport . . . . .	55
4.2	Vertical Cutoff Rigidities . . . . .	57
4.3	Directional Cutoff Rigidities . . . . .	72
<b>5</b>	<b>Computing the Secondary Particle Environment</b>	<b>75</b>
5.1	Dependence on the LIS model . . . . .	78
5.2	Dependence on the Hadronic Interaction Model . . . . .	81
<b>6</b>	<b>Modeling the Cosmic Ray Induced Ionization</b>	<b>87</b>
6.1	The Cosmic Ray Induced Ionization . . . . .	87
6.2	Modeling the Cosmic Ray Induced Ionization due to Galactic Cosmic Rays . . . . .	89
<b>7</b>	<b>Modeling the Production of Cosmogenic Radionuclides</b>	<b>111</b>
7.1	The Production of Cosmogenic Radionuclides . . . . .	113
7.2	Modeling the Production of Cosmogenic Radionuclides . . . . .	117
7.3	Local Production Rates . . . . .	125
7.4	Global Production Rates . . . . .	131
7.5	Global Production Rates between 1940 and 2010 . . . . .	137
7.6	Global Production Rates between 9400 BP and 0 BP . . . . .	140
<b>8</b>	<b>Summary</b>	<b>161</b>
<b>9</b>	<b>Outlook</b>	<b>163</b>

<b>Bibliography</b>	<b>177</b>
<b>A GEANT4 and PLANETOCOSMICS</b>	<b>193</b>
A.1 The GEANT4 toolkit . . . . .	193
A.2 The PLANETOCOSMICS Code . . . . .	195
<b>B PLANETOCOSMICS - Macro File Examples</b>	<b>201</b>
B.1 Computation of the Vertical Cutoff Rigidity Distribution . . . . .	201
B.2 Computation of the Secondary Particle flux and the Atmospheric Ionization . . . . .	202
<b>C On the Computation Time</b>	<b>207</b>
<b>D Information on the SDE model</b>	<b>209</b>
<b>E The Cosmogenic Radionuclide Production Rates</b>	<b>211</b>

# Erratum

In Chapter 7 the global  $^{14}\text{C}$  production rates by [Reimer et al. \(2009\)](#), reconstructed using an ocean-atmosphere diffusion box model (see e.g. [Oeschger et al., 1975](#); [Stuiver and Braziunas, 1993b](#), for further information), are used in order to reconstruct the solar modulation parameter during the Holocene from the computations performed in this work. Note that it is not clear whether the data by [Reimer et al. \(2009\)](#) really reflect absolute values.

The reconstructed solar modulation parameters are then used to compute the global  $^{10}\text{Be}$  production rates during the Holocene. Note that the measurements by [Berggren et al. \(2009\)](#), which reflect the  $^{10}\text{Be}$  flux between the years 0 and 600 BP, do not reflect absolute values. The fact that both measurements and reconstructed global production rates are in good agreement is therefore not to be expected. An explanation for the good agreement may be that the solar modulation parameters reconstructed from the global  $^{14}\text{C}$  production rates by [Reimer et al. \(2009\)](#) are too high. Further studies therefore are necessary.





# Introduction

---

*“... und während du ’nen Schneeball machst  
und ich so Deine Spuren im Schnee seh’ ...”*

Phillip Poisel - Seerosenteich -

When I was a little child the world was a mystery to me and I often wondered whether or not other people are able to see the world as I do. Some things, however, were save and sound: trees were there to climb on and snow was a great opportunity for a snow fight with my siblings. Throughout the years I learned that the Earth not only possesses an atmosphere but also a magnetic field shielding us from a flow of (galactic) cosmic rays (CRs), a flux of high-energetic particles which is influenced by the varying activity of the Sun. And: I had to realize that trees and snow have something in common I never could have imagined, because once these primary particles penetrate into the atmosphere they interact with atmospheric matter by producing secondary particles like electrons, neutrons and protons, which not only ionize the atmosphere but also produce so-called cosmogenic radionuclides. These cosmogenic radionuclides are mixed and transported in the atmosphere, and finally stored in natural archives like trees, ice sheets or sediments, preserving the information on the solar activity of thousands of years. In principle, cosmogenic radionuclide measurements can, thus be used to reconstruct solar activity back in time. This work focuses on the past 11,500 years, the time period since the last ice age that is called the Holocene.

The most prominent cosmogenic radionuclide is  $^{14}\text{C}$ , which is stored mainly in organic materials like, e.g., tree rings. With a half-life of 5730 years it is mainly used to determine the age of e.g. archeological samples. Of importance for reconstruction purposes also is the cosmogenic radionuclide  $^{10}\text{Be}$  with a half-life of  $1.39 \cdot 10^6$  years, which is stored in the ice sheets of Greenland and Antarctica. The solar activity reconstructed using tree ring measurements ( $^{14}\text{C}$ ), however, deviates significantly from that using ice cores ( $^{10}\text{Be}$ ) (see e.g. [Usoskin and Kromer, 2005](#); [Steinhilber et al., 2008](#)). The reason for this discrepancy can presumably be found in the links of the simulation chain responsible for the production of cosmogenic radionuclides, starting beyond the solar system and ending with the deposition of the radionuclides in terrestrial archives shown in Fig. 1.1:

- The local interstellar spectrum (LIS), the energy spectrum in the medium surrounding the heliosphere, i.e. the bubble-like structure around the Sun formed by the continuous particle stream of the solar wind. Because the LIS could not be measured by now several models exist in the literature.

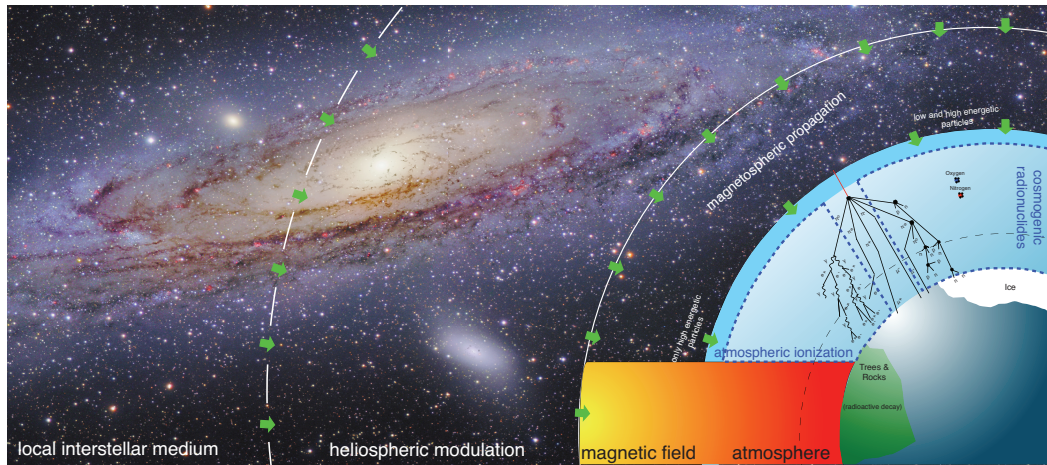


Figure 1.1: *Sketch of the processes involved in order to model the atmospheric ionization as well as the production of the cosmogenic radionuclides.*

- The modulation (see Section 2.2) of the LIS inside the heliosphere
- The propagation of particles in the Earth's magnetosphere
- Interactions of particles with atmospheric matter, which, amongst other, leads to the production of cosmogenic radionuclides
- Atmospheric mixing and transport processes of cosmogenic radionuclides and their storage inside natural archives like trees, ice sheets and sediments

Previous approaches a) are restricted to a single LIS model (see e.g. Webber et al., 2007), b) only simulate the influence due to primary protons while modeling alpha particles as composite of two protons and two neutrons (see e.g. Masarik and Beer, 1999), c) only take into account the production rate values due to a fixed angle of incidence of the cosmic ray (see e.g. Masarik and Beer, 2009), d) take into account only one of the two cosmogenic nuclides,  $^{10}\text{Be}$  or  $^{14}\text{C}$ , preventing them from being able to adjust the reconstructed solar activity (see e.g. Kavaltsov et al., 2012).

Taking into account the above mentioned chain as self-consistent as possible, this work provides a reconstruction of solar activity, which, in the estimation limitations, for the first time is consistent with both the  $^{10}\text{Be}$  and  $^{14}\text{C}$  archive data. The steps to achieve this main goal are given in the following.

Chapter 2 gives an overview of the theoretical background, focusing on the CRs and their modulation due to fluctuations of the heliospheric magnetic field embedded in the solar wind. In addition, basic information about the structure of the Earth's magnetic field and atmosphere are provided, and, moreover, the most

relevant particle interactions are described. Following the simulation chain from outside our solar system inwards, Chapter 3 is devoted to the investigation of the different LIS models used in the literature, where it is of particular interest whether or not the Voyager spacecrafts, which are currently around the outer boundary of the heliosphere, will be able to measure the "true" LIS in the near future as well as how the LIS model-dependent modulated spectra can be converted into each other. Chapter 4 concentrates on the computation of the galactic CR transport in the Earth's magnetosphere and atmosphere, and investigates the geometry of the field, represented as a measure of the difference between the vertical and horizontal components, and its connection with the vertical cutoff-rigidity, a measure for the ability of a cosmic ray particle to reach a given geographical location. In a detailed study the time-dependent longitudinal and latitudinal variations of both measures between 1900 and 2010 will be performed, and the question whether or not the magnetic field variations throughout this time play an important role will be addressed. Chapter 5 presents the results of the secondary particle computations (see also [Matthiä, 2009](#)). Here, in particular the dependence on the used LIS model as well as the atmospheric interaction model will be investigated. In addition, Chapter 6 is devoted to the investigation of the different hadronic interaction models on the CR-induced ionization. Taking into account the above-mentioned full simulation chain, Chapter 7 focuses on the computation of new, self-consistent, local and global production rates of the cosmogenic radionuclides  $^{10}\text{Be}$ ,  $^7\text{Be}$ ,  $^3\text{H}$ ,  $^{36}\text{Cl}$ ,  $^{26}\text{Al}$  and  $^{14}\text{C}$ . Furthermore, the computations of the global production rates of  $^{14}\text{C}$  and  $^{10}\text{Be}$  will be used to reconstruct the solar activity throughout the Holocene and to verify whether or not the computations of this work based on the self-consistent simulation chain are able to provide a reconstruction of solar activity being for the first time consistent with both  $^{10}\text{Be}$  and  $^{14}\text{C}$  archive data. A summary of the main results of this work as well as an outlook discussing possible improvements are given in Chapter 8, while a detailed outlook, presenting studies of the influence of galactic and heliospheric variations on the production of cosmogenic radionuclides, is given in Chapter 9.



# The Sun-Earth Environment

---

*“... how simple it can be,  
the sunlight on a tree ...”*

K's Choice - How simple it can be -

The space between stars is filled with charged and neutral particles but also more complex structures such as molecules and dust, an environment nowadays known as the Interstellar Medium (ISM). In the vicinity of the Sun, the ISM is pushed radially outwards by the solar wind (SW), a particle stream evolving from the Sun. As a result, a local bubble, the so-called heliosphere is built up. Additionally the Sun possesses a magnetic field being frozen into the SW and therewith carried outwards into the heliosphere, resulting in a heliospheric magnetic field (HMF). Both the size of the heliosphere and the strength of the HMF today are known to strongly depend on the solar activity.

In 1611, shortly after the invention of the telescope, Galileo Galilei, Christoph Scheiner and Johannes Fabricius independently discovered black spots on the solar surface, the sunspots, and their temporal evolution. About 250 years later, Heinrich Schwabe discovered the sunspot number to follow a quasi-periodicity of 11 – 13 years, the eleven year solar cycle, as shown in Fig. 2.1. Here the observed sunspot number from 1600 – 2010 is displayed, where periods of low sunspot number are followed by periods of high ones, implying the sunspot number to be an indicator for the solar activity. As we know today the conditions of the solar corona during these two phases change considerably.

In 1908, George Ellery Hale and coworkers discovered that sunspots always appear as pairs of opposite magnetic polarity reversing about every eleven years. They concluded that the Sun's magnetic field polarity also had to reverse itself within this period. Today one of the theories for the existence of the solar magnetic field is the turbulent dynamo theory (see e.g. Jiang et al., 2007; Choudhuri, 2008). During the evolution within a solar cycle, the solar magnetic field lines penetrate through the photosphere into the corona, thus the solar and coronal magnetic field structures undergo drastic changes. In order to discuss the effects occurring on the source surface Fig. 2.2 is shown. During solar minimum conditions (left panel), open field lines can be found over the solar poles, the so-called polar coronal holes (PCHs), while a closed field line configuration, also known as the Streamer Belts, occur in equatorial regions. During solar maximum conditions (middle panel) this picture changes dramatically. The well defined and almost symmetric structure

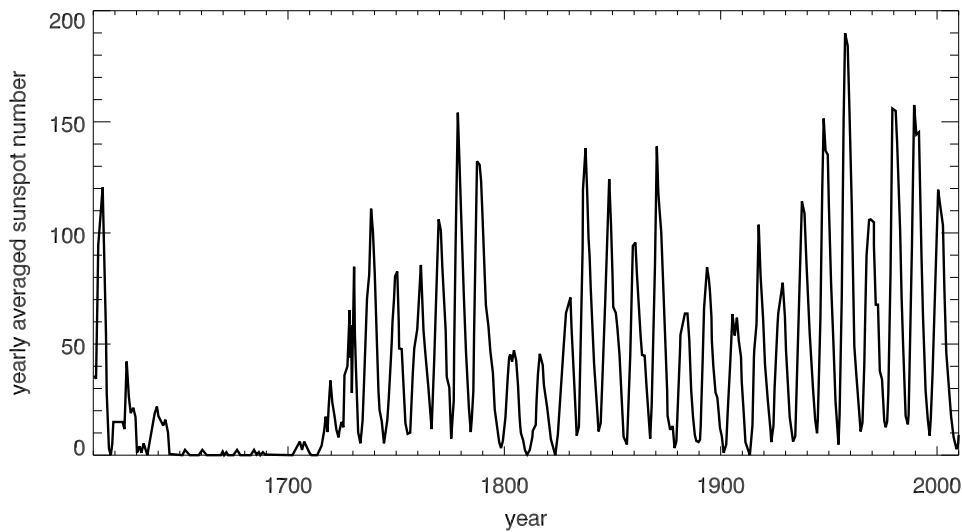


Figure 2.1: *The yearly average sunspot number between 1610–2010 (data taken from <http://solarscience.msfc.nasa.gov/SunspotCycle.shtml>).*

during solar minimum conditions is now revoked. Here closed loops as well as open field lines can be found all around the solar surface. After eleven years (right panel), however, the coronal magnetic field returns to its original configuration (solar minimum configuration) by showing an opposite polarity. Thus, another full solar cycle is needed in order to transverse the solar magnetic polarity back to initial conditions. Hence, a second solar cycle known as the solar magnetic cycle (also Hale-cycle) with a periodicity of 22 years exists.

This Chapter will summarize the theoretical background of this work. After introducing the cosmic ray components taken into account as well as their modulation with the solar activity cycle (see Section 2.2), the configuration and functionality of the Earth’s magnetic field (see Section 2.3), the Earth’s atmosphere and the particle interactions within (see Section 2.4) will be investigated.

## 2.1 Cosmic Radiation Environment

Cosmic rays (CRs) are energetic charged particles. Their discovery goes back to the year 1912 when Victor Hess during multiple balloon flights detected that the intensity of the ionizing radiation was increasing with increasing altitude. Because the measurements during the daytime showed only minor differences to those during the nighttime he concluded that the Sun and its solar particles

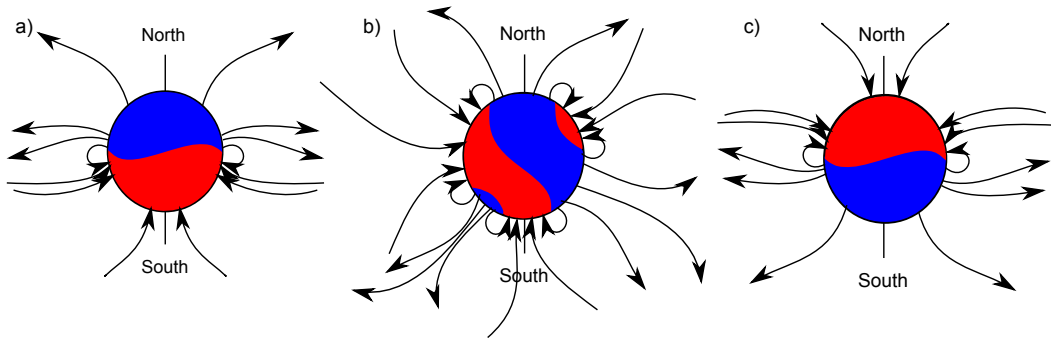


Figure 2.2: *The eleven year solar activity cycle. Starting with solar minimum conditions (left panel), where a well defined and almost symmetric structure occurs, the solar magnetic field changes dramatically in time. During a solar maximum (middle panel) closed loops as well as open field lines are mixed and distributed all over the solar surface. After eleven years, the coronal magnetic field is back in its original configuration (left panel) but with an opposite polarity (adapted from Forsyth, 2001).*

could not be the source of this phenomena. In contrast to the expectations, he discovered the discharging to be much faster at higher altitudes than on the ground, leading to the assumption of an electromagnetic radiation inside the atmosphere. Furthermore, during the 1930's the influence of the Earth's magnetic field on CRs was discovered, thus since then CRs are known to be electrically charged particles. By using spatially separated detectors in 1939 Pierre Auger additionally discovered extensive air showers (EAS). He concluded that the primary cosmic ray particles are interacting with the atmospheric atoms and molecules by initiating the production of second generation particle cascades (see Section 2.4).

With respect to their origin today between three main CR components can be differentiated:

#### a) Anomalous Cosmic Rays (ACRs)

ACRs are particles accelerated within the heliosphere (see e.g. Fichtner, 2001). Formally being interstellar neutral particles, ACRs are believed to undergo photo-ionization or charge exchange in the vicinity of the Sun, therefore becoming pick-up ions (PUIs). Once these particles are charged they are coupled to the interplanetary magnetic field and carried outwards with the solar wind. Fisk and Gloeckler (2009) suggested that most PUIs are accelerated at the heliospheric shock to ACR energies. Thereby, the energization is believed to result as a consequence of momentum diffusion and/or energization at the shocks in the solar wind, effects known as the first- and second-order Fermi acceleration. After sufficient energization the ACRs escape from the shock and are able to diffuse back into the inner heliosphere again. However, note

that there exist multiple theories to explain the ACR anomaly.

b) **Solar Energetic Particles (SEPs)**

SEPs are energetic particles originating from the Sun, mainly consisting of protons, electrons and heavier ions in the energy range of several keV up to GeV. However, only about one percent of the SEP events produces particles with energies above 500 MeV which can be registered by ground based detectors like e.g. Neutron Monitors (NMs, see e.g. [Simpson, 2000](#)). Such high energetic events are so-called **Ground Level Events (GLEs)** which have been found to strongly impact the upper as well as middle atmospheric chemistry (see recent investigations by [Sinnhuber et al., 2012](#)). The most recent GLE occurred on May, 17<sup>th</sup> 2012. Since 1942 70 GLEs have been detected which are summarized e.g. by [Belov et al. \(2009a\)](#).

c) **Galactic Cosmic Rays (GCRs)**

GCRs are highly energetic particles originating from far outside our solar system which reach the Earth isotropically. Because GCRs are the basic motor for the production of cosmogenic nuclides inside the Earth's atmosphere they are of great importance for this work, and thus are discussed in more detail in the following Section.

## 2.2 Galactic Cosmic Rays (GCRs)

Originating from far outside of our solar system GCRs are able to reach energies up to  $10^{20}$  eV. Most of these particles are accelerated by supernova explosions and supernova remnants (see e.g. [Büsching et al., 2005](#)), which, for example in our galaxy, occur on average once every 50 years ([Diehl et al., 2006](#)). However, this explanation is still under scientific debate.

### The Composition of GCRs

To investigate a) the origin, b) the acceleration as well as c) the propagation of GCRs their chemical composition needs to be studied. Because of satellite based measurements, the composition of GCRs nowadays is known to consists of 98 % hadrons and 2 % electrons and photons (see e.g. [Amsler et al., 2008](#), and references therein), but due to their small contribution to the total flux, the latter particles will not be considered in this work. The hadronic component itself thereby consists of approximately 87 % protons (H), 12 % helium nuclei (He) and a small fraction of 1 % heavier elements up to iron (Fe) (see e.g. [Wefel, 1991](#)). In order to investigate the compositional abundances inside as well as outside the solar system Fig. 2.3 shows the abundances as function of the atomic number  $Z$  (see e.g. [Simpson, 1983](#); [Wefel, 1991](#); [Wiebel-Sooth et al., 1998](#), and references therein). It shows that most of the elemental compositions are similar, suggesting the GCR elements to be produced by the same process taking place in the solar system. Note that although still under debate, it is generally believed



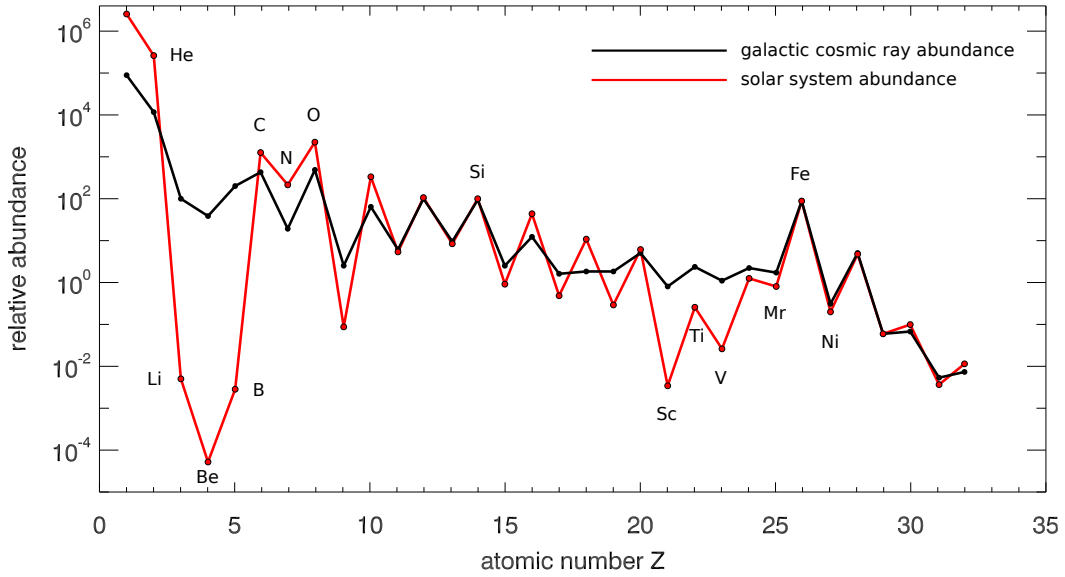


Figure 2.3: *The relative chemical abundances of particles in the solar system compared to GCRs. The abundances are normalized to silicon (adapted from [Wefel, 1991](#)).*

that in the universe most of the elements heavier than helium are created in stars when lighter nuclei fuse to create heavier nuclei, a process known as nucleosynthesis.

There are, however, two groups of elements, in particular Li, Be and B as well as Sc, Ti, V, Cr and Mr, which are much less abundant in the solar system compared to their abundance in the GCRs. An explanation can be found in the interaction of GCRs with the interstellar medium. Furthermore, the galactic hydrogen and helium abundances with high **F**irst **I**onization **P**otential (FIP) are much smaller compared to the abundance in the solar system. Here, due to the conditions inside the galaxy, a significant amount of these high FIP elements can not be ionized, and thus will not be accelerated to GCR energies (see e.g. [Müller et al., 1991](#)).

In order to reach the Earth's atmosphere, GCR particles have to traverse the galactic magnetic field, the heliospheric magnetic field (HMF) as well as the Earth's magnetosphere, leading to a strong modulation of the GCR energy spectrum, as discussed in the following.

### The Heliospheric Modulation of GCRs

As described in [Herbst et al. \(2010\)](#) the intensity of GCRs is modulated as they traverse the turbulent heliospheric magnetic field embedded into the solar wind.

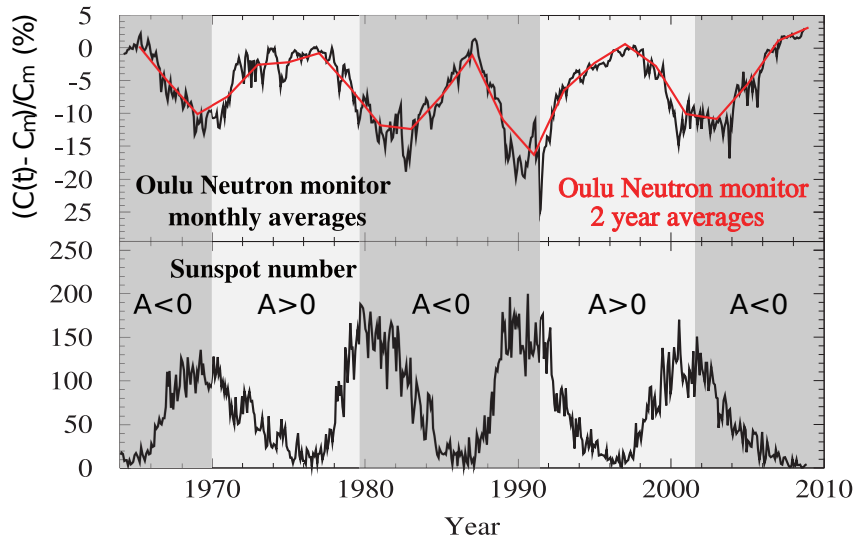


Figure 2.4: Galactic cosmic ray intensity variation as measured by the Oulu neutron monitor (upper panel). The quantity  $\xi = (C(t) - C_m)/C_m$  represents the relative change of the count rate  $C(t)$  with respect to the rate  $C_m = 6481$  counts/s, measured during the 1960’s solar minimum. The sunspot number is displayed in the lower panel (data from, <http://sidc.oma.be>). It is evident that the intensities of GCRs and the sunspot number are anti-correlated. Also shown is the “flat” (green intervals) and “peak” (red intervals) structure of the NM count rates which correlates well with the solar Hale cycle (see e.g. Heber et al., 2009).

They are scattered by irregularities in the HMF and undergo convection as well as adiabatic deceleration in the expanding solar wind. The large-scale HMF also leads to gradient and curvature drifts of the GCRs inside the heliosphere. Since all these transport processes depend on the solar magnetic activity, the GCR intensity is directly correlated to the solar activity cycle. Figure 2.4 shows the monthly averaged Neutron Monitor (NM) count rate measured at the NM station in Oulu as well as the corresponding sunspot number for the time period from 1964–2010. It shows that the neutron count rate measured at the Earth’s surface is anti correlated to the sunspot number, leading to the conclusion that the GCR flux as well as the production of secondary particles inside the atmosphere (see Section 2.4) is high during solar minimum conditions while being low during solar maximum ones, respectively.

Because of the large scale heliospheric magnetic field GCRs undergo gradient and curvature drifts, and thus the different polarities of two consecutive solar minima lead to two different drift patterns, as sketched in Fig. 2.5: If the solar magnetic field is directed outward from the sun in the northern polar region and inward in the southern polar region (left panel), also known as  $A > 0$  solar epoch, positively charged cosmic rays are expected to drift into the inner heliosphere over

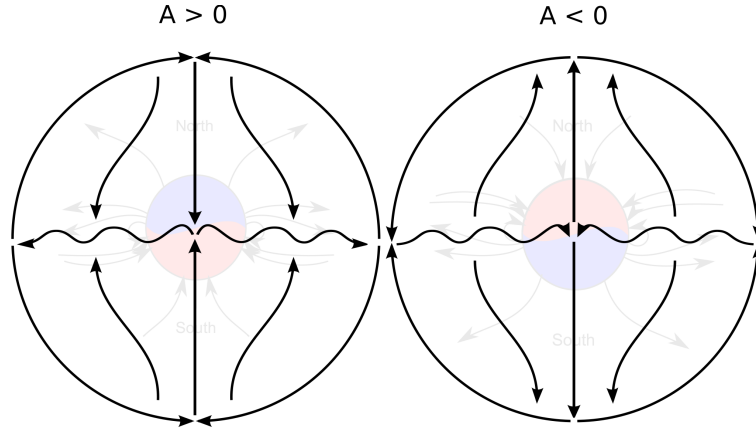


Figure 2.5: *The two different drift cycles,  $A > 0$  (left) and  $A < 0$  (right), during solar minimum conditions. While in an  $A > 0$  positively charged particles drift into the inner heliosphere over the solar poles and outwards along the heliospheric current sheet, they enter the inner heliosphere along the heliospheric current sheet and drift outwards through the polar regions during an  $A < 0$  cycle (adapted from [Dunzlaff et al., 2008](#)).*

the solar poles and outwards along the heliospheric current sheet ([Jokipii et al., 1977](#)), while in an  $A < 0$  cycle (right panel), where the drift directions are reversed, positively charged particles enter the inner heliosphere along the heliospheric current sheet and drift outwards through the polar regions ([Potgieter and Moraal, 1985](#)). Note that the situation sketched in Fig. 2.5 describes the cases when the heliospheric current sheet, the plasma sheet which separates the northern and southern magnetic polarity, is flat and coincides with the Sun's equatorial plane. Additionally from Fig. 2.4 it is evident that the count rates show alternating “flat” and “peaked” time profiles in correlation with the solar magnetic Hale cycle of about 22 years. This different pattern can be understood in terms of the different intensity variation with the inclination of the heliospheric current sheet due to gradient, curvature and current sheet drift ([Potgieter and Ferreira, 2001](#)). In an  $A < 0$  solar magnetic epoch, like in the 1980's, the intensity of cosmic rays is expected to depend on the tilt angle of the heliospheric magnetic field, and varies strongly for smaller tilt angles (“peaked” structure), while the intensity in an  $A > 0$  solar magnetic epoch varies significantly less (“flat” structure, see [Potgieter and le Roux, 1992](#)).

In order to understand the measured intensity time-profile, the transport of GCRs inside the heliosphere has to be modeled (see [Parker, 1965](#)). If  $f(\mathbf{r}, P, t)$  is the differential cosmic ray phase space distribution function, with  $\mathbf{r}$  the spatial coordinates,  $P$  the particle rigidity, and  $t$  the time, the transport equation can be

described by

$$\frac{\partial f}{\partial t} = -(\underbrace{\mathbf{V}}_1 + \underbrace{\langle \mathbf{v}_D \rangle}_2) \cdot \nabla f + \underbrace{\nabla \cdot (\overleftrightarrow{\kappa} \cdot \nabla f)}_3 + \underbrace{\frac{1}{3}(\nabla \cdot \mathbf{V}) \frac{\partial f}{\partial \ln R}}_4 + \underbrace{S}_5, \quad (2.1)$$

consisting of five different terms:

- (1) the outward convection with the solar wind speed  $v$
- (2) gradient and curvature drifts in the global HMF (Jokipii et al., 1977) with  $A > 0$  conditions in the 1970's and 1990's and  $A < 0$  conditions in the 1980's of Fig. 2.4.
- (3) the diffusion through the irregular heliospheric magnetic field: the diffusion tensor  $\overleftrightarrow{\kappa}$  consists of a coefficient parallel to the magnetic field line ( $\kappa_{\parallel}$ ) and two perpendicular diffusion coefficients for radial ( $\kappa_{\perp r}$ ) and polar directions ( $\kappa_{\perp \vartheta}$ ).
- (4) the adiabatic energy change due to the divergence of the expanding solar wind.
- (5) the local sources, e.g. particles accelerated at the Sun.

Thus, a detailed description of ground based observations would rely on a time-dependent numerical solution of Parker's transport equation (see e.g. (see e.g. Scherer and Ferreira, 2005; Ferreira et al., 2007; Florinski et al., 2008)).

Especially the adiabatic energy change due to the divergence of the expanding solar wind,  $\frac{1}{3}(\nabla \cdot \mathbf{V}) \frac{\partial f}{\partial \ln R}$ , strongly depends on the local interstellar spectrum (LIS). However, because the LIS has not yet been measured several approximations exist in the literature. Five of these models and their modulation due to the solar activity are investigated in detail in Chapter 3.

## 2.3 The Terrestrial Magnetosphere

The Earth's magnetic field is generated by highly complex systems via dynamo processes originating in the inner core as well as in the outer interplanetary space surrounding the Earth. Between internal and external magnetic field has to be distinguished, as described in the following.

### The Internal and External Magnetic Field Structure

The Earth's magnetosphere itself evolves due to the interaction of the solar wind particles with the terrestrial magnetic field. Thereby, today the Earth's magnetic field is believed to be generated in the Earth's liquid core (see e.g. Wicht et al., 2009), where slowly moving convection currents keep stirring the core as the Earth is cooling down. Because the iron core is electrically conducting, this movement generates a dipole-shaped geomagnetic field. The charged solar wind particles are

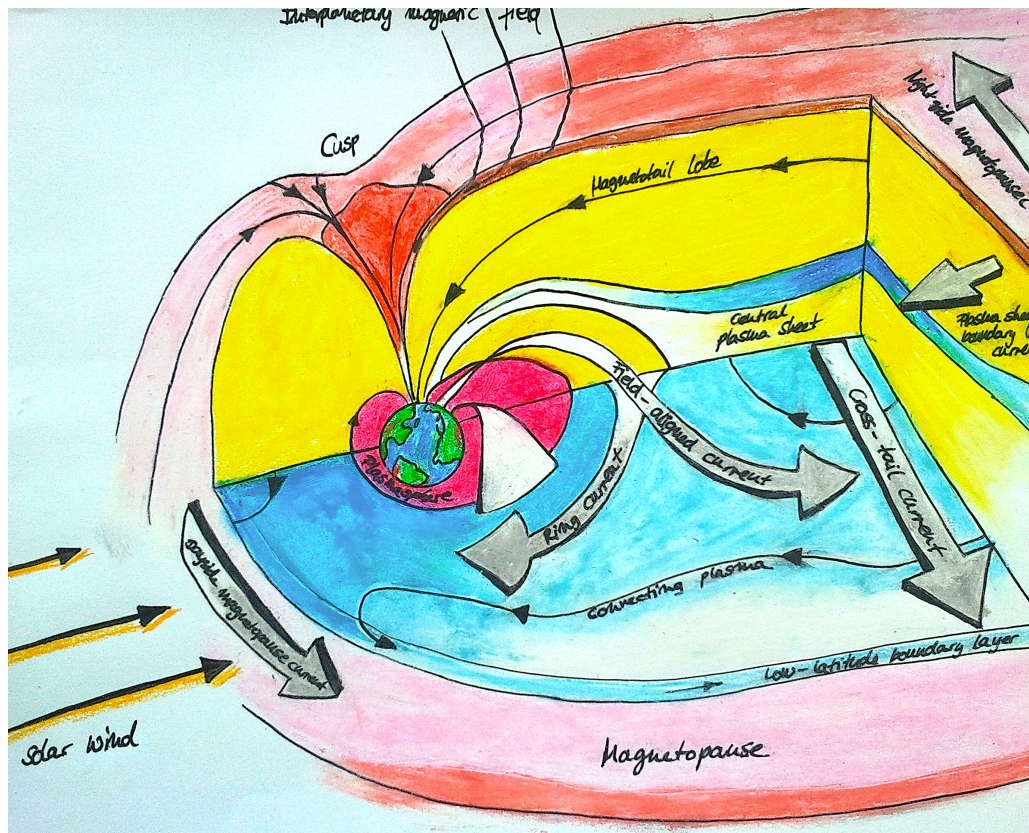


Figure 2.6: Sketch of the external terrestrial magnetic field, for further information see text. Artists impression after [Russell and Luhmann \(1997\)](#).

streaming towards the magnetic field and, due to the Lorentz force, are deflected. Therewith they are forced to flow around the Earth, thus, a magnetosphere is evolving.

As mentioned above, the internal magnetic field can be described by a dipole field which is slightly inclined with respect to the terrestrial rotation axis. Currently, e.g., the geomagnetic north pole is calculated to be at a longitude of  $72.21^\circ\text{W}$  and a latitude of  $80.08^\circ\text{N}$  with an inclination of  $9.98^\circ$  (see <http://www.ngdc.noaa.gov/geomag/faqgeom.shtml> for more information). Furthermore the magnetic center, which is shifted in comparison to the geographical center, is approximately located at a radius of 563 km,  $22.49^\circ\text{N}$  and  $140.22^\circ\text{E}$ , respectively.

The dipole-approximation, however, is only valid for regions between one and six Earth radii. While near the surface the higher dipole moments play an important role. For regions further out, however, the interaction with the solar wind

becomes more and more important. As shown in Fig. 2.6, the Earth's magnetic field interacts as an obstacle for the arriving supersonic solar wind, forming a bow shock during the deceleration from supersonic to subsonic solar wind speeds. The boundary between the Earth's magnetosphere and the solar wind plasma, the magnetopause, is thereby shaped non-uniformly along the Sun-Earth axis by forming

- a) a bullet-shaped front, which extends approximately eleven Earth radii in direction towards the Sun (dayside), which is characterized by a compression of the Earth's magnetic field lines

and

- b) a magnetic tail, which is extending up to several hundred of Earth radii in direction away from the Sun (nightside), formed by stretched magnetic field lines.

At the Cusp-regions, which are located at the magnetic poles, the compressed magnetic field lines from the dayside are bent towards the nightside. In order to describe the magnetospheric effects a complex current system is needed (see e.g. Baumjohann and Treumann, 1997), with the most important ones being:

- **Chapman-Ferraro-Currents (also magnetopause currents):** Due to the law by Ampere,  $\nabla \times \vec{B} = \mu_0 \cdot \vec{j}$ , distorted magnetic field lines always induce electric currents. The field lines inside the dayside of the Earth's magnetic field are compressed by the interaction of the charged solar wind particles with the terrestrial magnetic field. Charged particles with a certain energy start to gyrate along the magnetic field lines when they arrive at the magnetopause, thereby inducing the Chapman-Ferraro-currents in the dayside.
- **Tail Currents:** The dayside Chapman-Ferraro-currents merge into the tail currents of the nightside, where the currents of the northern as well as southern hemisphere circulate in the same direction, leading to a build up of an additional current, the **neutral sheet current**.
- **Ring Current:** The ring current, mainly induced by high energetic protons which are drifting inside the equatorial plane and additionally perform highly complex drift-, bounce- as well as gyration motions, circulates in westward direction around the Earth.
- **Birkeland Currents:** Additionally there are currents which circulate parallel to the magnetic field along the magnetic field lines from the magnetosphere to the polar regions of the ionosphere, the so-called Birkeland currents. Inside the ionosphere this system is closed by the **Hall- and Pedersen currents**.

From the mathematical point of view the Earth's magnetic field  $\vec{B}$  can be derived by a summation of the contributions from internal and external sources. According

to e.g. [Gauß \(1863\)](#)  $\vec{B}$  can be written as the gradient of the scalar potential  $\vec{V}$ :

$$\vec{B} = -\nabla\vec{V}. \quad (2.2)$$

By using a spherical harmonic model of  $\vec{V}$  (a multipole expansion) instead of a simple dipole approximation, the geomagnetic field can be modeled more realistically, and in spherical coordinates is given by:

$$V(r, \theta, \phi) = r_0 \sum_{n=1}^{\infty} \left\{ \left( \frac{r}{r_0} \right)^n T_n^{\text{ext}}(\theta, \phi) + \left( \frac{r_0}{r} \right)^{n+1} T_n^{\text{int}}(\theta, \phi) \right\}, \quad (2.3)$$

see e.g. [Connerney \(1993\)](#), with  $r_0$  as the Earth's radius and  $T_n^{\text{ext}}$  and  $T_n^{\text{int}}$  as external as well as internal source region contributions given in the following way:

$$T_n^{\text{ext}}(\theta, \phi) = \sum_{m=0}^n \{ P_n^m(\cos \theta) (G_n^m \cos(m\phi) + H_n^m \sin(m\phi)) \} \quad (2.4)$$

$$T_n^{\text{int}}(\theta, \phi) = \sum_{m=0}^n \{ P_n^m(\cos \theta) (g_n^m \cos(m\phi) + h_n^m \sin(m\phi)) \}. \quad (2.5)$$

Here  $P_n^m$  gives the Schmidt-normalized associated Legendre polynomial of degree  $n$  and order  $m$ , which are defined by

$$P_n^m(x) = N_{nm} \sqrt{(1-x)^m} \frac{d^m P_n(x)}{dx^m}, \quad (2.6)$$

with  $N_{nm} = \begin{cases} 1, & m = 0 \\ \sqrt{\frac{2(n-m)!}{(n+m)!}}, & m \neq 0 \end{cases}$  and  $P_n(x) = \frac{1}{2^n n!} \frac{d^n (x^2-1)^n}{dx^n}$ , while  $G_n^m, H_n^m, g_n^m$  as well as  $h_n^m$  represent the time-dependent Gauss coefficients describing the Earth's magnetic field.

As shown by e.g. [Pilchowski et al. \(2010\)](#) a first order approximation of the internal terrestrial magnetic field is that of a tilted geocentric dipole field, where dipole center and the Earth's center coincide. For a certain position  $\vec{r}$  the magnetic field  $\vec{B}$  is given by

$$\vec{B}(\vec{r}) = \frac{3(\vec{m} \cdot \vec{r})}{r^5} \vec{r} - \frac{\vec{m}}{r^3}, \quad (2.7)$$

with  $\vec{m}$  as the magnetic moment and  $r = |\vec{r}|$ . Considering only internal sources Eq. (2.3) reduces to

$$V(r, \theta, \phi) = r_0^3 \begin{pmatrix} g_1^1 \\ h_1^1 \\ g_1^0 \end{pmatrix} \cdot \frac{1}{r^3} \begin{pmatrix} x \\ y \\ z \end{pmatrix} = \frac{\vec{m} \cdot \vec{r}}{r^3}. \quad (2.8)$$

However, the magnetic moment  $\vec{m}$  can be expressed by

$$\vec{m} = m_0 \begin{pmatrix} \sin \Theta \cos \Phi \\ \sin \Theta \sin \Phi \\ \cos \Theta \end{pmatrix} = r_0^3 \begin{pmatrix} g_1^1 \\ h_1^1 \\ g_1^0 \end{pmatrix} \quad (2.9)$$

if  $\vec{m}$  is assumed to be tilted with respect to the rotation axis (z-axis,  $\Theta$ ) as well as by the angle  $\Phi$  around it. Therefore the magnetic field strength as well as the angles can be expressed by the expansion coefficients:

$$\begin{aligned} m_0 &= r_0^3 \sqrt{(g_1^1)^2 + (h_1^1)^2 + (g_1^0)^2}, \\ \Theta &= \arccos \left( g_1^0 / \sqrt{(g_1^1)^2 + (h_1^1)^2 + (g_1^0)^2} \right), \\ \Phi &= \arctan (h_1^1, g_1^1). \end{aligned}$$

For a tilted geocentric dipole the coefficients are given by  $\Theta = 168.6^\circ$ ,  $\Phi = 109.9^\circ$  and  $|\vec{B}| = 30760$  nT, while in case of the International Geomagnetic Reference Field (IGRF) expansion they result in  $\Theta = 169.7^\circ$ ,  $\Phi = 108.2^\circ$  and  $|\vec{B}| = 30037$  nT. Thereby the IGRF by the International Association of Geomagnetism and Aeronomy (IAGA, see e.g. [Finlay et al., 2010](#)) provides a set of Gaussian coefficients,  $g_n^m$  and  $h_n^m$ , that are computed every five years, so a reconstruction of the internal terrestrial magnetic field between 1900 and 2010 is possible.

## 2.4 The Earth's Atmosphere

The Earth's atmosphere is characterized by variations of the temperature and pressure with increasing altitude. Multiple models exist, describing the atmospheric characteristics, e.g. the Mass Spectrometer - Incoherent Scatter Model of the Upper Atmosphere developed in 1990 (MSISE90) (see [Hedin, 1991](#), and references therein) or the US Naval Research Laboratory Mass Spectrometer and Incoherent Scatter Radar Model of 2000 (NRLMSISE00) (see [Picone et al., 2002](#), and references therein). The atmosphere is in a nearly local hydrostatic equilibrium state, i.e. the difference of atmospheric pressures between two levels is always close to the weight of a column of air with unit cross section. The atmospheric temperature profile, as shown in the left panel of [Fig. 2.7](#), however, indicates the existence of multiple zones with different thermal gradients and properties classifying the atmosphere in the following way:



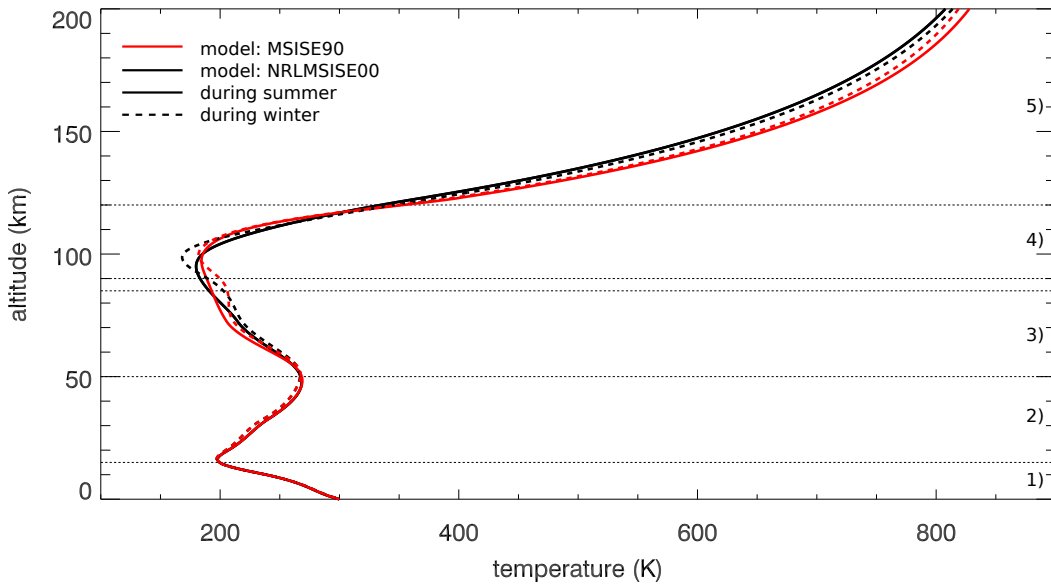


Figure 2.7: The atmospheric temperature profile for two different atmospheric models, MSISE90 (red) and NRLMSISE00 (black) during two different seasonal conditions (summer (solid lines) and winter (dashed lines)). Also shown are the temperature-based classifications of the Earth's atmosphere numerated as 1)–5) (detailed description see text).

- 1) Troposphere** The Troposphere (0 – 15 km) is the most important latitude-dependent atmospheric layer, because it contains about three-quarters of the atmospheric mass. Additionally, because of the amount of water vapor occurring in this layer and its relation to the formation of clouds, the troposphere is the layer where the terrestrial weather is formed. It is characterized by a decreasing temperature with increasing altitude, the thermal gradient depends on the humidity and is in the order of  $-6.5$  K/km, and a rapid vertical atmospheric mixing.
- 2) Stratosphere** Due to the absorption of the solar UV radiation by the trace gas ozone, the temperature increases again with increasing altitude in the Stratosphere (15 – 50 km). In contrast to the troposphere it is characterized by slow vertical atmospheric mixing.
- 3) Mesosphere** In the Mesosphere (50 – 85 km) the temperature decreases again. Here, the lowest temperatures in the entire atmosphere can be found.
- 4) Thermosphere** Inside the thermosphere (90 – 120 km) the temperature increases immediately as a result of the absorption of short-wavelength radiation by the atmospheric gases  $N_2$  and  $O_2$ . In this layer the ionosphere is embedded, i.e. the region where ions are produced by photoionization.
- 5) Exosphere** In the Exosphere (120 – 500 km) gas molecules with sufficient energy are able to escape from the Earth's gravitational force.

However, that this classification does not take into account all characteristic layers.

### Atmospheric Composition

The terrestrial atmosphere extends up to several thousand kilometers with 99.9% of the mass being concentrated in the lowest 100 km. It is primarily composed of 78 % N<sub>2</sub>, 21 % O<sub>2</sub>, 0.9 % Ar, 0.03 % CO<sub>2</sub> and a number of trace gases like CO and CH<sub>4</sub> occurring in relatively small amounts. Thereby, two of the most important parameters describing the atmosphere are a) the amount of mass contained above a certain point of interest, the atmospheric depth  $x = \frac{m}{A}$ , and b) the atmospheric pressure  $p = \frac{F}{A}$  at this location. Note that the atmospheric pressure varies between the poles and the equator, which leads to a variation of the atmospheric pressure and therewith a variation in the amount of mass contained above different locations.

### Particle Interactions in the Earth's Atmosphere

While the shielding of the Earth's magnetic field against energetic charged particles depends on the geomagnetic location, thus increasing from no shielding over the geomagnetic poles to reflecting protons with several GeV over the geomagnetic equator, the shielding of the atmosphere only depends on the atmospheric depth. This effect is known as the atmospheric cutoff (Konradi et al., 1987). In what follows the interaction of charged particles with the Earth's atmosphere will be discussed, and the atmospheric ionization as well as the production of secondary particle cascades and thus the production of cosmogenic radionuclides is investigated.

### Energy Loss by Ionization (The Bethe-Bloch-Formula)

If heavy charged particles (in this context all charged particles heavier than electrons and positrons) penetrate the Earth's atmosphere, they cause an excitation as well as an ionization of the atmospheric atoms and molecules due to inelastic scattering. Therefore, these penetrating particles experience a characteristic energy loss  $dE/dx$  depending on the particles charge and velocity.

The correct quantum-mechanical calculation was performed by Bethe, Bloch and other authors in the early 1930s, using Coulomb interactions to describe the momentum transfer of the primary particle to the target's atomic shell electrons:

$$-\frac{dE}{dx} = 2\pi N_A r_e^2 c^2 \rho \frac{Z}{A} \frac{z^2}{\beta^2} \left[ \ln \left( \frac{2m_e \gamma^2 v^2 W_{max}}{I^2} \right) - 2\beta^2 \right], \quad (2.10)$$

known as the Bethe-Bloch-formula. For energies above a few GeV two corrections have to be taken into account: a) the density effect correction  $\delta$  and b) the shell

correction  $C$  (for details see [Leo, 1994](#)), leading to:

$$-\frac{dE}{dx} = 2\pi N_A r_e^2 c^2 \rho \frac{Z}{A} \frac{z^2}{\beta^2} \left[ \ln \left( \frac{2m_e \gamma^2 v^2 W_{max}}{I^2} \right) - 2\beta^2 - \delta - 2 \cdot \frac{C}{Z} \right], \quad (2.11)$$

with

$2\pi N_A r_e^2 c^2 = 0.1535 \text{ MeV cm}^2 \text{ g}^{-1}$	$r_e = 2.817 \cdot 10^{-13} \text{ cm}$ , e <sup>-</sup> radius
$m_e$ : the e <sup>-</sup> rest mass	$\rho$ : density of the target material
$N_A = 6.022 \cdot 10^{23} \text{ mol}^{-1}$ , Avogadro number	$\beta = \frac{v}{c}$
I: mean excitation potential	z: projectile charge
Z: atomic number of the absorber	A: atomic mass
$\gamma = \frac{1}{\sqrt{1-\beta^2}}$	$\delta$ = density correction

and  $W_{max}$  representing the maximum energy transfer in a single collision:

$$W_{max} = \frac{2m_e c^2 \eta^2}{1 + 2s\sqrt{1 + \eta^2 + s^2}}, \quad (2.12)$$

with  $s = \frac{m_e}{M}$ ,  $M$  the projectile mass and  $\eta = \beta\gamma$ . If the projectile's mass is much greater than the electron mass, i.e.  $s \rightarrow 0$ , this reduces to  $W_{max} \approx 2m_e c^2 \eta^2$ .

By solving them numerically, Eq.(2.11) can be used to track the energy loss of an ion along its atmospheric path, as shown in Fig. 2.8. As can be seen, the higher the energy of the primary proton the deeper it is able to penetrate into the Earth's atmosphere, and, due to the  $v^2$  dependence of the energy loss,  $dE/dx$  is increasing with increasing primary particle energy. Note that for the same reason most of the energy of the primary particle is deposited near its stopping altitude. Because the energy loss results in an ionization of the Earth's atmosphere the deposited energy is directly linked to the atmospheric ion pair production rate (see Section 6).

According to [Kallenrode \(2004\)](#) in a first order approximation the ionization rate is given by the product of the energy loss  $dE/dx$  and the flux of the incident primary particles  $F$ , and thus depending on the collisional ionization rate  $\kappa_e$ , the energy of the ions  $E_{ion}$ , the interaction cross sections  $\sigma_n$  and the number density  $n_0$ . Taking into account the barometric height formula (see e.g. [Berberan-Santos et al., 1997](#)) the stopping altitude of a particle, given by

$$x_s = H \ln \left( \kappa_e \sigma_n n_0 H \frac{E_{ion}}{E_0} \right), \quad (2.13)$$

can easily be calculated.

### Atmospheric Production of Secondary Particles

High energetic CRs penetrating the Earth's atmosphere also undergo collisions with atmospheric nuclei. The mean free-path length  $\lambda$  of a CR inside the atmosphere is

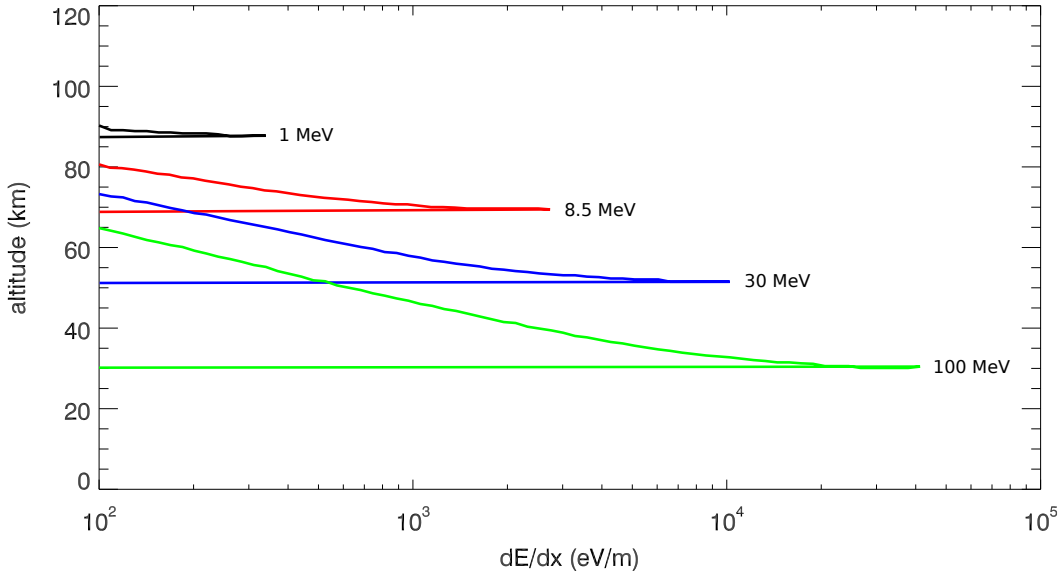


Figure 2.8: The atmospheric energy loss of primary protons with energies varying between 1 and 127 MeV. Figure after [Herbst \(2007\)](#).

defined by the inelastic cross section  $\sigma$  of the interaction between the primary CR particle and the atmospheric nuclei. Thereby

$$\lambda = \frac{1}{N \cdot \sigma}, \quad (2.14)$$

with  $N$  the number density of possible scattering centers per atmospheric volume and  $\sigma$  the specific cross sections for the process of interest, describing the probability of a certain nuclear reaction to occur. Thereby  $\sigma$  is given by

$$\sigma = \frac{\text{number of incident particles per unit time per unit area}}{\text{number of reactions per unit time per nucleus}},$$

a quantity which strongly depends on the type as well as the energy of the projectile.

Since the mean free path  $\lambda$  is not only a function of the energy dependent cross section but also on the density of the atmosphere, the altitude of the first interaction is not fixed for a particle with a specific energy, leading to fluctuations in the shower development. Thus its evolution is characterized by two terms, a source term due to a) the production of secondary particles due to the interaction of CRs with atmospheric nuclei and b) the decay of particles. The produced secondary particles themselves interact with the atmospheric atoms, thus, forming a particle cascade, an air shower (AS). How far into the atmosphere the cascade

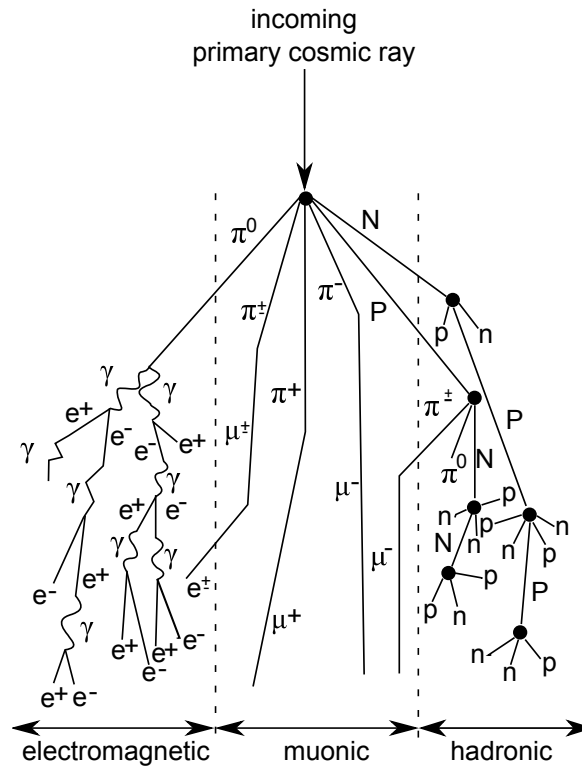


Figure 2.9: Schematic view of the development of an air shower showing the three components: electromagnetic, muonic and hadronic cascade. Figure after *Simpson (2000)*.

can develop strongly depends on the energy of the primary particle. The most important cascade components thereby are mesons, in particular  $\pi^\pm$  and  $\pi^0$ , as described in the following:

The secondary particle components produced in an air shower can be divided into three different parts: the electromagnetic, the hadronic and the muonic component (see Fig. 2.9).

During the first interaction of a CR particle with an atmospheric nucleus, a high energetic first generation of secondary particles is produced. These secondaries either decay (e.g. in  $\pi^0$ ) and/or produce a second generation of secondaries, which may also decay or interact with each other. While propagating towards the Earth's surface, an increasing production of secondary particles with increasing atmospheric depth occurs. Each new generation of secondaries is less energetic, so that at a specific altitude, the probability for a decay exceeds that of a further interaction, leading to a production maximum at a specific atmospheric depth followed by an exponential decrease. Because the atmosphere corresponds to about eleven

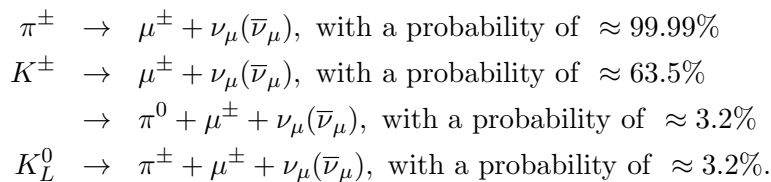
hadronic interaction lengths, only air showers generated by primaries of sufficiently high energies can be observed at sea level.

### The hadronic component

The hadronic component consists mainly of neutral and charged pions, kaons, protons and neutrons. Although only about 1% of the total number of the produced secondary particles are hadrons, this component builds the main origin of as well as feeds the electromagnetic and muonic component. The reason for this mechanism is the following: One third of the pions produced in the hadronic shower are neutral. They are short-lived and most of them decay into a pair of photons before interacting with atmospheric nuclei. These photons are able to interact with the atmospheric nuclei by producing electron-positron pairs which produce photons themselves due to bremsstrahlung, an electromagnetic radiation which is generated by a sudden, impact-related, deceleration of a charged particle during a deflection from another charged particle. The muonic component on the other hand is generated by decays of charged mesons. Note that the composition of the air shower changes from high to low altitudes. While being proton-dominated at the top of the atmosphere a neutron-dominated composition occurs at sea level (see e.g. [Masarik and Beer, 1999](#)).

### The muonic component

The muonic component is generated by decays of mesons generated in the hadronic component. While the decay of charged pions is the dominant process for the muon production, also neutral kaons excite a small contribution. Whether a meson decays or interacts with the atmospheric nuclei, depends strongly on the relative magnitudes of its mean decay length and its mean free path length with respect to hadronic interactions. The following reactions contribute to the muon production (see e.g. [Brüggemann, 2006](#)):



Due to the atmospheric density profile, the possibility of an interaction of mesons with an atmospheric nucleus increases with decreasing altitude. Therefore, mesons are able to decay only at high altitudes before they interact, so most muons are produced high in the atmosphere, i.e. in an early stage of the shower development, accounting for 5% of the total number of particles in an extensive air shower.

### The electromagnetic component

The electromagnetic component mainly consists of electrons, positrons and photons generated by the decay of the neutral pions produced in the hadronic component. As mentioned above, about one third of all pions produced in the hadronic

component are neutral and decay into a pair of photons. These photons are able to interact with the atmospheric nuclei by producing electron-positron pairs:

$$\gamma + \text{nucleus} \rightarrow \text{nucleus} + e^+ + e^-.$$

Due to bremsstrahlung, these electron-positron pairs generate further photons:

$$e^\pm + \text{nucleus} \rightarrow \text{nucleus} + e^\pm + \gamma.$$

An electromagnetic sub-cascade develops, because both processes feed each other. In addition, neutral pions which are generated along the shower axis also create sub-cascades, thus they become the most numerous particles in an air shower. If the energy of the electrons and positrons decreases below a certain critical energy (for air  $E_{crit} = 84.2$  MeV) the electromagnetic cascade is dying out.





# The Solar Modulation

---

★ *As denoted in the corresponding Sections parts of this Chapter are published as [Herbst et al. \(2010\)](#) and are in press as [Herbst et al. \(2012a\)](#).*

---

*“... I went out to walk through distant streets  
and a distant mind ...”*

Alin Coen Band - Halo -

As mentioned in Section 2.2 the CR flux inside the heliosphere shows temporal variations due to the 11-year solar and 22-year magnetic cycle. Nowadays it is known that processes like, e.g., the ionization of the atmosphere as well as the production of the cosmogenic radionuclides are strongly influenced by this modulation (see e.g. [Moraal, 2011](#)). Based on the transport equation (see Eq.(2.1)) in the following two approaches and their results will be investigated in more detail.

## Force Field Solution

According to the approximations by [Caballero-Lopez and Moraal \(2004\)](#) (see also [Gleeson and Axford, 1968](#)), the Parker equation can be reduced to a simple convection-diffusion equation, if there is (a) no source of cosmic rays inside the heliosphere, (b) a steady state, (c) the adiabatic energy loss rate is zero, and (d) there are no drifts. If only the radial direction is taken into account, a single parameter, the so called modulation parameter or modulation potential  $\phi$ , can be obtained:

$$\phi = \int_r^{r_b} \frac{v(r')}{3\kappa} dr', \quad (3.1)$$

with  $v$  the solar wind speed,  $\kappa$  the global averaged diffusion coefficient and  $r_b$  the outer modulation boundary, like the solar wind termination shock or the heliopause ([Caballero-Lopez and Moraal, 2004](#)), from which the solution of the transport equation can be computed. A typical form of the resulting distribution function is  $f = f_b \exp(-3\phi/(\beta\kappa))$ , with  $f_b$  representing the local interstellar spectrum (LIS) and  $\beta = v/c$  ([Moraal, 2011](#)). Since  $\phi$  has the dimension of an electric potential, it also is often called the Force Field potential. Typical values of  $\phi$  vary from 300 MV in current solar minimum conditions up to 2,000 MV during solar maximum conditions. Notice that the Force Field formalism results in a modulation potential that causes energy, rigidity, or momentum changes, while the original assumption was that the adiabatic energy loss term is negligible compared to the two spatial streaming terms (see Eq. (2.1)). There is no straight forward physical reason why

this field, force, or energy loss, is related to the true adiabatic loss. The Force Field energy loss originates from the introduction of the Compton-Getting spectral term  $-(1/3)\partial \ln f / \partial \ln R$ .

Nevertheless, Caballero-Lopez and Moraal (2004) (see also Moraal, 2011) investigated the validity of these simplifications by comparing the results of the Force Field solution with those of a numerical computation and found that the approximation is able to describe the modulation of the LIS at 1 AU by using the following equation:

$$J(E, \phi) = J_{LIS}(E + \Phi) \frac{(E)(E + 2E_r)}{(E + \Phi)(E + \Phi + 2E_r)} \quad (3.2)$$

Here, the modulation function  $\Phi$  is given by  $\Phi = (Ze/A)\phi$ , with  $Z$  and  $A$  as charge and mass number of cosmic ray nuclei, respectively,  $\phi$  the modulation parameter in MV,  $E$  the particles kinetic energy in MeV/nuc,  $E_r$  the rest energy, thereby  $E_r \approx 938$  MeV for protons, of the GCR particle and  $J_{LIS}$  the differential intensity spectra of the Local Interstellar Spectrum (LIS), representing the boundary condition of the Force Field model.

Due to the fact that the LIS until now has not been measured in-situ, different representations of these spectra exist. The LIS is well determined in the high energy range beyond several GeV, however, note that due to the adiabatic cooling processes of ions in the energy range below a few hundred MeV the LIS model is practically unknown in this energy interval. Thus, several LIS-approximations for the energy spectrum of primary protons, alpha particles as well as heavier particles exist.

### 3.1 The Local Interstellar Spectrum

The Force Field model is only a first order approximation of the influence of the particle transport in the heliosphere. Nevertheless this approximation in the following will be used to investigate the modulation of the galactic cosmic proton and alpha spectra by Garcia-Munoz et al. (1975), Webber and Higbie (2003), Langner et al. (2003), Usoskin et al. (2005) and Webber and Higbie (2009).

#### Approximation by Usoskin et al. (2005) (Abbrev.: US05)

The latitudinal gradients of GCRs as measured by the Ulysses spacecraft (Heber et al., 1996) have been a challenge for numerical transport models. A first approach to model the variation using a two-dimensional code solving Parker's transport equation was made by Burger et al. (2000). A parametrization of the LIS computations

given in [Burger et al. \(2000\)](#) was found by [Usoskin et al. \(2005\)](#):

$$J_{p,US05}(E) = \frac{1.9 \cdot 10^4 \cdot P(E)^{-2.78}}{1 + 0.4866 \cdot P(E)^{-2.51}}$$

Here  $P(E) = \sqrt{E(E + 2 \cdot E_{rest})}$ ,  $E$  is expressed in units of (GeV/nuc) and  $J_{p,\alpha,US05}$  in (particles/(m<sup>2</sup> sr s GeV/nuc)). Additionally the ratio of alpha to proton particles is in the order of 0.03 [Gaisser and Stanev \(2006\)](#) or 0.05 ([Usoskin et al., 2005](#)) in the local interstellar medium. In this work the ratio is assumed to be 0.05, thus the primary alpha particle spectra is given by:

$$J_{\alpha,US05}(E) = 0.05 \cdot \frac{1.9 \cdot 10^4 \cdot P(E)^{-2.78}}{1 + 0.4866 \cdot P(E)^{-2.51}},$$

### Approximation by [Langner et al. \(2003\)](#) (Abbrev.: *LA03*)

The proton LIS by [Langner et al. \(2003\)](#) is based on a complex GCR propagation model by [Moskalenko et al. \(2002\)](#) and is given by:

$$J_{p,LA03} = \begin{cases} \exp\left(a - b(\ln E)^2 + c \ln E - d\sqrt{E}\right) & E < 1,000 \text{ MeV/nuc} \\ \exp\left(e - f \ln E - \frac{g}{E}\right) & E \geq 1,000 \text{ MeV/nuc} \end{cases} \quad (3.3)$$

with  $a=0.823$ ,  $b=0.08$ ,  $c=1.105$ ,  $d=9.202 \cdot 10^{-2}$ ,  $e=22.976$ ,  $f=2.86$  and  $g=1.5 \cdot 10^3$ , as well as  $E$  given in MeV/nuc, and the differential proton flux  $J_{p,LA03}$  in particles m<sup>-2</sup> s<sup>-1</sup> sr<sup>-1</sup> (MeV/nuc)<sup>-1</sup>.

Unfortunately [Langner et al. \(2003\)](#) only presents the proton LIS. However, by using the alpha to proton ratio method by [Gaisser and Stanev \(2006\)](#), as previously mentioned, the alpha LIS is given by

$$J_{\alpha,LA03} = 0.05 \cdot J_{p,LA03}. \quad (3.4)$$

### Approximation by [Garcia-Munoz et al. \(1975\)](#) (Abbrev.: *GM75*)

The proton and alpha LIS models by [Garcia-Munoz et al. \(1975\)](#) are given by

$$\begin{aligned} J_{p,GM75}(E) &= 9.9 \cdot 10^8 [E + 780 \exp(2.5 \cdot 10^{-4} E)]^{-2.65} \\ J_{\alpha,GM75}(E) &= 1.8 \cdot 10^8 [E + 660 \exp(1.4 \cdot 10^{-4} E)]^{-2.77}, \end{aligned}$$

with  $E$  in units of (MeV/nuc) and  $J_{p,\alpha,GM75}$  in (particles/(m<sup>2</sup> sr s MeV/nuc)).

### Approximation by [Webber and Higbie \(2003\)](#) (Abbrev.: *WH03*)

This spectrum is derived from galactic cosmic ray propagation calculations by [Webber and Lockwood \(2001a\)](#) and [Webber and Lockwood \(2001b\)](#). They are given in the following way:

$$\begin{aligned} J_{p,WH03}(E) &= 21.1 \cdot \left[ E^{-2.8} \cdot (1 + 5.85E^{-1.22} + 1.18E^{-2.54})^{-1} \right] \\ J_{\alpha,WH03}(E) &= 1.075 \cdot \left[ E^{-2.8} \cdot (1 + 3.91E^{-1.09} + 0.9E^{-2.54})^{-1} \right], \end{aligned}$$

with  $E$  in units of (GeV/nuc) and  $J_{p,\alpha,WH03}$  in (particles/(m<sup>2</sup> sr s MeV/nuc)).

### Approximation by **Webber and Higbie (2009)** (Abbrev.: *WH09*)

Employing a Monte Carlo Diffusion Model, **Webber and Higbie (2009)** calculated interstellar proton, helium, carbon and iron spectra on the base of recent Voyager measurements. The determined proton LIS was parameterized by **Herbst et al. (2010)** as well as **Webber and Higbie (2010)**. For the latter approximation the following equations were presented:

$$\begin{aligned} J_{p,WH09}(E) &= (18.9/E^{2.79})/(1 + 6.75/E^{1.22} + 1.3/E^{2.8} + 0.0087/E^{4.32}) \\ J_{\alpha,WH09}(E) &= (0.99/E^{2.77})/(1 + 4.14/E^{1.09} + 0.65/E^{2.79} + 0.0094/E^{4.2}), \end{aligned}$$

with  $E$  given in GeV/nuc and  $J_{p,\alpha,WH09}$  in units of (particles/(m<sup>2</sup> sr s MeV/nuc)).

However, the previous work by **Scherer et al. (2011)** and the results displayed in Chapter 3.2 will show that the LIS model by **Webber and Higbie (2009)** is rather the heliopause spectrum (HPS) than a LIS spectrum.

### Comparison of the Different Proton and Helium Spectra

Figure 3.1 shows the ratios of the proton (upper panel) and alpha particle (lower panel) LIS-model dependent differential intensities with respect to the energy spectrum by **Usoskin et al. (2005)**. It shows that all spectra are in good agreement with each other at energies above 30 GeV/nuc. At lower energies, however, differences up to a factor of two for both primary particle types exist.

In addition Fig. 3.2 shows the modulation of the LIS models investigated at 1 AU for two different solar modulation parameters. While the upper panel shows the particle flux during solar minimum condition ( $\phi=500$  MV) the lower panel displays the results for typical solar maximum condition ( $\phi=1,500$  MV). Here protons are given by the black lines, alpha particles by the red ones. For all LIS models it is evident that the higher the solar modulation parameter  $\phi$  the lower the intensity of the modulated primary particle flux. However, strong differences between the proton as well as alpha particle models becomes evident too.

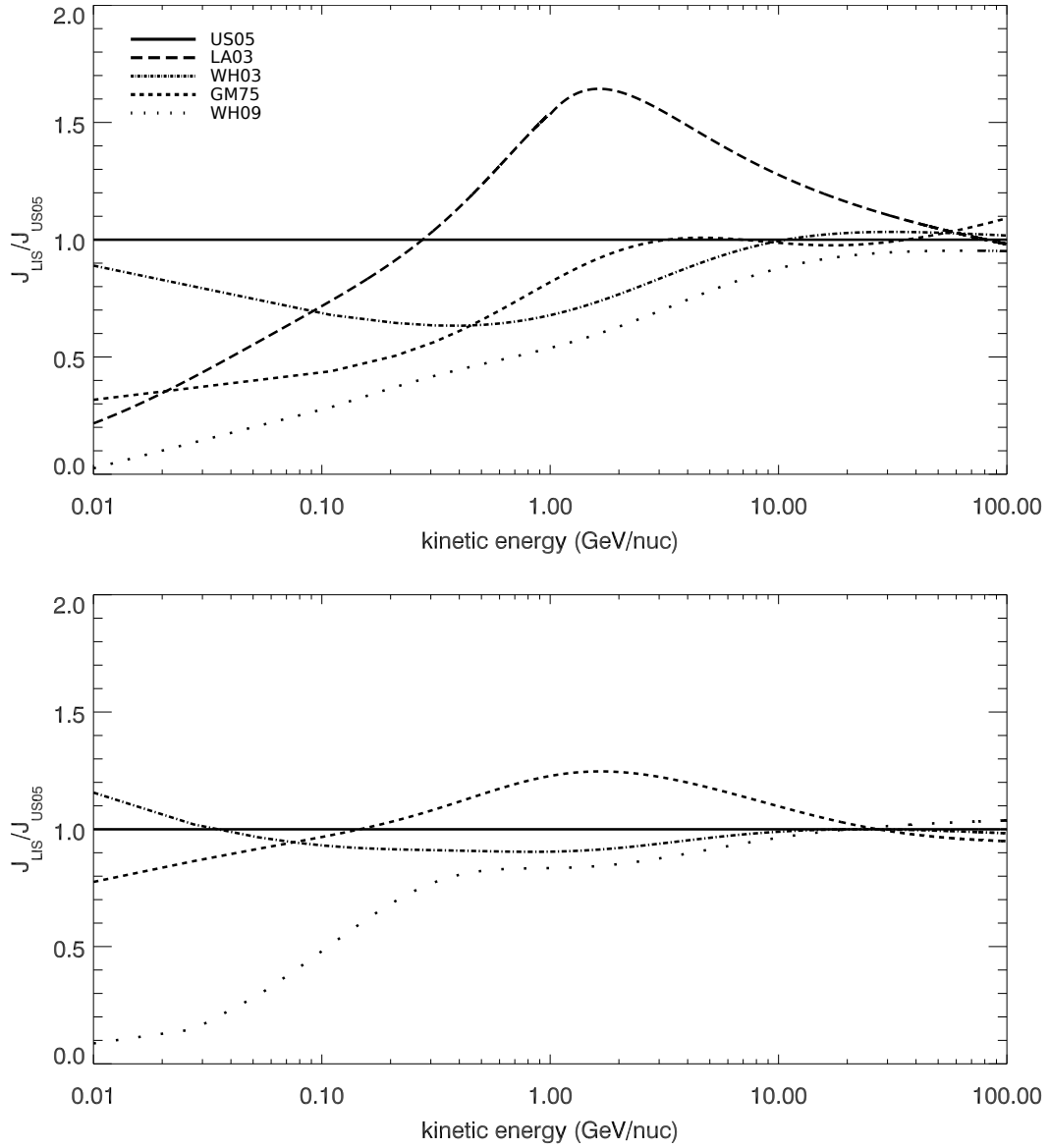


Figure 3.1: Ratios of the proton (upper panel) and alpha particle (lower panel) LIS spectra by Garcia-Munoz et al. (1975), Webber and Higbie (2003) and Webber and Higbie (2009) with respect to model by Usoskin et al. (2005).

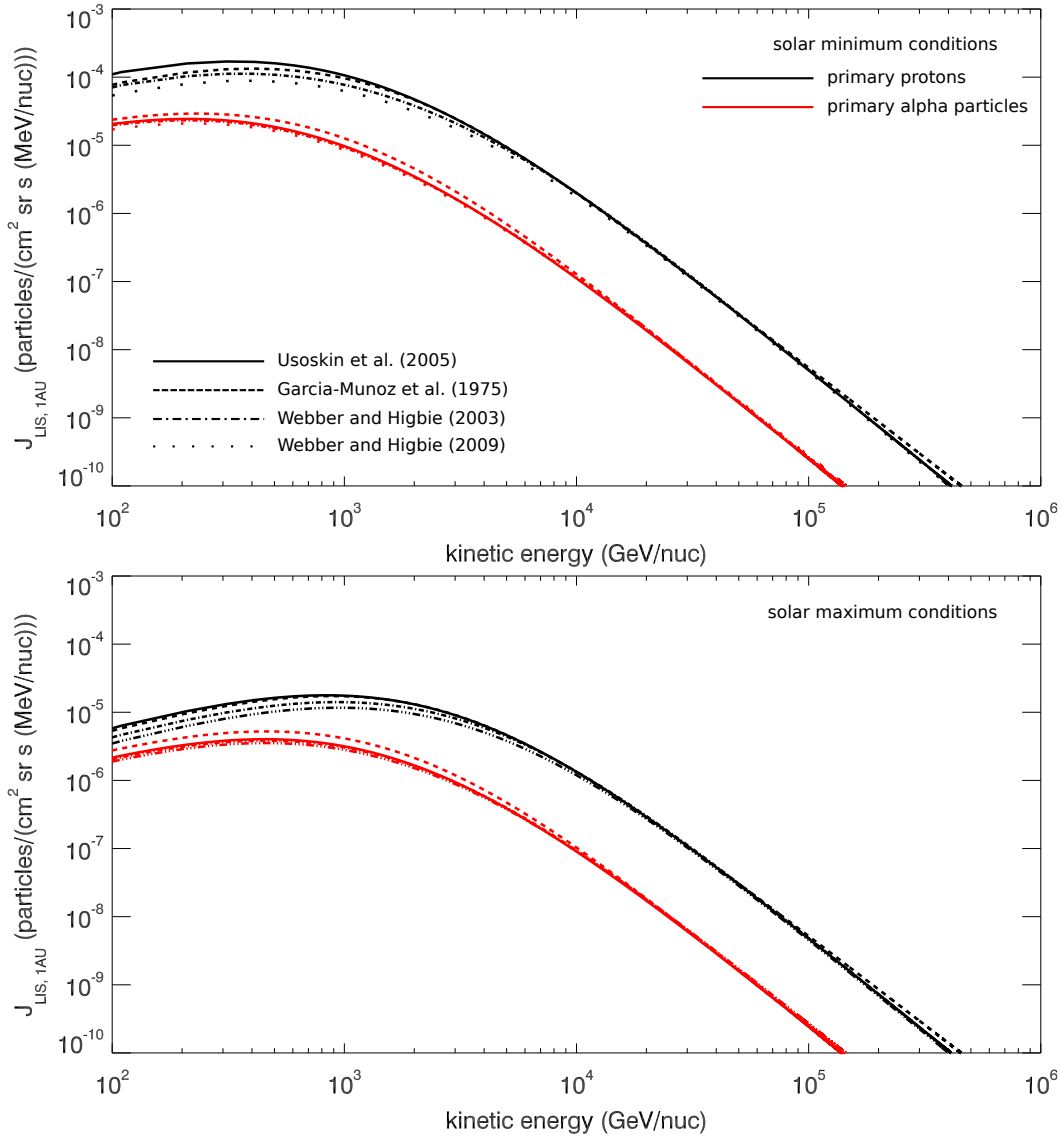


Figure 3.2: The proton (left panel) and alpha (right panel) LIS spectra by *Usoskin et al. (2005)*, *Garcia-Munoz et al. (1975)*, *Webber and Higbie (2003)* and *Webber and Higbie (2009)*.

## 3.2 The Local Interstellar Spectrum Beyond the Heliopause:

### What can be Learned from Voyager in the Inner Heliosheath?★

K. Herbst<sup>1</sup>, B. Heber<sup>1</sup>, A. Kopp<sup>1</sup>, O. Sternal<sup>2</sup> and F. Steinhilber<sup>3</sup>

<sup>1</sup> IEAP, Christian-Albrechts-Universität zu Kiel, Kiel, Germany

<sup>2</sup> MINT-Kolleg, Universität Stuttgart, Germany

<sup>3</sup> Swiss Federal Institute of Aquatic Science and Technology, Eawag, 8600 Dübendorf, Switzerland

★ *in press, ApJ as Herbst et al. (2012a)*

---

*The local interstellar spectrum (LIS) is one of the most important but unknown parameters in all model efforts to describe the modulation of Galactic Cosmic Rays on their way from the galaxy through a possible bow shock, heliosheath and heliosphere towards the Earth. Because it could not be measured so far, several LIS models derived from numerical simulations or data at Earth were developed. A new perspective to determine the LIS was opened when the Voyager spacecraft crossed the termination shock and entered the heliosheath. Webber and Higbie (2009) derived a new LIS, which is lower than all previous LIS models over the entire energy range, on the base of these measurements. Numerical simulations by Scherer et al. (2011) showed that already particles in the outer heliosheath (OHS) are modulated, suggesting that the LIS by Webber and Higbie (2009) is a heliopause spectrum rather than the “true” LIS. By using the same simplified simulation model we estimate the diffusion coefficient in the OHS to be consistent with several  $10^{26}$  to  $10^{27}$   $\text{cm}^2 \text{s}^{-1}$  for all LIS models under consideration by mapping them to this HPS and conclude that the Voyager measurements will not be able to determine the LIS in the next future. We then discuss the circumstance under which terrestrial archive can be used to at least exclude LIS models unless one has to await a dedicated mission like e.g. the Interstellar Probe.*

## Introduction

The three-dimensional region around the Sun controlled by the solar wind and its embedded magnetic field is called the heliosphere (see Fig. 3.3, dark gray region). The interaction of the supersonic solar wind with the local interstellar medium (LISM) leads to a transition of the solar wind from supersonic to subsonic speeds at the termination shock (TS). Such a transition might also occur for the interstellar wind at a possible heliospheric bow shock (BS) (cf. McComas et al., 2012); the heliopause (HP) is the boundary layer separating the LISM and the solar wind. The

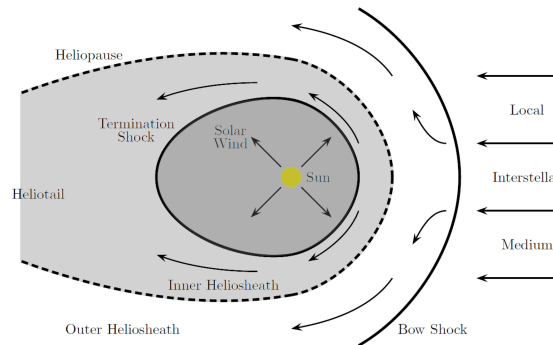


Figure 3.3: Projection of the heliosphere onto the equatorial plane, showing the streaming of the LISM from the right towards the Sun. The charged plasma interacts with the expanding solar wind and forms three discontinuities, the termination shock, the heliopause and possibly a bow shock. This structure has so far been investigated by the two Voyager spacecraft, which are currently approaching the heliopause (adapted from [Fichtner and Scherer, 2000](#)).

layer between the TS and the HP is called inner heliosheath (IHS, light gray region in Fig. 3.3), while the layer between the HP and a possible BS is called outer heliosheath (OHS). The structure of the OHS became subject of several investigations, triggered by recent observations of the Interstellar Boundary Explorer (IBEX) mission (cf. [McComas et al., 2009, 2012](#)).

The heliosphere is a protection shield against Galactic Cosmic Rays (GCRs). These highly energetic particles enter it at the HP and encounter the outward-flowing solar wind plasma, which carries a turbulent magnetic field that in average can be approximated by an Archimedean spiral. On their passage through the heliosphere the CGRs undergo modulation (e.g. [McDonald, 1998](#); [Scherer et al., 2006](#); [Potgieter, 2011](#)), so that their spectra measured at Earth are different from the spectrum at the outer boundary, the local interstellar spectrum (LIS). In lack of the possibility to directly measure this LIS in-situ several parametrizations of the proton LIS were developed with the help of galactic propagation models or derived indirectly from measurements at Earth, four of which will be investigated subsequently: [Usoskin et al. \(2005\)](#) (US05), [Garcia-Munoz et al. \(1975\)](#) (GM75), [Webber and Higbie \(2003\)](#) (WH03) and [Langner et al. \(2003\)](#) (LA04).

In order to compare these various LIS models with measurements at Earth's orbit, a full solution of Parker's transport equation ([Parker, 1965](#)) is required, for which the knowledge of the spatial, temporal and rigidity dependence of all parameters involved in the modulation of GCRs as well as the size of the modulation volume is needed. The LIS enters such transport models as an outer boundary condition.

This overall picture was changed in the last few years from the data point of



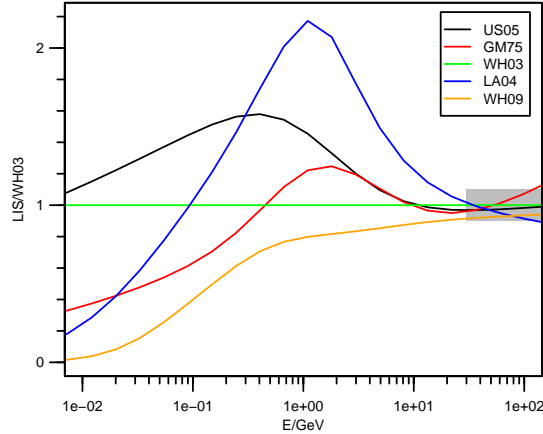


Figure 3.4: The relative intensities of the different LIS models investigated here with respect to the spectrum by [Webber and Higbie \(2003\)](#) (WH03), illustrating the differences between the spectra and especially the problem that all spectra deviate from each other at energies above several 10 GeV where hardly any modulation is expected, indicated by a tolerance interval of  $\pm 10\%$  around the WH03 spectrum.

view, but also by numerical simulations: on the one hand the Voyager 1 and 2 spacecraft crossed the TS on December 16, 2004 (at 94 AU) and July 31, 2008 (at 84 AU), respectively. [Webber and Higbie \(2009\)](#) derived a new LIS from these measurements in the IHS ([Stone et al., 2005, 2008](#)), which, as will be shown later, lies over the entire energy range below the four LIS models mentioned above. On the other hand, [Scherer et al. \(2011\)](#) used a simplified modulation model in order to demonstrate that particles detected in the OHS are modulated rather than to represent the LIS. In consequence, the boundary value at the HP for modulation studies is a modulated heliopause spectrum (HPS) rather than the LIS, which instead is applicable further out, e.g. at a possible BS. Combining these two results we conclude that the LIS by [Webber and Higbie \(2009\)](#) can be regarded as such a heliopause spectrum, and the transport parameters in the OHS (i.e. the diffusion coefficient in a simplified approach) can be estimated by comparing the modulated LIS models with this spectrum. Moreover, they have to be compatible with the HPS in the sense that they fit to the HPS for reasonable diffusion coefficients. The goal of our investigations is to compare the OHS modulation for the four LIS models and to discuss possible consequences rather than to develop a new modulation model, so that we use the simplified approach by [Scherer et al. \(2011\)](#) and can validate our modulation spectra with their results. Figure 3.4 shows the relative intensities of the LIS by US05 (black), GM75 (red), LA04 (blue) and WH09 (orange) normalized to the spectrum by WH03 (green), revealing significant variations over the entire energy range, in particular also at energies above several tens of GeV, where no modulation is expected. The Figure, moreover, reveals that the LIS by [Webber and Higbie \(2009\)](#) is the lowest spectrum over the entire energy range. As

mentioned above, this may be seen as consistent with the findings by Scherer et al. (2011) that the Voyager spacecraft measured a modulated HPS, rather than the LIS.

The amounts of modulation for the four LIS models required to “map” them to the HPS must be computed numerically by solving Parker’s transport equation (Parker, 1965)

$$\begin{aligned} \frac{\partial j}{\partial t} = & - (\vec{v}_{sw} + \langle \vec{v}_d \rangle) \cdot \nabla j + \nabla \cdot (\mathbf{K}_S \cdot \nabla j) \\ & + \frac{1}{3} (\nabla \cdot \vec{v}_{sw}) \frac{\partial}{\partial E} (\Gamma E j), \end{aligned}$$

with  $j$  representing the differential intensity that is related to the CR distribution function  $f$  by  $j = P^2 f$ , where  $P$  is the particle rigidity.  $\vec{v}_{sw}$  is the solar wind velocity,  $\langle \vec{v}_d \rangle$  represents the mean drift velocity, while  $\mathbf{K}_S$  is the diffusion tensor. The factor  $\Gamma$  is given by  $\Gamma = (E + 2E_0)/(E + E_0)$ , where  $E$  is the kinetic energy of the particle and  $E_0$  its rest energy (cf. Strauss et al., 2011). The modulation process is studied by means of numerical simulations with stochastic diffusion equations (SDEs). Like Scherer et al. (2011) we use the numerical propagation code by Strauss et al. (2011) (see also Kopp et al., 2012). The physical model is based on Potgieter (1996), the essential parts of which are given in the Appendix. Like Scherer et al. (2011) we merely vary the value of the diffusion coefficient in the OHS which can be either constant or proportional to the rigidity, scenarios which reflect two extreme cases (cf. Büsching and Potgieter, 2008; Sternal et al., 2011).

The term  $\frac{1}{3} (\nabla \cdot \vec{v}_{sw}) \frac{\partial}{\partial E} (\Gamma E j)$  in the transport equation represents the adiabatic energy change within the TS due to the divergence of the expanding solar wind. Because of the dependency of this term on the variation of  $j$  (and thus on the LIS as its outer boundary condition) with energy the various LIS models undergo different modulation. Scherer et al. (2011) demonstrated that the adiabatic energy change (under the present model assumptions always cooling) is the dominating effect responsible for the modulation in the OHS. This is illustrated further in Fig. 3.5 (cf. also Fig. 4 of Scherer et al., 2011), where the energy change (in arbitrary units) of two sample trajectories of GCR protons for constant diffusion coefficients of  $\kappa = 10^{27} \text{ cm}^2 \text{ s}^{-1}$  (left panel) and  $\kappa = 10^{25} \text{ cm}^2 \text{ s}^{-1}$  (right panel) in the OHS are shown. The numerical code calculates the particle trajectories backwards, i.e. the (pseudo) particle starts at the HP (red point) and leaves the system when it penetrates the (possible) BS (green point). The physical particle, thus, enters the heliosphere at the green point and is detected at the red one (cf. Kopp et al., 2012, for a discussion of forward/backward methods).

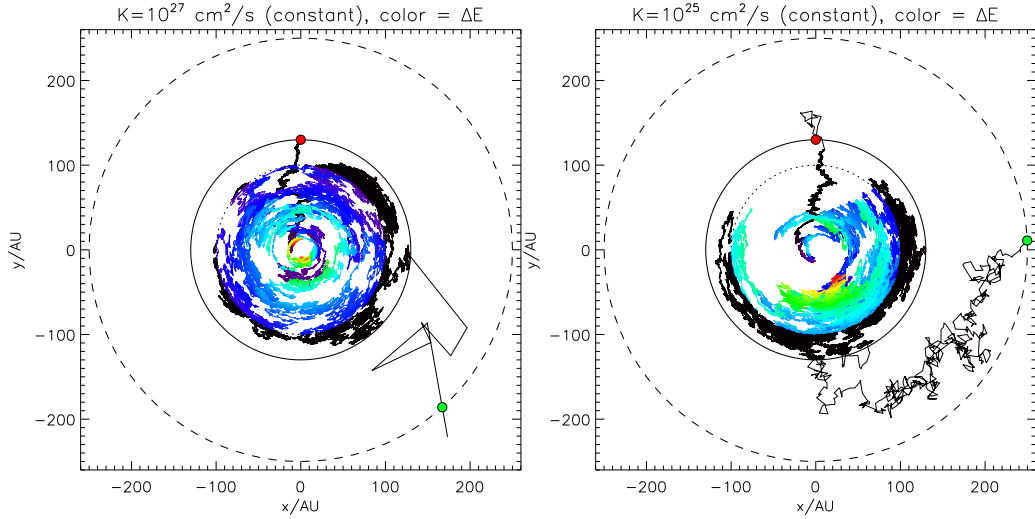


Figure 3.5: Sample trajectories of protons illustrating the OHS modulation due to adiabatic cooling within the TS for OHS diffusion coefficients of  $\kappa = 10^{27} \text{ cm}^2 \text{ s}^{-1}$  (left panel) and  $\kappa = 10^{25} \text{ cm}^2 \text{ s}^{-1}$  (right panel). The particles enter the heliosphere at a possible BS (green point), propagate through the heliosphere, undergo adiabatic cooling inside the TS and finally penetrate the HP at the red point. The color indicates the energy loss (in arbitrary units) on a scale ranging from black (no energy loss) over blue and green to red. The dotted lines represent the TS, the solid ones show the HP, while the dashed lines represent the boundary of the computational volume.

## Analysis and Discussion

### The Diffusion Coefficient in the OHS

The modulated spectra as the result of our SDE simulations for the four LIS are shown in Figs. 3.6 and 3.7 for OHS diffusion coefficients  $\kappa$  being constant and proportional to the particle rigidity, respectively. While the line style stands for the LIS model (US05: short dashes, GM75: dotted, WH03: dashed-dotted and LA04: long dashes), the color represents the value of the diffusion coefficient in the OHS:  $\kappa = 10^{25}$  (red, upper left panel),  $\kappa = 10^{26}$  (green, upper right panel),  $\kappa = 10^{27}$  (blue, lower left panel) and  $\kappa = 10^{28}$  (orange, lower right panel). Furthermore, in all four panels gray stands for the LIS itself. The colored bands indicate the range covered by all four LIS models together: the upper boundary is formed by the spectra of US05 (0.01 - 0.3 GeV) and LA04 ( $E > 0.3$ ), the lower one by the spectra of LA04 ( $E < 0.02$  GeV), GM75 (0.02 - 0.4 GeV) and WH03 ( $E > 0.4$  GeV). As expected, the modulation decreases with increasing  $\kappa$ , so that it nearly vanishes for  $\kappa = 10^{28} \text{ cm}^2 \text{ s}^{-1}$  and is stronger at lower energies for the case  $\kappa \propto P$ . The bands show in both cases a widening towards lower energies.

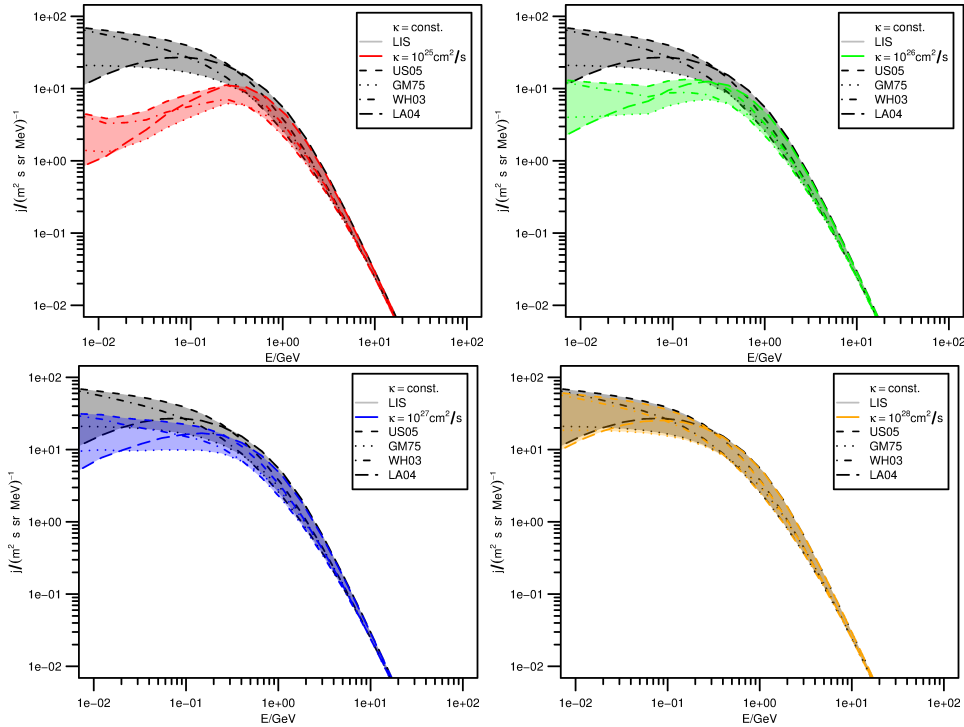
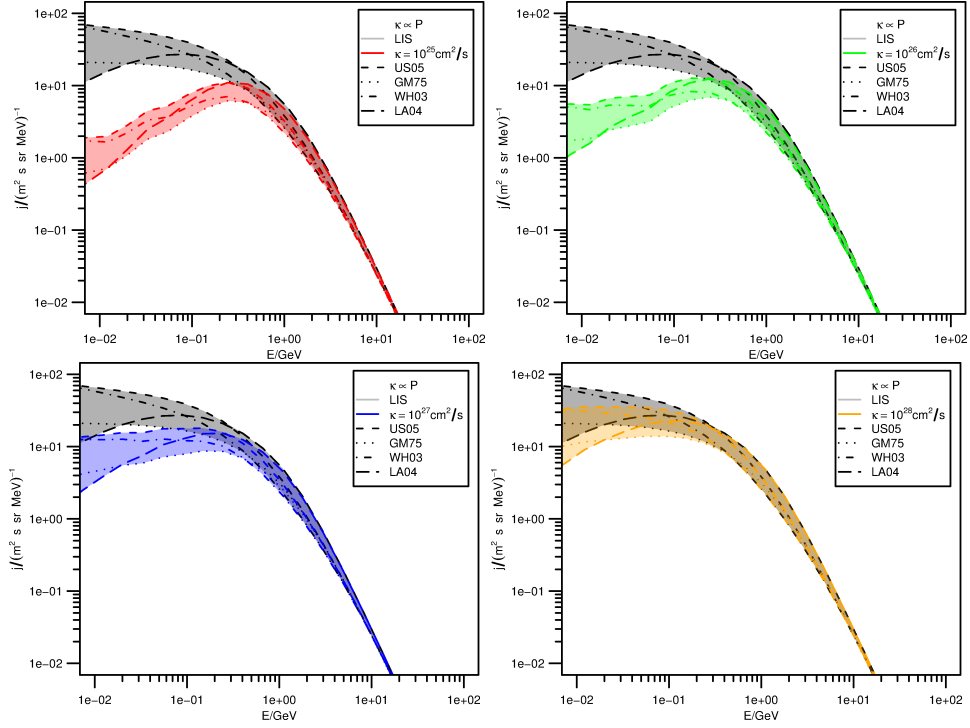
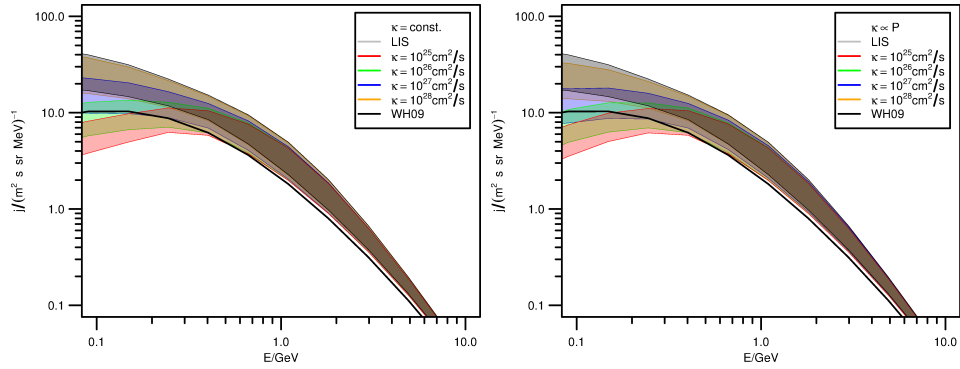


Figure 3.6: The colored bands show the modulated spectra for a constant diffusion coefficient  $\kappa$  in the OHS for the four LIS models by US05 (short dashes), GM75 (dotted), WH03 (dashed-dotted) and LA04 (long dashes), with the upper left panel showing the simulation results for  $\kappa=10^{25} \text{ cm}^2 \text{ s}^{-1}$  (red), the upper right panel for  $\kappa=10^{26} \text{ cm}^2 \text{ s}^{-1}$  (green), the lower left panel for  $\kappa=10^{27} \text{ cm}^2 \text{ s}^{-1}$  (blue) and the lower right panel for  $\kappa=10^{28} \text{ cm}^2 \text{ s}^{-1}$  (orange). In all four panels the LIS themselves are represented by the gray bands.

### Estimation of the Diffusion Coefficient in the Outer Heliosheath

We estimate the diffusion coefficient  $\kappa$  in the OHS by comparing the modulated spectra shown in Figs. 3.6 and 3.7 with the “measured” HPS by [Webber and Higbie \(2009\)](#). Fig. 3.8 shows the bands displayed in Figs. 3.6 and 3.7 in the left and right panel, respectively, together with the WH09 spectrum (black line). Although for lower energies the HPS lies in a reasonable  $\kappa$  range between  $10^{26}$  (green) and  $10^{27} \text{ cm}^2 \text{ s}^{-1}$  (blue), the simulation results as well as the unmodulated LIS models themselves exceed the HPS in the high-energy range above several 10 GeV, where essentially no modulation should be present. Allowing for a tolerance of  $\pm 10 \%$  around the LIS model by WH03 (gray area in Fig. 3.4) we shift the HPS by [Webber and Higbie \(2009\)](#), which is essentially at the lower end of this area, upwards by 10 and 20 %. The result is shown in Fig. 3.9, where only the two relevant modulation bands for  $\kappa=10^{26} \text{ cm}^2 \text{ s}^{-1}$  (green) and  $10^{27} \text{ cm}^2 \text{ s}^{-1}$  (blue) are shown. The HPS


 Figure 3.7: Same as Fig. 3.6 but for energy-dependent diffusion ( $\kappa \propto P$ ) in the OHS.

 Figure 3.8: Combination of our simulations for a constant (left panel) and rigidity-dependent (right panel) diffusion coefficient. The colored bands are taken from Fig. 3.6 and Fig. 3.7, the HPS by [Webber and Higbie \(2009\)](#) is displayed as the black line.

is represented again by the solid line, while the HPS being shifted upwards by 10% and 20% are depicted by long and short dashes, respectively. As in Fig. 3.8 the left panel shows the case of constant  $\kappa$ , the right one that of  $\kappa \propto P$  in the OHS. It

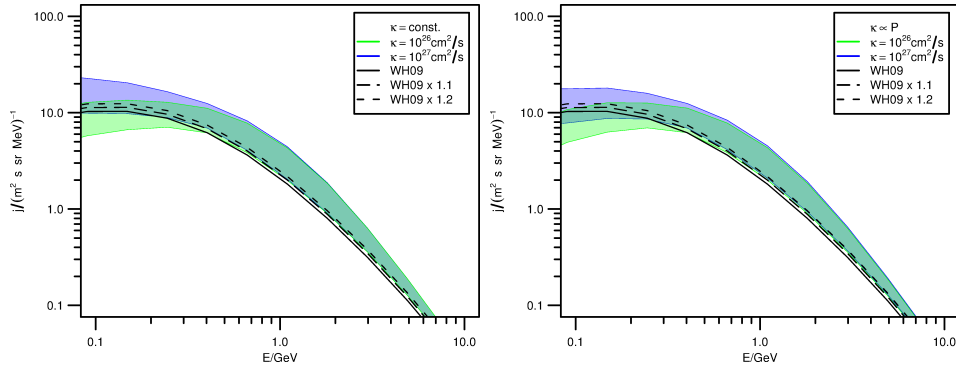


Figure 3.9: Bands for  $\kappa=10^{26} \text{ cm}^2 \text{ s}^{-1}$  (green) and  $\kappa=10^{27} \text{ cm}^2 \text{ s}^{-1}$  (blue) are shown together with the HPS (solid line), which was shifted up by factors of 10% (long dashed line) and 20% (short dashed line) within the “tolerance” area in Fig. 3.4 in order to account for deviations of the LIS models above 10 GeV, where no modulation should occur.

follows:

- a) If we permit that the spectrum proposed by [Webber and Higbie \(2009\)](#) may be shifted upwards by 10 to 20% all four modulated LIS models investigated in this study are consistent with the (modulated) HPS,
- b) the diffusion coefficient  $\kappa$  in the OHS can be estimated to a few  $10^{26}$  up to  $\kappa = 10^{27} \text{ cm}^2 \text{ s}^{-1}$

Because the colored bands in Fig. 3.9 cover all four LIS models as well possible refinements of the model, none of them can be excluded due to the Voyager measurements, and, moreover, we conclude that the Voyager spacecraft will not measure the "true" LIS, but a modulated spectrum with a diffusion coefficient in the range given above. For the access to further information on the LIS a dedicated space mission like the Interstellar Probe (ISP) has to be awaited.

Another line was followed by [Herbst et al. \(2010\)](#) who studied the variation of the so-called modulation parameter, a proxy for solar activity, with the different LIS models. In order to do so they investigated the value of this quantity during grand solar minima derived from measurements of the cosmogenic radionuclide  $^{10}\text{Be}$  in terrestrial archives like ice cores. They found that the spectra by GM75 and WH03 as well as the HPS by WH09 lead to negative modulation parameters during such periods of time, corresponding to a modulated spectrum at Earth exceeding the LIS in this approach, while all four LIS models, except perhaps the very low spectrum by [Webber and Higbie \(2009\)](#), are consistent with recent  $^{10}\text{Be}$  data, reflecting the solar activity over the last centuries. In the still simple, but more elaborated approach used in the present study such minimum conditions would

correspond to a diffusion coefficient above several  $10^{27}$  or  $10^{28}$   $\text{cm}^2 \text{s}^{-1}$ , leading to mean free paths large enough to cause almost negligible diffusion in the OHS.

### Summary and Conclusions

In this paper we used numerical simulations with the SDE approach by [Strauss et al. \(2011\)](#) and [Kopp et al. \(2012\)](#) to compute and compare the modulated spectra in the outer heliosheath for the four LIS models by [Usoskin et al. \(2005\)](#), [Garcia-Munoz et al. \(1975\)](#), [Webber and Higbie \(2003\)](#) and [Langner et al. \(2003\)](#). A fifth LIS model was derived by [Webber and Higbie \(2009\)](#) from recent Voyager measurements and lies below the other four LIS models over the entire energy range. Motivated by the findings by [Scherer et al. \(2011\)](#) who demonstrated that modulation occurs already in the outer heliosheath instead at the heliopause we concluded that this spectrum is a modulated heliopause spectrum rather than the “true” LIS. By comparing the four modulated LIS spectra with this heliopause spectrum we can estimate the diffusion coefficient to lie in the range between a few  $10^{26}$  and  $10^{27}$   $\text{cm}^2 \text{s}^{-1}$ . Since all four LIS models are, thus, compatible with the Voyager data, none of them can be excluded. And since Voyager obviously detected a modulated spectrum rather than the LIS, there will be no way to measure LIS in the next future, and only a dedicated mission like e.g. the Interstellar Probe (ISP) can be expected to do so.

Boundary conditions for the proper choice of the LIS, although no simple way to derive the LIS exists, may, however, come from the other end of the modulation chain: the results by [Herbst et al. \(2010\)](#) indicate that some of the LIS models are not consistent with data of cosmogenic radionuclides in so far as the modulated spectra at Earth would exceed the LIS during grand solar minima, as discussed in Section 3.4. These findings, however, are based on the usage of simplifying proxies for solar activity, so that a fully self-consistent model chain (e.g. [Scherer et al., 2006](#); [McCracken and Beer, 2007](#)) is probably required to learn more about the LIS.

### 3.3 Parker Equation Versus Solar Modulation Parameter

Although being much more physical, following the full Parker Equation (see Eq.(2.1)) with 3D simulations is a time-consuming process. In addition for each set of conditions, e.g. over thousand of years, new computations need to be performed. Because this is far beyond present computational capabilities in the following the Force Field solution is used in order to describe the solar activity throughout the Holocene. In the energy-range of interest for the computation of the cosmogenic radionuclides, 0.4 – 8 GeV, this is a valid simplification, as shown in Fig. 3.10. Here, the LIS by [Usoskin et al. \(2005\)](#) is shown as solid line, the computations for a mod-

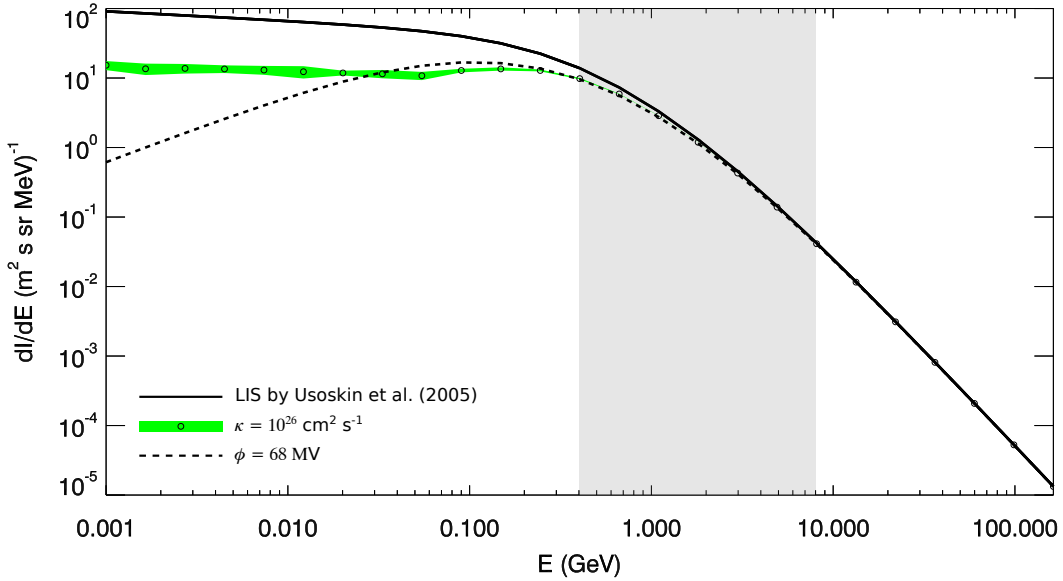


Figure 3.10: Modulation of the LIS by Usoskin et al. (2005) due to the SDE simulation results for a diffusion tensor of  $\kappa = 10^{26} \text{ cm}^2 \text{ s}^{-1}$  in comparison to a Force Field solution based modulation parameter of  $\phi = 68 \text{ MV}$ . Shaded in gray is the energy range of interest for the production of cosmogenic radionuclides (0.4 – 8 GeV).

ulation of  $\kappa=10^{26} \text{ cm}^2 \text{ s}^{-1}$  are displayed as open dots, the green band corresponds to its variations, while the results for a solar modulation parameter of  $\phi=68 \text{ MV}$  are given as dashed line. In addition, the energy-range of interest is displayed as gray shaded area. Although strong differences in the low energy range can be observed, the results of both approaches, moreover, within the shaded area are in good agreement, revealing that for the purpose of the following investigations the solar modulation is a sufficiently good approximation.

### 3.4 Conversion of the Solar Modulation Parameter

★ *Parts of this Section are published as Herbst et al. (2010)*

As already shown in Section 3.1 the modulation parameter  $\phi$  strongly depends on the used LIS model (see also Usoskin et al., 2005). In the following Section this dependency will be investigated further and an energy range dependent method to convert the different LIS dependent modulation parameters into each



LIS models	$\phi$ in MV	$\eta^2$
<i>US05</i>	526	0.059
<i>LA03</i>	749	0.129
<i>GM75</i>	481	0.034
<i>WH03</i>	378	0.040
<i>WH09</i>	322	0.097

Table 3.1: *The model-dependent modulation parameters  $\phi_i$  adapted by the best-fit method and the corresponding goodness values ( $\eta_i^2$ , see Equation (3.5)).*

other is introduced and examined (see also [Herbst et al., 2010](#)). As a first step the proton LIS-dependent  $\phi$  values will be calculated using proton measurements by the PAMELA experiment ([Casolino et al., 2009](#)) at 1 AU. Note, that the following investigations at the end of this Section also will be applied to the alpha LIS models.

In order to calculate the solar activity parameter, the individual  $\phi$  values are determined by fitting the modulated proton LIS spectra to recent measurements. For this purpose the proton spectrum measured by the PAMELA instrument ([Casolino et al., 2009](#)) during the solar minimum conditions in July 2006 was used. To describe the observations for each LIS model an individual modulation parameter  $\phi_i$  can be found by minimizing the function

$$\eta_i^2 = \sum (J_{1\text{AU}}(\text{E}, \phi_i, \text{LIS}_i) / J_{1\text{AU}}^{\text{PAM}}(\text{E}) - 1)^2 \quad (3.5)$$

between the PAMELA measurements ( $J_{1\text{AU}}^{\text{PAM}}(\text{E})$ ) and the modulated GCR spectra ( $J_{1\text{AU}}(\text{E}, \phi_i, \text{LIS}_i)$ ).

The resulting modulation parameters  $\phi_i$  as well as the corresponding best fit values ( $\eta_i^2$ ) are listed in Table 3.1. Additionally the ratio of the adapted spectra to the PAMELA measurements are shown in Fig. 3.11. Note, that the values of  $\eta^2$  represent the goodness values of the LIS models for an energy range of 0.4 to 8 GeV/nuc, the energy range most important for the production of the cosmogenic radionuclide  $^{10}\text{Be}$  (see e.g. [McCracken, 2004](#); [Masarik and Beer, 2009](#)).

From Fig. 3.11 it is evident that the proton LIS model by [Langner et al. \(2003\)](#) shows higher  $\eta^2$  values compared to the other models, a fact which is caused by high deviations from the measurements in the lower energy range. However, it also shows that all LIS models are able to represent the observed spectrum fairly well within the applied energy range of 0.4–8 GeV. Note, that the LIS dependent modulation parameter range from  $\phi_{\text{WH09}}=322$  MV up to  $\phi_{\text{LA03}}=749$  MV. The best fit to the measurements provides the modulated LIS model by [Usoskin et al. \(2005\)](#) resulting in a modulation parameter of  $\phi_{\text{US05}}=526$  MV. However, it is important to note that differences of up to 10% are observed at certain energies. Thus, it

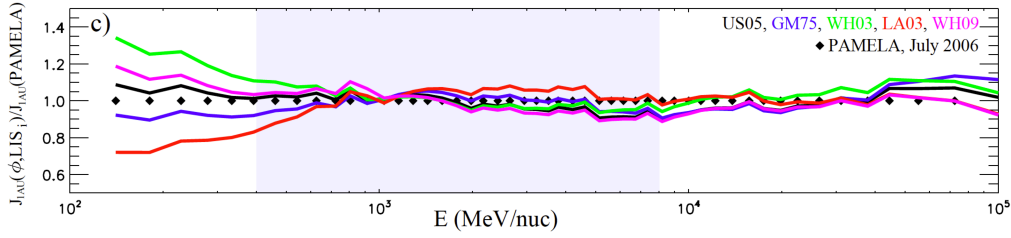


Figure 3.11: *Ratio of the modulated proton LIS models to the PAMELA measurements (US05 (black), GM75 (blue), WH03 (green), LA03 (red) and WH09 (magenta)). The spectra show strong variations in the low energy range. Nevertheless, in the highlighted energy range, which is referring to the energy range of interest (0.4 - 8 GeV), all spectra are able to reproduce the measurements fairly well.*

needs to be emphasized that the choice of the modulation parameter is only useful if the corresponding LIS model is specified. The following investigations will show that a linear correlation between all investigated LIS model dependent modulation parameter exists.

Following an approach first described by [Usoskin et al. \(2005\)](#), the LIS dependent  $\phi$  values can be related to a given one, e.g the one by [Usoskin et al. \(2005\)](#), by using the equations

$$\phi_{\text{LIS},i} = m_i \cdot \phi_{\text{US05}} + b_i. \quad (3.6)$$

In order to obtain the coefficients  $m_i$  and  $b_i$  for the primary proton spectra the following procedure is applied:

1. For a given value of  $\phi_{\text{US05}}$  the spectrum at 1 AU,  $J_{\text{US05}}$ , is calculated according to Equation (3.2).
2. The modulated spectrum  $J_{\text{p,US05}}$  then is used as reference spectrum in order to fit the other modulated LIS by minimizing the function given in Equation (3.5).
3. The resulting data sets for primary protons are used to obtain the parameters  $b_i$  and  $m_i$  by linear regression.

Thus, for primary protons in the energy range of interest, 0.4–8 GeV, the following equations can be obtained:

$$\begin{aligned} \phi_{\text{GM75}} &= 1.03378 \cdot \phi_{\text{US05}} - 48.0287 \text{ MV} \\ \phi_{\text{LA03}} &= 1.06925 \cdot \phi_{\text{US05}} + 234.871 \text{ MV} \\ \phi_{\text{WH03}} &= 0.983462 \cdot \phi_{\text{US05}} - 121.360 \text{ MV} \\ \phi_{\text{WH09}} &= 0.978454 \cdot \phi_{\text{US05}} - 197.676 \text{ MV}. \end{aligned}$$

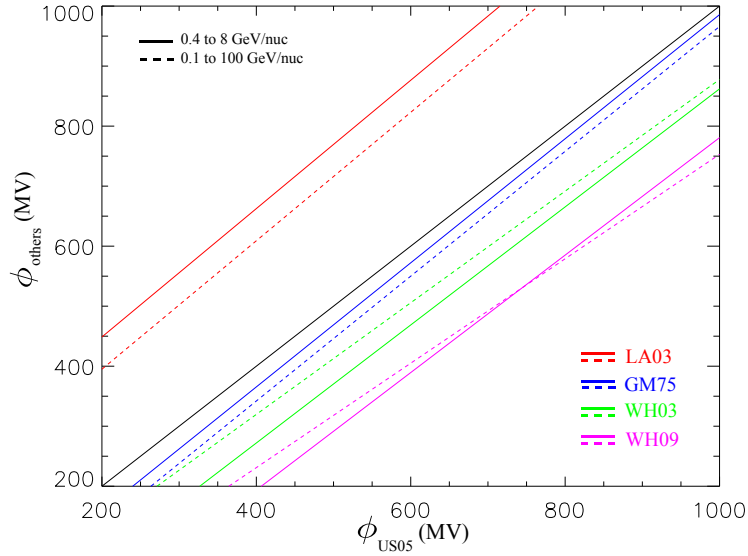


Figure 3.12: LIS dependent linear regressions corresponding to the energy range investigated in this work, 0.4–8 GeV (solid lines) and the one used by *Usoskin et al. (2005)*, 0.1–100 GeV (dashed lines).

Figure 3.12 displays the LIS dependent modulation parameter by *Garcia-Munoz et al. (1975)* (blue), *Langner et al. (2003)* (red), *Webber and Higbie (2003)* (green) and *Webber and Higbie (2009)* (magenta) as function of the solar modulation parameter by *Usoskin et al. (2005)* between 0–2,000 MV. Here the solid lines represent the results using the energy range applied in this work, 0.4–8 GeV, while the dashed lines represent the LIS dependent modulation parameter calculated by *Usoskin et al. (2005)* using an energy range of 0.1–100 GeV. As can be seen, the fit parameter strongly depend on the energy range applied.

In order to investigate this effect as well as to estimate the uncertainties of the parameters  $m_i$  as well as  $\phi_{LIS}$  for the usage of the energy range of 0.4–8 GeV the equations for a broader energy range between 0.6–6 GeV as well as a wider energy range of 0.2–12 GeV are applied in the following.

### On the Influence of the used Energy Range

As shown above, the fit parameter strongly depend on the applied energy range. In order to investigate this dependence as well as to determine the systematic errors of the LIS model dependent modulation parameters in the following a broader (0.6–6 GeV) as well as wider (0.2–12 GeV) energy range will be examined.

As an example for the influences of the used energy ranges Fig. 3.13 shows the energy range dependent regressions for the LIS model by *Garcia-Munoz et al.*

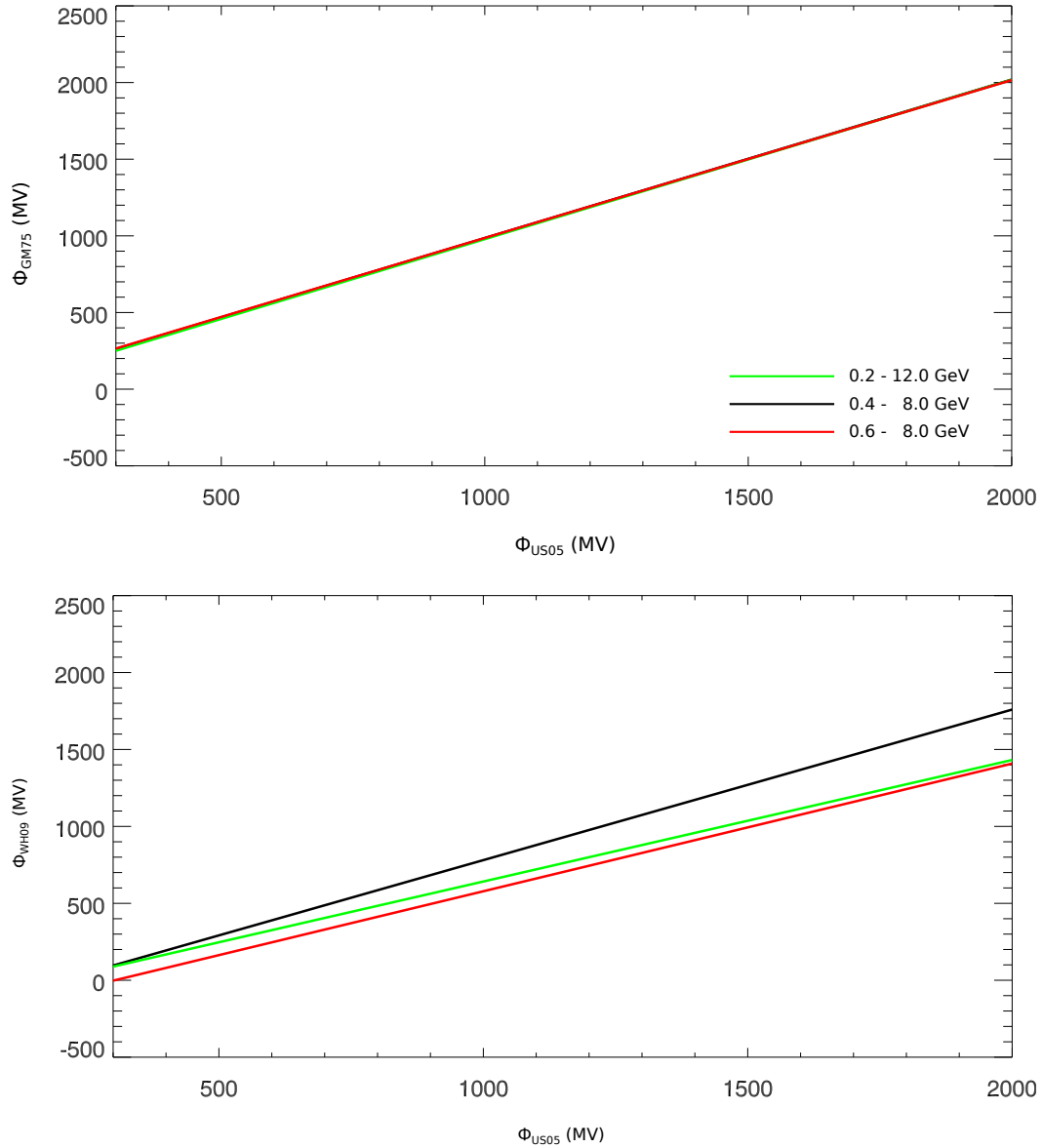


Figure 3.13: Influence of the used energy ranges on the linear relations between  $\phi_{GM75}$  (upper panel),  $\phi_{WH09}$  (lower panel) and  $\phi_{US05}$ . Investigated energy-ranges: 0.4 to 8 GeV (black curve), 0.2 to 12 GeV (green line) and 0.6 to 6 GeV (red line). For more details see text.

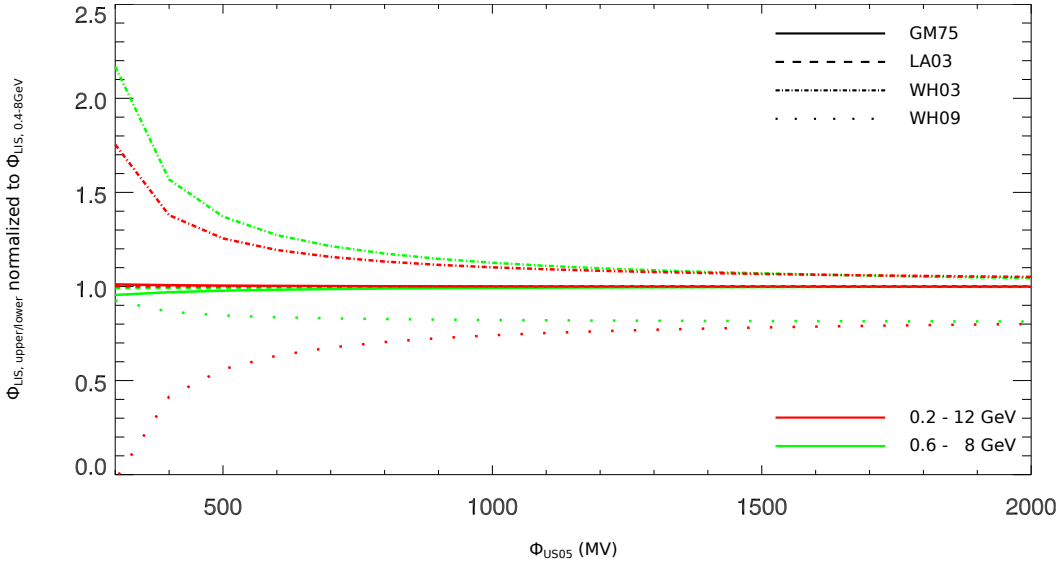


Figure 3.14: Deviations of the proton LIS dependent linear relations between the broader (wider) energy ranges with respect to the results using the energy range between 0.4 and 8 GeV. Upper left: GM75, upper right: LA03, lower left: WH03 and lower right: WH09. Here the same coloring as in Fig. 3.13 is applied.

(1975) (left panel) as well as Webber and Higbie (2009) (right panel) as function of the modulation parameter  $\phi_{U505}$ . The previously investigated regression functions corresponding to an applied energy-range of 0.4 to 8 GeV are represented as black lines while those applying an energy range of 0.6 to 6 GeV and 0.2 to 12 GeV are colored in red and green, respectively. While the modulation parameters  $\phi_{GM75}$  only show minor differences all three linear functions of the LIS model by Webber and Higbie (2009) differ significantly from each other, thus the used energy range is of great importance.

To investigate the dependencies in even more detail Fig. 3.14 displays the model dependent deviations between the modulation parameters obtained from the linear relations applying an energy-range of 0.4 – 8 GeV and the broader (red lines) as well as wider (green lines) energy limits. Due to the variety in the spectral shape the linear equations of the investigated LIS models respond differently to changes in the applied energy range. It becomes evident that the LIS model dependent linear equations using the spectra by Garcia-Munoz et al. (1975) (solid lines) and Langner et al. (2003) (dashed lines) only show minor dependences on the energy range, while, in contrast, the spectra by Webber and Higbie (2003) (dashed-dotted lines) as well as Webber and Higbie (2009) (dotted lines) show deviations of up to 100%. Additionally a modulation parameter dependent behavior becomes obvious in the deviations.

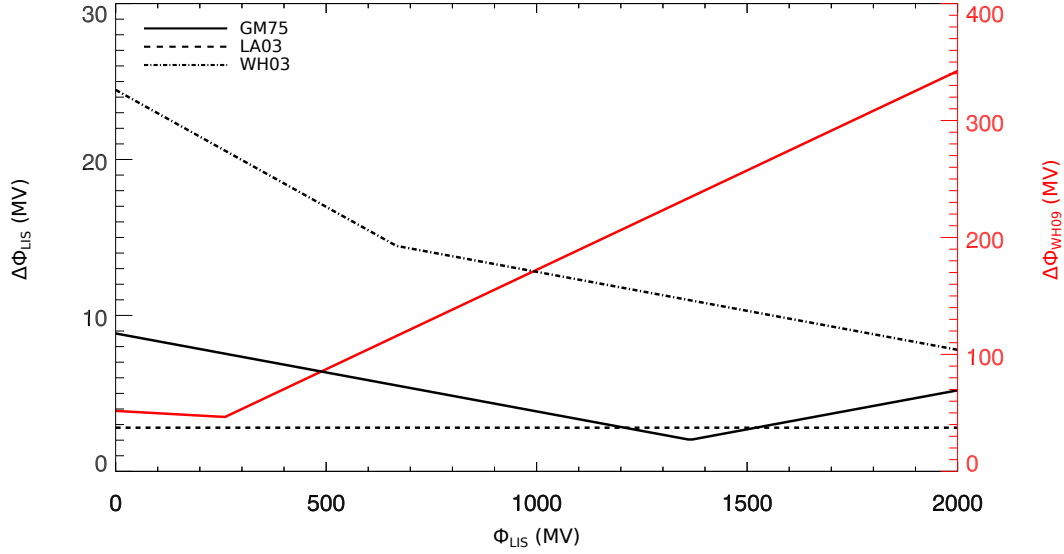


Figure 3.15: Proton LIS and modulation dependent error in  $\phi_{LIS}$ .

The previous findings are now used as a measure for LIS model dependent systematical errors, in the following denoted as  $\Delta\phi$ . However, note that because the deviations show modulation parameter dependent values the estimated errors will also show a similar behavior .

### On the Estimation of $\Delta\phi$

The LIS dependent systematical error is calculated by

$$\Delta\phi_{LIS} = \frac{|\phi_{LIS} - \phi_{LIS,broad}| + |\phi_{LIS} - \phi_{LIS,wide}|}{2}, \quad (3.7)$$

as displayed in Fig. 3.15 as function of the LIS dependent modulation parameter  $\phi_{LIS}$ , revealing that

- a) all  $\Delta\phi_{LIS}$  show a strong dependence with the modulation parameter, as predicted previously
- b) the dependences between the systematical errors  $\Delta\phi_{LIS}$  and the modulation parameter strongly depends on the used LIS models
- c) the models by Garcia-Munoz et al. (1975), Langner et al. (2003) as well as Webber and Higbie (2003) show only minor errors within  $\pm 25$  MV, while the model by Webber and Higbie (2009) predicts errors within  $\pm 340$  MV.

To verify these findings Fig. 3.16 shows the LIS dependent best fit to the PAMELA proton measurements by Casolino et al. (2009) (filled squares, see also Fig. 3.11)

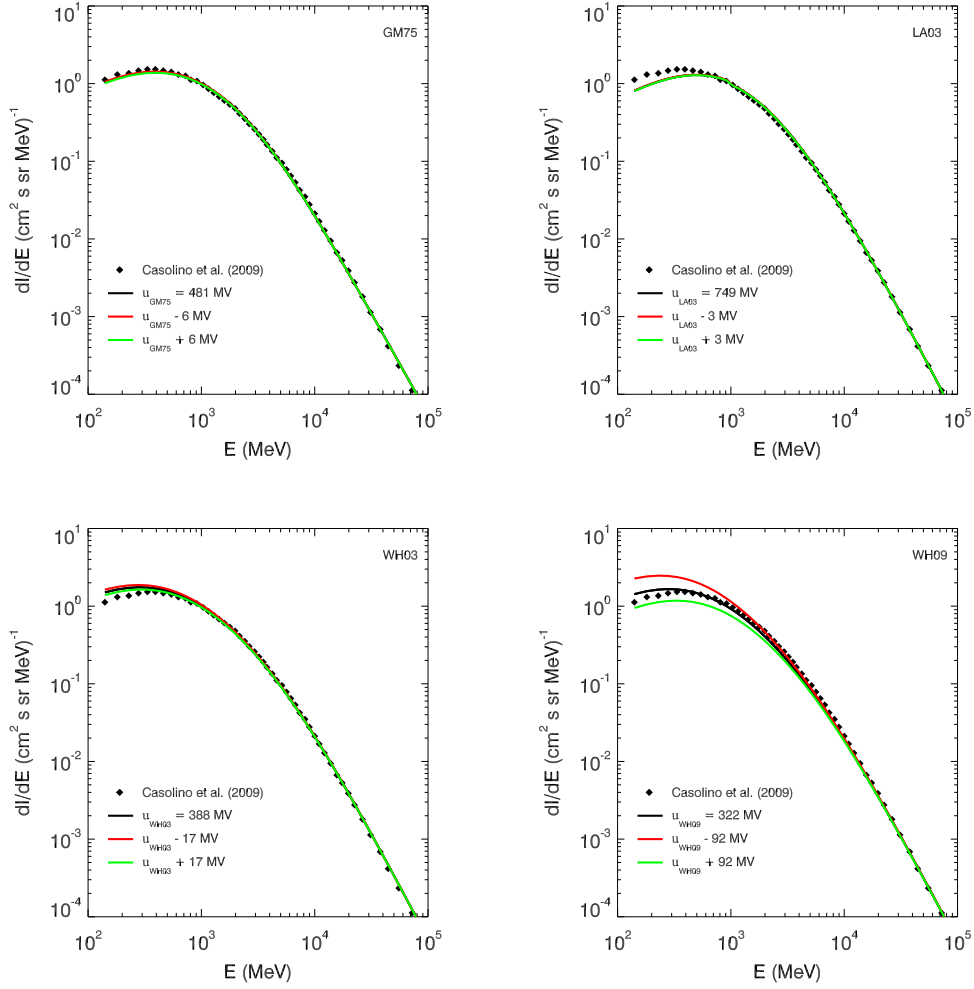


Figure 3.16: Comparison of the  $\Delta\phi_{\text{LIS}}$  corrected primary proton spectra with the PAMELA measurements. Upper left: GM75, upper right: LA03, lower left: WH03, lower right: WH09.

as well as the results including the estimated LIS and solar modulation phase dependent errors  $\Delta\phi_{\text{LIS}}$ . While the black lines represent the uncorrected results red and green lines display the modulated LIS models for the lower and upper limits affiliated with the corrected modulation parameter. Due to the small differences within the lower and upper modulation volume the corrected results using the LIS model by Garcia-Munoz et al. (1975) and Langner et al. (2003) (upper left and right panel) show only minor energy-dependent differences.

Furthermore from the investigations using the LIS model by [Webber and Higbie \(2003\)](#) it shows that variations of the modulation parameter within  $\pm 17$  MV can lead to differences of up to 10% between the investigated results (lower left panel). Because of this effect, the results using the lower modulation boundary result in a better fit to the data than the previously investigated ones. However, note that significant changes can be observed for the LIS by [Webber and Higbie \(2009\)](#). Due to a modulation dependent estimated error of  $\pm 92$  MV now differences of up to 50% at low energy ranges occur.

However, in order to provide a full description of the dependence of the used primary LIS models on the solar modulation as well as the results of this work the conversion of  $\phi$  between the different LIS models also needs to be applied for the primary alpha spectra given in Section 3.1. Following the instructions given above one of the few primary alpha particle spectra measured with the PAMELA instrument (see [Adriani et al., 2011](#)) is used in order to compute the individual modulation parameter of the different alpha LIS models during recent times using the  $\eta^2$  method given by Eq. (3.5). The results of this investigation are given in Fig. 3.17, showing the best fit of the individual LIS models as well as the resulting LIS-dependent modulation parameter and their goodness with respect to the reference data. As already seen in case of the proton LIS all alpha particles LIS models are able to reproduce the measurements. The spectra by e.g. [Webber and Higbie \(2003\)](#) and [Usoskin et al. \(2005\)](#) are able to represent the measurements when a modulation parameters of  $\phi_{\text{WH03}} = 199$  MV and  $\phi_{\text{US05}} = 215$  MV is applied.

The conversion equations between the different alpha spectra can be calculated by applying the same method introduced for protons. In the energy range of interest, 0.4–8 GeV, the linear equations, thus, are given by:

$$\begin{aligned}\phi_{\text{GM75}} &= 1.07 \cdot \phi_{\text{US05}} + 141.6 \text{ MV} \\ \phi_{\text{LA03}} &= 1.08 \cdot \phi_{\text{US05}} + 228.6 \text{ MV} \\ \phi_{\text{WH03}} &= 1.00 \cdot \phi_{\text{US05}} - 10.1 \text{ MV} \\ \phi_{\text{WH09}} &= 0.98 \cdot \phi_{\text{US05}} - 43.4 \text{ MV}.\end{aligned}$$

To investigate the influence of the used energy range on the resulting linear equations Fig. 3.18 shows the LIS-model dependent  $\Delta\phi_{\text{LIS}}$  as function of solar modulation parameter values between 0 and 2,000 MV. It becomes obvious that only modest  $\Delta\phi_{\text{LIS}}$  values of up to  $\pm 19$  MV occur which only play a minor role, and thus can be neglected.

### 3.5 Application to a Long-Term Record of $\phi$

In recent publications by [Vonmoos et al. \(2006\)](#) and [Steinhilber et al. \(2008\)](#) the modulation parameter  $\phi$  has been reconstructed for the past 9300 years using  $^{10}\text{Be}$ , mainly measured in the GRIP ice core from Greenland. Note that [Vonmoos](#)



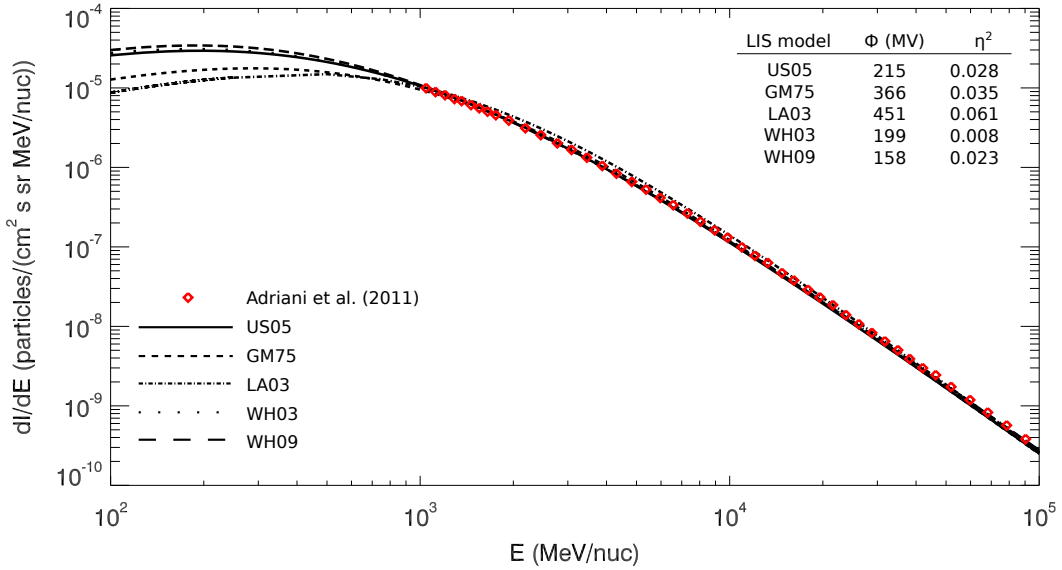


Figure 3.17: Best fit of the investigated alpha LIS models to measurements by the PAMELA instrument (see [Adriani et al., 2011](#)). The different black lines represent the modulated LIS models while the red squares show the measurements performed within solar modulation phases of  $\phi = 450 - 550$  MV. The integrated table gives the LIS dependent modulation parameter as well as the  $\eta^2$  values of each model.

[et al. \(2006\)](#), [Steinhilber et al. \(2008\)](#) use the modulation function  $\Phi$  in units of MeV. This record is based on the  $^{10}\text{Be}$  production calculations of [Masarik and Beer \(1999\)](#). In these calculations, besides protons also alpha particles and heavier particles have been taken into account merely by increasing the corresponding proton fluxes. This implies that the effect of the different rigidity cutoffs, but also the different solar modulation due to the diverse Z/A ratios has been neglected. However, the estimated differences are smaller than 10%, so the original  $\Phi$  (MeV) record has the meaning of a modulation potential  $\phi$  (MV).

Figure 3.19 displays the long-term reconstruction of  $\phi$  given by [Steinhilber et al. \(2008\)](#). The left y-axis shows the  $\phi$  record using the LIS by *GM75*. As can be seen, for most of the time, the calculated modulation parameter is in the range of presently observed values. However, in some periods (marked as red vertical lines)  $\phi$  becomes very small or even negative, for example around the years 500 BP and 1300 BP. Further periods with negative values are found between 7400 and 5000 before present (BP) with the lowest values around 5600 BP.

The fact that the modulation parameter reaches zero or even negative values implies that the modulation vanishes. The negative values could be interpreted

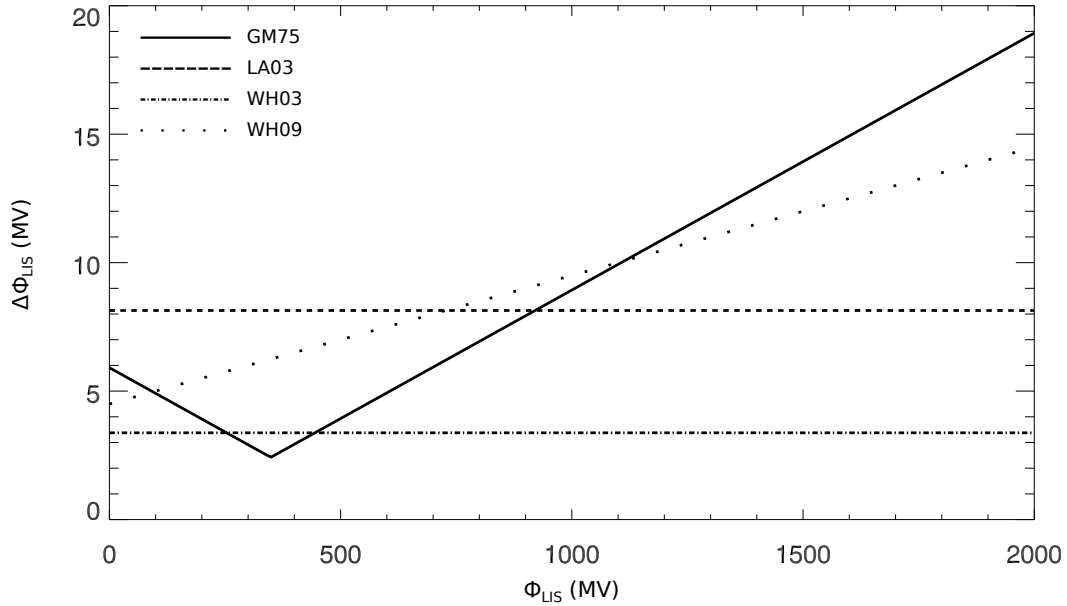


Figure 3.18: *Deviations of the alpha LIS dependent linear relations between the broader (red) and wider (green) energy ranges with respect to the results using the energy range between 0.4 and 8 GeV (upper four panels) and the corresponding modulation dependent errors (lower four panels).*

as an acceleration against the solar wind, which is unphysical. However, several physical reasons for such negative values exist, which can be divided into "outer-heliospheric" and "inner-heliospheric" ones. "Inner-heliospheric" reasons for the negative  $\phi$  values are due to uncertainties in a) the measurement of  $^{10}\text{Be}$ , b) the geomagnetic field intensity and its geometry in the past, c) temporal changes in the transport of  $^{10}\text{Be}$  from the atmosphere into the ice (atmospheric mixing), and d) the  $^{10}\text{Be}$  production calculations. Besides these "inner-heliospheric" reasons, also "outer-heliospheric" ones exist, such as e) the LIS model used in the production calculations, and f) a possible temporal variation of the LIS by additional contributions e.g. from supernovae.

So far no extraordinary events like nearby supernova explosions are known to have taken place during the periods with negative  $\phi$  values. Hence, the negative values must be caused by the effects a)–e). Possible reasons for the negative  $\phi$  values may be found in the uncertainties in the  $^{10}\text{Be}$  measurement and in particular in the palaeo-geomagnetic field intensity reconstruction. As was pointed out by [Snowball and Muscheler \(2007\)](#), the latter contains a large uncertainty. Since the geomagnetic field has to be considered for calculating the  $\phi$  values, also the calculated  $\phi$  itself holds a large error. Using the Monte-Carlo technique, [Vonmoos](#)

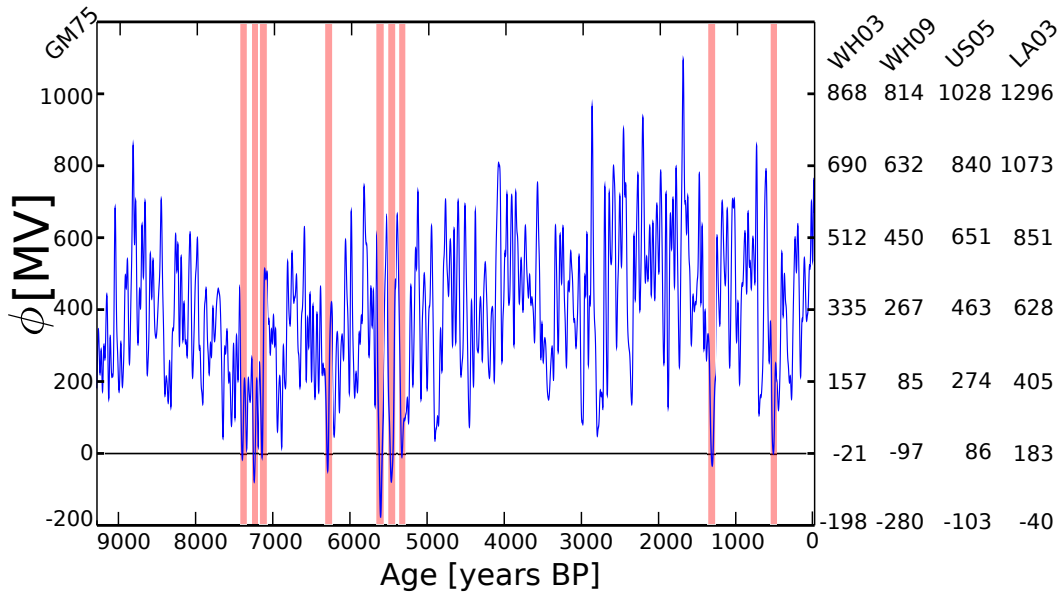


Figure 3.19: *The modulation parameter reconstruction for the past 9300 years based on  $^{10}\text{Be}$  mainly measured in the GRIP ice core (see Vonmoos et al. (2006) and Steinhilber et al. (2008)). The left y-axis shows the reconstructed  $\phi$  using the GM75 LIS (blue curve). For most time intervals, the parameter is in the range of presently observed values, but there are times (marked with the red vertical lines) where the parameter gets zero or even negative (e.g. around the years 500, 1300, and 5600 BP). The modulation values are converted to the other LIS used in this work (US05, LA03, WH03 and WH09), using Equation (3.6). The resulting modulation parameters are shown on the right y-axes.*

et al. (2006) and Steinhilber et al. (2008) found that the error in  $\phi$  due to the  $^{10}\text{Be}$  measurement and the palaeo-geomagnetic field varies in the range of 40–150 MV with an average value of 80 MV. To investigate this effect, the averaged value was added to the long-term reconstruction, providing an upper limit of  $\phi$ . Since some of the reconstructed modulation potentials are even smaller than -80 MV this upper limit cannot explain all negative  $\phi$  values. Although such negative  $\phi$  values could be a consequence of the geomagnetic field, it is not likely that these discrepancies were present during all the time periods where negative  $\phi$  values are calculated.

Besides the first two "inner-heliospheric" effects, the other ones, i.e. c), d) and e) might be of importance. This work, however, only concentrates on the possible impacts of "outer-heliospheric" processes on the reconstruction of the modulation parameter by neglecting the effects c) and d), the influence of the uncertainties in the  $^{10}\text{Be}$  transport and production models. Therefore, the following

study is restricted to the heliospheric effect e) which implies that the choice of the LIS itself gives an explanation for the negative values. Note that by neglecting the "inner-heliospherical" effects c) and d), they are not ruled out as possible sources for the negative  $\phi$  values at all.

As shown in Section 3,  $\phi$  itself strongly depends on the used LIS model. It is possible that the LIS model by Garcia-Munoz et al. (1975), which has been used for calculating the long-term  $\phi$  record by Vonmoos et al. (2006) and Steinhilber et al. (2008), does not represent the true LIS. To study the influence of the LIS, the reconstructed values of  $\phi_{GM75}$  from the long-term  $\phi$  record given in Fig. 3.19 (see y-axis on the left hand side) are converted to the other LIS models by using the linear conversions as given in Section 3.4.

The resulting LIS-dependent reconstructed  $\phi$  values of *WH03*, *WH09*, *US05* and *LA03* are shown on the y-axes on the right hand side of Figure 3.19. The calculated model dependent  $\phi$  values show that the modulation parameter can be shifted to lower or higher values, depending on the applied LIS model. So the negative values of  $\phi$  occurring in the reconstruction by Vonmoos et al. (2006) and Steinhilber et al. (2008) can either become even more negative by using the LIS models *WH03* and *WH09*, or shift to positive ones and therefore to physically reasonable values of  $\phi$  when the models *US05* and in particular *LA03* are applied.

# Computation of the Particle Transport

---

★ *Parts of Section 4.2 have been published in Fichtner et al. (2012) and, moreover, are about to be submitted to Annales Geophys. as Herbst et al. (2012b)*

---

*"... I hold you in cupped hands,  
and shield you from a storm ..."*  
Keane - Sunshine -

## 4.1 Magnetospheric Transport

Arriving at Earth, mainly low-energetic particles are shielded by the Earth's magnetic field. As mentioned in Section 2.3 charged particles are deflected by the Lorentz force  $\vec{F}_L$

$$\vec{F}_L = -Ze \left( \vec{v} \times \vec{B} \right), \quad (4.1)$$

with  $\vec{v}$  representing the velocity of the primary particle,  $Z$  its mass number,  $e$  the elementary charge and  $\vec{B}$  the magnetic field vector. Due to the fact that  $\vec{F}_L$  is perpendicular to  $\vec{v}$  and  $\vec{B}$  the particles follow a curved path. Furthermore, if external forces  $F_{\perp}^{\text{ext}}$  have an additional influence on the primary particle the total force is given by

$$\vec{F}_{\text{tot}} = -Ze \left( \vec{v} \times \vec{B} \right) + F_{\perp}^{\text{ext}}. \quad (4.2)$$

In case of a homogeneous magnetic field with no additional external forces the path of the primary particle resembles a helical orbit with radius  $r_L$ , known as the Larmor radius, perpendicular to the magnetic field defined by

$$r_L = \frac{\gamma m_0 v_{\perp}}{Z e B}, \quad (4.3)$$

where  $\gamma = \frac{1}{\sqrt{1-(v/c)^2}}$  gives the Lorentz factor, which becomes important for high energetic particles, and  $m_0$  represents the rest mass of the primary particle. When the particle additionally possesses a velocity parallel to the magnetic field it performs a helical path along the magnetic field line. In addition to  $r_L$  the particle motion then is also described by the pitch angle  $\alpha$ , the angle between the velocity vector and the magnetic field line. With  $v_{\perp} = v \cos \alpha$  as well as  $v_{\parallel} = v \sin \alpha$  the Larmor

radius then is given by

$$\begin{aligned}
 r_L &= \frac{\gamma m_0 v \cos \alpha}{Z e B} \\
 &= \frac{p c \cos \alpha}{Z e B} \\
 &= R \frac{1}{c} \frac{\cos \alpha}{B},
 \end{aligned} \tag{4.4}$$

where  $R = \frac{p c}{Z e}$  defines the rigidity of the primary particle. Since the rigidity characterizes the particle motion, it is possible to use the rigidity as a quantity to describe the magnetospheric influence on a particle.

It was Carl Størmer (Størmer, 1955) who found out that in case of a magnetic dipole an eastward-directed axial symmetric cone exists to which the access for particles below a specified rigidity is forbidden. For a given geographic location and for particles with fixed rigidities the space of all incoming particle directions can be divided into a) the allowed cone, b) the main cone, c) the forbidden cone, d) the Størmer cone as well as e) the penumbra sketched in Fig. 4.1. According to

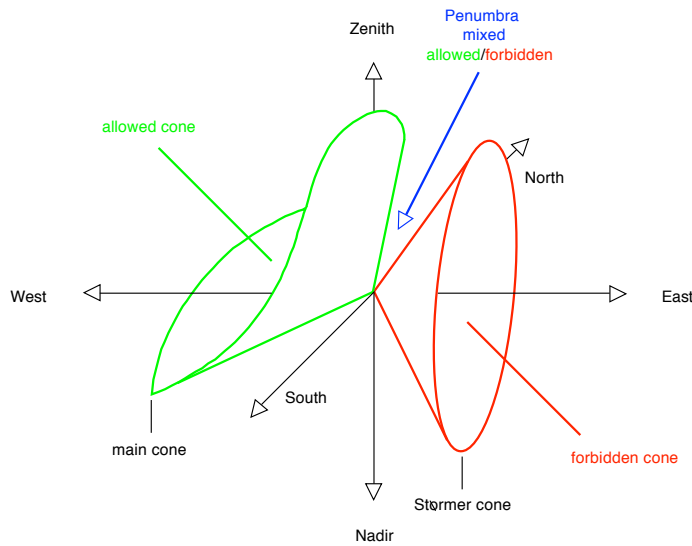


Figure 4.1: A geometric visualization of the three subspaces for particles with given rigidities. The Størmer cone (forming the boundary of the forbidden cone, colored in red), an intrinsic property of a dipole field, is a circular cone in the magnetic east direction. The appearance of this cone is defined by an exact solution of the Størmer integral (Figure adapted from Smart and Shea (2005)).

Cooke et al. (1991) these regions can be described the following way:

**The allowed cone** represents the solid angle containing all trajectories which do not intersect with the Earth's surface.

**The main cone** is the boundary of the allowed cone, which is composed of trajectories asymptotic to the simplest bound periodic orbits, and trajectories that scratch the Earth's surface.

**The forbidden cone** is the solid angle containing all trajectories which could permanently be bound in the geomagnetic field, and therewith can not access the Earth's magnetic field from outside.

**The Størmer cone** is the boundary of the forbidden cone which, in case of an axial symmetric magnetic field, forms a right circular cone.

**The penumbra** is the solid angle region between main and Størmer cones, containing a complex structure of allowed and forbidden bands of arrival directions.

For an explanation on the East-West asymmetry of the cones please see Section 4.3.

## 4.2 Vertical Cutoff Rigidities

The cutoff rigidity  $R_C$  is defined as the minimum rigidity and thus the minimum energy a particle must have in order to penetrate the geomagnetic field at a given location. The definition of the cutoff rigidity allows to describe the particle trajectory in a given magnetic field as a quantity independent from the type of the particle. However, it is also important to note that  $R_C$  strongly depends on the arrival direction of a primary particle, revealing effects like e.g. the East-West asymmetry investigated in Section 4.3.

Unfortunately, several concepts describing the cutoff rigidity exist in the literature, which shortly will be discussed in the following (see e.g. [Cooke et al., 1991](#); [Smart and Shea, 2009](#)).

**The Størmer cutoff rigidity  $R_C$ :** Approximating the geomagnetic field by a geocentric dipole the cutoff rigidity can be described by the Størmer cutoff rigidity  $R_C$ , the rigidity value for which the Størmer cone lies in the given direction

$$R_C = \frac{M \cos^4 \lambda}{r^2 \left[ 1 + (1 - \sin \vartheta \cos \varphi \cos^3 \lambda)^{\frac{1}{2}} \right]^2}, \quad (4.5)$$

with  $M$  the dipole moment,  $\lambda$  describing the geographic latitude,  $\vartheta$  and  $\varphi$  as the zenith and azimuthal angle, respectively and  $r$  the distance from the dipole center (in units of Earth radii). The azimuthal angle is measured clockwise from the given direction to the magnetic north pole. However, approaching  $\cos \lambda$  in Equation (4.5) to be zero the equation can be re-written as

$$R_C = \frac{M \cdot \cos^4 \lambda}{4 \cdot r^2}. \quad (4.6)$$

Since Eq.(4.6) is easy to calculate, and thus widely used in literature it should be pointed out that this expression is only valid for high latitudes as shown in recent studies by [Pilchowski et al. \(2010\)](#) (see also discussion Section 7.4).

The rigidity of a primary particle as well as its direction of incidence on top of the atmosphere play an important role in determining its path through the terrestrial magnetosphere. As mentioned above, not all particles with a fixed rigidity are able to penetrate the terrestrial magnetic field from all directions of incidence at a given geographic location. To see whether or not the particle characteristics allow for a passage through the magnetic field numerical simulations have to be performed. These simulations acquire inversely-charged particles which start their way through the magnetosphere at the Earth's surface, a method first introduced by [McCracken and Fréon \(1962\)](#). By using this so-called backward-trajectory tracing method the path of particles can be traced by numerical integration through a mathematical model of the terrestrial magnetic field. Consequently, particles which are able to exit the magnetosphere therefore also are allowed to reach the given location from outside the magnetosphere.

However, in order to compute the cutoff rigidities of primary particles the concept of upper, lower and effective cutoff rigidity need to be introduced. Following the investigations by [Cooke et al. \(1991\)](#) three quantities can be described:

**The lower cutoff rigidity  $R_L$**  represents the rigidity value of the lowest detected allowed/forbidden transition among a set of computed rigidities. Thus, if the rigidity of the particles is below this threshold they are **not** able to access the given geographic location.

**The upper cutoff rigidity  $R_U$**  gives the rigidity value of the highest detected allowed/forbidden transition among a set of computed rigidities. Thus, if the rigidity value of the particles is above the upper cutoff rigidity then **all** particles can access the given geographic location.

**The effective cutoff rigidity  $R_C$**  represents rigidity values which lie within the penumbra region, describing the total effect of the penumbral structure for a given particle direction.

For more detailed information on the numerical computations see e.g. [Shea and Smart \(1970\)](#), [Dorman et al. \(1972\)](#) as well as [Scherer et al. \(2006\)](#).

Starting at a fixed location Fig. 4.2 shows selected trajectories resulting from the backward-trajectory tracing method for particles of different rigidities. It shows that particles with high rigidities, represented by trajectories 1 and 2, starting from the Earth's surface show simple trajectories with only small bending before they leave the Earth's magnetosphere. With decreasing rigidity, however, this picture changes. Now the amount of bending increases, and the trajectories show



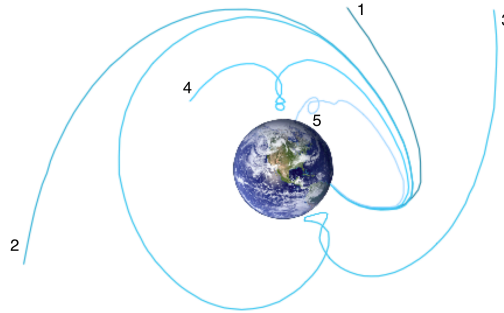


Figure 4.2: *Illustration of the backward-trajectory-tracing method using particles with different rigidities. Here the rigidity decreases from trajectory 1 to 5 (Figure adapted from Smart and Shea (2005)). See text for further information.*

intermediate loops, like e.g. trajectories 3 and 4. Although these particles are bent stronger than trajectories 1 and 2 they still are able to escape the magnetic field. Particles with trajectories like the one given in example 5, however, show multiple intermediate loops as well as an intersection with the terrestrial surface. Consequently their trajectories are forbidden and they would not be able to reach the location from outside the magnetic field.

In a first step the cutoff rigidity of particles with vertical incidence using the simulation code PLANETOCOSMICS is computed. The colored contour plot of Fig. 4.3 displays the results for a  $5^\circ \times 5^\circ$  geographical latitude-longitude grid at an altitude of 20 km. Here the IGRF for the year 2010 is applied, revealing the lowest vertical cutoff rigidities to be found at high latitudes, where almost all charged particles are able to reach the Earth's atmosphere. Higher vertical cutoff rigidities, however, can be found at lower latitudes, showing a rigidity maximum with values up to 18 GV over India and Southern Asia. At these high cutoff rigidities only protons with energies above 17.4 GeV will be able to reach the given location. Note that the asymmetric shape near the equator reflects the tilt of the magnetic dipole axis with respect to the Earth's rotation axis as well as the higher moments of the field. Since it is known that the geomagnetic field changes over time the vertical cutoff rigidities may show spatial, geometrical as well as the temporal dependencies, as studied in the following.

### The Vertical Cutoff Rigidity and its Altitude Dependency

In order to investigate the spatial influence the vertical cutoff rigidity is calculated at different altitudes between 100 and 5000 km above sea-level. The results presented in the panels of Fig. 4.4 are computed for the IGRF in 2010, showing the computations for 100 and 500 km in the upper two panels while the results for 1000 and 5000 km

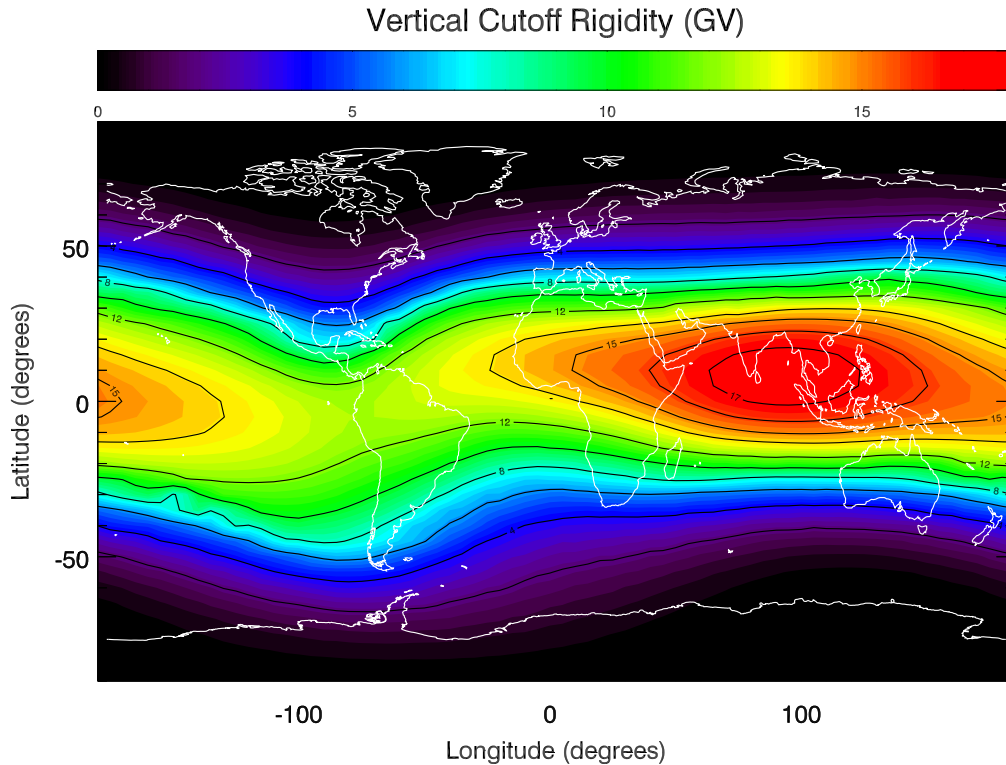


Figure 4.3: *Global vertical cutoff rigidity distribution for the IGRF field of 2010 at an altitude of 20 km.*

are displayed in the lower ones. While the shape of the cutoff rigidity distribution only shows slight variations with changing altitude the cutoff rigidity value decreases from 17 GV at 100 km to 5 GV at 5000 km. Accordingly primary protons and alpha particles need at least an energy of 16.24 GeV/nucleon and 7.69 GeV/nucleon in order to reach locations within the cutoff rigidity maximum at an altitude of 100 km, respectively, whereas they only need energies of 4.12 GeV/nucleon as well as 1.71 GeV/nucleon at an altitude of 5000 km. As illustrated in Fig. 4.2 particles with lower rigidities may be forced to perform highly complex trajectories in order to reach a given location. Note that in the following Chapters per nucleon is denoted as per nuc.

### **Influence of the Geometry of the Earth's Magnetic Field**

On the basis of the investigations by [Pilchowski et al. \(2010\)](#) in the following the influence of the magnetic field geometry and its magnitude on the computed vertical cutoff rigidity is investigated in more detail.

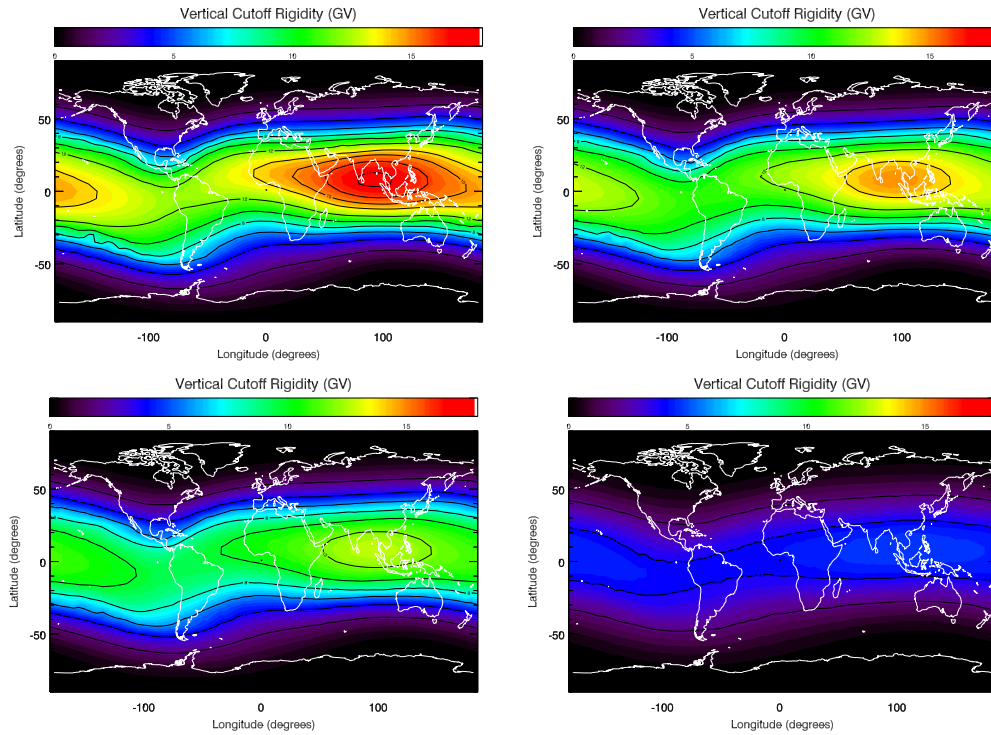


Figure 4.4: *Computed global vertical cutoff rigidities at 100 km (upper left), 500 km (upper right), 1000 km (lower left) as well as 5000 km (lower right).*

### Temporal Evolution of the Vertical Cutoff Rigidity and its Connection to the Magnetic Field Geometry

Although the Earth's magnetic field may be regarded as a tilted dipole field in a first order approximation, already C. F. Gauss noted in the 19th century that the field may be better represented by a series of Legendre polynomials, finally leading to the so-called International Geomagnetic Reference Field (IGRF, see [Finlay et al., 2010](#)). Using the IGRF the results of the previous investigation clearly revealed a strong dependence on the altitude. Further studies show that the higher moments of the IGRF vanish in altitudes above one Earth radius (6370 km) and that the dipole component becomes dominant. Thus, in this work the influence of the magnetic field geometry on the cutoff rigidity is studied in more detail.

The investigations by [Pilchowski et al. \(2010\)](#) and [Fichtner et al. \(2012\)](#) suggest to introduce the difference between horizontal and vertical components as

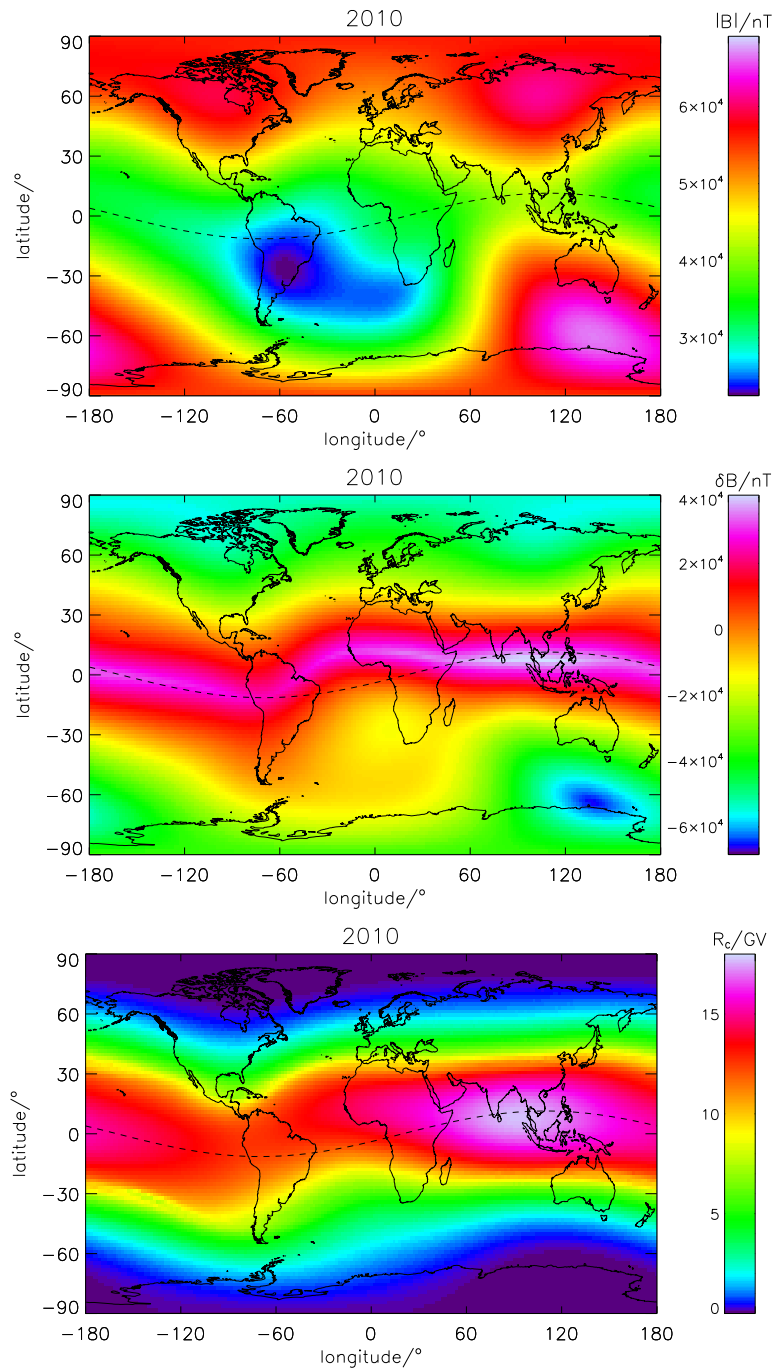


Figure 4.5: The three measures describing the geomagnetic field: the magnitude  $|B|$  (upper panel), the geometry based on the introduced magnetic field parameter  $\delta B$  (middle panel) in comparison with the vertical cutoff rigidity (lower panel) using the IGRF for 2010.

measure for the geometry of the magnetic field given by  $\delta B = \sqrt{B_{\vartheta}^2 + B_{\varphi}^2} - |B_r|$ .

Figure 4.5 shows the distribution of magnitude and geometry measure (upper and lower panel) in comparison to the vertical cutoff rigidity  $R_C$  (lower panel) as function of latitude and longitude.

As shown above, the cutoff rigidity values are always lowest at polar regions while reaching amounts well above 10 GV close to the equator. The magnitude of the field on the other hand shows a less order structure with islands of high  $|B|$  values, especially below Australia, as well as low values, in particular between South-America and South-Africa, a region known as the South Atlantic Anomaly (SAA), which can not be seen in the values of the vertical cutoff rigidity. In contrast to  $|B|$  the geometry of the field, represented by  $\delta B$  (middle panel), shows a very similar behavior compared with  $R_C$ . Despite the curvy shape of the magnetic field also the significant maximum at equatorial regions can be found at the same geographic region. Note, however, that  $\delta B$  is only a first order approximation because of the differences at e.g. polar regions and that in the geometry measure also artifacts of  $|B|$  are visible.

The previous findings clearly reveal that the vertical cutoff rigidity is much better reflected by the geometry than the magnitude  $|B|$ . However, in order to test and investigate the results in more detail in a second step the temporal variation of a) the vertical cutoff rigidity, b) the magnitude  $|B|$  as well as c) the geometry  $\delta B$  between 1900 and 2010 are studied in the following.

The values of  $R_C$  (left panels),  $|B|$  (middle panels) as well as  $\delta B$  (right panels) the global distributions for the years 1900 (upper panels), 1955 (middle panels) and 2010 (lower panels) are displayed in Fig. 4.6, from which it shows that:

- 1) The temporal variation of the cutoff rigidity  $R_C$  reveals a slight shift of the band of the high vertical cutoff rigidity in northwestern direction, which can especially be seen in the increase of the cutoff rigidity values at the region between North America, North Africa and Southern Europe. In addition an increase as well as a longitudinal widening of the maximum values can be observed.
- 2) The quantity  $\delta B$  follows the temporal evolution of the vertical cutoff rigidity i.e. the westward moving of the high-value band. In contrast temporal variations at polar regions can be observed.
- 3) The magnitude of the magnetic field also shows significant variations, which, however, again do not show an obvious correlations with  $R_C$ . The most prominent effect is a significant decrease of the magnetic field intensity in the SAA and an extension of this area.

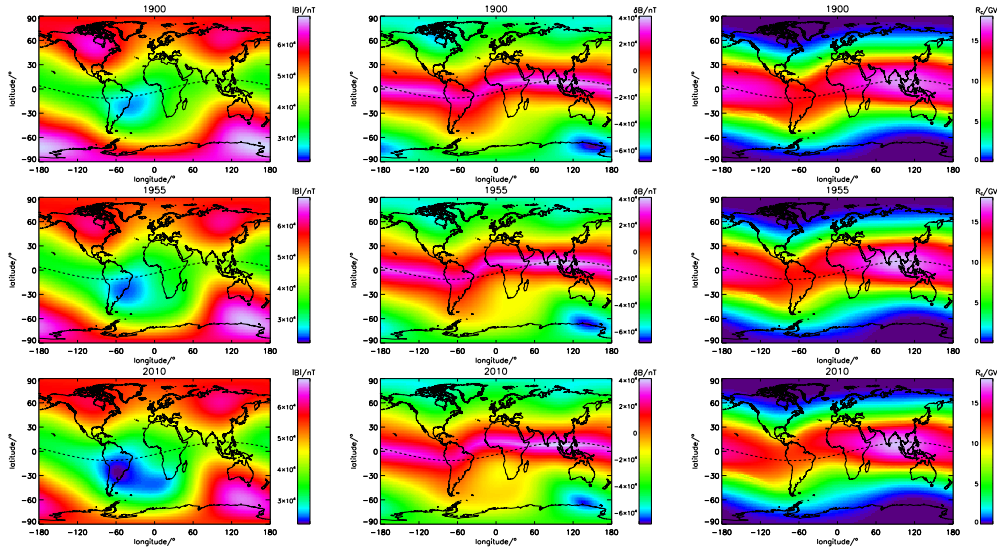


Figure 4.6: The parameters  $|B|$  (left panels),  $\delta B$  (middle panels) and  $R_C$  (right panels) for the IGRF model of the years 1900 (upper panels), 1955 (middle panels) as well as 2010 (lower panels). A detailed description is given in the text.

Because no obvious correlation between the magnitude of the magnetic field and the vertical cutoff rigidity was found the temporal variations of  $|B|$  will not be studied further.

Figure 4.7 displays the absolute difference of the vertical cutoff rigidity and  $\delta B$  between the years 1900 and 2010 as function of latitude and longitude. It shows that the cutoff rigidity (upper panel) has significantly changed within the last century especially over Europe, Russia, Asia, Australia as well as South Africa while only little changes can be observed at high latitudes. Here three regions of significant variations beyond  $\pm 3$  GV can be found: the region over Mexico, the region between South America and South Africa (both decrease) as well as the region between North America, North Africa and Southern Europe (increase). Similar behavior can be found in the low and mid latitudes of  $\delta B$  values (lower panel), while at high latitudes significant differences are observed. The regions of significant value de- as well as increases, however, correlate with those occurring in the changes of the cutoff rigidity.

Another important fact, which may not be neglected, is that the geomagnetic field did undergo much stronger changes between 1955 and 2010 than in the years between 1900 and 1955, as displayed in the left panels of Fig. 4.8. Additionally the corresponding  $\delta B$  variations are shown in the right panels, revealing again a quite similar behavior. Accordingly, in this Section we could find a quantity  $\delta B$ ,

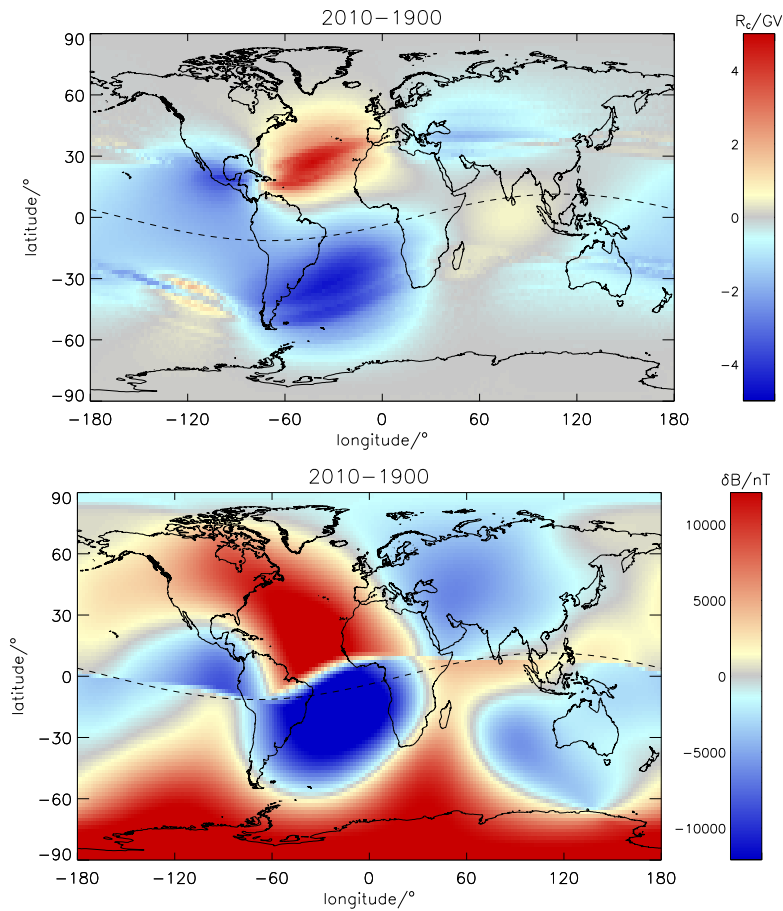


Figure 4.7: The absolute differences of  $R_C$  and  $\delta B$  between 1900 and 1955 (upper panels) as well as 1955 and 2010 (lower panels).

the difference between the horizontal and vertical components of the magnetic field, which is able to reflect

- a) the geometry of  $R_C$  as well as
- b) its temporal evolution

Since the 1950s the secondary particle component has been measured constantly by ground-based instruments like e.g. Neutron Monitors (NMs, see e.g. [Simpson, 2000](#)). Especially the temporal evolution of the vertical cutoff rigidity should have an effect on the secondary particle environment, and thus should be visible in NM data. Therefore the influence of the temporal vertical cutoff rigidity variations at selected locations is investigated in the following.

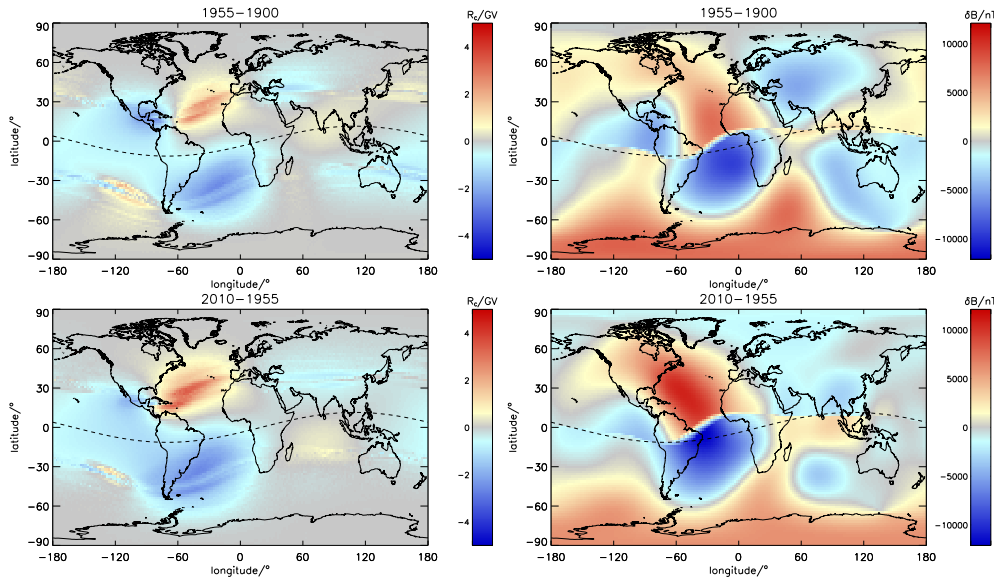


Figure 4.8: The absolute differences of  $R_C$  and  $\delta B$  for different time intervals between 1900 and 1955 (upper panels) and 1955 and 2010 (lower panels).

### Influence of the Temporal $R_C$ Variations on Ground-Based Measurements

Neutron monitor stations with locations of low cutoff rigidity show higher variations over a solar cycle than those at equatorial regions. Furthermore the altitude of a NM station determines the amount of absorbing atmosphere above the station, and thus, the higher the altitude of the station, the higher the measured counting rate.

The green filled stars in Figure 4.9 show the NM stations which have been active between 1955 and today. However, only a few of these stations have been able to provide data over a longer period of time. The red and blue ellipses mark the areas of significant de- as well as increases, within which, however, none or only a few NM stations are located.

In order to investigate the influence of the rigidity changes on the NM counting rates in the following the four specific locations colored in magenta are investigated further: Kiel (54°N 11°E), Moscow (56°N 38°E), Mexico City (19°N 100°W, within the blue circle) as well as a hypothetical Neutron Monitor on British Virgin Islands (18°N 64°W, within the red circle, denotes as BVIs).

The panels of Fig. 4.10 show the temporal variations between the years 1900 and 2010 of the cutoff rigidity (left panels) as well as the geometry measure  $\delta B$  (right panels) for Moscow and Kiel given as the red and black dots in the



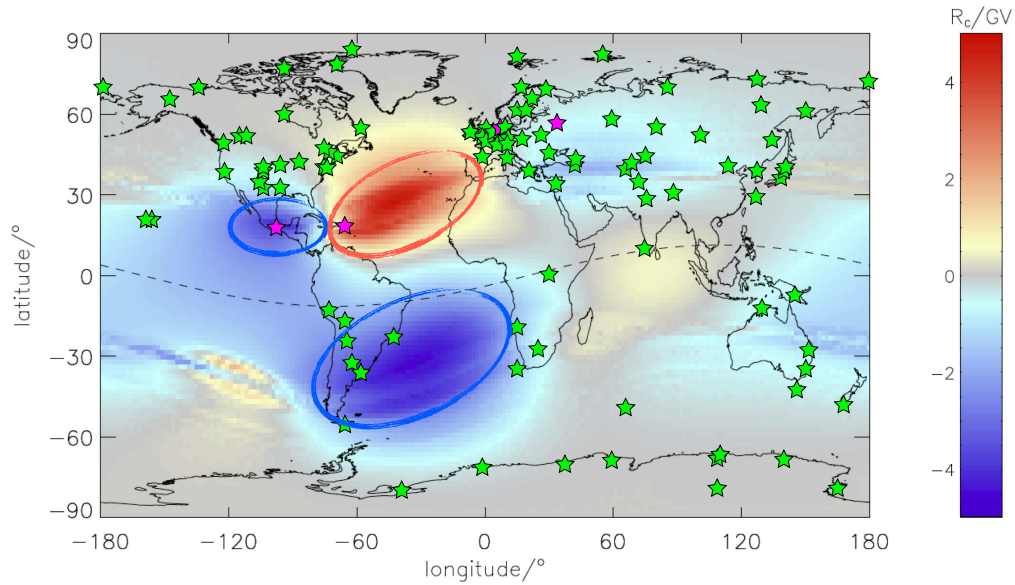


Figure 4.9: Neutron Monitor stations established between 1950 and 2012 (filled green stars).

upper panels, respectively, while Mexico (black dots) and the BVIs (red dots) are displayed in the lower panels, revealing that:

- Although Kiel and Moscow are located at nearly equal latitudes significant differences in the temporal evolution of both, the cutoff rigidity values (upper left panel) and  $\delta B$  (upper right panel) between 1900 and 2010 can be observed. While at Kiel (black dots) only minor variations are visible at Moscow (red dots) a clearly visible decrease of both values occurs.
- Considerably stronger temporal variations become obvious at Mexico City (lower left panel, black dots) and the British Virgin Islands (red dots).
- The temporal evolution of both quantities for all locations investigated are in good agreement with each other. Note that in spite of the deviations at high latitudes the computed temporal variations of  $\delta B$  are nevertheless in reliable agreement with the rigidity values, showing even similarities in the temporal behavior.

Thus, in addition to the previous investigations the results show that  $\delta B$  not only can be seen as a first order approximation of the vertical cutoff rigidity computed for 2010 but is also able to reflect the temporal evolution of the Earth's magnetic field. In addition the panels displaying the vertical cutoff rigidity show dashed lines, referring to years 1913, 1955 and 1997 and their corresponding cutoff rigidity

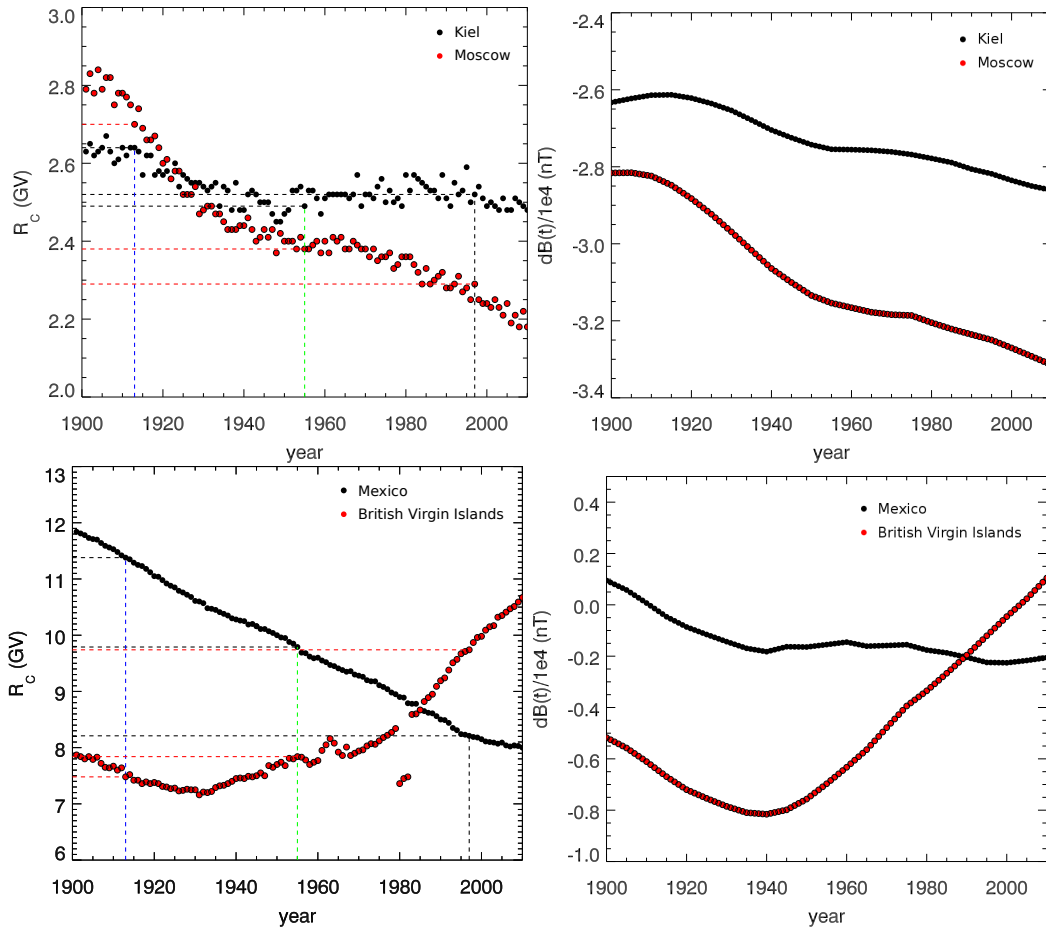


Figure 4.10: Vertical cutoff rigidities (left panels) as well as  $\delta B$  (right panels) values between 1900 and 2010 at Kiel (black dots) and Moscow (red dots) both displayed in the upper panels and Mexico City (black dots) and the British Virgin Islands (BVI, red dots) in the lower panels. While the cutoff rigidities at Kiel can be assumed as constant over time those at Moscow show a decrease over the period investigated. This effect, however, is much stronger for locations like Mexico City and the BVI. The geometry-based quantity  $\delta B$  shows a similar behavior.

values. Red horizontal lines thereby correspond to Moscow (upper panel) and the BVI (lower panel), while black ones display the values of Kiel and Mexico, respectively. Note that both, the mentioned times as well as the time-dependent cutoff rigidity values are of great importance for the following study.

However, only data of the NM in Kiel and Moscow are available. Due to the fact that both stations are located within regions of only small cutoff rigidity changes of up to 0.3 GV here only effects which are well within the statistical noise

	$R_{C,1913}$ (GV)	$R_{C,1955}$ (GV)	$R_{C,1997}$ (GV)
Kiel	2.64	2.49	2.52
Moscow	2.70	2.38	2.29
Mexico	11.38	9.79	8.21
BVI	7.48	7.84	9.74

Table 4.1: The vertical cutoff rigidities for Kiel, Moscow, Mexico and the British Virgin Islands in 1910, 1955 and 1997

of the detector are expected. Therefore another approach has to be found.

A possibility to investigate the influence of the rigidity changes on the counting rates at certain locations lies in the analysis of NM latitude surveys (see e.g. [Clem and Dorman, 2000](#)). In such surveys a mobile NM is used to measure the counting rates while covering several geomagnetic location, and thus geomagnetic cutoffs (see [Moraal et al., 1989](#)). For our analysis we use the counting rates recorded on the Italian Antarctic Program 3-NM-64 survey (see [Villoresi et al., 1997](#)), performed during the solar minimum conditions in 1997, described by the solar modulation parameter  $\phi = 410$  MV ([Usoskin et al., 2011](#)). Because NMs show a strong dependence on the solar activity it is of great importance to only compare times with identical modulation conditions. Thus, in the following only the count rate changes of all four stations during solar conditions with  $\phi \approx 400 - 420$  MV are investigated, conditions which apply for the solar minima of 1955 and 1997 (see [Usoskin et al., 2011](#)). Furthermore, due to the 11 year solar cycle as well as the 22 year solar cycle, the conditions mentioned above are assumed to be present around 1913, thus they will be investigated as well.

The panels of Fig. 4.11 show the measured normalized counting rates (open circles) as function of the cutoff rigidity  $R_C$ . In addition a Gaussian profile has been fitted to the measurements, shown as the red solid line. As mentioned above the latitude scan was performed during the solar minimum in 1997, within the NM era the corresponding solar conditions also occurred in the solar minima of 1955 as well as are believed to also have occurred around 1913. Using the information on the time-dependent cutoff rigidity values found in Fig. 4.10, also given in Table 4.1, from Fig. 4.11 the corresponding normalized counting rate values,  $N(R_C)/N(0)$ , can be determined. Their temporal dependence also can be found in Table 4.2.

Assuming the normalized counting rates as function of cutoff rigidity to be constant over time from Fig. 4.11 it appears that over the investigated three solar cycles the counting rate values increased about 12% at Mexico City (upper left panel), while a count rate decrease of about 9% at the British Virgin Island (upper right panel) would have been recorded due to the strong de- as well as increases of

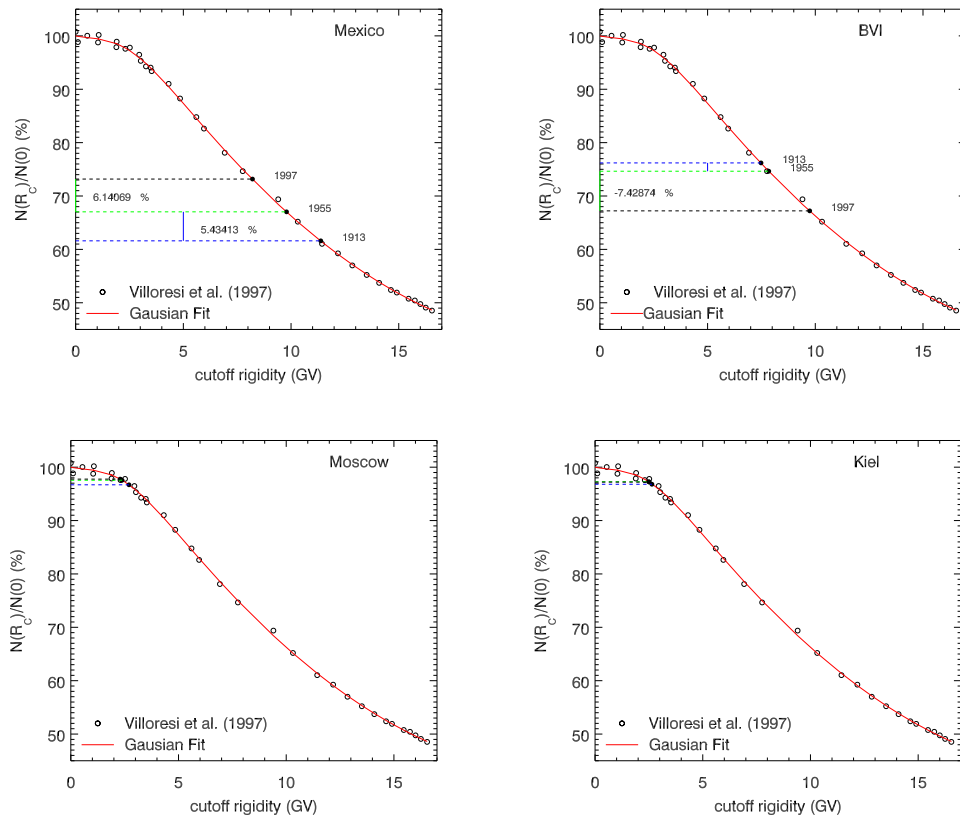


Figure 4.11: NM latitude scan by Villaresi et al. (1997) (black dots) and the corresponding counting rate variations at Kiel, Moscow, Mexico and the BVIs (color-coded lines).

	$N/N(0)_{1913}$ (%)	$N/N(0)_{1955}$ (%)	$N/N(0)_{1997}$ (%)
Kiel	96.8	97.2	97.2
Moscow	96.7	97.6	97.8
Mexico	61.6	67.0	73.2
BVI	76.2	74.6	67.2

Table 4.2: The measured normalized counting rates for Kiel, Moscow, Mexico and the British Virgin Islands in 1910, 1955 and 1997

the vertical cutoff rigidity, respectively. Stations with smaller temporal cutoff decrease or increases show less strong variations within the counting rates, as can be seen e.g. for Moscow (lower left panel) and Kiel (lower right panel). These minor variations could not be distinguished from the statistical noise of the detector, and thus can

be neglected.

## Summary

The results of the previous investigations clearly reveal that

- a) the analytic quantity  $\delta B$ , the difference between the horizontal and vertical components of the magnetic field, can be seen as a first order approximation of the vertical cutoff rigidity, whereas the SAA is only visible in  $|B|$  but not in the single magnetic field moments
- b) the vertical cutoff rigidity is more of a geometrical effect while the existence of the South Atlantic Anomaly occurs due to the higher moments of the magnetic field configuration

However, in order to be able to study the effect the results of this work on the secondary particle environment long-term measurements of selected locations are needed. Unfortunately none of the Neutron Monitor stations within regions of strong cutoff rigidity changes is able to provide the necessary data.

## 4.3 Directional Cutoff Rigidities

By now only the vertical cutoff rigidity distribution was calculated and investigated. However, due to the fact that galactic cosmic rays reach the Earth's magnetic field isotropically the directional cutoff rigidities have to be taken into account as well in order to calculate the secondary particle environment and thus the global cosmogenic radionuclides production rates correctly. Thus the cutoff rigidities of primary particles arriving from arbitrary directions will be computed, taking into account the cutoff rigidity distribution  $R_C(r, \vartheta, \varphi)$  for particles with zenith angles of  $-90^\circ \leq \vartheta \leq 90^\circ$  and azimuthal angles of  $0^\circ \leq \varphi \leq 360^\circ$ , as displayed in the panels of Fig. 4.12. As can be seen the azimuthal angle  $\varphi$  is measured counter-clockwise, whereas a zenith angle of  $\vartheta = 0^\circ$  represents the geographical northern (vertical) direction. Both angles are varied within a  $10^\circ \times 10^\circ$  grid in the following computations.

While more positively charged particles are able to penetrate the terrestrial magnetic field from western direction, negative particles are deflected in the opposite way, with more particles arriving from eastern direction. The positively charged low energetic cosmic rays from eastward direction are suppressed compared to those from the west, because the Earth's presence effectively shadows certain trajectories, which therefore are forbidden. The effect is known as the East-West effect (see e.g. [Jacklyn and Fenton, 1957](#)), revealing that positive charged particles arriving from eastward directions ( $\varphi = 90^\circ$ ) exhibit much higher cutoff rigidities than particles with western directions of incidence ( $\varphi = 270^\circ$ ). The strength of this effect, thus, is increasing with increasing zenithal angle  $\vartheta$ .

To illustrate the East-West effect in the following the global directional cutoff rigidity distributions for different zenithal and azimuthal angles are studied.

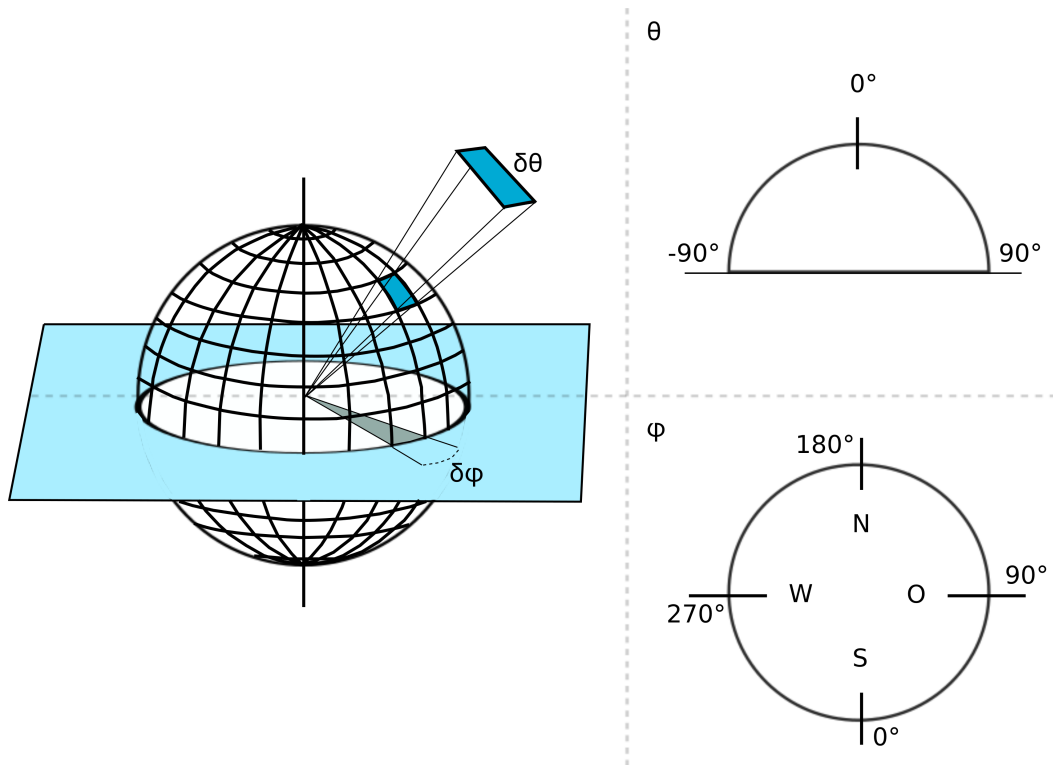


Figure 4.12: Sketch of the angular connection of incident particles. Left panel: Determination of the nomenclature, after *Michaelsen (2010)*. Right panels: Angular dependence of  $\vartheta$  (upper panel) and  $\varphi$  (lower panel).

Selected results are shown in Figure 4.13, presenting the global cutoff rigidity distributions for three different zenithal angles ( $\vartheta = 0^\circ$ : upper panels,  $\vartheta = 50^\circ$ : middle panels and  $\vartheta = 90^\circ$ : lower panels), each for eastward ( $\varphi = 90^\circ$ , left panels) and westward ( $\varphi = 270^\circ$ , right panels) direction of incidence.

It shows that

- the effect is negligible for low zenithal angles ( $\varphi = 0^\circ - 30^\circ$ ) but
- increases with increasing zenithal angles, as shown in the middle and lower panels of Figure 4.13, so that
- particles arriving from eastward directions encounter a maximum cutoff rigidity of approximately 18 GV at an zenithal angle of  $0^\circ$  (vertical direction, see results in Fig. 4.3) while looking at a maximum values of around 79 GV for zenith angles of  $90^\circ$ .

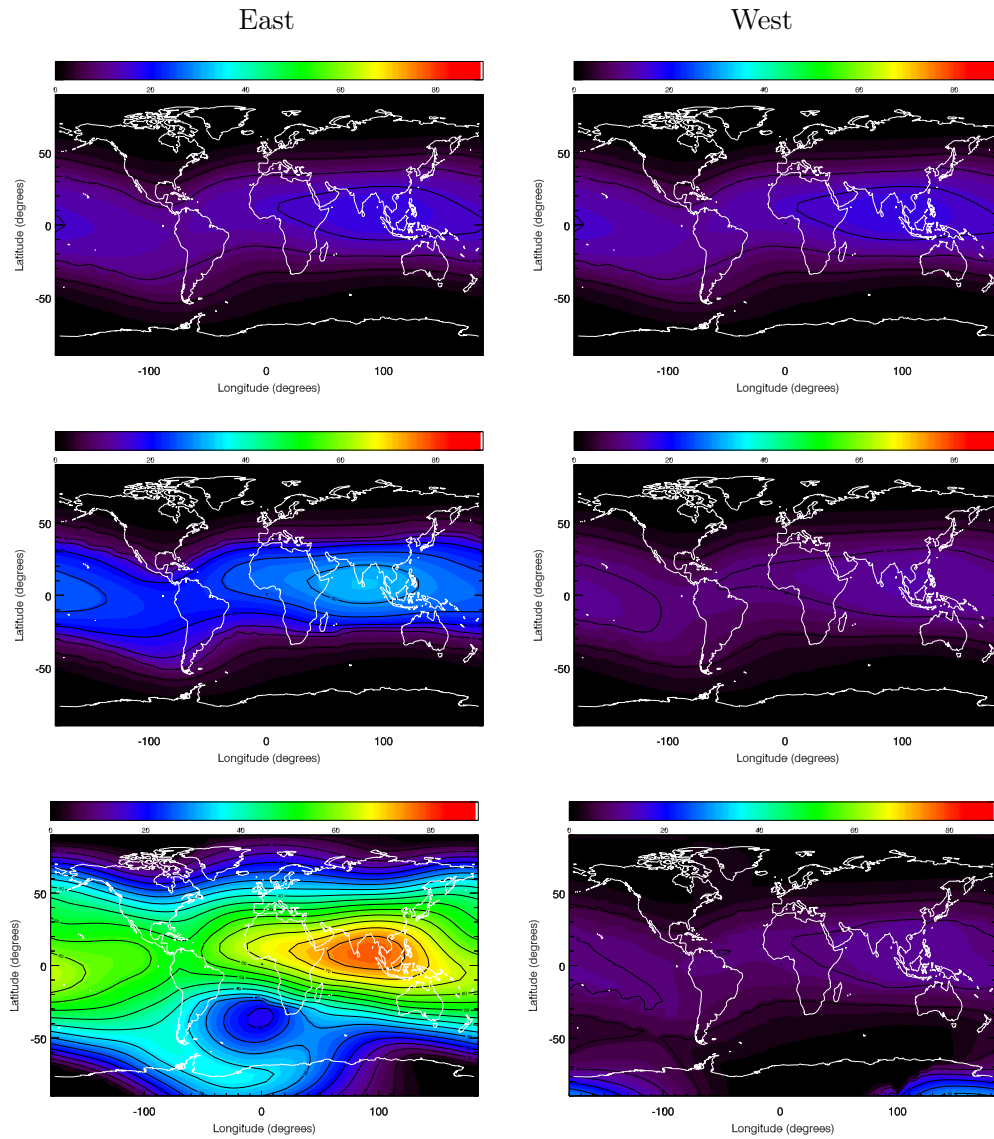


Figure 4.13: Selected results presenting the global cutoff rigidity distributions for three different zenith angles (upper panels:  $\vartheta = 0^\circ$ , middle panel:  $\vartheta = 50^\circ$  and lower panels:  $\vartheta = 90^\circ$ ) each for eastward ( $\phi = 90^\circ$ , left panels) and westward ( $\phi = 270^\circ$ , right panels) direction of incidence.

Thus, the investigations reveal that the directional cutoff rigidities need to be taken into account.



# Computing the Secondary Particle Environment

---

*"... like a child with old eyes  
cynical, sensible, always full of surprises..."*  
Kosheen - Hungry -

In order to quantify the influence of galactic cosmic rays on the atmospheric ionization as well as the production of cosmogenic radionuclides it is essential to know the flux of secondary particles like those of the electromagnetic as well as hadronic branch evolving when high-energetic particles interact with the atmospheric matter. Of special interest for this work are the evolving secondary proton and neutron fluxes as a function of geomagnetic location, atmospheric depth and time, as studied in the following.

As described in Appendix A.2 a primary particle spectrum at Earth has to be defined in the PLANETOCOSMICS code in order to compute the secondary particle production in the atmosphere. This can either be done by choosing the built-in modulated galactic cosmic ray spectrum by Garcia-Munoz et al. (1975) or by defining an arbitrary cosmic ray spectrum as input. Unfortunately for both methods time-consuming numerical computations have to be performed for each set of new input parameters such as the modulation value. Because of this and the fact that the primary particle spectrum strongly depends on a) the heliospheric modulation, b) the temporal evolution of the solar magnetic field, and thus the solar activity as well as c) the geomagnetic propagation in this work the atmospheric transport of secondary particles is calculated for a set of logarithmic equally-binned primary particle energy intervals, where over each energy-bin is uniformly distributed.

Applying this method the secondary particle environment can be simulated independent from a) the use of a specific LIS model, b) the solar activity given by the solar modulation parameter  $\phi$  as well as c) the propagation within a specific geomagnetic field. The results thereby are obtained in the following way (see also Matthiä et al., 2008; Matthiä, 2009, for a more detailed description):

In the following the secondary particle fluence, which represents the number of particles per area, in the energy interval  $\Delta E_{sec} = [E_{sec}, E_{sec} + \delta E_{sec}]$  at a given atmospheric depth  $x$  is denoted by  $F_{\Delta E_{prim}}^s(\Delta E_{sec}, x)$ , where  $s$  represents the

secondary particle species. In a first step the secondary particle fluences induced by primary particles within the energy range of  $\Delta E_{\text{prim}} = [E_{\text{prim}}, E_{\text{prim}} + \delta E_{\text{prim}}]$  with the corresponding fluence  $F(\Delta E_{\text{prim}})$  for secondary neutrons, protons, electrons and muons are computed in this work.

Assuming the primary particle flux to be constant over a small energy interval the normalized secondary particle fluence  $f_{E_{\text{prim}}}^s(\Delta E_{\text{sec}}, \text{depth})$  per primary particle with an energy  $E_{\text{prim}} \in \Delta E_{\text{prim}}$ , is given by

$$f_{E_{\text{prim}}}^s(\Delta E_{\text{sec}}, x) \approx \frac{F_{\Delta E_{\text{prim}}}^s(\Delta E_{\text{sec}}, x)}{F(\Delta E_{\text{prim}})}. \quad (5.1)$$

For an arbitrary primary particle spectrum of species  $p$ , denoted by  $F^p(\Delta E_{\text{prim}})$ , with the particle-type dependent specific intensity  $F^p(\Delta E_{\text{prim}})$  the secondary particle flux at a fixed atmospheric depth  $x$ , however, is given by

$$F^{s,p}(\Delta E_{\text{sec}}, x) = \sum_{E_{\text{prim}}=E_0^p}^{E_{\text{max}}^p} F^p(\Delta E_{\text{prim}}) \cdot f_{\Delta E_{\text{prim}}}^{s,p}(\Delta E_{\text{sec}}, x). \quad (5.2)$$

Due to a summation over the primary particle energy an upper as well as lower limit of the arbitrary primary spectrum needs to be defined. The upper limit,  $E_{\text{max}}^p$  in this work thereby is defined by the maximum energy simulated, thus 10 TeV. The lower energy limit on the other hand,  $E_0^p$ , is limited by the cutoff rigidity defined by the Earth's magnetic field, thus the geographic location and therefore is also known as the cutoff energy  $E_C$ . Using

$$E_C = \sqrt{(R_C \cdot q)^2 c^2 + m^2 c^4} - mc^2, \quad (5.3)$$

where  $q$  represents the charge of the primary particle,  $m$  gives its mass while  $c$  the speed of light, thereby a given cutoff rigidity can easily be converted into its cutoff energy  $E_C$ .

Taking into account all primary particle species of interest the total secondary particle flux  $F^s(\Delta E_{\text{sec}}, x)$  is given by a summation over all primary particle types

$$F^s(\Delta E_{\text{sec}}, x) = \sum_p \sum_{E^p}^{E_{\text{max}}^p} F^p(\Delta E_{\text{prim}}) \cdot f_{\Delta E_{\text{prim}}}^{s,p}(\Delta E_{\text{sec}}, x). \quad (5.4)$$

However, in order to compute the secondary particle fluxes, the following assumptions were made:

- a) The intensity of primary particles is assumed to be constant over a small energy interval  $\Delta E_{\text{prim}}$ .

- 
- b) The analysis of this work's results is restricted to the investigation of primary hydrogen and helium nuclei.
  - c) The investigation on the computation of the secondary particles and their dependence on the LIS models as well as changes due to the usage of different hadronic interaction models is restricted to secondary protons and neutrons.
  - d) The influence of solar energetic particles on the CR-induced ionization and the production of secondary particles is neglected.

In the following only the secondary neutron and proton production is investigated because they are the main motor for the production of cosmogenic radionuclides. For a more detailed study on e.g. muons see [Matthiä \(2009\)](#).

However, as mentioned in Section 2.4, secondary neutrons as well as protons play an important role in the atmospheric radiation-environment and additionally are the basic source of the production of cosmogenic radionuclides, and thus are of major interest for this work.

Secondary neutrons are either produced by a) collisions of primary particles with atmospheric matter, b) as fragments of the projectile of target nuclei or c) from nuclei excited in evaporation processes. According to [Dunai \(2010\)](#) the energy spectra of secondary neutrons produced at a certain atmospheric depth can be divided into thermal neutrons ( $1 \cdot 10^{-8}$  MeV to  $1 \cdot 10^{-6}$  MeV), epithermal neutrons ( $1 \cdot 10^{-6}$  MeV to  $1 \cdot 10^{-4}$  MeV), slow neutrons ( $1 \cdot 10^{-4}$  MeV–0.1 MeV), fast neutrons (0.1–10 MeV) as well as high-energy neutrons (10 MeV – 10 GeV). Secondary neutrons with energies above 10 GeV, however, are less frequently in the atmosphere. In order to validate the following results a comparison with measurements will be performed. For this study recent secondary neutron measurements by [Goldhagen et al. \(2003\)](#), using a multi-sphere neutron spectrometer (Bonner spheres) in order to determine the neutron energy spectrum of various locations, thus different cutoff rigidities ranging within  $0.7 \text{ GV} \geq R_C \leq 11.6 \text{ GV}$ , as well as different atmospheric depths, will be used.

Secondary protons, on the other hand, form the second largest population of the secondary particle environment. Due to energy losses while traversing the Earth's atmosphere, primary protons with sufficient energies are able to contribute to the total proton flux at any specific atmospheric depth. Thereby the contribution becomes much stronger with decreasing atmospheric depth. If the energy of the primary particle is high enough, for protons in the range of  $E \sim 2.75 \text{ GeV}$  ( $R \sim 3.6 \text{ GV}$ ), the particle is able to reach the Earth's surface, otherwise it is stopped at an energy-dependent atmospheric depth. Recent measurements by [Boezio et al. \(2003\)](#) will be used for comparisons with the computations.

## 5.1 Dependence on the LIS model

As investigated before, several primary proton and alpha particle LIS models exist, which can be converted into each other by the linear equations given in Section 3.4. However, although the spectra can be converted into each other they still show energy-dependent differences. Thus, the influence of these models on the computed secondary neutron as well as proton fluxes needs to be studied further.

### Secondary Neutrons

As mentioned above recent measurements by Goldhagen et al. (2003) were performed at different atmospheric depths as well as locations. The measurements were performed during the solar minimum conditions in 1997 a time for which Usoskin et al. (2011) reconstructed a solar modulation parameter of  $\phi_{\text{US05}}=404$  MV. Using the conversion equations given in Section 3.4 as well as their corresponding errors  $\Delta\phi$  calculated in Section 3.4 the following LIS-dependent modulation parameter were applied in the computations:

LIS Model	Primary Protons	Primary Alpha Particles
GM75	$380 \pm 7$ MV	$356 \pm 4$ MV
LA03	$667 \pm 3$ MV	$447 \pm 8$ MV
WH03	$276 \pm 18$ MV	$192 \pm 3$ MV
WH09	$198 \pm 71$ MV	$155 \pm 5$ MV

The panels of Figure 5.1 show the results of the computations (black lines, error-dependent light blue band) in comparison with the measurements (red dashed dotted line) for a location with  $R_C = 2.7$  GV at Sea-Level ( $1030 \text{ g/cm}^2$ ) as function of the secondary neutron energy. Note that the differential intensities are multiplied by the secondary particle energy in order to be able to study the differences in more detailed. From top to bottom the panels display the results applying the LIS models by Usoskin et al. (2005), Garcia-Munoz et al. (1975), Webber and Higbie (2003) as well as Webber and Higbie (2009). In general the shape of the neutron flux at Sea-Level, which can be described as a multiple peak structure with three significant peaks around  $5 \cdot 10^{-8}$  MeV, 1 MeV and 100 MeV, shows only slight LIS model-dependent intensity variations, revealing that at low energies all LIS dependent computations are able to represent the measurements fairly well, while they tend to overestimate the peak around 100 MeV, results which are in good agreement with the computations by Matthiä (2009). Furthermore, Fig. 5.1 investigates the significance of the calculated LIS-dependent modulation parameter error  $\Delta\phi_{\text{LIS}}$ , shown by the light blue bands. It shows that the LIS models by Garcia-Munoz et al. (1975), Langner et al. (2003) as well as Webber and Higbie (2003) are only weakly affected by the slight changes in the corrected modulation parameter, while the model by Webber and Higbie (2009) with a corresponding error of  $\Delta\phi_{\text{WH09}} = \pm 71$  MV shows significant changes in the neutron flux intensities. Using the upper

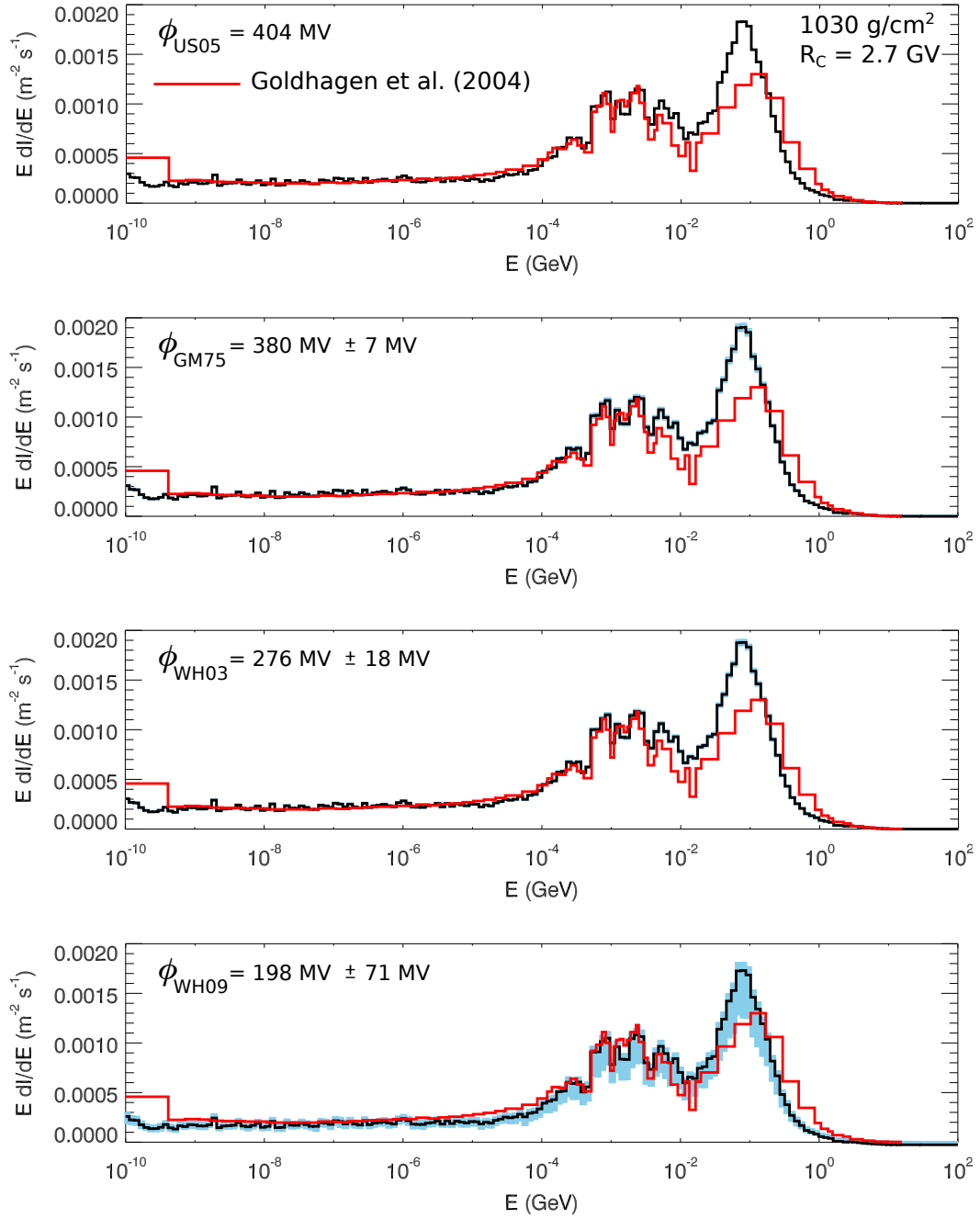


Figure 5.1: Omnidirectional differential secondary neutron intensities at different atmospheric depths and geomagnetic locations in comparison to measurements by *Goldhagen et al. (2003)* (red curves) at an atmospheric depth of  $1030 \text{ g/cm}^2$  performed at a region with  $R_C = 2.7 \text{ GV}$ . The calculations were performed for the different LIS models discussed in Section 3.1ff. using the LIS-dependent modulation parameter retrieved by Equation (3.6) (black lines) as well as their uncertainties (light blue bands).

modulation limit of  $\phi_{\text{WH09}} + \Delta\phi_{\text{WH09}} = 269$  MV shows only minor influence on low energetic secondary neutrons while at higher energies an even stronger overestimation of the measurements occurs. Adapting the lower modulation limit of  $\phi_{\text{WH09}} - \Delta\phi_{\text{WH09}} = 127$  MV leads to a strong underestimation of the measurements in the low energy range, while now the computations at higher energies are in good agreement with the measurements. Note, however, that the different influences of the corrected computations at low and high energies are grounded in the multiplication of the secondary neutron intensity with the secondary particle energy, thus minor influences at low energies occur while a strong influence is visible in higher energy ranges.

### Secondary Protons

The LIS dependent computed differential secondary proton fluxes as function of the secondary proton energy is shown in Figure 5.2. Here the measurements performed by the **Cosmic AntiParticle Ring Imaging Cherenkov Experiment (CAPRICE)98** (Boezio et al., 2003) at an atmospheric depth of  $5.5 \text{ g/cm}^2$  for a fixed cutoff rigidity of 4.3 GV are compared with this works computations. Note that the measurements were performed in the solar minimum conditions of May 1998, where a modulation parameter of  $\phi_{US05} = 570$  MV was present (see Usoskin et al., 2011).

The corresponding adapted LIS dependent modulation parameters and their systematical errors are given by:

LIS Model	Primary Protons	Primary Alphas
GM75	$541 \pm 6$ MV	$447 \pm 3$ MV
LA03	$844 \pm 3$ MV	$536 \pm 8$ MV
WH03	$439 \pm 16$ MV	$275 \pm 3$ MV
WH09	$360 \pm 99$ MV	$236 \pm 6$ MV

Figure 5.2 shows the secondary proton flux as function of the secondary particle energy. Note that, as above, the flux is multiplied by the secondary proton energy in order to provide a better comparability between the calculations and the measurements. As can be seen this works computations (black lines, light blue bands) are in good agreement with the measurements available only for the high energy range (red squares).

In general it shows that the intensity profile within the energy range of  $10^{-2} \geq E < 3.4$  GeV shows a decreasing characteristic while it abruptly spikes to a much higher intensity level at around 3.4 GeV. This effect is a cutoff rigidity dependent one. As mentioned before, the measurements were performed at a cutoff rigidity of  $R_C = 4.3$  GV corresponding to a cutoff energy of  $\sim 3.4$  GeV, the energy where the abrupt increase is located. The effect is most visible at low atmospheric depths where only minor low energetic particles are produced.

However, all modulated LIS models are able to represent the measurements fairly well. Again it shows that the estimated modulation parameter error only plays an important role for the model by [Webber and Higbie \(2009\)](#).

### Consequences

Because both investigation revealed that all LIS models are able to represent the measurements equally good when a) the proper LIS model dependent modulation parameter and b) their corresponding error is applied all further investigations will only be performed using the LIS model by [Usoskin et al. \(2005\)](#), if not stated otherwise.

## 5.2 Dependence on the Hadronic Interaction Model

As described in Appendix [A.1](#) the GEANT4 collaboration suggests two models to simulate the hadronic interactions within the Earth's atmosphere. According to the collaboration unfortunately neither the BIC nor the Bertini interaction model can replace one another and each model has its own advantages and disadvantages. In order to test which model may be the better choice for the investigations of this work in the following the hadronic model dependent secondary neutron as well as proton flux computations are compared with the measurements by [Goldhagen et al. \(2003\)](#) (secondary neutrons), [Sanuki et al. \(2003\)](#) and [Diggory et al. \(1974\)](#) (secondary protons).

### Secondary Neutrons

As a first step the secondary neutron fluxes computed with both models here are compared to the measurements by [Goldhagen et al. \(2003\)](#). As shown in Fig [5.3](#) two different atmospheric depths as well as cutoff rigidities are applied. The upper two panels show the computations at an atmospheric depth of  $1030 \text{ g/cm}^2$  at a location with  $R_C=2.7 \text{ GV}$  and their deviations from the measurements, respectively. the lower two panels, furthermore investigate the computations at a much lower atmospheric depth of  $53.5 \text{ g/cm}^2$  at a much higher cutoff rigidity of  $11.6 \text{ GV}$ .

In general the multiple peak structure with its two significant peaks around  $1 \text{ MeV}$  and  $100 \text{ MeV}$  shows slight variations for the two different atmospheric depths and their corresponding cutoff rigidities. Note that the  $100 \text{ MeV}$  peak is dominant at sea level while the peak around  $1 \text{ MeV}$  dominates at lower atmospheric depths. At an atmospheric depth of  $1030 \text{ g/cm}^2$  an additional peak around  $5 \cdot 10^{-8} \text{ MeV}$  occurs while for the computations at  $53.5 \text{ g/cm}^2$  one in the energy range of  $2.3\text{--}20 \text{ GeV}$  is evolving. The latter peak corresponds to a) fragments of primary alpha particles (dominating effect) and b) neutrons which originate from either nucleon-nucleus or nucleus-nucleus interactions (see e.g. [Matthiä, 2009](#)).

Here the intensity maximum is located at 5 GeV/nuc, which, in fact, is similar to the primary alpha particle energy corresponding to a cutoff rigidity of  $R_C \geq 11.6$  GV. Thus, below this rigidity value the peak is dissembled by secondary neutrons produced from low rigidity primary alpha particle fragmentations and, therewith, not visible.

However, the first two panels reveal that the computations using the Bertini model (dashed black line) are in good agreement with the low-energetic measurements by Goldhagen et al. (2003) (red line), while a slight overestimation occurs at higher energies. The results using the BIC hadronic interaction model (solid black line) on the other hand are in good agreement with the measurements at thermal energies while a significant overestimation over the following energy range occurs (see also Matthiä, 2009). However, the picture changes when the neutron flux at an atmospheric depth of 53.5 g/cm<sup>2</sup> with a rigidity of 11.6 GV is investigated (lower two panels). Now the low energetic secondary neutron flux is better represented by the computations using the BIC model while both models overestimate the measurements at higher energies.

### Secondary Protons

In this Section the influence of the used hadronic model on the computation of the secondary proton flux and their energy dependent deviations to the measurements are investigated.

The first two panels of Fig. 5.4 display the results at an atmospheric depth of 720 g/cm<sup>2</sup> for a cutoff rigidity of 11.2 GV. Here the same line-style as in Fig. 5.3 is applied, whereas the measurements by Sanuki et al. (2003) are given as red squares. The lower two panels shows the secondary proton flux at sea level at locations with  $R_C=1.9$  GV in comparison to the measurements by Diggory et al. (1974) (green squares). Note that in both cases a good agreement between the computations using the Bertini model and both measurements occur, while the computations using the BIC model overestimate the measurements by up to 80%, findings which also are consistent with the investigations by Matthiä (2009).

### Consequences

Although the secondary particle flux computations show the Bertini model to fit the measurements better this works investigations by now are not able to favor a particular hadronic interaction model. Therefore the following investigations of the cosmic ray induced ionization will be performed for both hadronic models.



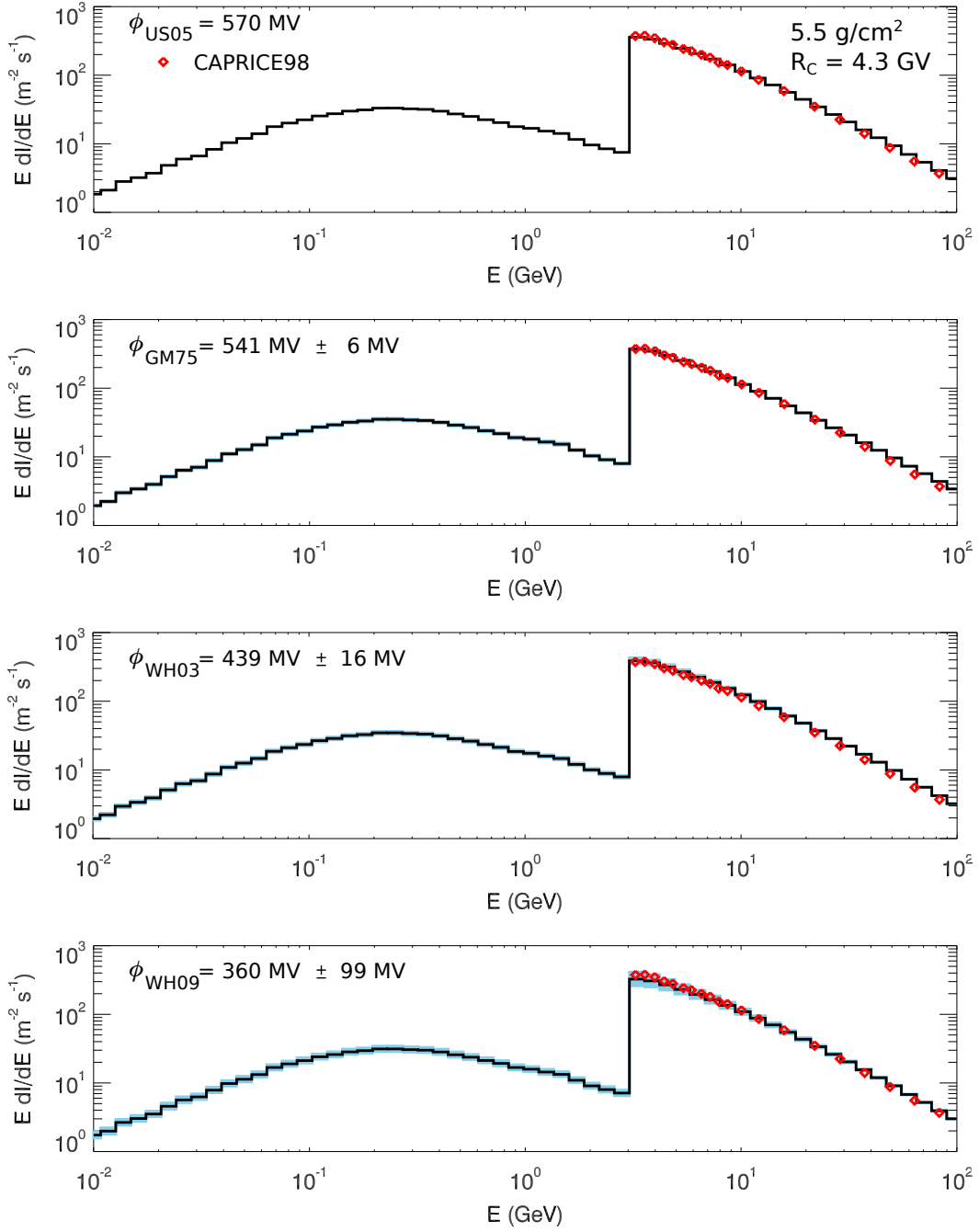


Figure 5.2: Omnidirectional differential secondary proton intensities at different atmospheric depths and geomagnetic locations in comparison to measurements by *Goldhagen et al. (2003)* (red curves) at an atmospheric depth of  $1030 \, \text{g/cm}^2$  performed at a region with  $R_C = 2.7 \, \text{GV}$ . The calculations were performed for the different LIS models discussed in Section 3.1. using the LIS-dependent modulation parameter retrieved by Equation (3.6) (black lines) as well as their uncertainties (light blue band).

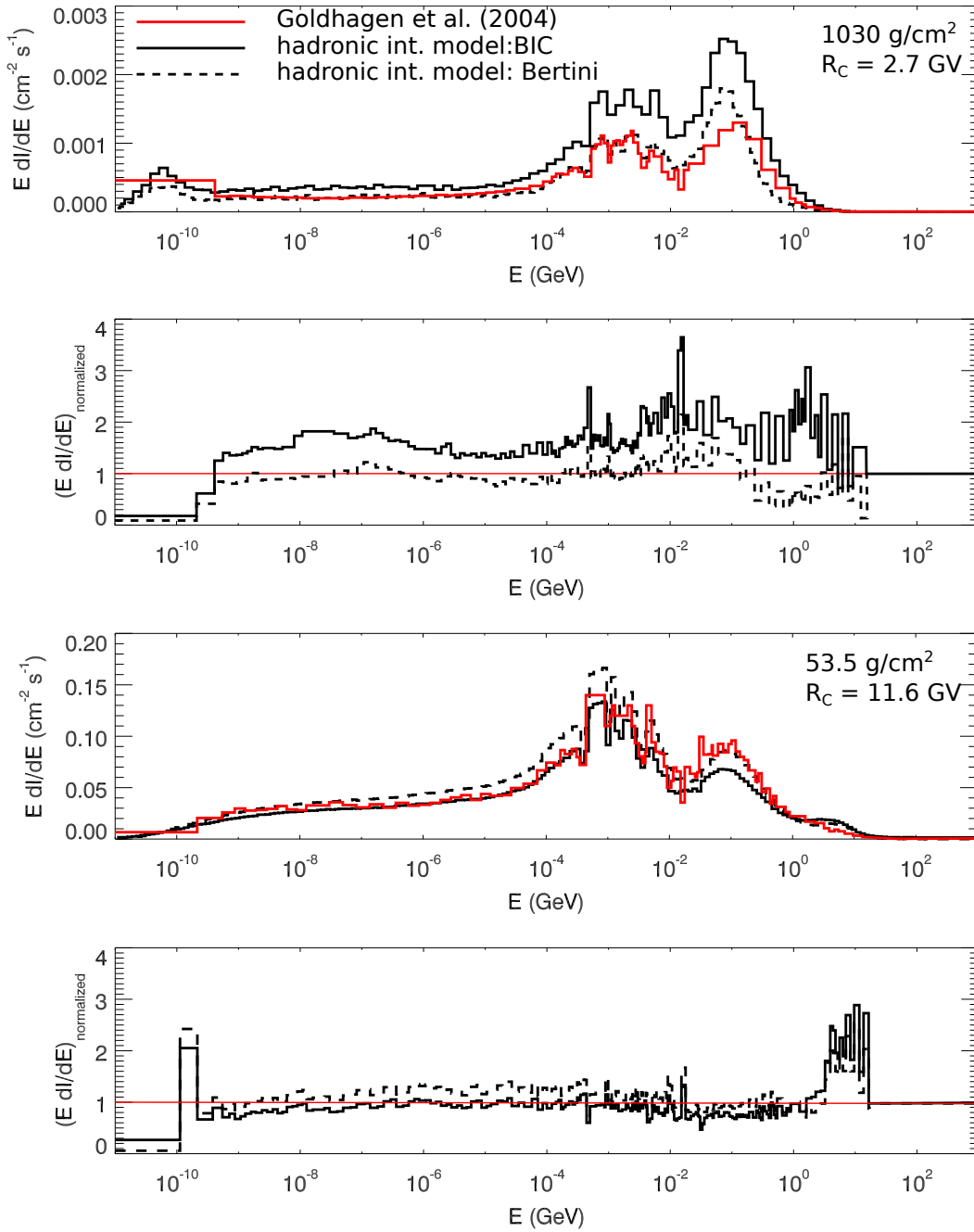


Figure 5.3: Computed differential neutron intensities for different atmospheric depths and cutoff rigidities in comparison to the measurements by Goldhagen et al. (2003) (red lines). Here the influence of the two used hadronic models BIC (dashed black lines) and Bertini (solid black lines) is investigated.

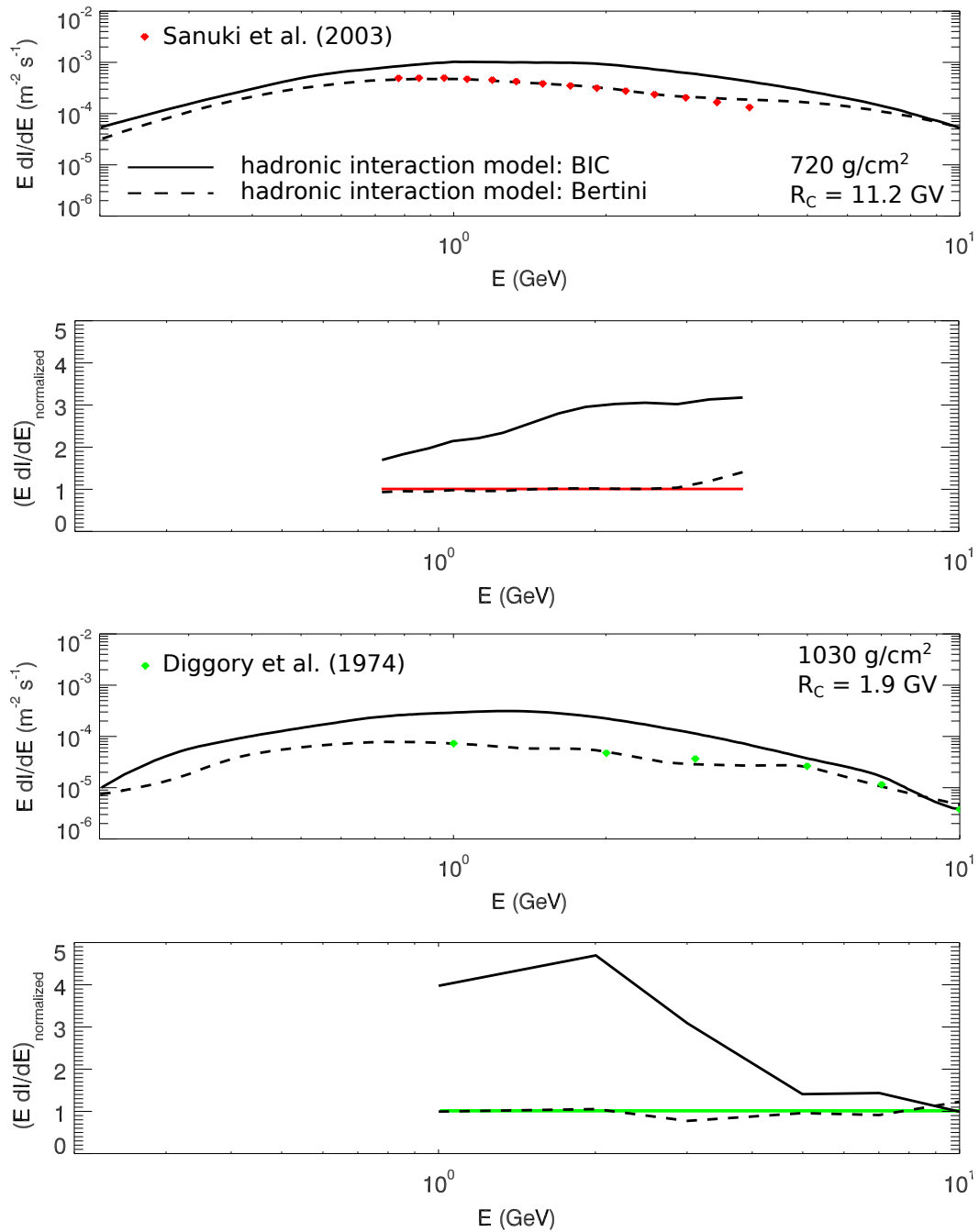


Figure 5.4: Computed differential proton intensities for different atmospheric depths and cutoff rigidities in comparison to the measurements by *Sanuki et al. (2003)* (upper panels) and *Diggory et al. (1974)* (lower panels). The influence of the two hadronic models BIC (solid black lines) and Bertini (dashed black lines) is investigated.



# Modeling the Cosmic Ray Induced Ionization

---

★ *Parts of this Chapter are published in [Fichtner et al. \(2012\)](#)*

---

*"... I'd rather be floating in space somewhere  
or worry about the ozone layer ..."*  
K's Choice - 20,000 seconds -

Some atmospheric electrical phenomena, like e.g. the atmospheric lightning, were known since the beginning of mankind. The understanding of the involved processes, however, is a relative recent development.

Since the late 18<sup>th</sup> century the Earth is known to possess atmospheric electrical properties. In addition in 1784 Charles-Augustin Coulomb discovered the electrical conductivity of air and its dependence on the atmospheric humidity (see e.g. [Aplin et al., 2008](#)). Afterwards the atmospheric electrical properties have been investigated continuously, and, in the early 19<sup>th</sup> century, with Faraday and Maxwell, a more mathematical as well as theoretical interpretation of the effects was developed. These developments finally lead to the prediction and subsequently to the discovery of a global atmospheric electric field.

## 6.1 The Cosmic Ray Induced Ionization

Today the global atmospheric electric field is known to be induced by cosmic rays entering the Earth's atmosphere (see e.g. [Harrison et al., 2004](#); [Bazilevskaya et al., 2008](#)). While in the upper atmosphere CRs mainly lose their energy due to ionization of the ambient matter, with decreasing altitude the probability of an interaction with the surrounding atmospheric gases drastically increases. The nuclear interaction mean free path of a primary proton for example is in the order of 100 g/cm<sup>2</sup>. As shown in Section 2.4, CRs are able to initiate nucleonic-electromagnetic cascades consisting of an electromagnetic, a hadronic and a muonic component. Thus, the production of the charged secondary particles of the electromagnetic component instantaneously leads to a further ionization of the middle as well as lower atmosphere, an effect strongly depending on a) the energy of the primary particle, b) the secondary particle type as well as the c) the atmospheric depth (see [Usoskin et al., 2006](#), and references therein).

Because GCRs are modulated by solar activity the ionization due to GCRs

is anti-correlated to the eleven year solar cycle, and thus is high for low solar activity and vice versa. In case of **Solar Energetic Particle** (SEP) events, however, only very high energetic ones, such as particles of a Ground Level Events (GLEs), are able to induce and contribute significantly to the atmospheric ionization.

The first direct measurements of the atmospheric ionization go back to the year 1912 when Victor Hess detected the atmospheric ion pair production rate during his balloon flights. In addition in 1934/35 Erich Regener and his co-worker Johann Georg Pfozter investigated the altitude dependent ionization profile (see e.g. [Regener and Pfozter, 1935](#)), discovering the ionization to be a transition curve with a maximum at altitudes around 15–20 km, a value strongly depending on the geographic latitude as well as the solar activity (see [Bazilevskaya and Svirzhetskaya, 1998](#); [Bazilevskaya et al., 2008](#)).

A series of detailed studies was first carried out by [Neher \(1967\)](#), [Neher \(1971\)](#) as well as [Lowder et al. \(1972\)](#), studies which were continued by e.g. [Rosen et al. \(1985\)](#) and [Ermakov et al. \(1997\)](#). Nowadays the atmospheric ionization is believed to strongly affect atmospheric physical and chemical properties like e.g. the atmospheric ion-balance (see e.g. [Dorman et al., 2004](#)), the atmospheric cloud-coverage (see e.g. [Marsh and Svensmark, 2000](#)) as well as the atmospheric aerosol formation (see e.g. [Vitt and Jackmann, 1996](#)).

Especially because these effects are not fully understood by now it is of great importance to numerically compute the atmospheric ionization in order to understand the basic principles and the dominating processes of the mechanisms involved. Therefore this Chapter will present the numerical computations of the atmospheric depth- as well as location dependent galactic cosmic ray induced ionization rates using the PLANETOCOSMICS simulation code (see [Appendix A](#)). Adopting a method first described by [Usoskin et al. \(2006\)](#) the ionization yield  $Y(E, x)$ , the ionization function  $F(\phi, E, x)$  as well as the ionization rate  $Q(\phi, R_C, x)$  of primary protons and alpha particles will be calculated. Moreover, in order to verify the results of this work comparisons with numerical computations of the **Cosmic Ray Atmospheric Cascade** (CRAC) model by [Usoskin et al. \(2006, 2010\)](#) as well as measurements performed by [Neher \(1971\)](#) as well as [Lowder et al. \(1972\)](#) will be presented. Furthermore a comparison with the measured ionization rates of a latitude survey by [Neher \(1967\)](#) at multiple atmospheric depths and the influence of the used magnetic field configuration is studied.

In addition note that the following Sections will investigate the influence of the used hadronic interaction models BIC and Bertini, leading to a decision which hadronic model will be used to compute the production of the cosmogenic radionuclides investigated in [Chapter 7](#).

## 6.2 Modeling the Cosmic Ray Induced Ionization due to Galactic Cosmic Rays

By now only two models are able to compute the cosmic ray induced ionization, both using the Monte-Carlo method (see e.g. Nelson et al., 1985; Binder and Heermann, 2010) to simulate the nucleonic-electromagnetic interactions:

- a) The CRAC model by Usoskin et al. (2006) and its updated version **CRAC:CRII** by Usoskin et al. (2010) are based on the **COsmic Ray SIMulations for KAscade** (CORSIKA) Monte-Carlo package. In order to simulate the low-energetic nuclear interactions the model is extended by FLUKA, a fully integrated particle physics simulation package. The CRAC model in addition was also used as the ground-base model of the **Sofia model** by Velinov and Mateev (2005, 2007) as well as Velinov et al. (2009), which includes an analytical approximation of the direct cosmic ray induced ionization.
- b) **PLANETOCOSMICS**, which is used in this work (see Appendix A for a detailed description).

In general the cosmic ray induced ionization rate  $Q$ , representing the number of ion pairs produced in one gram of the surrounding atmospheric material per second, is given by

$$Q(\phi, R_C, x) = \sum_i \int_{E_{C,i}}^{\infty} J_i(\phi, E) \cdot Y_i(E, x) dE, \quad (6.1)$$

with  $i$  representing the investigated primary cosmic ray particle type, in this work primary protons and alpha particles,  $J_i(\phi, E)$  the corresponding modulated differential primary particle flux at Earth, while  $Y_i(E, x)$  represents the ionization yield. As explained later in more detail the total cosmic ray induced ionization rate strongly depends on a) the solar activity ( $\phi$ ), b) the geographic location ( $R_C$ ) and c) the atmospheric depth ( $x$ ).

In order to compute the cosmic ray induced ionization and to compare the results of this work with those of the CRAC:CRII model the computation method first described by Usoskin et al. (2006) is applied, thus the following steps will be performed and investigated:

1. Calculation of the Ionization Yield  $Y_i$  due to primary particles of type  $i$  according to:

$$Y_i(E, x) = \alpha \cdot \frac{1}{E_{\text{ion}}} \cdot \frac{\Delta E_i}{\Delta x},$$

with  $\Delta E_i$  as the mean specific energy loss at a certain atmospheric depth  $x$  per simulated primary particle of type  $i$  with the energy  $E$ , while the average atmospheric ionization energy  $E_{\text{ion}}$  in air is defined as 35 eV (Porter et al.,

1976). In order to take into account the influence of the zenith incidence angle of the primary particle additionally a geometrical normalization factor  $\alpha = 2\pi \int \cos(\theta) \sin(\theta) d\theta$  has to be considered.

2. By multiplying the ionization yield  $Y_i(E, x)$  with an arbitrary cosmic ray spectrum  $J_i(\phi, E)$  the differential ionization function  $F_i(\phi, E, x)$  of type  $i$  primary CRs is obtained.  $F_i(\phi, E, x)$  therefore is given by

$$F_i(\phi, E, x) = Y_i(E, x) \cdot J_i(\phi, E).$$

3. The ionization rate  $Q_i$  is obtained by integrating the ionization function  $F_i(\phi, E, x)$  over the primary particle energy,

$$Q_i(\phi, R_C, x) = \int_{E_{C,i}}^{\infty} F_i(\phi, E, x) dE,$$

where the lower energy limit  $E_{C,i}$  is given by the cutoff energy of the primary particle at a given location (see Eq.(5.3)).

4. By summing up the ionization rates of all primary particle types investigated the total atmospheric ionization rate is achieved:

$$Q(\phi, R_C, x) = \sum_i Q_i(\phi, R_C, x)$$

These four steps in the following are investigated in more detail. Thereby comparisons with the computations by [Usoskin et al. \(2006\)](#) and [Velinov et al. \(2009\)](#) are performed. Moreover, the measurements by [Neher \(1967\)](#), [Neher \(1971\)](#) and [Lowder et al. \(1972\)](#) will be used in order to verify which hadronic interaction model is the more suitable one.

### On the Computation of the Ionization Yield $Y_i$

The first step to determine the cosmic ray induced ionization is to compute the yield function  $Y_i$ , representing the number of produced ions in one gram of the surrounding atmospheric environment due to a single primary particle of type  $i$  with a given energy  $E$ . As mentioned above, the yield function is given by

$$Y_i(E, x) = \alpha \cdot \frac{1}{E_{\text{ion}}} \cdot \frac{\Delta E_i}{\Delta x}. \quad (6.2)$$

As described in Section 5 for the computation of  $Y_i(x, E)$  the energy loss of primary protons and alpha particles in the energy range of 0.1 GeV/nuc – 10 TeV/nuc is calculated mono-energetically with logarithmic equally binning. For each primary particle bin furthermore multiple events are simulated and thus an averaged specific energy loss value is obtained. For a discussion on the energy-interval dependent number of computed events and its limitations see Appendix C.



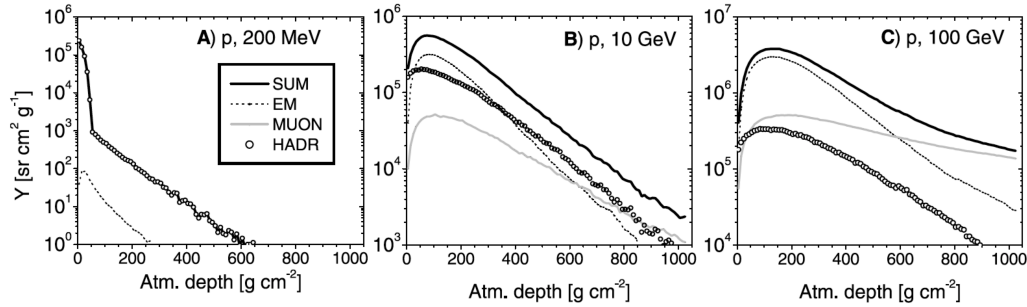


Figure 6.1: Influence of the Secondary cascade branches on the cosmic ray induced ionization (taken from *Usoskin et al. (2006)*).

PLANETOCOSMICS offers the computation of the total specific energy loss at 1000 atmospheric layers with an equally spaced thickness of  $\Delta x = 1.035 \text{ g/cm}^2$ . A disadvantage of this method, however, is that the deposited energy inside of each of these layers can not be separated into the components of electromagnetic, hadronic or muonic interactions, as show e.g. in Figure 6.1, which is taken from *Usoskin et al. (2006)*. Here the ionization yield function  $Y_i$  for primary protons with energies of 200 MeV (left panel), 10 GeV (middle panel) as well as 100 GeV (right panel) as function of the atmospheric depth between 0 and 1030  $\text{g/cm}^2$  are shown. Also displayed is the influence of the hadronic (open dots), electromagnetic (dotted) and muonic (grey) component on the total ionization yield (solid line).

It shows that the hadronic component clearly dominates the atmospheric ionization in case of low primary proton energies (left panel), revealing that a significant ionization is only present in the upper atmosphere. In case of an energy of 10 GeV (middle panel) all secondary particle components are equally important, however, showing a strong dependence on the atmospheric depth. On one hand below 300  $\text{g/cm}^2$  the electromagnetic component dominates the ionization while at 300 – 900  $\text{g/cm}^2$  secondary particles of the hadronic branch are more important. Near the Earth’s surface, on the other hand, the muonic component dominates the cosmic ray induced ionization (see also Section 2.4). For high energetic primary protons (right panel) the hadronic component has only a minor influence, whereas electromagnetic branch particles dominate at depths below 600  $\text{g/cm}^2$ , while muonic ones dominate above 600  $\text{g/cm}^2$ .

Comparisons of the results of this work with those computed by *Usoskin et al. (2006)* and *Velinov et al. (2009)* are shown in the panels Fig. 6.2. The upper panel displays the ionization yields due to primary protons with an energy of 1 GeV as function of the atmospheric depth between 0 and 1000  $\text{g/cm}^2$ . The black solid

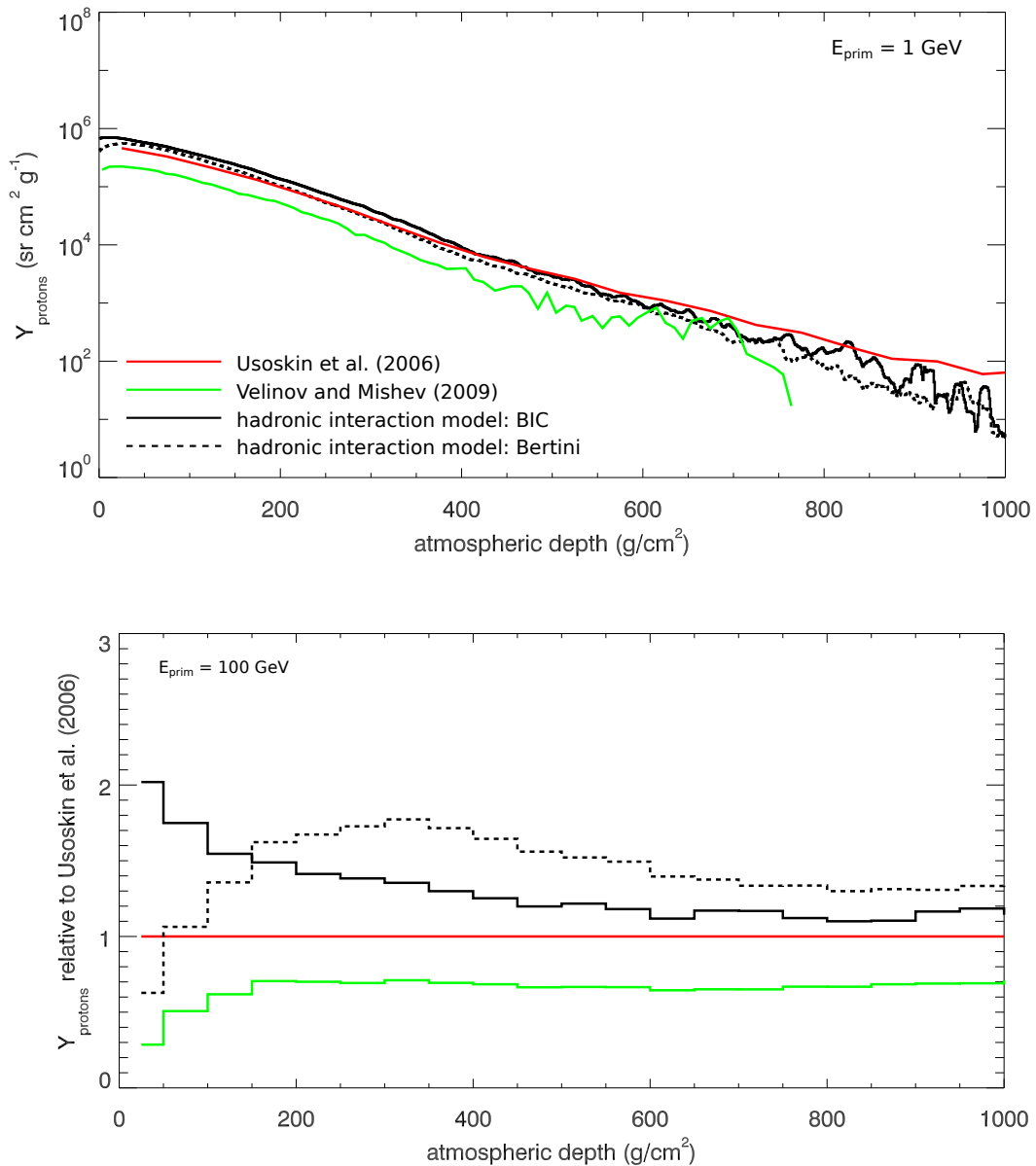


Figure 6.2: *Upper panel: Ionization Yield  $Y$  for a primary protons with an energy of 1 GeV computed using the BIC (BERT) model given as solid (dashed) black lines as well as in comparison with the computations by Usoskin et al. (2006) (red line) and Velinov et al. (2009) (green line). Lower panel: Ionization Yield  $Y$  relative to the computation by Usoskin et al. (2006) for a primary proton with an energy of 100 GeV.*

and dashed lines thereby represent the results using the hadronic BIC and Bertini model, respectively, while the simulations by [Usoskin et al. \(2006\)](#) and [Velinov et al. \(2009\)](#) are displayed as red and green solid lines. A good agreement between the results of this work and the computations by [Usoskin et al. \(2006\)](#) at atmospheric depths below  $600 \text{ g/cm}^2$  exists, while stronger deviations can be observed at larger atmospheric depths. The computations by [Velinov et al. \(2009\)](#), however, show significantly lower yield values compared to the other computations. Nevertheless, all model results show that at these primary particle energies severe decreases of the ionization yield values with increasing atmospheric depth occur. In addition the lower panel of Fig. 6.2 shows the yield function values of primary protons with an energy of 100 GeV normalized to the results by [Usoskin et al. \(2006\)](#), revealing the different models to vary up to a factor of two. However, good agreements of the computations of this work using the BIC model and the results by [Usoskin et al. \(2006\)](#) at atmospheric depths above  $200 \text{ g/cm}^2$  occur.

In the following the influence of the two hadronic models and their deviation to the calculations performed by [Usoskin et al. \(2006\)](#) will be investigated further. For this purpose the primary proton induced ionization yield as function of particle energies between 0.1 and 100 GeV is studied for atmospheric depths of  $100 \text{ g/cm}^2$  and  $700 \text{ g/cm}^2$ , as shown in the upper and lower panel of Fig. 6.3. Again solid and dashed lines represent the results using the hadronic BIC and Bertini model, respectively, while the red solid lines show the computations by [Usoskin et al. \(2010\)](#) using the CRAC:CR11 model. As can be observed the results of this work are in good agreement with each other at lower atmospheric depths, while increasing deviations between both models as well as the computations by [Usoskin et al. \(2010\)](#) become obvious. For primary proton energies between 0.1 and 20 GeV the computations using the BIC and Bertini model, however, predict higher ionization yield values than the ones computed by [Usoskin et al. \(2010\)](#).

The previous investigations showed the occurrence of significant depth-dependent differences between the investigated models. To study the variations further the total primary particle induced ionization yield (composite of primary proton and alpha particle induced ionizations) as function of primary particle energy at atmospheric depths between 100 and  $800 \text{ g/cm}^2$  is given in Fig. 6.4. Here the red lines represent the computations using the BIC, while black ones display the results of the Bertini model. Different line-styles represent different atmospheric depths.

As before the ionization yield  $Y$  increases with increasing primary particle energy while a decrease with increasing atmospheric depth becomes obvious. In addition a steep increase in the low energy range due to the dominance of the hadronic component is visible, while a flatter increase in mid and high energy ranges is present. The results are in good agreement with the findings by [Usoskin et al. \(2010\)](#).

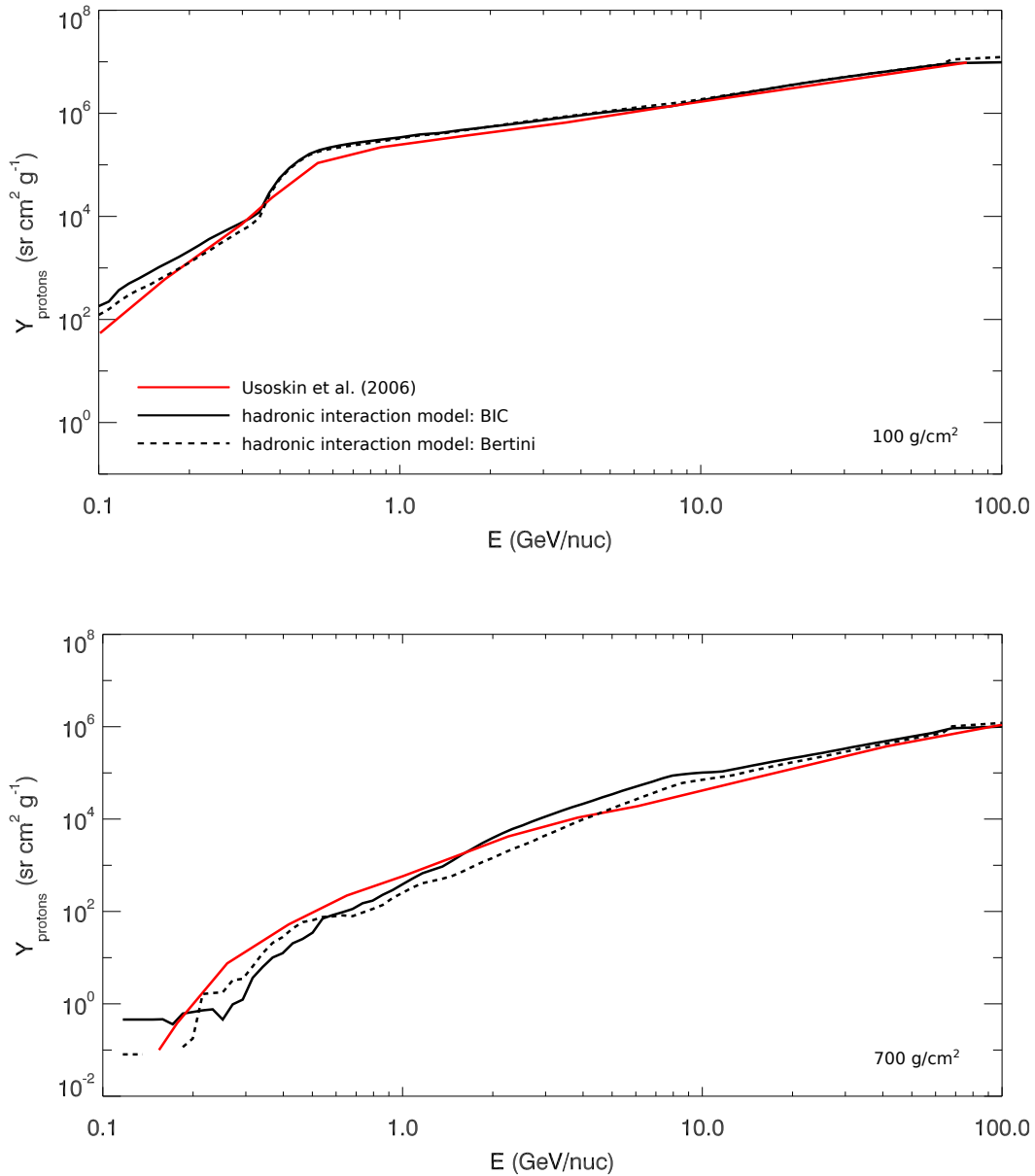


Figure 6.3: The ionization yield  $Y_{\text{protons}}$  due to primary protons at different atmospheric depths between  $100 \text{ g/cm}^2$  (upper panel) and  $700 \text{ g/cm}^2$  (lower panel) as function of the primary particle energy. The solid and dashed black lines represent the computations of this work using the BIC and Bertini hadronic interaction model, respectively. Additionally the ionization yield function computed by *Usoskin et al. (2006)* is given by the red solid lines.

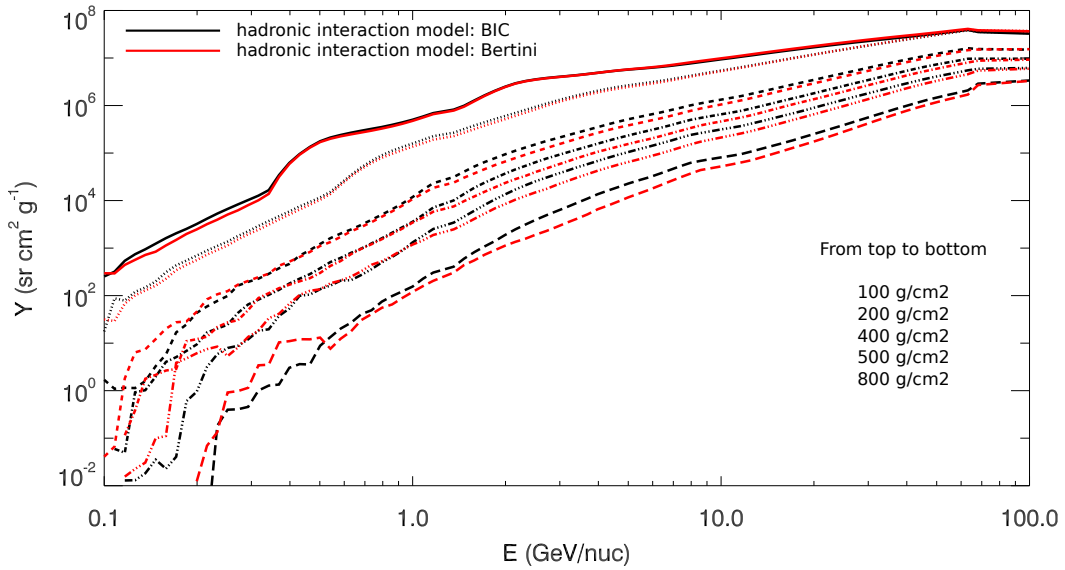


Figure 6.4: Ionization Yield  $Y$  due to primary protons and alpha particles as function of the primary particle energy at multiple atmospheric depths between 100 and 800  $g/cm^2$ .

### On the Computation of the Ionization Function $F_i$

By multiplying the previously investigated primary particle type  $i$  dependent yield function  $Y_i(x, E)$  with an arbitrary cosmic ray spectrum  $J_i(E, \phi)$ , like e.g. a solar energy particle event or a modulated galactic cosmic ray spectrum, the differential ionization function  $F_i(\phi, E, x)$  is obtained:

$$F_i(\phi, E, x) = Y_i(x, E) \cdot J_i(E, \phi). \quad (6.3)$$

Due to the folding with the galactic cosmic ray spectrum, which has its maximum intensities at around 1 GeV, the shape of the ionization function will significantly differ from the previous investigations. Thus, the differential ionization function due primary protons depending on primary particle energies between 0.1 and 100 GeV at atmospheric depths of 100  $g/cm^2$  and 700  $g/cm^2$  are given in the upper and lower panels of Fig. 6.5, respectively. Because such investigations strongly depend on the solar activity here the galactic cosmic proton spectrum by [Usoskin et al. \(2005\)](#) during solar modulation conditions of  $\phi = 700$  MV, a value corresponding to the mean solar modulation value of the last solar cycles ([Usoskin et al., 2011](#)), is applied. Again the results of this work are displayed as solid and dashed black lines while the results by the CRAC:CR11 model ([Usoskin et al., 2010](#)) are given as red solid lines.

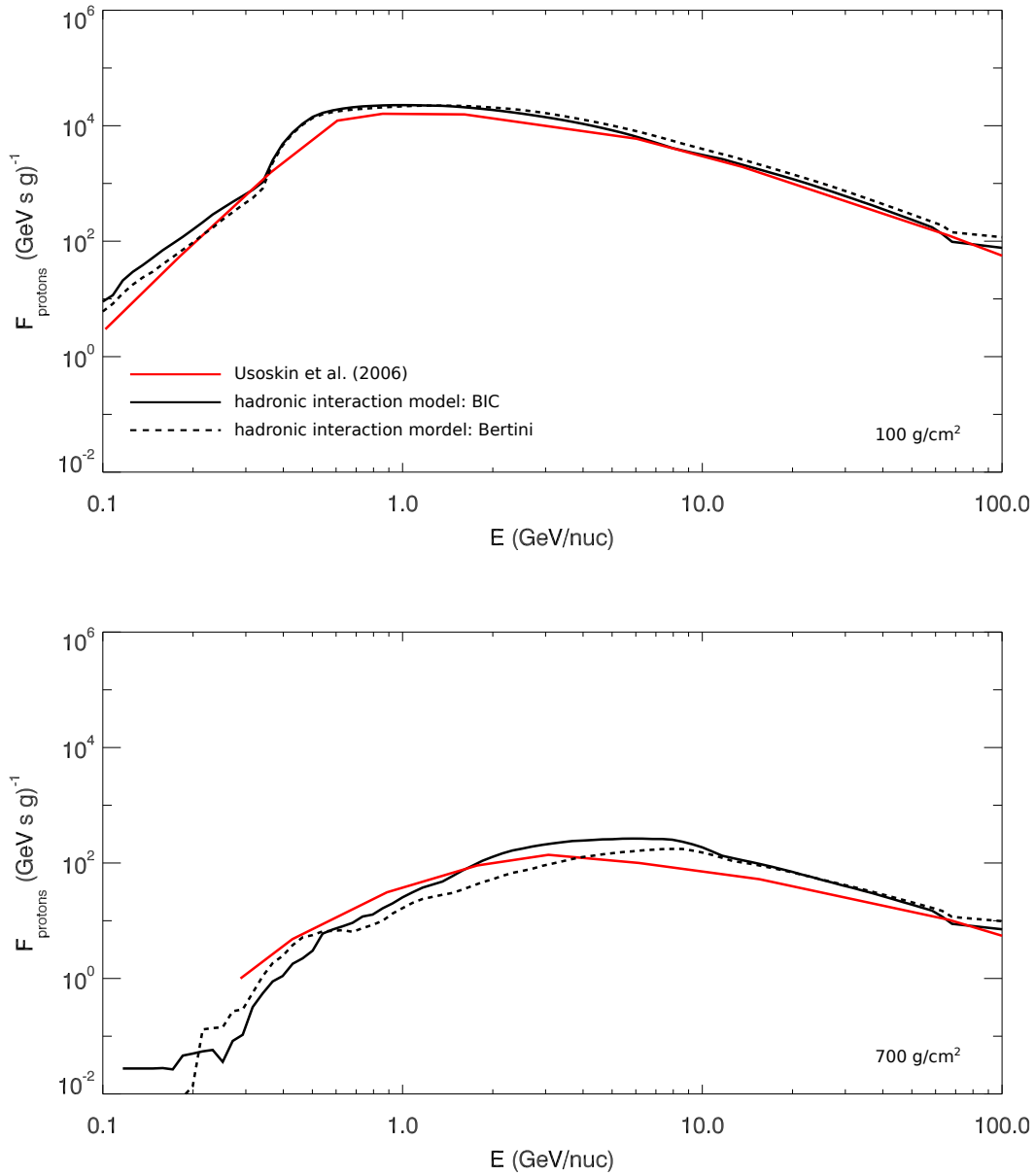


Figure 6.5: Ionization Function due to primary protons as function of the primary particle energy between 0.1 and 100 GeV at an atmospheric depths of  $100 \text{ g/cm}^2$  (upper panel) and  $700 \text{ g/cm}^2$  (lower panel). Lower panels: Ionization Function  $F_i$  due to primary protons (left) and alpha particles (right) as function of the primary particle energy at atmospheric depths between 100 and  $800 \text{ g/cm}^2$ .

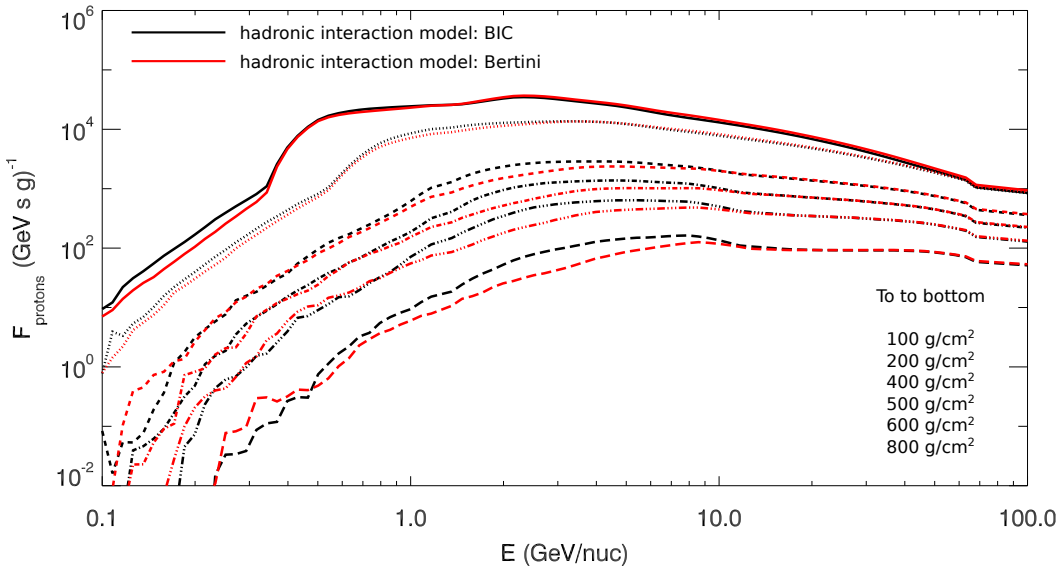


Figure 6.6: *Total ionization function at multiple atmospheric depths.*

As supposed above due to the convolution with the primary particle spectrum the shape changes drastically. Now a steep increase to the ionization function maximum occurs, which is followed by a slow decrease at higher energies.

At an atmospheric depth of  $100 \text{ g/cm}^2$ , the computations of this work are in good agreement with each other over the entire investigated energy range, and, furthermore with the results by [Usoskin et al. \(2010\)](#) slightly overestimating them at low and mid primary particle energies, however, revealing the ionization to be most effective at primary proton energies of 1 GeV. At an atmospheric depth of  $700 \text{ g/cm}^2$  the picture slightly changes. Here significant variations within the mid energy ranges within 1 and 30 GeV between the three models become obvious. In addition a shift of the ionization maximum to higher primary proton energies can be observed, which, however, slightly differs from the results by [Usoskin et al. \(2010\)](#).

Furthermore, the total ionization function of the primary particle energy and atmospheric depth is given in Fig. 6.6. Here the same color- and line-style coding as in Fig. 6.5 is applied.

In summary the previous investigations show the following picture:

- a) The difference between the two hadronic interaction models investigated in this work for low energetic primary particles is increasing with increasing atmospheric depth. While both models are in good agreement with each other at an atmospheric depth of  $100 \text{ g/cm}^2$  significant variations up to a factor of

four at 800 g/cm<sup>2</sup> occur.

- b) Depending on the atmospheric depth and the used hadronic interaction model a shift of the energy dependent ionization function maximum, and thus the effective primary proton as well as alpha energy, occurs.

### On the Computation of the Ionization Rate $Q$

The ionization rates  $Q_i$  of different cosmic ray species  $i$  are obtained by integrating the ionization function  $F_i(\phi, E, x)$  over the primary particle energy, thus,

$$Q_i(\phi, R_C, x) = \int_{E_{C,i}}^{\infty} J_i(\phi, E) \cdot Y_i(E, x) dE \quad (6.4)$$

$$= \int_{E_{C,i}}^{\infty} F_i(\phi, E, x) dE, \quad (6.5)$$

where  $E_{C,i}$  refers to the latitude and longitude dependent cutoff energy (see Eq. (5.3)) of the primary particle investigated, which additionally corresponds to the cutoff rigidity. By summing up the ionization rates of all investigated primary particle types  $i$  the total atmospheric ionization rate  $Q(x, R_C, \phi)$  in units of (g s)<sup>-1</sup> can be achieved.

$$Q(x, R_C, \phi) = \sum_i Q_i.$$

To verify the results of this work in the following the total ionization rate at polar as well as equatorial regions is computed and a comparison with measurements by [Neher \(1971\)](#) and [Lowder et al. \(1972\)](#) are performed.

#### $Q(\phi, R_C, x)$ at Polar Regions ( $R_C = 0$ GV)

From 1954 to 1969 [Neher \(1971\)](#) performed multiple balloon flights measuring the ion pair production rate for multiple solar modulation phases, locations as well as atmospheric depths. Moreover a study of a latitude survey from Thule, Greenland to Peru in the year 1965 was performed. In this Section measurements for solar minimum conditions in 1955 ( $\phi = 404$  MV) at Thule, Greenland ( $R_C = 0$  GV) are compared with the results of this work using the hadronic BIC and Bertini model.

Note that in order to compare the results of this work with the measurements performed by [Neher \(1971\)](#) as well as [Lowder et al. \(1972\)](#), which are given in units of (cm<sup>3</sup> s atm)<sup>-1</sup>, a convolution of the computations with the location and altitude-dependent density (in units of g/cm<sup>3</sup>) and pressure (in units of atm, 1 atm = 1013.25 hPa) has to be performed.

The upper and lower panels of Figure 6.7 show the total ionization rate  $Q(\phi, R_C, x)$



at polar regions during the solar minimum conditions in 1955 as well as the solar maximum conditions in 1959 as function of atmospheric depths between 0 to 1000 g/cm<sup>2</sup>, respectively. The measurements by [Neher \(1971\)](#) are displayed as open circles. The computations for the BIC and Bertini model are displayed as black solid and dashed lines, respectively. In addition the computations by [Usoskin et al. \(2006\)](#) are given as red curves.

During solar minimum conditions in general the ion pair production rate is constantly decreasing with increasing atmospheric depth, displaying a steep decrease between 0–600 g/cm<sup>2</sup> which flattens within 600–1000 g/cm<sup>2</sup>. It shows that the computations of this work are in good agreement with the measurements. However, the simulations using the Bertini model seem to be the more suitable ones, although only measurements up to 300 g/cm<sup>2</sup> are available.

To study the latter in more detail also the ionization rates during solar maximum conditions, which are displayed in the lower panel of Fig. 6.7, are investigated. Here a comparison with measurements by [Neher \(1971\)](#) (open circles) and [Lowder et al. \(1972\)](#) (crosses) is performed. In addition note that, although both measurements were performed during similar solar modulation conditions the measurements show differences of up to 20% from each other in between atmospheric depths of 0 to 200 g/cm<sup>2</sup>, a result which is still under scientific debate (see e.g. [Bazilevskaya et al., 2008](#)). However, while during solar minimum conditions a constant decrease over the entire atmospheric depth range is visible here a slightly ionization rate increase within the first 55 g/cm<sup>2</sup> becomes obvious, occurring because of the shielding of the low energy part of the primary spectrum due to increasing solar activity. Furthermore this increase is followed by a production maximum at around the same atmospheric depth, leading to a steep decrease between 55–600 g/cm<sup>2</sup> which is similar to the investigations during solar minimum conditions.

It shows that the computations of this work are in good agreement with both measurements. In particular the computations using the hadronic Bertini interaction model are able to represent both measurements well within atmospheric depths of 0 to 600 g/cm<sup>2</sup>, slightly underestimating them at higher atmospheric depths. Also shown are the computations by [Usoskin et al. \(2006\)](#) which themselves underestimate the measurements between 0–100 g/cm<sup>2</sup> while slightly overestimating them at higher atmospheric depths up to 600 g/cm<sup>2</sup>.

#### $Q(\phi, R_C, x)$ at Equatorial Region ( $R_C = 13$ GV)

In addition to the investigations at polar regions here the results of both hadronic models at equatorial regions are compared with measurements by [Neher \(1971\)](#) performed during the solar minimum conditions of 1965 near Peru, as shown in Fig 6.8. Applying the previous color and line-style coding it becomes obvious that the ion pair production rate at equatorial regions shows a steep increase

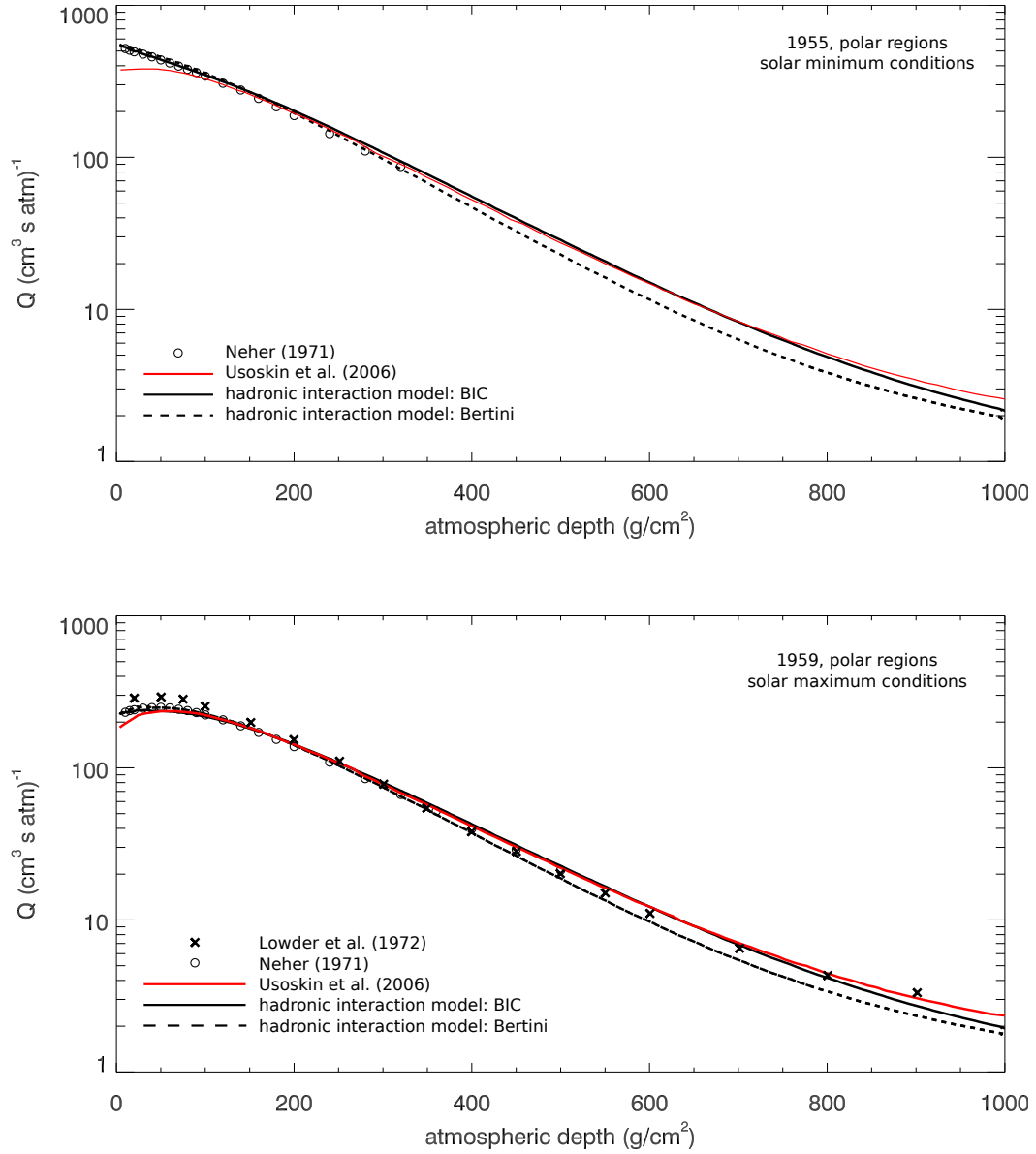


Figure 6.7: Polar ionization during solar minimum (upper panel) and solar maximum (lower panel) conditions. Here this works computations are displayed by the solid and dashed black lines, the computations by *Usoskin et al. (2006)* are shown as red solid lines while the measurements by *Neher (1971)* and *Lowder et al. (1972)* are represented by the black open circles ( $x$ ).

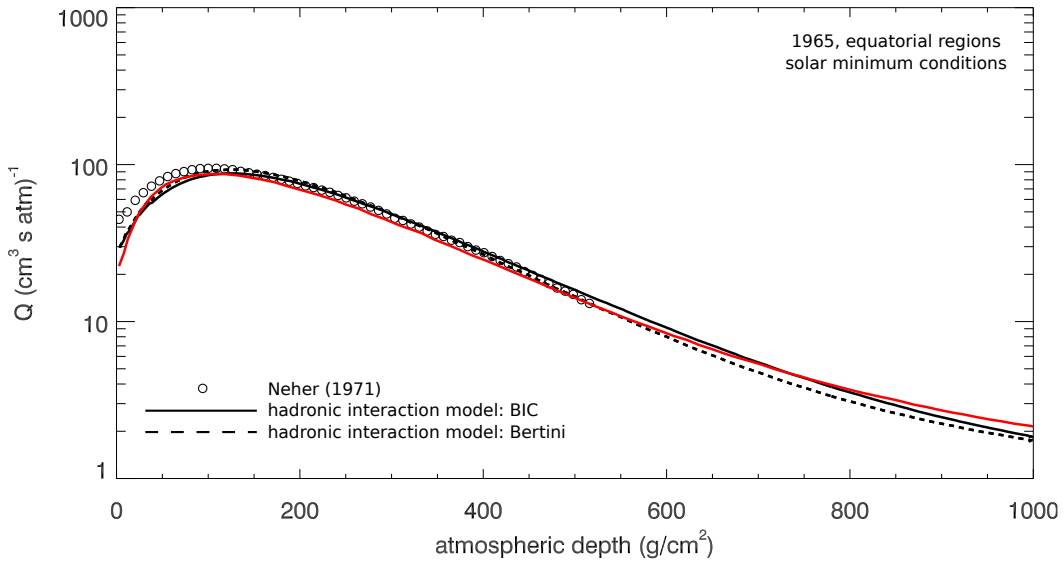


Figure 6.8: *Equatorial ionization during solar minimum conditions. The results of this work are displayed by the solid and dashed black lines corresponding to the hadronic interaction models BIC and Bertini, while the computations by Usoskin et al. (2006) are shown as red solid lines. Additionally the measurements by Neher (1971) are given by the black open circles.*

within the first 50 g/cm<sup>2</sup> which is followed by a smeared out maximum covering atmospheric depths between 50 to 100 g/cm<sup>2</sup>. Like in the previous investigations the computations using the Bertini model show a slightly better agreement with the measurements over the entire atmospheric depth range.

Thus, based on the previous investigations, from now on only the hadronic Bertini interaction model will be taken into account.

### Selected Applications

To confirm the previous finding in the following Section the reconstruction of a latitude scan performed by Neher (1967) is compared with the computations using the hadronic Bertini interaction model. As shown in Section 4.2 the temporal evolution of the geomagnetic field can not be neglected, thus to take into account the influence of the magnetic field configuration on the latitude scan reconstructions in the following the three different IGRF parameter sets of 1900, 1965 the year in which the latitude was performed as well as 2010 will be studied.

latitude	-10.3	-3.1	-2.3	3.3	12.1	17.3	23.4	30.2
longitude	-78.6	-80.7	-80.3	-80.4	-78.3	-75.7	-74.3	-74.3
latitude	37.0	38.0	41.6	46.5	52.8	65.6	76.5	
longitude	-74.2	-73.3	-65.6	-59.5	-55.3	-56.7	-68.8	

Table 6.1: Locations of the latitude survey measurements performed by *Neher (1967)*.

### Computation of the Ionization Rate in 1965 and its Application to the Latitude Survey by *Neher (1967)*

Among other measurements *Neher (1967)* performed a latitude survey during the solar minimum conditions of July 1965. Throughout 30 balloon flights, of which half were made from shipboard (mobile stations) while the other half was being launched at Bismarck, North Dakota, a northward directed latitudinal survey from Peru to Thule, Greenland was performed, measuring the cosmic ray induced ionization at atmospheric depths between  $5 \text{ g/cm}^2$  and Sea Level as function of the geomagnetic latitude.

In order to compute the ionization rate  $Q(\phi, R_C, x)$  for this setup, and to compare the results with the measurements, the cutoff rigidity dependent computations have to be converted into latitudinal and longitudinal ones. As a first calculation therefore  $Q(\phi, R_C, x)$  is "synchronized" with a global cutoff rigidity distribution as computed e.g. in Section 4.2. Thus, at each atmospheric depth  $x$  a latitude and longitude dependent ionization rate distribution can be computed. Such a distribution is shown in the colored contour plot of Fig. 6.9 displaying the results for an atmospheric depth of  $140 \text{ g/cm}^2$ . Here the LIS models by *Usoskin et al. (2005)* are used, which, according to *Usoskin et al. (2011)* in 1965 is modulated by  $\phi = 386 \text{ MV}$ . In addition also the locations of the performed latitudinal survey route, which also are given in Table 6.1, are displayed as filled stars. Red color represents ionization rates of  $270 \text{ ion pairs}/(\text{cm}^3 \text{ s atm})$ , blue ones of approximately  $80 \text{ ion pairs}/(\text{cm}^3 \text{ s atm})$ . Note that the shape of the global ionization distribution depends on the used magnetic field configuration, however, the production rates are anti-correlated to the cutoff rigidity distribution. Thus, regions with low cutoff rigidities, e.g. polar regions, show maximum ionization rate values.

Figure 6.10 uses the previous investigations as function of latitude to compare them with the depth dependent measurements of the latitude survey by *Neher (1967)*. Note that the computations as well as the measurements of each atmospheric depth investigated are colored differently: the results at  $140 \text{ g/cm}^2$ ,  $200 \text{ g/cm}^2$  and  $280 \text{ g/cm}^2$  are displayed in red, blue and green, respectively. The colored stars represent the locations of the mobile stations while the solid lines represent the computations of this work.

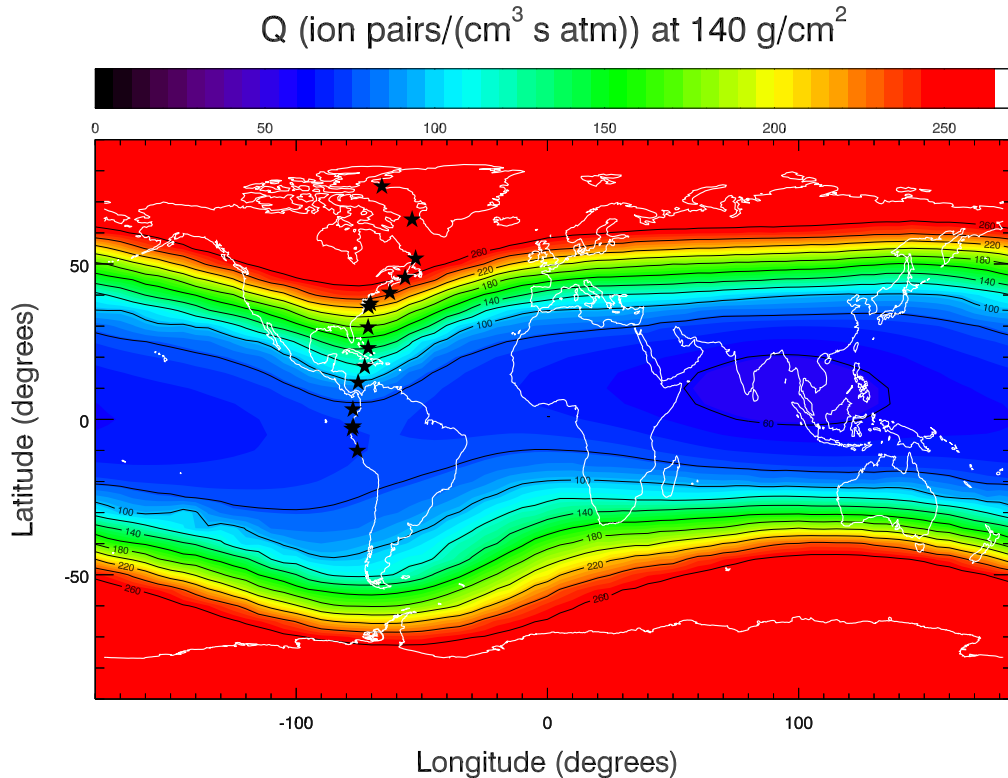


Figure 6.9: Color plot of the latitude and longitude dependent atmospheric ionization during solar minimum conditions ( $\phi=389 \text{ MV}$ ) at an atmospheric depth of  $140 \text{ g/cm}^2$ . In addition the locations of the latitude survey performed by *Neher (1967)* are displayed as black stars.

A good agreement between the measurements and the computations of this work is found, although at higher latitudes slight overestimations of the measurements occur. In addition Fig. 6.10 shows a black dashed line representing the so called latitudinal knee-effect (see e.g. *Compton and Turner , 1937*). According to *Dorman (2012)* the knee, which is caused by magnetospheric effects like shadow cone effects as well as due to the modulation of low energetic GCRs (see e.g. *Neher, 1967*), is defined to be the latitude of an atmospheric depth-dependent cutoff rigidity value above which the ionization rate becomes plateau-like. According to the measurements by *Neher (1967)* the depth-dependent knee effect follows a linear function given by  $f(\text{latitude}) = 30 \cdot \text{latitude} - 1235$  (black dashed line), which is in good agreement with the computations.

Taking into account the variation of the global cutoff rigidity distribution

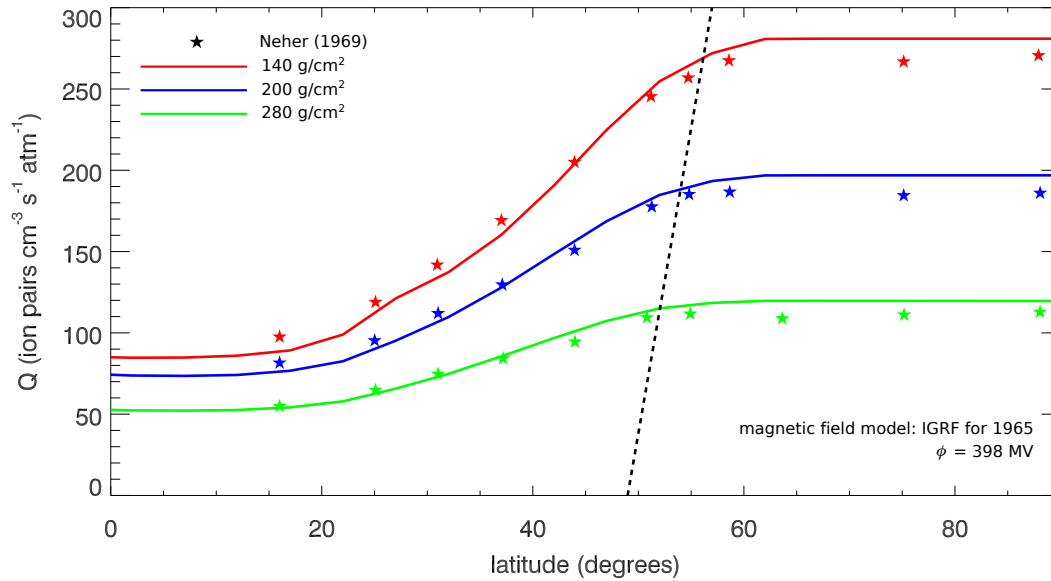


Figure 6.10: Latitude survey at  $140 \text{ g/cm}^2$  (blue),  $200 \text{ g/cm}^2$  (green) and  $280 \text{ g/cm}^2$  (cyan). The measurements performed by Neher (1967) are represented by the atmospheric depth dependent filled colored stars. Additionally a linear approximation of the so-called latitudinal knee (see text for more information) predicted by Neher (1967) as well as given by this work are given by the black and red dashed lines.

over the past 110 years (see Section 4.2) the question arises whether or not the computations of the reconstructed latitude survey are sensitive to the used magnetic field configuration. Thus, in the following the influence of the used magnetic field configurations of the IGRF model in 1900, 1965 and 2010 is investigated.

### On the Influence of the Magnetic Field Model Applied

The panel of Fig. 6.11 shows the difference between the cutoff rigidities computed for the magnetic field parameters of the year 1900 and 2010, as discussed in Section 4.2, also showing the locations of the performed latitude survey. It becomes obvious that the latitude survey by Neher (1967) was performed in regions which only show minor cutoff rigidity changes of  $\pm 0.5 \text{ GV}$  during the past 110 years, implying that the use of different magnetic field configurations should only have minor influence on the computed ionization rates.

Figure 6.12 shows the deviations of the computed latitude survey using either the IGRF parameters for 1900 (solid lines) or 2010 (dashed lines) to the actual survey using the configurations of 1965 at  $140 \text{ g/cm}^2$  (red),  $200 \text{ g/cm}^2$  (blue) as well as  $280 \text{ g/cm}^2$  (green), revealing that certain regions are more influenced

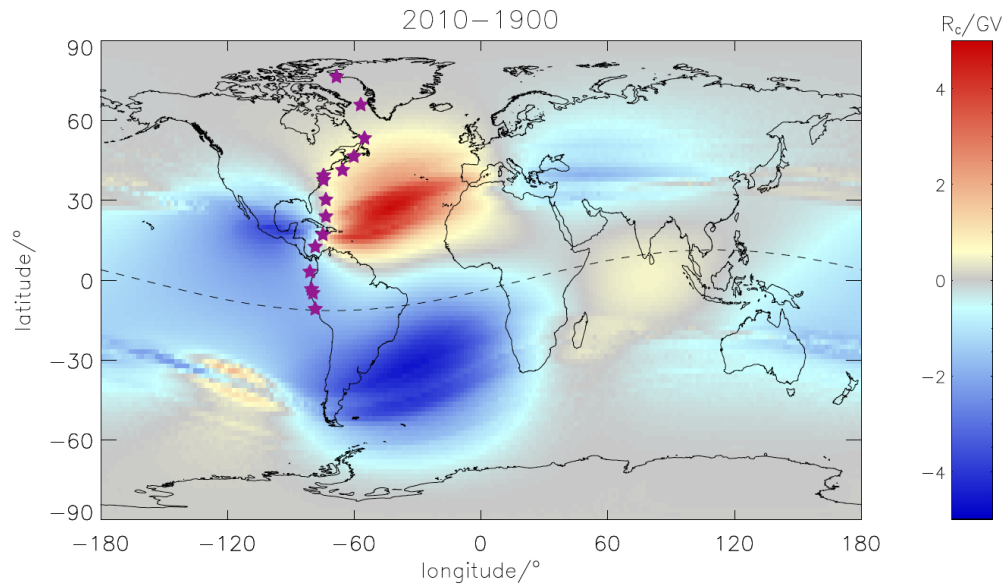


Figure 6.11: *Latitude survey* . The locations of the original latitude survey are represented by the filled purple stars in the left panel.

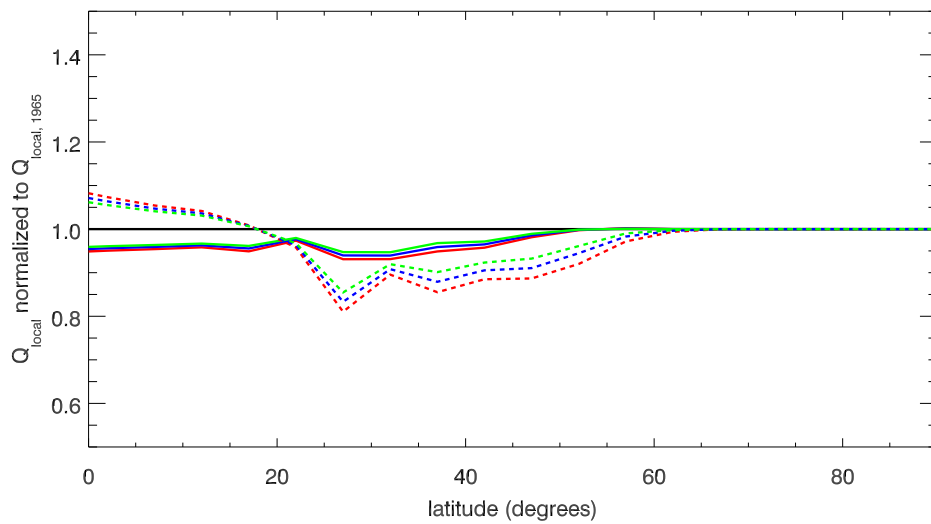


Figure 6.12: *Shifted latitude survey at  $140 \text{ g/cm}^2$  (blue),  $200 \text{ g/cm}^2$  (green) and  $280 \text{ g/cm}^2$  (cyan) using the magnetic field parameters of the year 1900 (solid lines) and 2010 (dashed lines).*

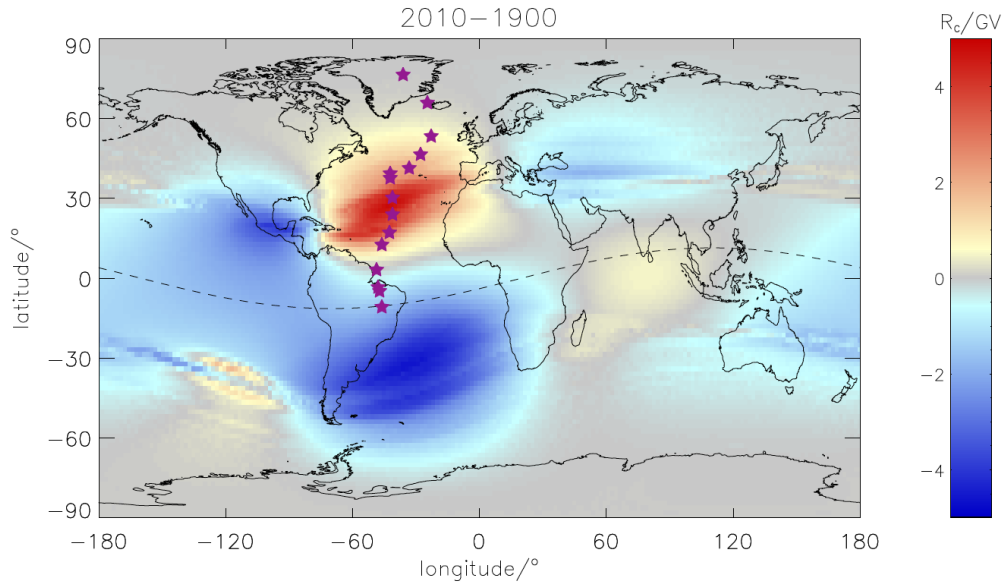


Figure 6.13: *Shifted latitude survey.* The locations of the shifted latitude survey are represented by the filled purple stars in the left panel.

by a change in the magnetic field properties than others. While no influence of the used magnetic field configurations on the ionization at polar regions can be observed, at low and mid latitudes differences are visible. Here ionization rate decreases/increases between  $\pm 10\text{--}20\%$ , and thus a much stronger variation than expected, occurs. This study alone reveals that it is of great importance to use the proper magnetic field configurations for the reconstruction of the measurements, however, furthermore, the question arises how strong the effects would be if the latitude survey would have been performed at regions about  $20^\circ$  further more east, a case study which is performed in the following.

### **Influence of the Magnetic Field During the Shifted Latitude Survey**

The shifted, hypothetic, latitude survey is shown in Fig. 6.13. As can be seen such a latitude scan would have been performed in regions of stronger cutoff rigidity changes, which would lead to even more severe deviations, as shown in Fig. 6.14. It becomes obvious that by using this setup now a much wider region within  $0\text{--}72^\circ$  shows severe differences between the computations using the proper magnetic field configurations and those using the parameters of the IGRF model for 1900 (2010). In this investigations differences of up to  $\pm 20\text{--}40\%$  occur, emphasizing the previous findings.



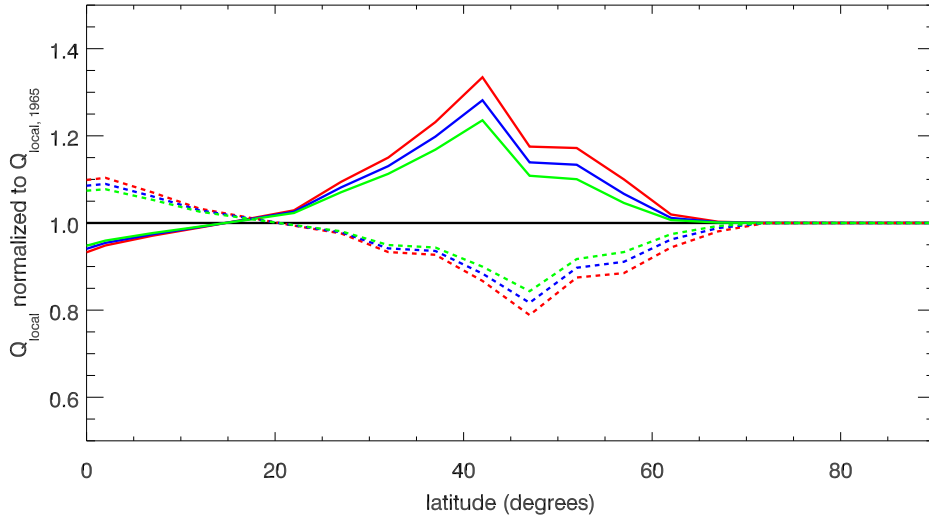


Figure 6.14: *Shifted latitude survey at  $140 \text{ g/cm}^2$  (blue),  $200 \text{ g/cm}^2$  (green) and  $280 \text{ g/cm}^2$  (cyan) using the magnetic field parameters of the year 1900 (solid lines) and 2010 (dashed lines).*

### Depth-Dependent Cosmic Ray Induced Ionization Between 1936 and 2010

The previous Section showed that the ionization rate distribution strongly depends on the used magnetic field configuration, however, a strong dependence on the solar modulation also exists. Therefore this Section will study the influence of the solar modulation on the atmospheric ionization rates at specific atmospheric depths as well as geographical locations. In order to investigate the solar influence on the atmospheric ionization during realistic conditions the reconstructed solar modulation parameter over the last 74 years (Usoskin et al., 2011) is taken as input for this study.

As shown in Fig. 6.15 the total ionization rates due to primary protons and alpha particles are displayed at atmospheric depths of  $700 \text{ g/cm}^2$  (left panel) and  $1000 \text{ g/cm}^2$  (right panel) as a function of time. Here black lines represent the computations at polar regions, while red lines show the results at equatorial regions. Note that the second y-axis give the ionization values at equatorial regions.

From this investigations it becomes obvious that the solar modulation cycle dependent ionization rates with the two minima-cycle dependent flat and peaked profiles can be observed at polar as well as equatorial regions. In general, independent from atmospheric depth and location, the ionization rates clearly show an anti-correlation to the solar activity cycle. Furthermore, independent from

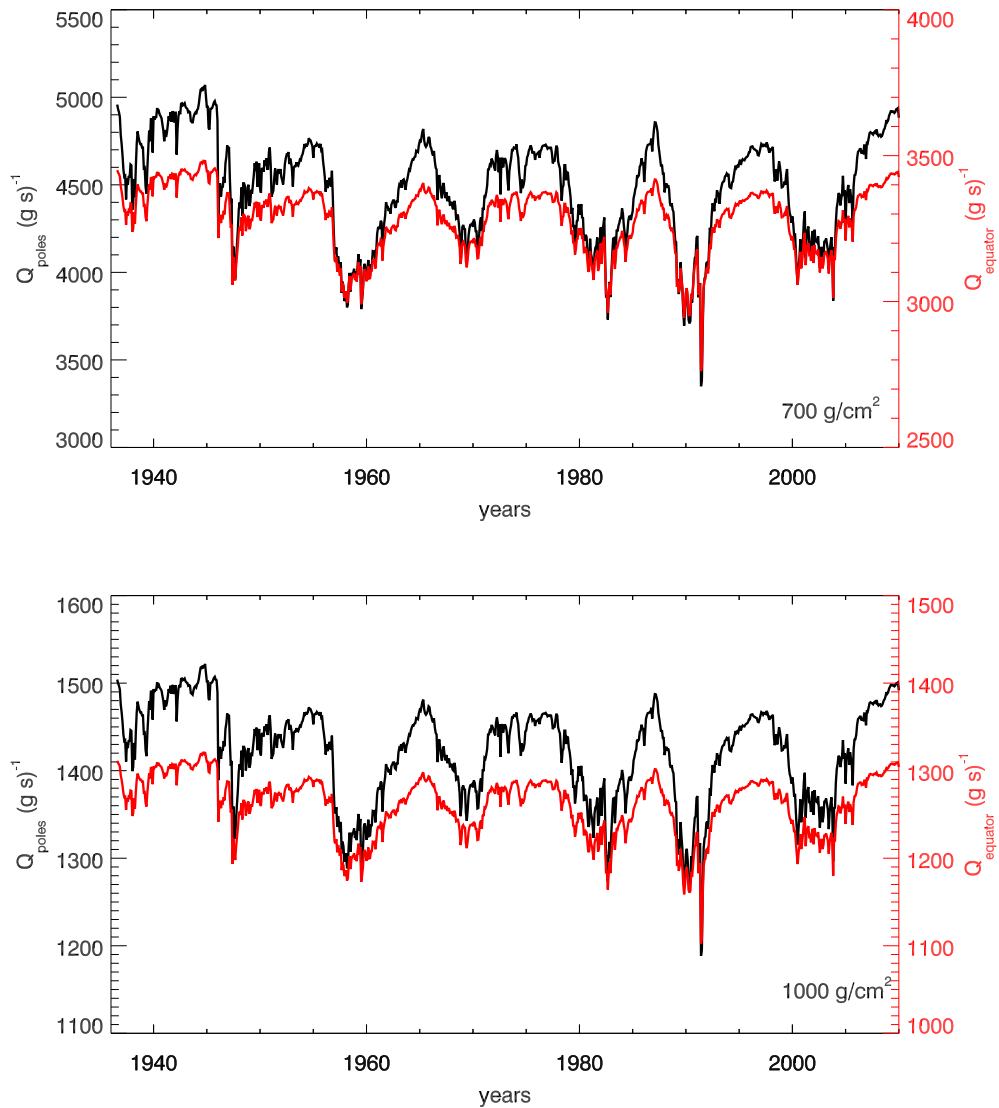


Figure 6.15: Influence of the solar modulation on the ionization rates at atmospheric depths of  $700 \text{ g/cm}^2$  (left panel) and  $1000 \text{ g/cm}^2$  (right panel) at polar (black lines) and equatorial regions (red lines). Note that the second y-axis correspond to the values computed at equatorial regions.

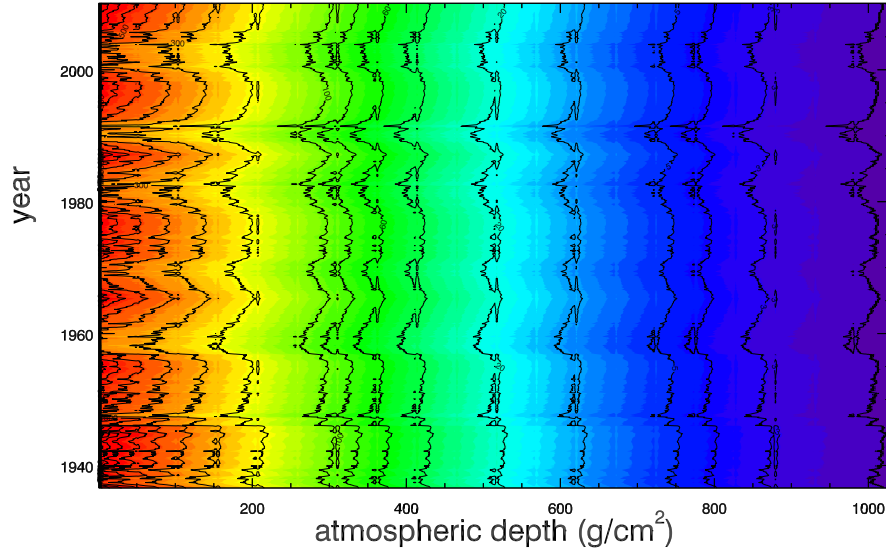


Figure 6.16: Contour plots of the atmospheric ionization (here in units of (ion pairs)/(cm<sup>3</sup> s atm)) as function of atmospheric depths between 0 and 1030 g/cm<sup>2</sup> and the solar modulation between 1939 and 2010 using the reconstructed solar modulation parameters by *Usoskin et al. (2011)*. The computations are performed for polar regions.

atmospheric depth and location, the eleven as well as 22 year cycle is visible in the ionization rate values.

However, in order to investigate the atmospheric depth dependence of the solar activity over the past 74 years Figs. 6.16 and 6.17 show logarithmically colored contour plots of the cosmic ray induced ionization as function of atmospheric depth and time at polar regions as well as equatorial regions, respectively. Here purple color indicates low ionization while red coloring represents high ionization values. In addition contour lines at specific ionization values are shown, combining and summarizing almost all results previously found:

- a) the cosmic ray induced ionization strongly depends on the atmospheric depth investigated
- b) the ionization strongly depends on the solar variation
- c) during solar minimum and maximum conditions at polar regions the ionization maximum can be found between 0-75 g/cm<sup>2</sup>, while it is smeared out between

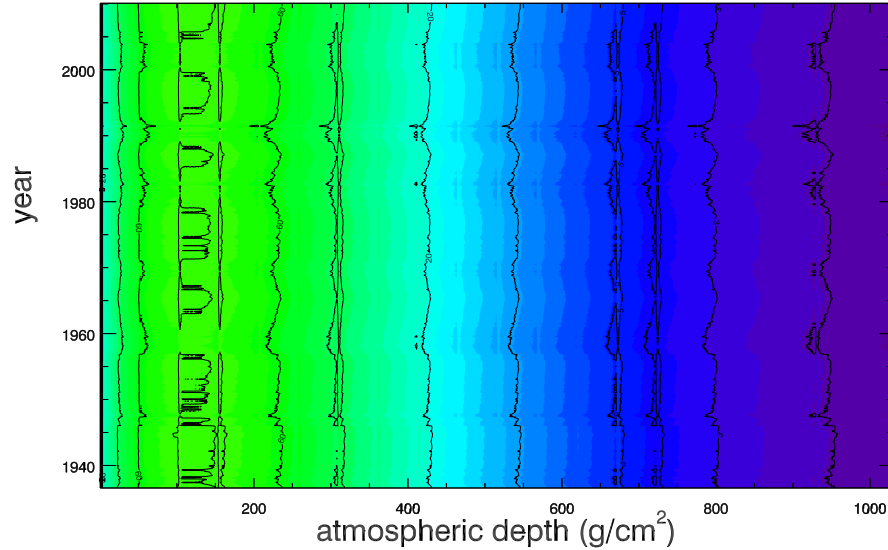


Figure 6.17: Contour plots of the atmospheric ionization (here in units of (ion pairs)/(cm<sup>3</sup> s atm)) as function of atmospheric depths between 0 and 1030 g/cm<sup>2</sup> and the solar modulation between 1939 and 2010 using the reconstructed solar modulation parameters by *Usoskin et al. (2011)*. The computations are performed for equatorial regions.

50 and 200 g/cm<sup>2</sup> at equatorial regions

- d) the ionization rates between 600 and 1000 g/cm<sup>2</sup> are independent of latitude, while an increase of a factor of up to 20 between both locations at lower atmospheric depths can be observed
- e) the variability due to the solar modulation is stronger at polar regions.

In summary the computations of this Chapter revealed that the hadronic Bertini model is the more suitable one for the purpose of this work. Thus, the following investigations on the local and global cosmogenic radionuclide production rates will be performed exclusively for this particular model.

# Modeling the Production of Cosmogenic Radionuclides

---

★ *Parts of Section 7.2 and Section 7.3 are published in [Matthiä et al. \(2011\)](#) and [Fichtner et al. \(2012\)](#). Furthermore, the results of Section 7.6 are in prep. as [Herbst et al. \(2012c\)](#).*

---

*"And we stare at the Sun  
but we never see anything there  
just a glare has become  
all that we'll ever see there..."*  
MuteMath - Stare at the Sun -

GCRs are modulated as they enter the heliosphere (see Section 2.2). During times of low solar magnetic activity this helio-magnetic modulation is less pronounced than during solar maximum conditions. Thus, during phases of low solar activity much higher particle intensities occur inside the heliosphere. Particles arriving at the Earth's vicinity additionally encounter the terrestrial magnetic field which shields the atmosphere from low energetic primary charged particles, a quantity described by the cutoff rigidity investigated in Section 4.2. However, particles which are able to enter the terrestrial atmosphere will interact with the atmospheric environment. While lower energetic particles mainly lose energy due to ionization processes in the upper atmosphere (see Chapter 6) the interaction of high-energetic primary particles deeper inside the atmosphere leads to the evolution of altitude-dependent secondary particle cascades mainly consisting of secondary neutrons, protons and muons (see Section 2.4). Of great importance for the production of both short- and long-lived cosmogenic radionuclides thereby in particular are secondary neutrons and protons. Due to the fact that the production is directly correlated with the primary particle intensity on top of the atmosphere it is directly anti-correlated to the solar activity.

Since the discovery of atmospheric particle showers in the early 1930s it was predicted that CRs could also lead to the production of cosmogenic radionuclides in the atmosphere as well as on the Earth's surface (see [Grosse, 1934](#)). This was only verified in the late 1940s when the cosmogenic radionuclide  $^{14}\text{C}$  was discovered (see e.g. [Libby, 1946](#); [Libby et al., 1949](#)). The discovery of other cosmogenic radionuclides, however, took about 30 more years, but with the development of the Accelerator Mass Spectrometry (AMS) in the late 1970s (see e.g. [Muller, 1977](#)) other cosmogenic radionuclides like  $^{10}\text{Be}$  as well as  $^{36}\text{Cl}$  were detected. Nowadays,

in times of space probing and satellite imaging the Sun and its interior can be studied in much more detail, providing huge amounts of information about the solar activity and the solar magnetic field evolution with time. In order to study e.g. the solar activity over past millennia (see e.g. Beer et al., 1990; Beer, 2000; Beer et al., 2000; Vonmoos et al., 2006; Steinhilber et al., 2008) or to reconstruct the solar as well as terrestrial magnetic field over thousands of years back in time (see e.g. Wagner et al., 2000; Steinhilber et al., 2010) several approaches have to be taken into account.

Because of the fact that a) cosmogenic radionuclides are directly linked to the primary particle intensity and b) they are stored in natural archives like ice sheets, tree rings or sediments information of former solar as well as geomagnetic conditions are well preserved. First studies by Beer et al. (1988, 1990) investigated the  $^{10}\text{Be}$  concentrations measured from the Camp Century ice core (North Greenland) dating back to the year 1783. A clear anti-correlation to the solar activity is visible in the data. By comparing the measured  $^{10}\text{Be}$  concentrations with the relative abundance of  $^{14}\text{C}$  measured from tree rings Bard et al. (1997) additionally identified delayed concentration maxima during persistent periods of low solar activity. Today these time periods are known as the Grand Solar Minima. Within the last millennium six of these minima occurred, the most recent ones of which are the Wolf minimum (between 1060 and 1320 AD), the Spoerer minimum (around 1500 AD), the Maunder minimum (around 1690 AD), the Dalton minimum (around 1820 AD) and the Gleissberg minimum (around 1890 AD). Besides these grand solar activity minima McCracken et al. (2004) could also identify six periods of unusually high solar activity between 850 AD and 1958 AD.

In addition, other parameters like e.g. the total solar irradiance (see e.g. Steinhilber et al., 2010) as well as the solar modulation parameter investigated in Section 3.4 can also be reconstructed from the measured data (see e.g. Vonmoos et al., 2006; Steinhilber et al., 2008). Using the latter results Herbst et al. (2010) (see also Section 3.4) concluded that the reconstructed solar modulation parameter values from  $^{10}\text{Be}$  data may strongly depend on the used LIS. Investigating different LIS models they found inconsistencies between the spectra and the  $^{10}\text{Be}$  production rates which may reveal information about the true LIS.

This Chapter will introduce the physical background of the production of cosmogenic radionuclides as well as present the process of modeling various nuclides using the simulation code PLANETOCOSMICS (see e.g. Appendix A.2). In order to do so in a first step the atmospheric altitude as well as primary particle energy dependent production rates of  $^{10}\text{Be}$ ,  $^7\text{Be}$ ,  $^{14}\text{C}$ ,  $^3\text{H}$ ,  $^{36}\text{Cl}$  and  $^{26}\text{Al}$  as function of the solar modulation parameter  $\phi$  and the geomagnetic location will be computed. Note that in contrast to previous approaches the cosmogenic radionuclide production rates due to primary protons as well as primary alpha particles is investigated separately here. In the following Sections particularly the

influence of the cross sections as well as the applied geomagnetic field configurations are studied. In order to validate the results of this work comparisons with other numerical approaches by e.g. Masarik and Beer (1999), Webber and Higbie (2003), Masarik and Beer (2009) or Kavaltsov et al. (2012) as well as measurements by e.g. Nir et al. (1966), Reimer et al. (2009) and Berggren et al. (2009) will be performed. Furthermore the computed  $^{14}\text{C}$  production rates will be used in order to reconstruct the solar modulation parameter  $\phi$  during the Holocene using the corresponding paleomagnetic field configurations given by Knudsen et al. (2008) as well as Korte et al. (2011). Using the reconstructed modulation parameter as well as the global  $^{10}\text{Be}$  production rates presented in this work for the first time also  $^{10}\text{Be}$  measurements will be shown to be reasonably well represented.

## 7.1 The Production of Cosmogenic Radionuclides

Cosmogenic Radionuclides are the product of an interaction of CRs with the atmospheric gases Oxygen, Nitrogen and Argon. By assuming the intensity of the LIS outside the heliosphere to be constant over the Holocene GCRs are modulated only by solar activity as well as the geomagnetic field.

Inside the atmosphere three main production mechanisms, which lead to the production of cosmogenic radionuclides, exist:

**Spallation reactions:** Protons as well as neutrons are sputtered off the atmospheric target nuclei during an interaction with high-energetic secondary neutrons (at Sea Level sporadically also protons). Furthermore evaporation processes may occur, and thus, more than one low-energetic nucleon may be emitted when the energy of the impactor is in the order of 7 – 9 MeV, an energy corresponding to the binding energy of the nucleon (see e.g. Masarik and Beer, 1999; Dunai, 2010).

**Thermal neutron capture:** Occurs because most of the neutrons produced in cascades and sub-cascades are slowed down to thermal energies in the energy range of  $1 \cdot 10^{-8} - 7 \cdot 10^{-7}$  MeV (Phillips et al., 2001). Due to the fact that most of these reactions are determined by large cross sections they produce a significant amount of cosmogenic radionuclides (see e.g. Phillips et al., 2001; Dunai et al., 2007; Dunai, 2010), the most prominent example of which e.g. is  $^{14}\text{C}$ .

**Negative muon capture:** Thermal-energetic muons are captured by the atomic electron shell of the target atom and subsequently cascade towards the lowest electron shell, where they decay or are captured by the nucleus (see e.g. Eidelman et al., 2004). Furthermore, muons are not stable. They decay with a half-life time of 1.52  $\mu\text{s}$ .

Furthermore, because of the much lower corresponding cross sections and the fact that thermal muons mainly occur near the Earth's surface the negative muon capture

CN	mass number	atomic mass number	half-life
<sup>10</sup> Be	4	10	1.39·10 <sup>6</sup> a
<sup>7</sup> Be	4	7	53d 6h 45min
<sup>36</sup> Cl	17	36	3.01·10 <sup>5</sup> a
<sup>3</sup> H	1	3	12a 117d
<sup>26</sup> Al	13	26	7.17·10 <sup>5</sup> a
<sup>14</sup> C	6	14	5730a

Table 7.1: *Characteristic of the cosmogenic radionuclides investigated in this work: <sup>10</sup>Be, <sup>7</sup>Be, <sup>36</sup>Cl, <sup>3</sup>H, <sup>26</sup>Al as well as <sup>14</sup>C (see e.g. [Steinhilber, 2010](#)).*

reactions are of minor importance and thus will not be taken into account in this work.

### The Cosmogenic Radionuclides Investigated in This Work

The following Section investigates the production reactions as well as the characteristics of the cosmogenic radionuclides studied in this work.

As shown in Table 7.1 and Table 7.2 Beryllium has at least two cosmogenic radionuclides, <sup>7</sup>Be and <sup>10</sup>Be, both of which are produced by spallation reactions of secondary neutrons and protons with the atmospheric Nitrogen and Oxygen atoms. Because of its long half-life of 1.39·10<sup>6</sup> a <sup>10</sup>Be has a long half-life before it decays to <sup>10</sup>B (see e.g. [McPherson et al., 2003](#)), a half-life time which, however, is still under scientific debate. [Chemeleff et al. \(2009\)](#) as well as [Korschinek et al. \(2010\)](#) refer to a half-life time of 1.39·10<sup>6</sup>a while [Nishiizumi et al. \(2007\)](#) and [Hofmann et al. \(1987\)](#) talk about 1.36·10<sup>6</sup>a and 1.51·10<sup>6</sup>a, respectively. The cosmogenic radionuclide <sup>7</sup>Be, with a half-life time of merely about 53 days, decays by electron capture where an electron is spontaneously swallowed by the nucleus, emitting a neutrino (see e.g. [Liu et al., 2003](#)). The reactions leading to the production of the cosmogenic radionuclides studied in this work are summarized in Table 7.2, showing the majority of those cosmogenic radionuclides to be produced by spallation reactions with the atmospheric atoms Nitrogen and Oxygen, while both <sup>36</sup>Cl and <sup>26</sup>Al are the result of interactions with the stable Argon isotopes <sup>36</sup>Ar and <sup>40</sup>Ar.

### The Cross Sections

As pointed out in Section 2.4 the probability for an interaction of a secondary particle with an atmospheric target atom is described by the cross section  $\sigma$ . For the production of the cosmogenic radionuclides studied here only neutron and proton cross sections play an important role. The main difference between both



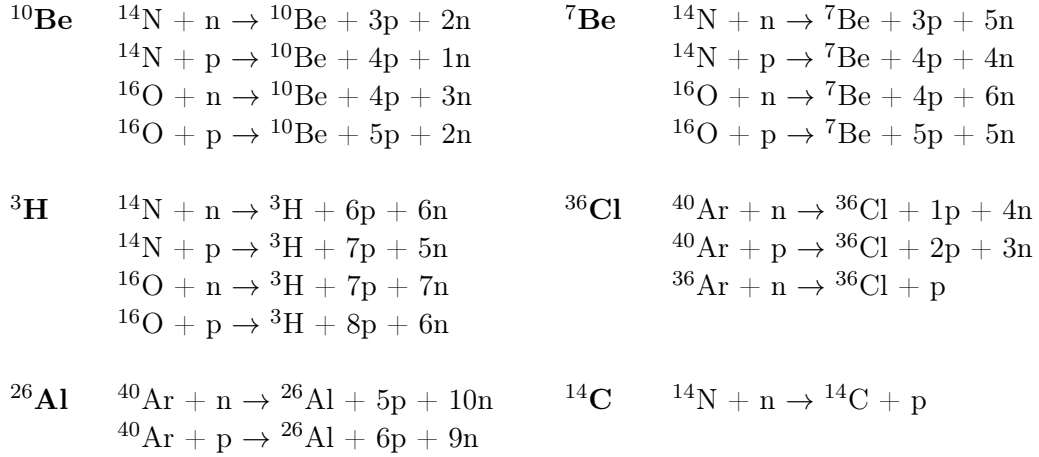


Table 7.2: Production reactions of the CNs investigated in this work (see e.g. [Vonsooms, 2005](#)).

can be found in the low energy range: Due to the existence of the Coulomb barrier the positively charged protons are repulsed by the protons located inside the nuclei of the target atom (see e.g. [Beer et al., 2012](#)).

The corresponding excitation functions are displayed in Fig. 7.1. It shows that each of the cross sections has a specific threshold energy which is an indicator for the minimum energy required to trigger the corresponding reaction.

The upper panels of Fig. 7.1 show the excitation functions of  $^{10}\text{Be}$  (left panel) and  $^7\text{Be}$  (right panel). The black and red solid lines represent the reactions of N and O with the secondary neutrons, respectively, while the dashed colored lines refer to interactions with secondary protons. The thresholds of e.g. the production of  $^{10}\text{Be}$  from interactions of the secondary neutrons and protons with Nitrogen thereby are in the order of 15 MeV and 33 MeV, respectively. However, in all cases the oxygen-based threshold energy is in the order of 30 MeV. For information on the experimental data used here see [Masarik and Beer \(1999\)](#) as well as [Webber and Higbie \(2003\)](#).

The left middle panel of Fig. 7.1 shows the cross sections for the production of  $^{36}\text{Cl}$  by interactions with the stable isotopes of atmospheric Argon. However, in the atmosphere Argon is much less abundant than Nitrogen or Oxygen. The black lines show the interaction probability for the spallation reaction with  $^{40}\text{Ar}$ , while the red line represents the interaction with  $^{36}\text{Ar}$ . Here the two peak structure of the dashed black line refers to the interaction of  $^{40}\text{Ar}(\text{p,x})^{36}\text{Cl}$ . The excitation function  $^{36}\text{Ar}(\text{n,p})^{36}\text{Cl}$ , however, has a much lower threshold than the other two, while showing an almost five times higher  $\sigma$  value. Note the partly compensation

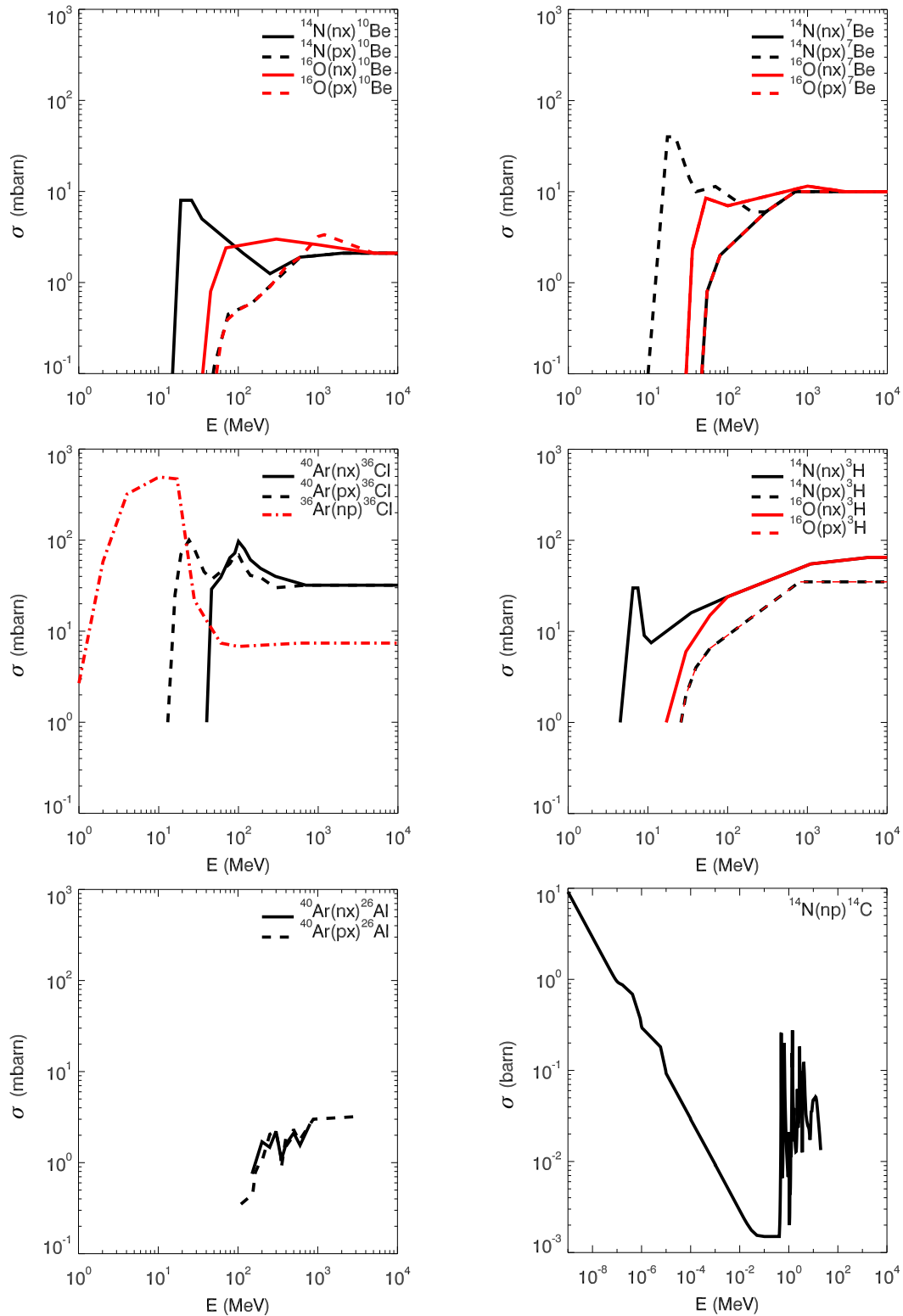


Figure 7.1: The cross-sections for the production of the cosmogenic radionuclides  $^{10}\text{Be}$ ,  $^7\text{Be}$ ,  $^{36}\text{Cl}$ ,  $^3\text{H}$ ,  $^{26}\text{Al}$  and  $^{14}\text{C}$ .

of the much less abundance of Argon by the much higher  $\sigma$  values of the three reactions. Moreover, in the middle right panel the cross sections for the production of  $^3\text{H}$  are displayed. Those cross sections were taken from experimental data by Nir et al. (1966) and references therein.

The lower panels display the energy-dependent cross sections of  $^{26}\text{Al}$  (left panel) and  $^{14}\text{C}$  (right panel). All previously investigated cross sections are located in the energy range between 1 MeV and 10 GeV, most of the time exceeding the binding energy of  $E > 8$  MeV. The only exception to this picture is  $^{14}\text{C}$  which is produced by thermal-neutron capture. Here much lower energies within  $1 \cdot 10^{-9} - 100$  MeV become important. In addition note that  $^{14}\text{C}$  is given in barn rather than mbarn.

The cross sections used in this work can also be found at e.g. the National Nuclear Data Center (see e.g. <http://www.nndc.bnl.gov/exfor/endlf.htm>).

Due to the strong energy-dependence of the cross sections the production of the cosmogenic radionuclides investigated here will strongly depend on the secondary particles fluxes, and thus different production rates as function of a) solar modulation, b) geomagnetic latitude as well as c) atmospheric depth will occur (see e.g. Beer et al., 2012).

However, once cosmogenic radionuclides are produced they become subject of complex atmospheric mixing and transport mechanisms, as sketched in Figure 7.2. After being transported and distributed by atmospheric circulation mechanisms, indicated by the black cycles, as well as being attached to atmospheric aerosols they are either removed by condensation, like e.g.  $^{10}\text{Be}$  as well as  $^{36}\text{Cl}$ , or become part of the carbon cycle (see e.g. Prentice et al., 2011) like the radionuclide  $^{14}\text{C}$  (see e.g. Dunai, 2010), processes leading to the storage of the cosmogenic radionuclides in natural archives like ice sheets, trees or sediments, where they preserve information about their production and transport. Moreover, Heikkilä et al. (2008) performed global circulation model computations on the example of  $^{10}\text{Be}$ . They found that the stratospheric production contributes in the order of 70 % to the total atmospheric production. As a result the signal stored e.g. in the Antarctic ice contains information of higher but also lower latitudes. Atmospheric transport and mixing processes, however, are beyond the scope of this work, thus all cosmogenic radionuclides investigated here are assumed to be globally mixed.

## 7.2 Modeling the Production of Cosmogenic Radionuclides

First attempts to calculate the production of the cosmogenic radionuclides were made in the mid of the 20<sup>th</sup> century. In those days, however, both the secondary

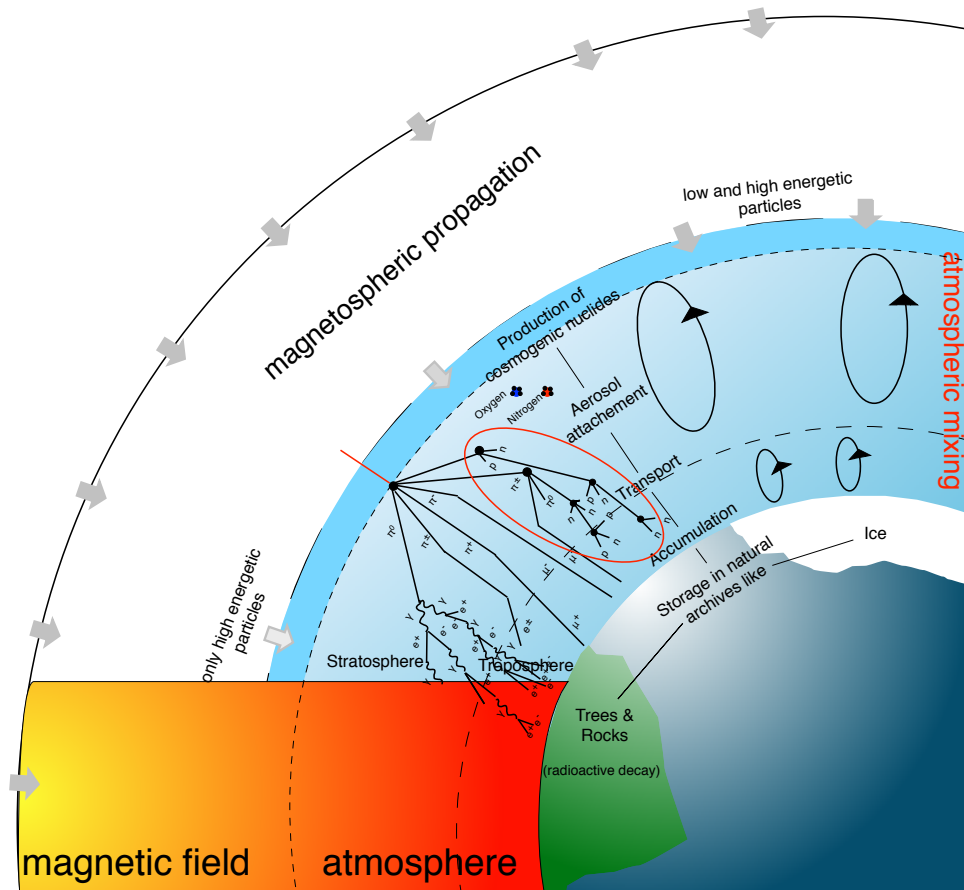


Figure 7.2: Sketch of the processes involved in the production of cosmogenic radionuclides. Primary particles entering the Earth's atmosphere trigger a secondary particle cascade. The evolving hadronic branch which, amongst others, leads to the production of the cosmogenic radionuclides investigated in this work. After being produced the radionuclides attach to aerosols and undergo atmospheric circulation and mixing processes. Depending on the residence time they undergo a mixing, which can either be global or altitude dependent. Eventually they are transported into natural archives like ice sheets, trees or sediments where they continue to decay radioactively. Both transport archiving processes can be influenced by the atmospheric circulation as well as the accumulation rate.

particle fluxes, and thus the cosmogenic nuclide production rates as well as the cross sections were not well known. Therefore the pioneers of this new field, D. Lal and B. Peters, invented another approach. Using photo-emulsion plates they determined the number of interactions between the CRs and the matter contained in the plates at different geographic locations and altitudes over several years. By multiplying the counting-rate with the yield function (see Section 6.2) they were able to obtain the production rate of a specific cosmogenic radionuclide without the exact knowledge of the physics involved (see e.g. Lal and Peters, 1967).

Nowadays computations by e.g. Masarik and Beer (1999, 2009), Webber and Higbie (2003, 2010), Usoskin et al. (2004), Kavaltsov and Usoskin (2010), Matthiä et al. (2011) as well as Kavaltsov et al. (2012) exist, investigating the cosmic ray induced atmospheric secondary particle environment as function of solar activity, latitude, longitude as well as atmospheric depth.

### On the Computation Algorithms

The production rate of a certain cosmogenic nuclide  $P_j$ , strongly depends on the the galactic cosmic ray flux and its modulation within the heliosphere. As demonstrated e.g. by Beer et al. (2012) the production of a cosmogenic nuclide at a specific atmospheric depth  $x$  in an infinitesimally thin layer of atmospheric gas is given by

$$P_j(x) = \frac{dJ}{dx} = \left( \frac{L\sigma_j}{A} \right) J_j(x), \quad (7.1)$$

where  $J_j(x) = J_0 \exp -x \cdot n \cdot \sigma$  represents the particle flux, while  $L$  and  $A$  give the Loschmidt number and the atomic weight, respectively.

The production of a specific cosmogenic radionuclide at a given atmospheric depth  $x$  is

$$P_j(\phi, R_C, x) = \sum_i N_i \sum_k \int_0^\infty \sigma_{ijk}(E_k) \cdot J_k(\phi, E_k, x) dE_k, \quad (7.2)$$

where  $N$  represents the density of the target atom of species  $i$ ,  $E_k$  gives the energy of the secondary particle of type  $k$  (neutrons or protons) while  $J_k(E_k, x)$  represents the atmospheric depth as well as energy-dependent secondary particle fluxes of type  $k$  as computed in Section 5.

### On the Computations using PLANETOCOSMICS

As discussed in Appendix A.2 interactions of the primary particles with the surrounding atmospheric atoms are simulated using the GEANT4 Monte-Carlo software, version 4.9.1 (Agostinelli et al., 2003), as well as the PLANETOCOSMICS simulation tool (Desorgher, 2006). In order to generalize the results as well as to derive the yield and response functions for the production of cosmogenic radionuclides the computations are performed for primary particles in logarithmic equally

binned energy intervals between 10 MeV and 10 TeV. Note that, in contrast to other approximations here the influences of primary hydrogen and helium particles are investigated separately, also primary protons and alpha particles with energies below 100 MeV are neglected because they contribute less than 0.1% to e.g. the total  $^{10}\text{Be}$  production rate (see e.g. [Matthiä et al., 2011](#)).

Using the approach introduced in Section 5 the energy range of the primary particles was divided into 150 logarithmically equidistant bins, where particles were equally distributed over each interval investigated. In order to take into account an isotropic spectrum, each primary particle was injected randomly into the entire  $2\pi$  atmospheric sphere, and the intensity was weighted with a cosine of the zenith angle. To investigate the production rates at different altitudes the secondary neutron and proton fluxes at 30 different atmospheric depths were simulated by means of the hadronic Bertini interaction model (see e.g. [Bertini and Guthrie, 1971](#)).

As improvement to other approximations this work in addition uses the JAM/JQMD model by [Koi et al. \(2008\)](#) in order to compute the inelastic nuclear scattering of alpha particles at energies above 10 GeV/nucleon, which is not yet implemented in the GEANT4 code (for further information on the implementation see [Matthiä, 2009](#)).

The production of cosmogenic radionuclides strongly depends on the secondary particle flux, and thus on the primary particle intensities at the top of the atmosphere which varies strongly with the solar cycle. Thus, during solar minimum conditions more secondary hadrons can be produced in the particle cascades induced by the primary particles impinging the Earth's atmosphere than during solar maximum conditions. Moreover, the production rate of the secondary particles depends on the primary particle energy as well as the atmospheric depth. Thus, the higher the primary particle energy

- a) the deeper it can penetrate into the Earth's atmosphere

and

- b) the higher is the number of secondary particles produced in the atmospheric cascades.

In order to study the influence of primary protons and alpha particles on the production of cosmogenic radionuclides the production rate as function of the primary particle energy and the atmospheric depth will be investigated in a first step.

### **On the Computation of the Yield Function**

As discussed in [Matthiä et al. \(2011\)](#) Eq.(7.2) can be re-written as function of the differential primary particle fluence rate  $dF_p/(dE_p dt)$ , representing the number of primary particles of species  $p$  per area and time on top of the atmosphere, and the

secondary particle fluence at a specific atmospheric depth  $x$ ,  $f(E_p, E_k, x)$ , giving the number of secondary particles of type  $k$  with an energy  $E_k$  produced by a primary particle with an energy  $E_p$ . Thus,

$$P_j(E_p, x) = \sum_i N_i \int_{E_C}^{\infty} \frac{dF_p}{dE_p dt} dE_p \sum_k \int_0^{\infty} \sigma_{ijk}(E_k) \cdot f(E_p, E_k, x) dE_k \quad (7.3)$$

$$= \int_{E_C}^{\infty} \frac{dF_p}{dE_p dt} Y_j(E_p, x), \quad (7.4)$$

where the primary particle energy and altitude-dependent yield function  $Y(E_p, x)$  reveals information about the number of cosmogenic nuclides of species  $j$  which, at a specific atmospheric depth  $x$ , are produced due to a single primary particle of type  $p$  with an energy  $E_p$ . The primary particle intensity on top of the atmosphere thereby strongly depends on the geographic location, represented by the cutoff energy  $E_C$  which is given by Eq.(5.3).  $^{10}\text{Be}$  production rates due to a single primary particle of a certain energy are displayed in the colored contour plots of Fig. 7.3 and Fig. 7.4 for primary protons and alpha particles, respectively. Both plots show the production as function of primary particles with energies between 100 MeV and 1 TeV as well as function of the atmospheric depth varying between 0 and 1000 g/cm<sup>2</sup>.

Obviously, the higher the energy of the primary particle the deeper it is able to penetrate into the atmosphere. As a consequence the production rate per primary particle is increasing with increasing primary particle energy until a production maximum at around 150–200 g/cm<sup>2</sup> is reached after which the yield is decreasing again. Additionally it shows that a) more  $^{10}\text{Be}$  atoms per cm are produced by primary alpha particles than by primary protons and b) in both cases primary particle energies below a few hundred MeV have only a minor contribution to the cosmogenic radionuclides production.

Figure 7.5 shows the yield functions of the long-lived cosmogenic radionuclides  $^{10}\text{Be}$  (black line),  $^{14}\text{C}$  (red line) and  $^{36}\text{Cl}$  (green line) at low atmospheric depths, normalized to the corresponding yield values at a primary particle energy of 10 GeV. At high primary particle energies only minor differences between the radionuclide-dependent normalized yields occur. Investigating the lower energy part, however, this picture changes. Here variations, in particular between  $^{10}\text{Be}$  and  $^{36}\text{Cl}$  can be observed. As a consequence this study reveals that the long-lived cosmogenic nuclide  $^{36}\text{Cl}$  may be much more sensitive to changes in the low energy range than the other two nuclides investigated, and thus should be more sensitive to so called Ground Level Events (GLEs), strong solar particle events evolving from the Sun which are high energetic enough to reach the Earth's surface. The strongest amongst them, therefore, should be visible in  $^{36}\text{Cl}$  measurements.

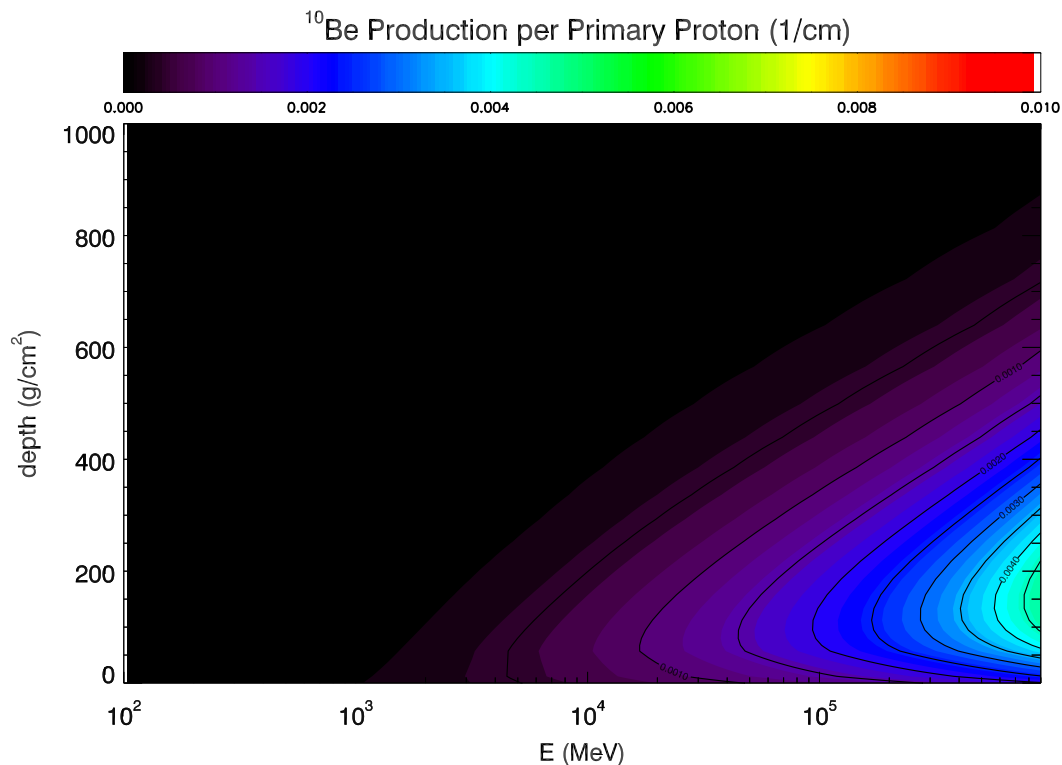


Figure 7.3: The production of the cosmogenic nuclide  $^{10}\text{Be}$  produced by primary hydrogen. Here the production per primary particle is given as function of primary particle energy and atmospheric depth. The results are also published in *Matthiä et al. (2011)*.

### On the Computation of the Response Function

Since the late 1920s several cosmic ray detection devices have been built. The use of ionization chambers (see Chapter 6) lead to the conclusion that the cosmic ray flux at Earth is not constant over time. In addition intensity-decreases occur about 24 hours after a solar flare, changes which nowadays are known as Forbush decreases (*Forbush, 1938*). It is the detailed work by Scott Forbush which today provides the only information about the solar activity before the year 1957. However, with the invention of the Neutron Monitor (NM) by John Simpson in the late 1940s and the formation of a worldwide NM network the ionization chamber era ended. Using Neutron Monitors it is possible to measure secondary particle intensities produced by the interaction of GCRs and/or SEPs within the Earth's atmosphere, and, therefore obtain information about the primary particles. The altitude of a particular station thereby determines the amount of absorbing atmosphere above



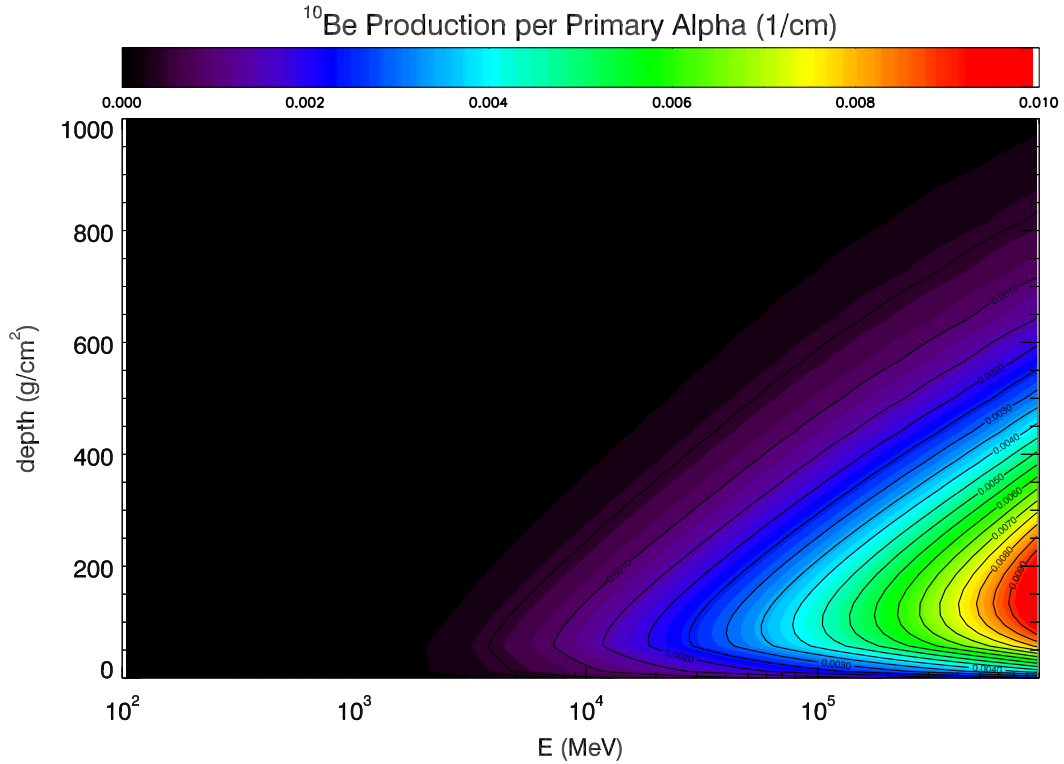


Figure 7.4: Same as in Fig. 7.3 but for primary alpha particles.

it and hence the amount of absorption of the secondary cosmic rays. Thus, the higher the station the higher the measured counting rate. Unfortunately, like the ionization chamber, NMs can not provide information about the cosmic ray composition because over the whole energy spectrum as well as the primary particle types is integrated. Nowadays multiple satellites like e.g. the Interplanetary Monitoring Platform (IMP) are able to measure the energy distribution as well as the charge of the particles entering the detector. Thus, using all these data provides the possibility to interpret the cosmogenic radionuclides data before the year 1933 (see e.g. Beer et al., 2012), which, after being stored in the natural archives like ice sheets, trees and sediments act as further cosmic ray detectors, the only ones allowing to look back in time.

For a quantitative comparison of such cosmic ray detectors the yield function  $Y_j(E_p, x)$  as well as the response function  $R_j(E_p, x)$  of the primary particle type  $j$  are used. In order to compute the response function  $R_j(E_p, x)$ , i.e. the product of the yield function and the differential energy spectrum of cosmic rays

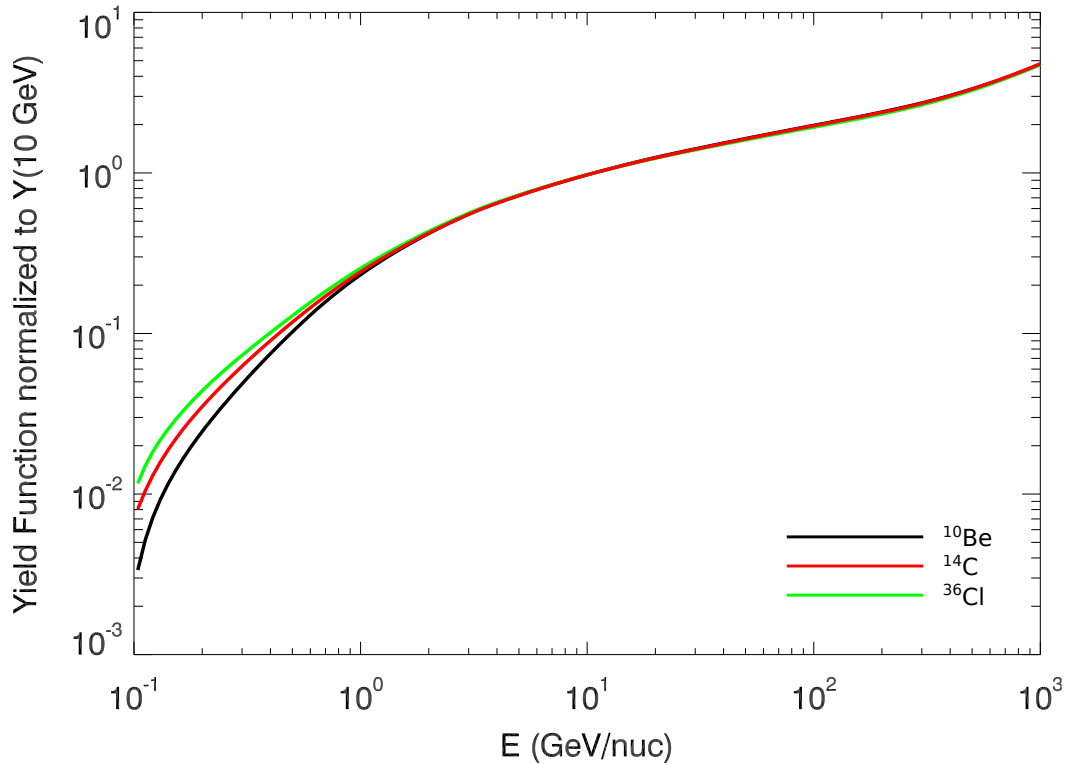


Figure 7.5: Yield functions of the cosmogenic radionuclides  $^{10}\text{Be}$ ,  $^{36}\text{Cl}$  and  $^{14}\text{C}$  as function of the primary particle intensity normalized to the value at an energy of 10 GeV.

near Earth,

$$R_j(E_p) = \frac{dF_p}{dE_p dt}(E_p) \cdot Y(E_p), \quad (7.5)$$

has to be calculated (see e.g. Clem and Dorman, 2000, and references therein for further information). As shown in Section 3.1 the GCR spectrum typically shows an intensity maximum around 1 GeV/nuc which causes the production maximum of the response function to shift towards much lower energies within a few hundred MeV/nuc up to 3 GeV/nuc. If not stated otherwise in the following investigations the LIS model by Usoskin et al. (2005) is used.

Figure 7.6 shows the response function  $R(E_p)$  of the cosmogenic radionuclides  $^{10}\text{Be}$  (black lines),  $^{14}\text{C}$  (red lines) and  $^{36}\text{Cl}$  (green lines) normalized to the corresponding response value maximum as function of the primary particle energy. In addition the dependence on the solar modulation parameter  $\phi$  for  $\phi=0$  MV (left curves),  $\phi=500$  MV (middle curves) and  $\phi=2,000$  MV (right curves). It shows that with increasing solar activity the response function maximum shifts towards higher

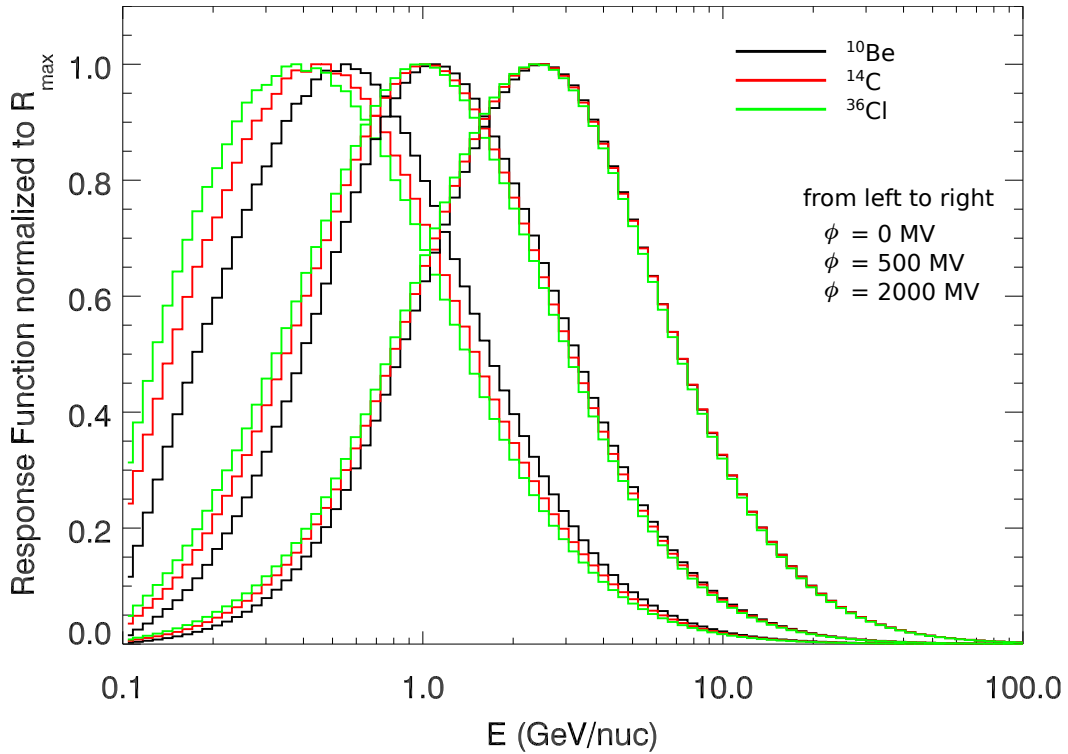


Figure 7.6: *The response function of  $^{10}\text{Be}$  (black lines),  $^{14}\text{C}$  (red lines) and  $^{36}\text{Cl}$  (green lines) as function of the primary particle energy due to primary protons and alpha particles. In addition the influence of the solar modulation parameter is shown from left to right:  $\phi = 0$  MV,  $\phi = 500$  MV and  $\phi = 2000$  MV.*

energies. As indicated in the previous investigations  $^{36}\text{Cl}$  as well as  $^{14}\text{C}$  show a response maximum at lower energies than the radionuclide  $^{10}\text{Be}$ . Thus, GLEs may more likely to be seen in the  $^{36}\text{Cl}$  and  $^{14}\text{C}$  measurements than in  $^{10}\text{Be}$  data.

### 7.3 Local Production Rates

However, in order to calculate the production rates at a specific location also the shielding of the Earth's magnetic field described in Section 4.2 as well as Section 4.3 has to be taken into account.

The local cosmogenic radionuclides production rate  $P_{\text{local}}(\phi, R_C)$  representing the depth-integrated production rate at a fixed location with the cutoff rigidity  $R_C$  as a function of the solar modulation parameter, is given by

$$P_{\text{local}}(\phi, R_C) = \int_x P(\phi, R_C, x) dx, \quad (7.6)$$

as shown in Fig. 7.7 displaying the results for the cosmogenic radionuclides  $^{10}\text{Be}$ ,  $^7\text{Be}$  (upper left and right panels),  $^{36}\text{Cl}$ ,  $^3\text{H}$  (middle right and left panels) as well as  $^{26}\text{Al}$  and  $^{14}\text{C}$  (lower right and left panels), as function of the cutoff rigidity between 0 and 17 GV using the LIS model by Usoskin et al. (2005). Each cosmogenic radionuclide production rate is investigated for different solar modulation parameters between 0 and 2,000 MV (from top to bottom). Although the production mechanisms and thus also the cross sections differ from each other, the production rates of the cosmogenic radionuclides investigated show a similar behavior:

- a) the lower the solar modulation the higher the local production rate.
- b) because the solar modulation mainly affects low-energetic particles the modulation effect is strongest in polar regions, while being almost negligible at equatorial regions where low-energetic particles only contribute to small amounts.

The local production rates for three different values of the solar modulation parameter,  $\phi = 500$  MV,  $\phi = 1000$  MV as well as  $\phi = 1500$  MV, are also given as Table E.2 in Appendix E.

### On the Influence of the Magnetic Field Configuration

As stated before the application of different magnetic field models like e.g. the IGRF or the non-tilted dipole model leads to strong variations of the geomagnetic cutoff rigidity distribution. Because the local production rate strongly depends on the location, and thus the cutoff rigidity  $R_C$ , a strong dependence of the local production rates on the magnetic field is expected.

Note that each cutoff rigidity corresponds to a certain latitude and longitude as shown on the example of  $^{10}\text{Be}$  in Fig. 7.8. Here the results for a non-tilted dipole field are presented for several solar modulation parameters between 0 and 2,000 MV.

In order to demonstrate the influence of the magnetic field configuration on the global distribution of the local cosmogenic radionuclides production rate the upper panel and lower panel of Fig. 7.9 show the simulation results for a non-tilted dipole and the IGRF in 2010, respectively. Here the results for a solar modulation of  $\phi = 400$  MV are shown (see orange line in Fig. 7.8). It shows that the local production rate is anti-correlated to the cutoff-rigidity values, where the highest values can be found at polar regions, while the lowest ones occur at equatorial regions. Furthermore the production rate strongly depends on the magnetic field. In case of the IGRF the values show the typical cutoff-rigidity course with minimum production over India as well as the typical shape corresponding to the magnetic field tilt. Whether the global cosmogenic radionuclides production rate also shows such a strong dependence on the magnetic field or if its information is smeared out due to the global mixing processes will be studied in Section 7.4.

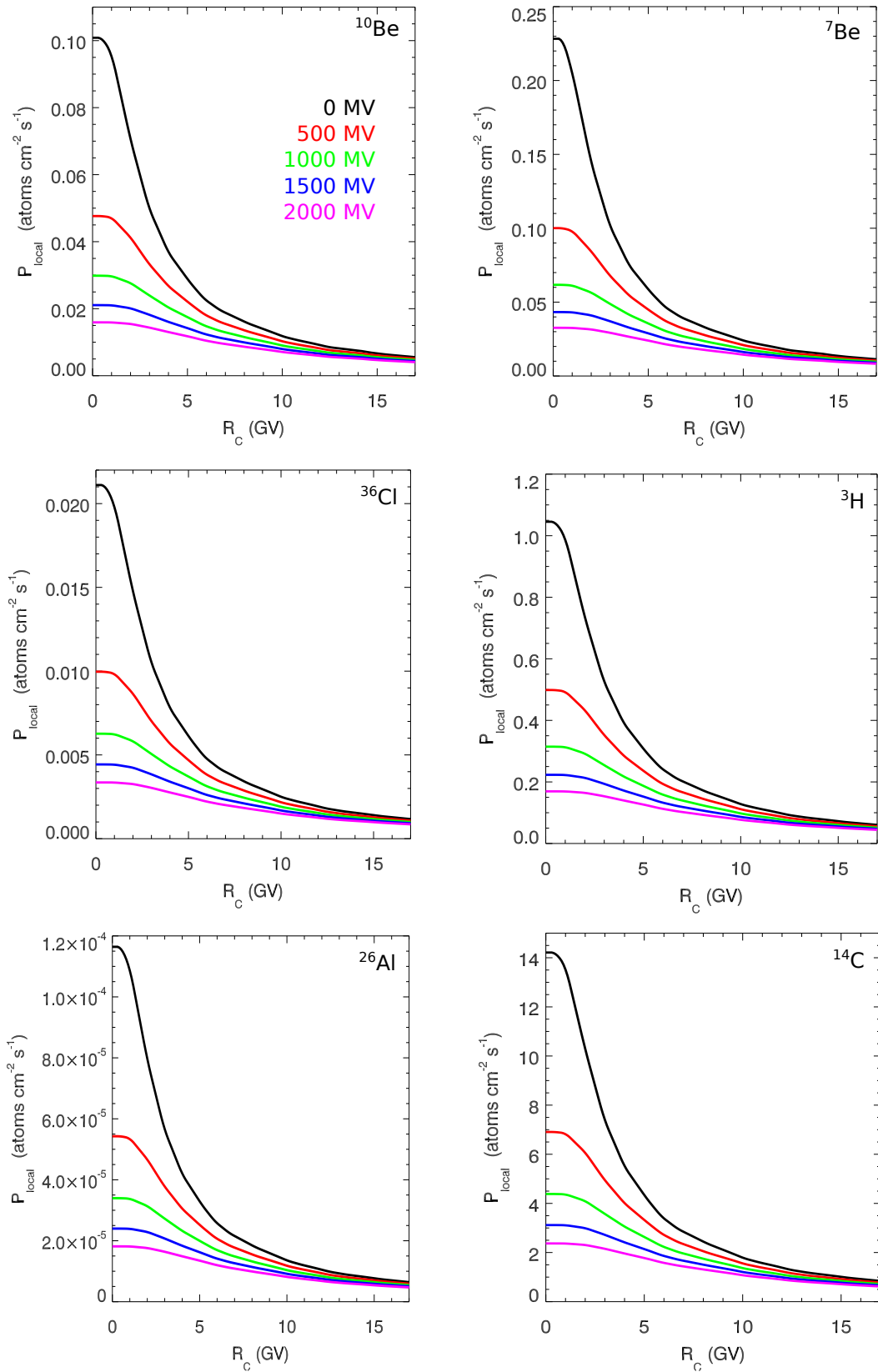


Figure 7.7: The local production rates of the cosmogenic radionuclides  $^{10}\text{Be}$ ,  $^7\text{Be}$ ,  $^{36}\text{Cl}$ ,  $^3\text{H}$ ,  $^{26}\text{Al}$  as well as  $^{14}\text{C}$  as function of  $R_c$ , for selected solar modulation parameters between 0 MV and 2000 MV. Note the different scaling.

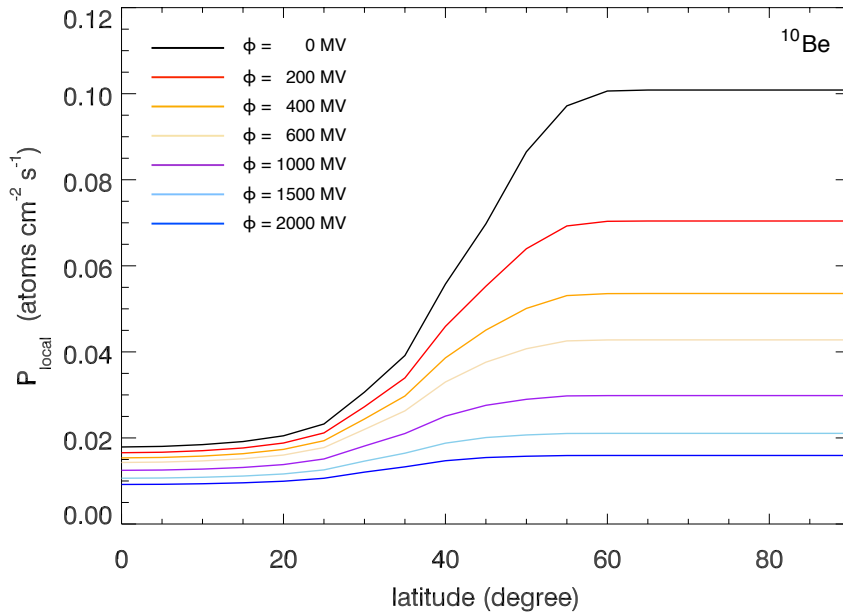


Figure 7.8: The local production rates of  $^{10}\text{Be}$  as function of latitude in a non-tilted dipole field. The results are presented for different modulation phases varying between 0 and 2,000 MV.

### On the Influence of the Cross Sections

Despite the strong dependence on the geomagnetic field model this work, for the first time, also investigates the influence of the cross sections used. It shows that for some cosmogenic radionuclides, in particular  $^{10}\text{Be}$  as well as  $^7\text{Be}$ , multiple cross sections exist in the literature. For both radionuclides the most frequently used ones are those by [Masarik and Beer \(1999\)](#) and [Webber and Highbie \(2003\)](#). Figure 7.10 shows the cross sections of  $^{10}\text{Be}$  (upper panels) and  $^7\text{Be}$  (lower panels). In addition nitrogen-based reactions are shown in the left panels while the oxygen-based ones are displayed in the right panels. The cross sections by [Masarik and Beer \(1999\)](#) are represented by the solid lines, while those by [Webber and Highbie \(2003\)](#) are given as dashed ones.

For both cosmogenic radionuclides differences between the two cross section sets occur. Figure 7.10 shows that the cross sections given by [Masarik and Beer \(1999\)](#) are larger than those by [Webber and Highbie \(2003\)](#), and thus, larger local production rates may be computed when the cross sections by [Masarik and Beer \(1999\)](#) are applied.

Shown in Fig. 7.11 are the local production rates of  $^{10}\text{Be}$  (left panel) and  $^7\text{Be}$  (right panel) as a function of the cutoff rigidity and the solar modulation

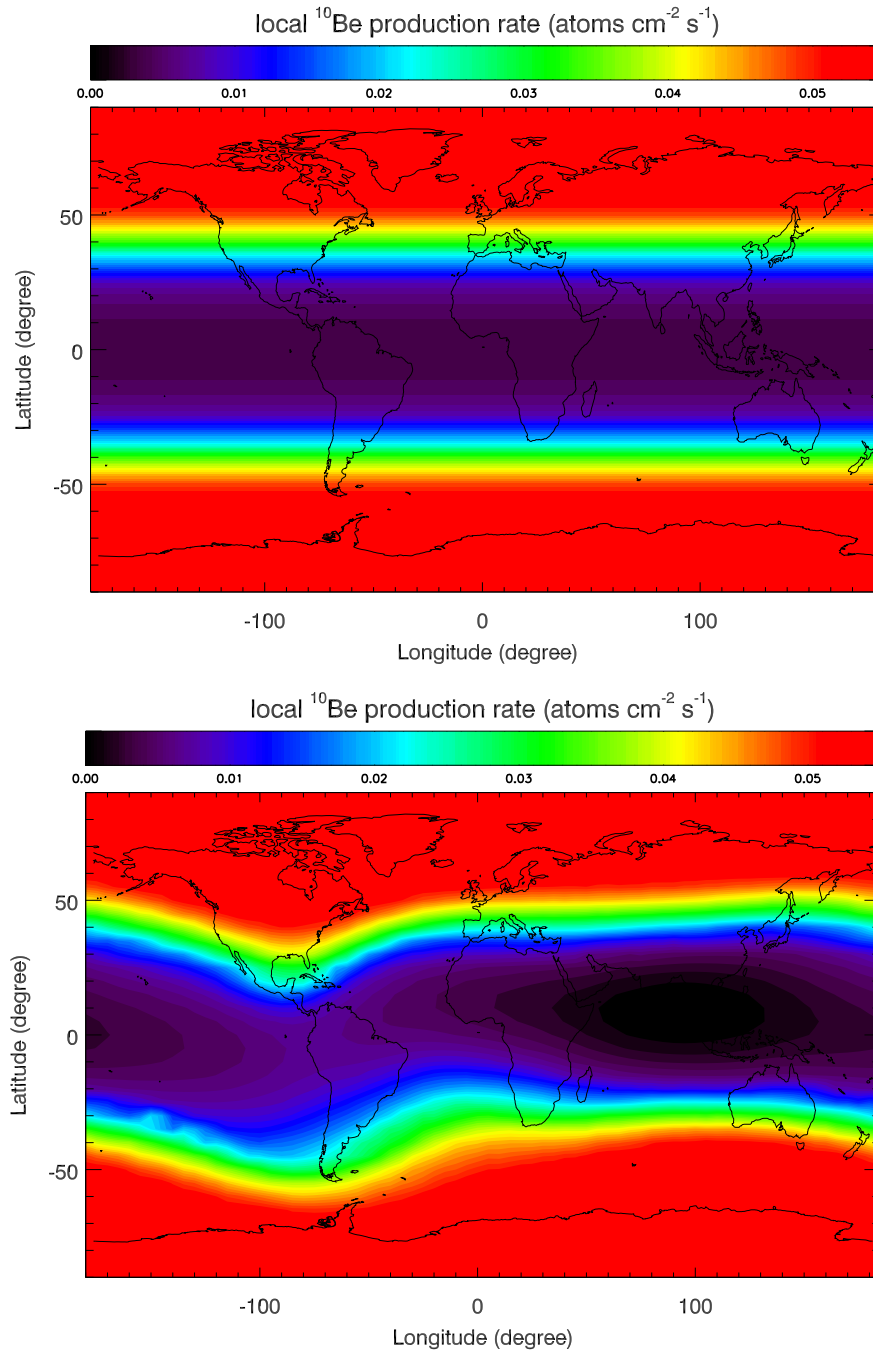


Figure 7.9: Contour plot of the local  $^{10}\text{Be}$  production rate as function of latitude and longitude using a non-tilted dipole field (upper panel) as well as the IGRF model parameters for the year 2010 (lower panel) with  $\phi=400$  MV.

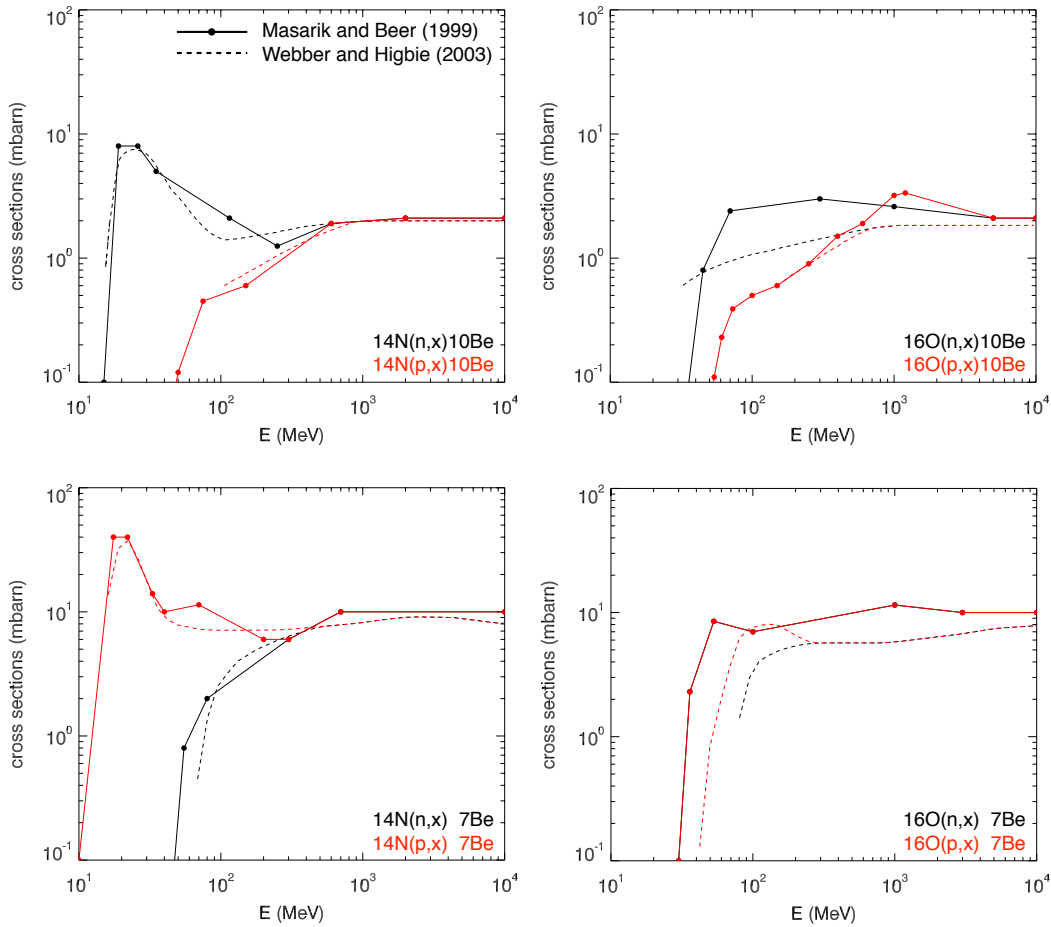


Figure 7.10: *Different cross section sets for the production of the cosmogenic radionuclides  $^{10}\text{Be}$  (upper panels) and  $^7\text{Be}$  (lower panels) provided by Masarik and Beer (1999) (solid lines) as well as Webber and Higbie (2003) (dashed lines). Black lines refer to neutron spallation reactions, while red ones show the proton spallation reactions.*

parameter. Here solid and dashed lines refer to the results using the cross section set by Masarik and Beer (1999) and Webber and Higbie (2003), respectively. As expected above, the local production rate of both cosmogenic radionuclides are higher for the cross sections by Masarik and Beer (1999). For both cosmogenic radionuclides the differences are in the order of 5 – 28%, and therefore are not negligible.

In summary the previous study showed two things:

- a) It is important to know the cross sections of the cosmogenic radionuclides as accurately as possible.



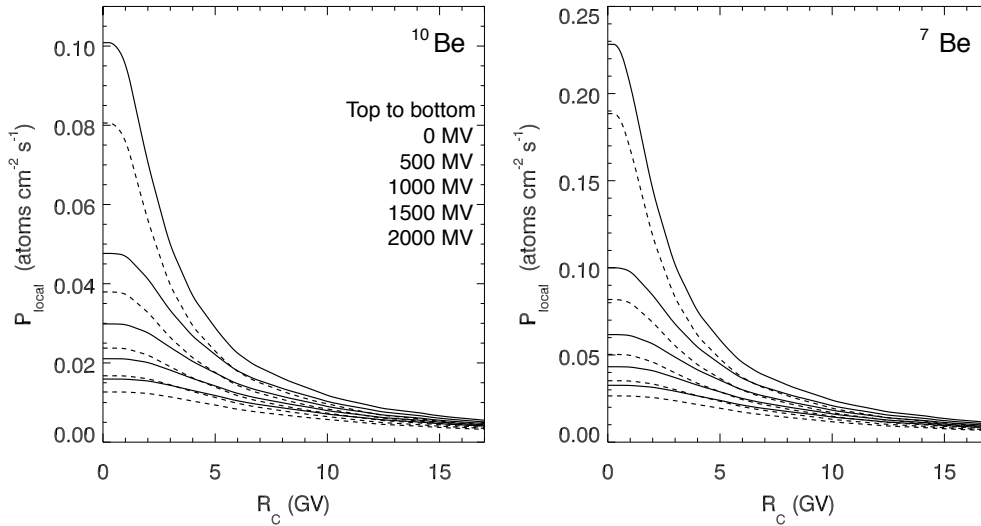


Figure 7.11: The local production rates of  $^{10}\text{Be}$  and  $^7\text{Be}$  depending on the the two cross sections sets by *Masarik and Beer (1999)* (solid lines) and *Webber and Higbie (2003)* (dashed lines) for a solar modulation between 0 and 2000 MV.

- b) Only those production rates given in the literature should be compared to each other that are based on a) the same LIS model, b) the same geomagnetic field and c) the same cross sections.

Unfortunately, only the minority of the published work give information on the latter topic.

## 7.4 Global Production Rates

Once cosmogenic nuclides are produced they are the subject of atmospheric transport and mixing processes. Thus, the knowledge of the mean global production rates is also of great importance.

In order to derive the mean global cosmogenic radionuclide production, which only depends on the solar modulation parameter, the following assumptions are made. A sketch of this approach can also be found in the panels of Fig. 7.12.

- a) The local cosmogenic nuclides production rates as functions of the solar modulation parameter as well as latitude and longitude (see e.g. Fig. 7.9) are segmented into  $5^\circ \times 5^\circ$  boxes.

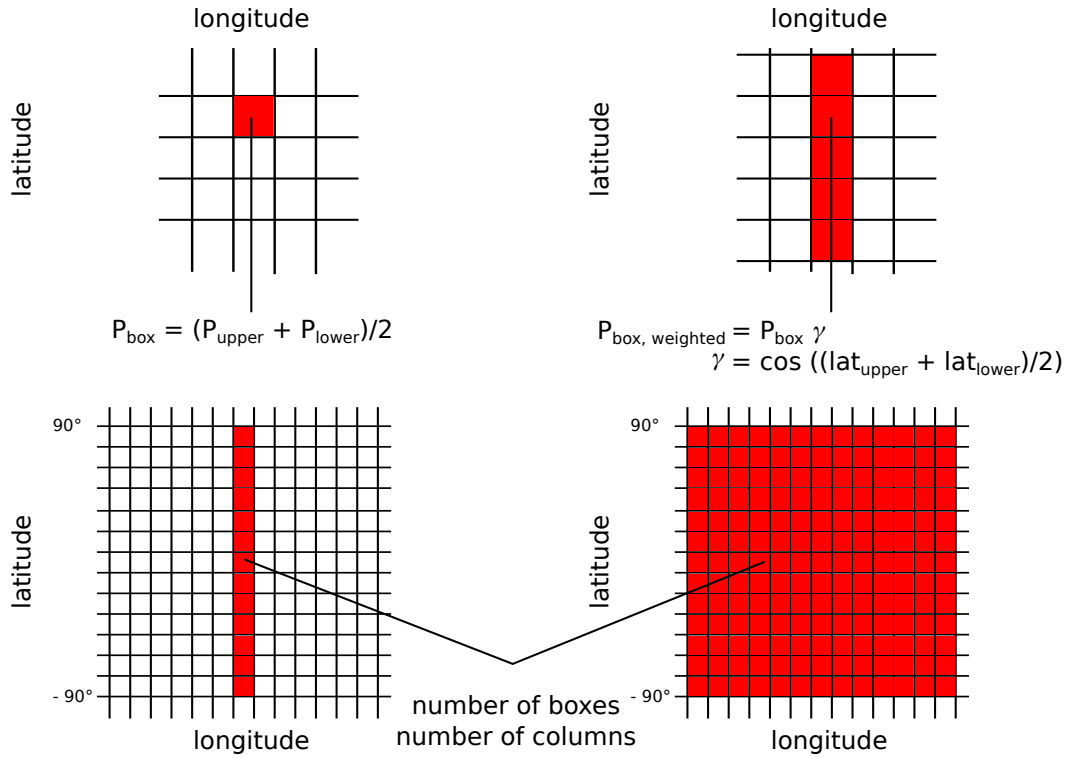


Figure 7.12: *Sketched method to calculate the global cosmogenic radionuclides production rates.*

b) The local production rate inside each box is calculated by

$$P_{\text{box}} = (P_{\text{upper}} + P_{\text{lower}}) / 2, \quad (7.7)$$

representing the mean production value between the upper and lower boundary of a box (see upper left panel of Fig. 7.12).

c) Each box is normalized with the weighting factor  $\gamma$  given by

$$\gamma = \cos [(\text{higher latitude} + \text{lower latitude}) / 2], \quad (7.8)$$

which reflects the geomagnetic latitudinal dependence of the local cosmogenic radionuclide production rates.

Depending on the geomagnetic field applied the global cosmogenic radionuclides production rate is given by

$$P_{\text{global}} = \frac{1}{c} \frac{1}{k} \sum_k P_{\text{box},k} \cdot \gamma, \quad (7.9)$$

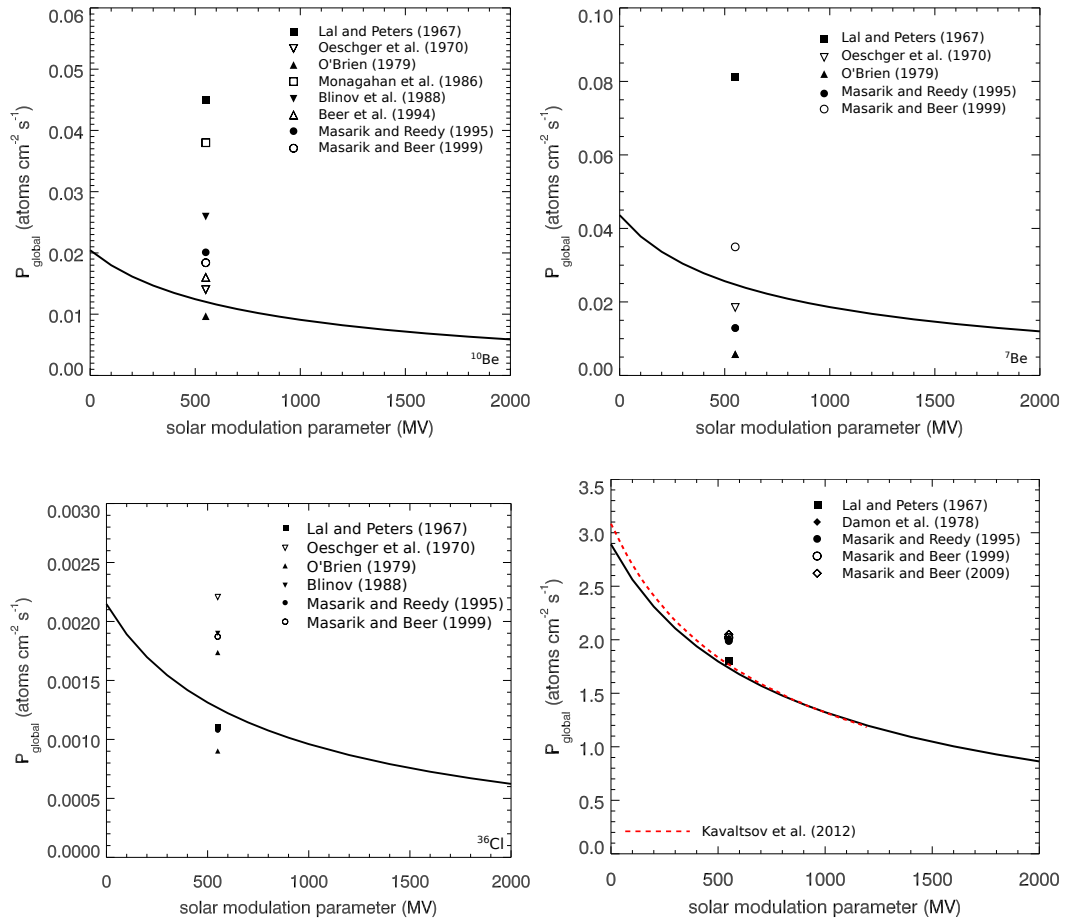


Figure 7.13: The global production rates of  $^{10}\text{Be}$ ,  $^7\text{Be}$ ,  $^{36}\text{Cl}$  and  $^{14}\text{C}$  depending for a modulation parameter between 0 and 2000 MV. The computed production rates are compared with other results given in the figure captions.

where  $c$  represents the number of columns taken into account and  $k$  gives the number of boxes of each column. As can be seen from the lower panels of Fig. 7.12 the global production rate for a non-tilted dipole field is limited to the investigation of only half a column due to the symmetry of the field (left panel), whereas the total number of columns has to be taken into account when the IGRF is applied (right panel).

Figure 7.13 shows the global production rates of  $^{10}\text{Be}$ ,  $^7\text{Be}$ ,  $^{36}\text{Cl}$  and  $^{14}\text{C}$  using a non-tilted dipole field. In order to compare the results of this work (solid lines) the Figure additionally shows computed and measured results of other groups for a solar modulation parameter of  $\phi=550$  MV, revealing a strong variation between the different computations. However, the results of this work are in good agreement with the computations of other groups. In case of, e.g.,  $^{14}\text{C}$  a good agreement with

the results by Lal and Peters (1967) as well as those by Kavaltsov et al. (2012) can be found. Note that Kavaltsov et al. (2012) also used the PLANETOCOSMICS simulation code, however, using the BIC hadronic interaction model and applying an alpha particle spectrum of 0.03 times the LIS by Usoskin et al. (2005). The reason why the results of this work are in good agreement with their computations is discussed in one of the following investigations. Moreover, a list of the global production rates of  $^{10}\text{Be}$  and  $^{14}\text{C}$  as function of the solar modulation parameter  $\phi$  are given in Table E.3 in Appendix E.

As mentioned earlier the computed production rates strongly depend on a) the LIS model used, b) the magnetic field model applied as well as c) the cross sections taken into account. Unfortunately, not all groups state which input parameters they use for their computations. However, because of the strong influence of the LIS, the magnetic field and the cross sections on the local production rate values it is expected that the global production rates will show a likewise behavior. Therefore the following topics are investigated: a) the influence of the two different cross section sets by Masarik and Beer (1999) and Webber and Higbie (2003) as well as b) the influence of the LIS model applied on the global production rate is studied. Furthermore, the investigations of this work reveal a strong dependence of the global cosmogenic nuclide production on the used cutoff rigidity distribution, and investigation which will be described in more detail. The investigations on the influence of the magnetic field, however, will follow in Section 7.6.

#### a) LIS model

The LIS model used by the various groups in most cases are not known, thus Fig. 7.14 shows the global  $^{10}\text{Be}$  production rates as function of the solar modulation parameter for four LIS models studied in Chapter 3.4. Investigated are the LIS models by Garcia-Munoz et al. (1975) (red lines), Usoskin et al. (2005) (black lines), Webber and Higbie (2003) (blue line) as well as Webber and Higbie (2009) (green lines) revealing large differences between the various LIS models. The computations by e.g. Masarik and Beer (1999) use the LIS model by Garcia-Munoz et al. (1975), a non-tilted dipole field and apply the cross sections published in the same article. Thus, a good agreement between their computations (open circle) and the results presented in this work (red curve) should be present. But the computations of this work show much lower production rate values, differences which may be explained by

- the use of computed cutoff rigidities rather than their approximation due to Eq.(4.6)
- the use of vertical as well as asymptotic cutoff rigidities
- the separated investigation of the cosmic ray induced cosmogenic nuclides production due to primary protons and alpha particles

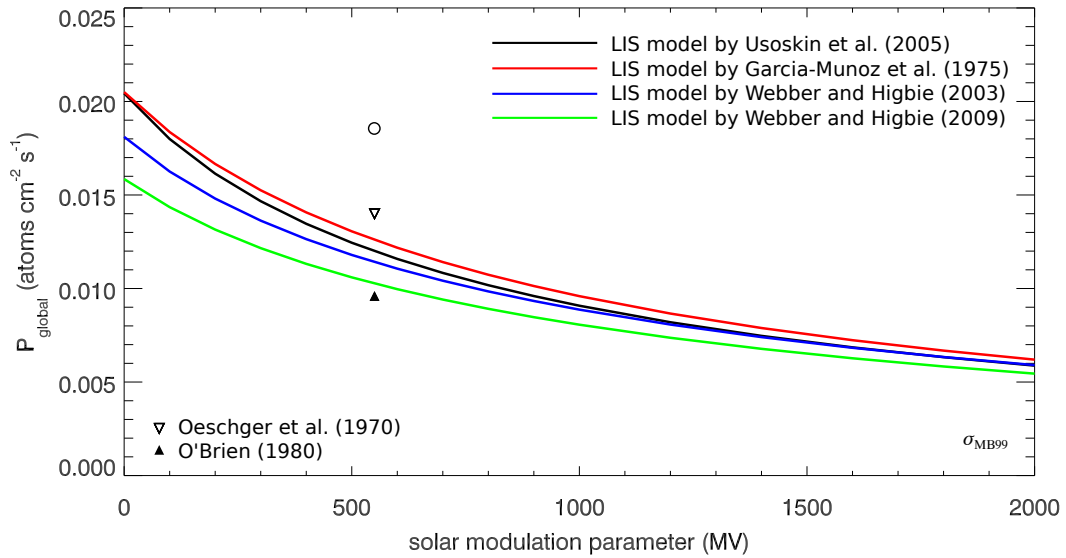


Figure 7.14: The local production rates of  $^{10}\text{Be}$  as function of the solar modulation between 0 and 2,000 MV applying the LIS models by *Usoskin et al. (2005)* (black line), *Garcia-Munoz et al. (1975)* (red line), *Webber and Higbie (2003)* (blue line) and *Webber and Higbie (2009)* (green line).

- the fact that primary alpha particles above 10 GeV/nuc are simulated using the integrated JAM/JQMD model by *Koi et al. (2008)* rather than treated as compound of primary protons
- different hadronic and electromagnetic interaction models may have been applied in the computation of the secondary particle cascades.

As shown earlier, see e.g. Section 5, especially the latter fact leads to non-negligible differences in the secondary particle fluxes and thus the production of the cosmogenic radionuclides. Furthermore, as shown in point c), the cutoff rigidity distribution taken into account has a strong impact.

## b) Cross Sections

Because of the larger cross section by *Masarik and Beer (1999)* the corresponding computed global production rates, as shown in Fig. 7.15 on the example of  $^{10}\text{Be}$  (left panel) and  $^7\text{Be}$  (right panel), have much larger values than those using the cross sections by *Webber and Higbie (2003)* (dashed lines). For  $^{10}\text{Be}$  and  $^7\text{Be}$  these differences are in the order of 25% and 22%, respectively. Looking more closely on the computations of  $^{10}\text{Be}$  reveals that a good agreement with the results by *Oeschger et al. (1970)* and *O'Brien (1979)* can be found when the cross sections

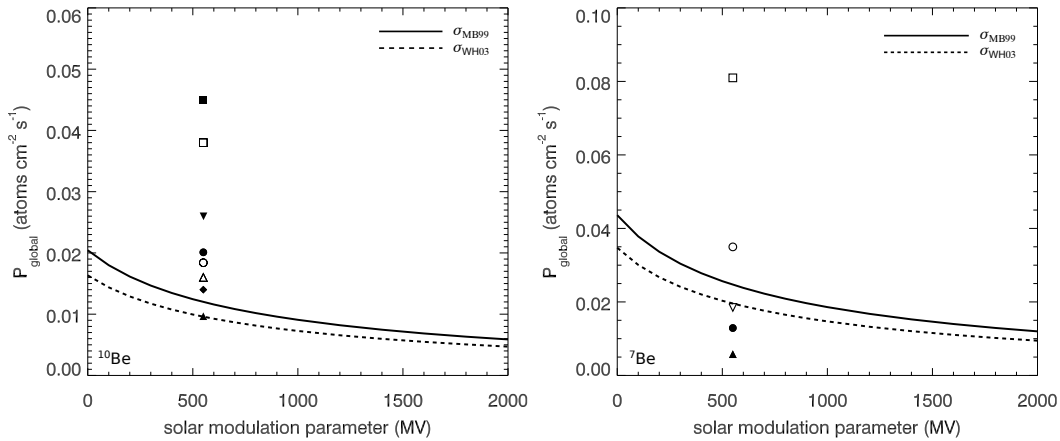


Figure 7.15: The global production rates of  $^{10}\text{Be}$  (left panel) and  $^7\text{Be}$  (right panel) depending on the two cross sections sets by *Masarik and Beer (1999)* (solid lines) and *Webber and Higbie (2003)* (dashed lines) for a solar modulation between 0 and 2000 MV.

by *Masarik and Beer (1999)* and *Webber and Higbie (2003)*, respectively, are used.

### c) Cutoff Rigidity Distribution

As mentioned above the computations reveal a strong dependence of the global production rates on the used cutoff rigidity distributions. Most of the other groups use the cutoff rigidity approximation given in Eq.(4.6), which, as stated before (see also *Pilchowski et al., 2010*), is only valid at polar regions. The differences between this approximation and the computed vertical cutoff rigidities of this work are displayed in Fig. 7.16. As predicted agreements between both methods can only be found at high latitudes. At mid and low latitudes much higher cutoff rigidities are presents for the computations of this work. As shown in Fig. 7.17 using the latter method thus leads to the computation of much lower global production rates. Here the global production rates of  $^{14}\text{C}$  for both the computations using the PLANETOCOSMICS simulation code (solid lines) and the approximation by *Elsasser et al. (1956)* are displayed. In addition the results are presented for the LIS models by *Usoskin et al. (2005)* (black lines) and *Garcia-Munoz et al. (1975)* (red lines). It shows that the results of this work are in good agreement with the computations by *Masarik and Beer (1999, 2009)* when a) the LIS by *Garcia-Munoz et al. (1975)* is applied as well as b) the cutoff rigidity approximation by *Elsasser et al. (1956)* is used (red dashed line), revealing that the groups which use this approximation overestimate the global production rates by approximately 10%. This finding also explains the good agreement of the computations of this work with the results by *Kavaltsov et al. (2012)*. Although using an alpha particle LIS

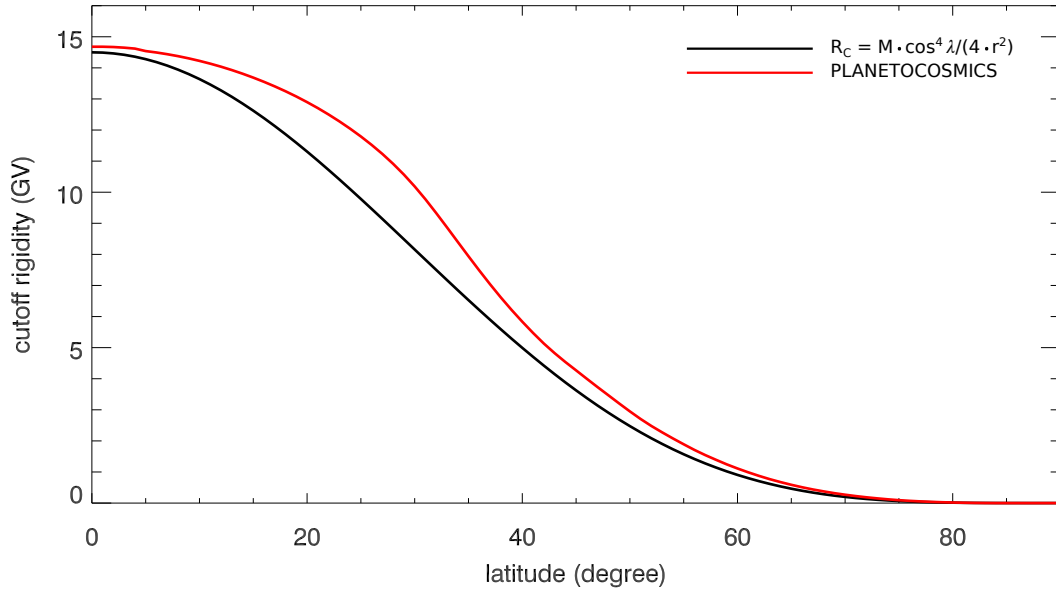


Figure 7.16: *Computed cutoff rigidities using PLANETOCOSMICS (red curve) in comparison to the results using the approximation given in Eq.(4.6) (black curve).*

model which is 1.7 times lower than the one used in this work and applying the BIC hadronic interaction model the results are comparable with the computations of this work. Note, however, that they also use the approximation by [Elsasser et al. \(1956\)](#). As a conclusion [Kavaltsov et al. \(2012\)](#) state that other groups overestimate the global  $^{14}\text{C}$  production rate due to the use of outdated primary particle spectra. This work, however, reveals that the overestimation is more likely an effect of the cutoff rigidity approximation by [Elsasser et al. \(1956\)](#) which is only valid at high latitudes.

## 7.5 Global Production Rates between 1940 and 2010

By now the global production rates as function of the solar modulation parameter between 0 and 2,000 MV have been computed. With this information it is possible to reconstruct the global production rate for times where the magnetic field strength and the solar modulation parameter are known or at least could be reconstructed.

Since the early 1930s the interactions of the cosmic rays with the atmosphere have been studied in detail. Thus, as a first investigation in the following the global  $^{10}\text{Be}$  and  $^{14}\text{C}$  production rates are studied between 1940 and 2010. For this investigation

- a) the LIS model by [Usoskin et al. \(2005\)](#),

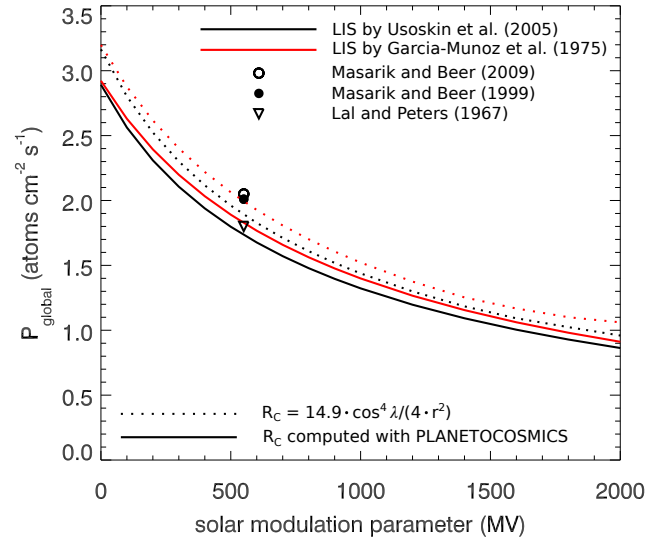


Figure 7.17: Global  $^{14}\text{C}$  production rates and their dependence on the used cutoff rigidity calculation method. Solid lines: Computations using the PLANETOCOSMICS simulation code, Dashed lines: Calculations using the approximation by *Elsasser et al. (1956)* for the LIS model by *Usoskin et al. (2005)* (black lines) and *Garcia-Munoz et al. (1975)* (red lines).

- b) the solar modulation parameter by *Usoskin et al. (2011)*, displayed in the upper panel of Fig. 7.18

and

- c) the computed cutoff rigidities for the IGRF between 1940 and 2010 simulated in Section 4.2 and Section 4.3.

are applied. For each month an individual global production rate can be computed, which is anti-correlated with respect to the solar modulation parameter. However, please note the discussion in Section 7.6 revealing that the reconstructions by *Usoskin et al. (2011)* may be systematically too low.

Figure 7.18 shows the monthly variations of the global production rates of  $^{10}\text{Be}$  (solid lines) and  $^{14}\text{C}$  (filled circles) with respect to the values of 2010. It becomes obvious that variations of up to 65% over the last 70 years occur in both computations. Also the 11-year solar activity as well as the 22-year solar magnetic cycle with its alternating peaked and flattened structures, caused by drift effects of the primary particles in the heliosphere, are visible in the computed production rates. Furthermore, the cosmogenic radionuclide  $^{14}\text{C}$  shows a 5% stronger modulation during solar maximum conditions, which is caused by the response to low energetic particles compressed during solar maximum conditions.



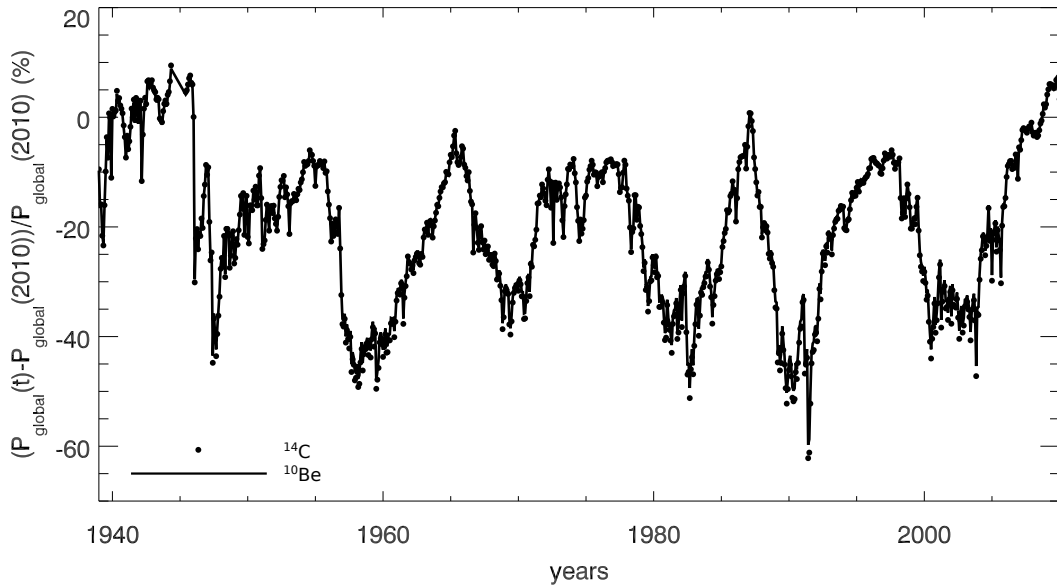


Figure 7.18: Global  $^{10}\text{Be}$  and  $^{14}\text{C}$  production variations between 1940 and 2010 with respect to recent values. Here the black line represents the results for  $^{10}\text{Be}$  while black dots show those of  $^{14}\text{C}$ .

The following studies will concentrate on the influence of the magnetic field as well as cross sections on the computations during the time between 1940 and 2010.

### Dependence on the Magnetic Field

Previous investigations on the computed local production rates of cosmogenic radionuclides showed that especially radionuclides with short half-lives, such as e.g.  $^7\text{Be}$ , which only can be measured in-situ are sensitive to the magnetic field and its changes with time. The following study investigates the temporal variations of the magnetic field using a) the IGRF model computations as well as b) a non-tilted dipole with the time-dependent magnetic field strength variations in order to compute the global production rates between 1940 and 2010.

The differences between the computations for the IGRF and the non-tilted dipole are shown in Fig. 7.19. Surprisingly, only minor differences of less than  $\pm 2\%$  between both computations occur, which in view of the global picture are of minor importance. Consequently, the magnetic field information is smeared out in the global production rate information due to global atmospheric mixing of the local production rates. These findings, furthermore, reveal that the use of a non-tilted

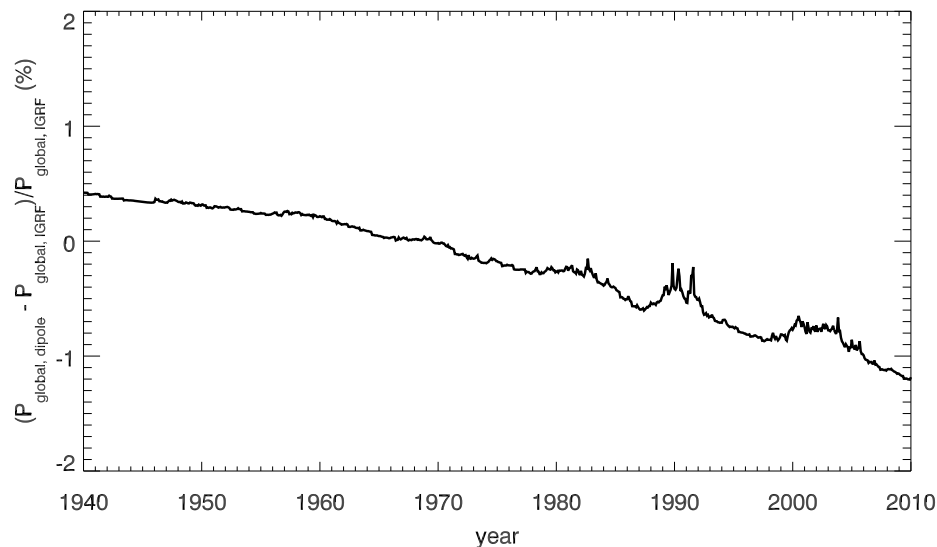


Figure 7.19: Differences between the computations for the IGRF compared to those applying the non-tilted dipole field. Only minor differences of less than 2% can be observed.

dipole with varying time-dependent magnetic field strengths is sufficient for the following investigations. This, moreover, leads to a considerable computation-time reduction.

### Dependence on the Cross Sections

As shown in Fig. 7.20 also the reconstructed global  $^{10}\text{Be}$  production rates between 1940 and 2010 strongly differ from each other when the cross sections by Masarik and Beer (1999) (black solid lines) and Webber and Higbie (2003) (red solid lines) are used. Again the computed global production rate values for the cross sections by Masarik and Beer (1999) are in the order of 25% higher than those applying the cross sections by Webber and Higbie (2003).

Consequently the investigations show that the global production rates strongly depend on the cross sections applied while the magnetic field geometry information is smeared out and the usage of a non-tilted dipole field becomes sufficient.

## 7.6 Global Production Rates between 9400 BP and 0 BP

Over the past 11,500 years the Earth is under "interglacial" conditions, a time also referred to as the Holocene. During 80% of the last two million years the

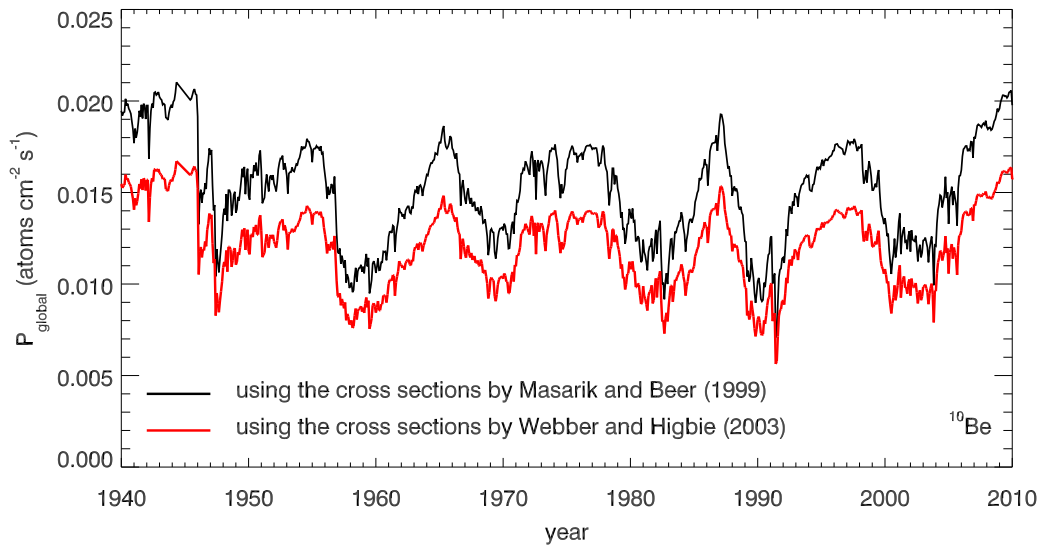


Figure 7.20: The global  $^{10}\text{Be}$  production rate values and their dependence on the applied cross sections. Black lines correspond to the use of the cross sections by Masarik and Beer (1999), red ones to the use of the cross sections by Webber and Higbie (2003).

Earth has been in ice ages (glacial conditions) which are intercepted by the interglacials every 100,000 years (see Beer et al., 2012). However, different from the Grand Solar Minima being caused by changes of the solar activity the ice ages occur due to long-term cyclic orbital changes of the Earth. This Section will show the reconstruction of the global production rate during the past 9,450 years. Furthermore the Grand Solar Minima between 1,000 BP (before present) and 0 BP are investigated in more detail. Note that 0 BP refers to the year 1950, which was set empirically. Since the beginning of the 1850s a continuously increasing fossil fuel consumption can be observed. These fuels, however, no longer possess detectable  $^{14}\text{C}$ , because they are much older than 50,000 years and only the non-radioactive nuclides  $^{12}\text{C}$  and  $^{13}\text{C}$  are emitted during the fossil burning. Thereby the natural  $^{14}\text{C}/^{12}\text{C}$  ratio is reduced, an effect known as the Suess effect (see e.g. Suess, 1955). Consequently, measured  $^{14}\text{C}$  data need to be calibrated.

In order to compute the global production rates throughout the Holocene in this work the solar modulation parameter reconstructed by Steinhilber et al. (2012) as well as the magnetic field strength reconstructions by Knudsen et al. (2008) are taken into account. The studies, however, only focus on the cosmogenic radionuclides  $^{10}\text{Be}$  and  $^{14}\text{C}$ .

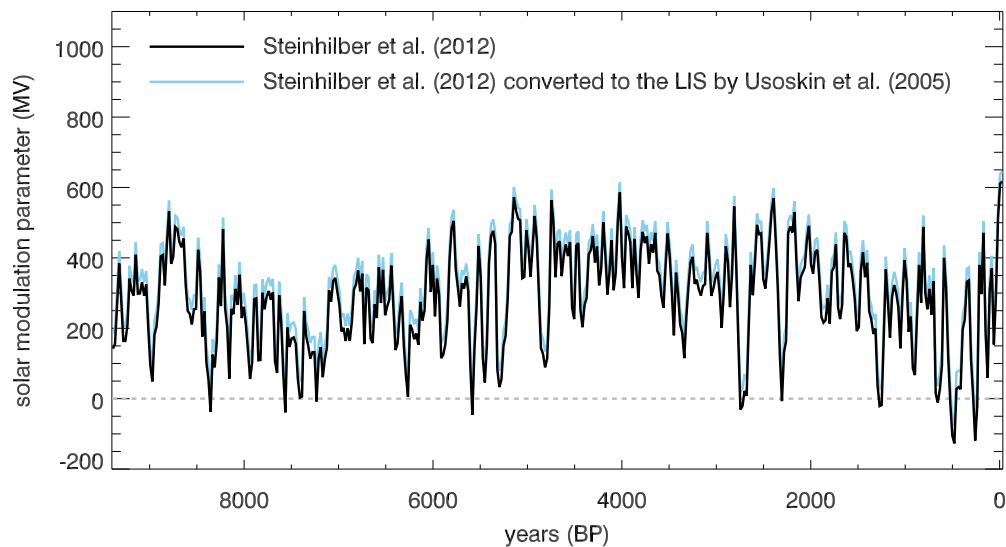


Figure 7.21: The solar modulation parameter  $\phi$  during the Holocene reconstructed by [Steinhilber et al. \(2012\)](#) as black solid line. In addition the conversion to the LIS by [Usoskin et al. \(2005\)](#) using the conversion equations by [Herbst et al. \(2010\)](#) are represented by the light blue line.

Using relative  $^{10}\text{Be}$  as well as  $^{14}\text{C}$  measurements [Steinhilber et al. \(2012\)](#) computed recently a new set of solar modulation parameter values throughout the Holocene on the base of the computations by [Masarik and Beer \(2009\)](#). The solar modulation potential is given as black line in Fig. 7.21, where the occurrence of non-physical negative modulation parameter values is still present. However, [Steinhilber et al. \(2012\)](#) use the LIS model by [Garcia-Munoz et al. \(1975\)](#). Thus, because the results of this Chapter are computed for the LIS by [Usoskin et al. \(2005\)](#), the solar modulation parameter values are converted by the LIS-dependent conversion equations given in Chapter 3, shown in addition as light blue curve. Although the modulation parameter now is shifted towards higher modulation values still times of negative  $\phi$  values are present.

Another important parameter for the study of the global production rates during the Holocene is the time-dependent magnetic field strength. Merely few reconstructions for this time exist, however, here in a first investigation the magnetic field strength values by [Knudsen et al. \(2008\)](#) are used. The mean terrestrial magnetic field strength (black curve) and its upper and lower error estimates (light blue band) is shown in Fig. 7.22 normalized to present values. It shows that the magnetic field strength during the Holocene may have varied between 0.8 and 1.5 times the present geomagnetic field strength.

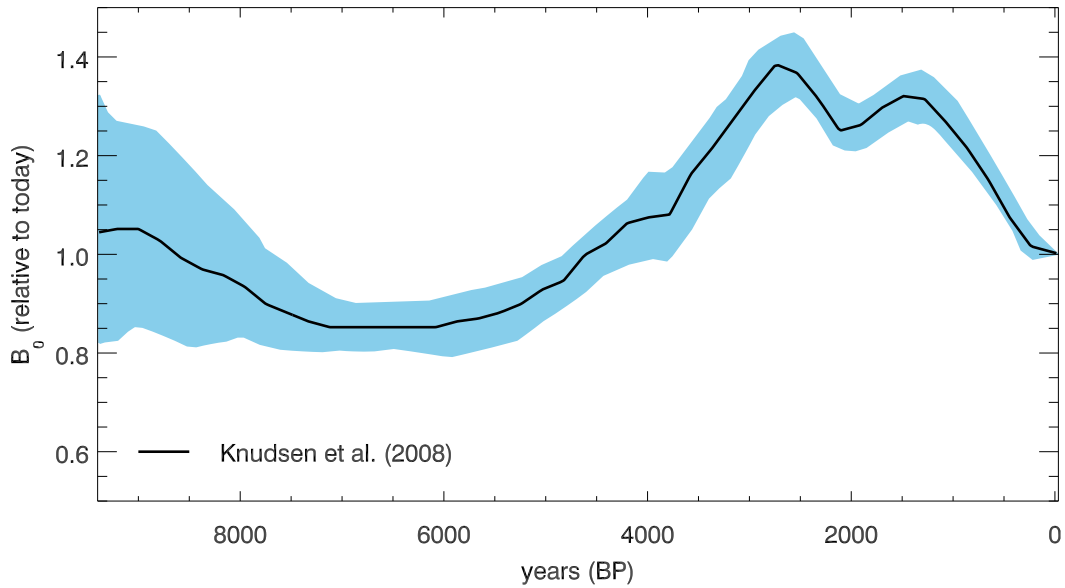


Figure 7.22: The mean magnetic dipole strength  $B_0$  during the Holocene reconstructed by [Knudsen et al. \(2008\)](#) as black solid line. The upper and lower limits are represented by the light blue band.

### The Global Production Rate as Function of $\phi$ and $B_0$

The process of reconstructing the global cosmogenic radionuclide production rates during the Holocene is a multi-step procedure as sketched in Fig. 7.23: taking into account the results by [Knudsen et al. \(2008\)](#) as a first step the global cutoff rigidity distributions for times of magnetic field strengths variations between zero and two times the present values are computed. The resulting distributions then are used to compute the corresponding global production rates for modulation parameter values between 0 and 2000 MV. Coupling the information of the solar modulation parameter variations and the temporal evolution of the geomagnetic field strength as well as normalizing the computations to the input parameter by [Steinhilber et al. \(2012\)](#) and [Knudsen et al. \(2008\)](#) the production during the Holocene can be reconstructed. The procedure and its results will be described in more detail in the following.

In order to reconstruct the production during the Holocene the global production rates as function of the solar modulation parameter and the terrestrial magnetic field strengths are investigated more detailed here.

The 3D plot of Fig. 7.24 shows the global  $^{10}\text{Be}$  production rates as function of the solar modulation parameter  $\phi$  and the magnetic field strength  $B_0$ , revealing

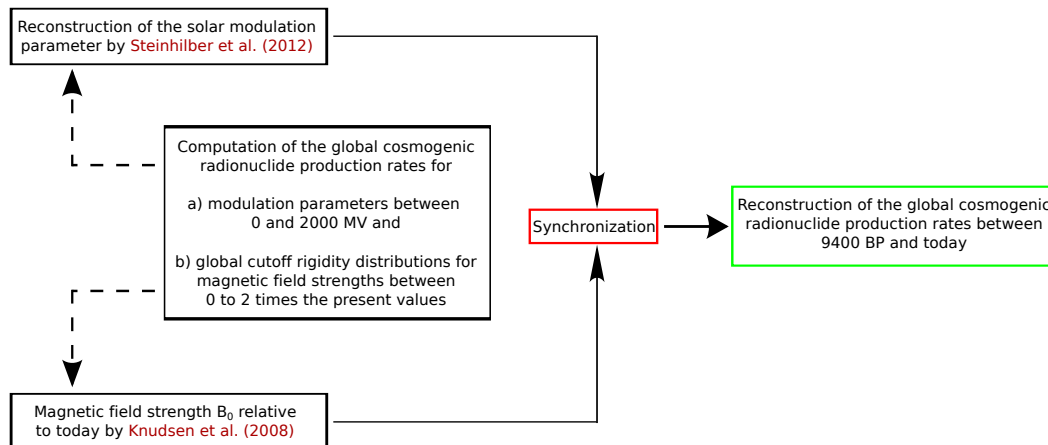


Figure 7.23: Sketch of the method used to reconstruct the global production rates during the Holocene.

that the highest production rates occur during solar minimum conditions coupled with low magnetic field strengths while the lowest ones occur for high magnetic field strengths and high solar activity, where almost one order of magnitude between the computed values can be observed.

By now the global production rates of the cosmogenic radionuclides  $^{10}\text{Be}$  and  $^{14}\text{C}$  has been computed as function of a) the solar modulation parameter  $\phi$  between 0 to 2,000 MV in steps of 1 MV and b) the magnetic field strengths  $B_0$  varying between 0 and two times present values in steps of 0.25. Thus, a 3D matrix has been achieved, which easily can be used in order to synchronize the computations with the reconstructed solar modulation parameter by Steinhilber et al. (2012) as well as the magnetic field strengths by Knudsen et al. (2008).

The corresponding reconstructed global  $^{10}\text{Be}$  production rates are shown in Fig. 7.25. Here results for the mean magnetic field strengths are displayed as black solid line, while the dependence on the reconstructed magnetic field strength error estimates are displayed as light blue band. The upper panel displays the period of time between 9,400 BP and 0 BP, whereas the lower panel shows a zoom in on the last millennium. Furthermore the upper panel includes the information on a) the solar modulation parameter (color bar on top), where white coloring refers to high solar activity while dark blue corresponds to low solar modulation, as well as b) the magnetic field strengths and their variations (shaded gray area). It shows that the computed global production rates reveal multiple spike-like production increases which are linked to drops in the solar modulation parameter value, and thus the solar activity.

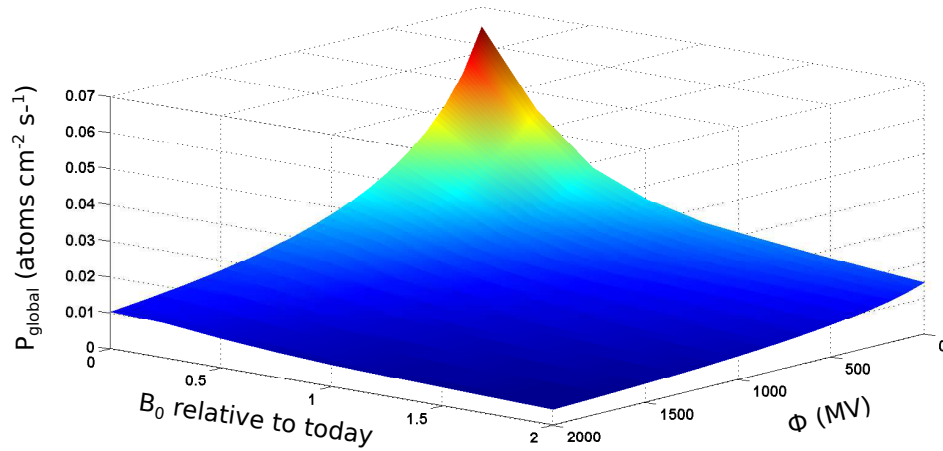


Figure 7.24: *Dependence of the global  $^{10}\text{Be}$  production rates on the strength of the magnetic field between zero and two times the present value as well as the solar modulation parameter between 0 and 200 MV.*

Zooming in on the last millennium (lower panel) it shows that these spike-like increases are connected with the occurrence of Grand Solar Minima. In the past 1,000 years there were six of these Grand Minima, in particular the Oort minimum (O), the Wolf minimum (W), the Spörer minimum (S), the Maunder minimum (M) as well as the Dalton (D) and Gleissberg (G) minima, a time period known as "little ice age". A similar picture shows for the global  $^{14}\text{C}$  production as investigated in Fig. 7.26.

In order to validate the reconstructed production rates a comparison with  $^{10}\text{Be}$  and  $^{14}\text{C}$  measurements and computations, respectively, needs to be performed. Unfortunately only a 600 year yearly-mean  $^{10}\text{Be}$  GRIP ice core data set is available on the internet (see also Berggren et al., 2009). Furthermore, in case of  $^{14}\text{C}$  only the relative  $^{14}\text{C}/^{12}\text{C}$  ratio can be measured, and thus further modeling by e.g. an ocean-atmosphere diffusion box model (see Oeschger et al., 1975; Hughen et al., 2004; Reimer et al., 2009, for more detailed information) is needed. This model is based on further simplifications like, e.g., taking into account only four reservoirs: atmosphere, biosphere, mixed ocean layers and deep sea. Using these relative production rates further simulations using e.g. a box-diffusion carbon cycle model (see Oeschger et al., 1975; Stuiver and Braziunas, 1993b, for further information) have to be performed in order to model global production rates.

However, as displayed in Fig. 7.27 showing the global production rates of

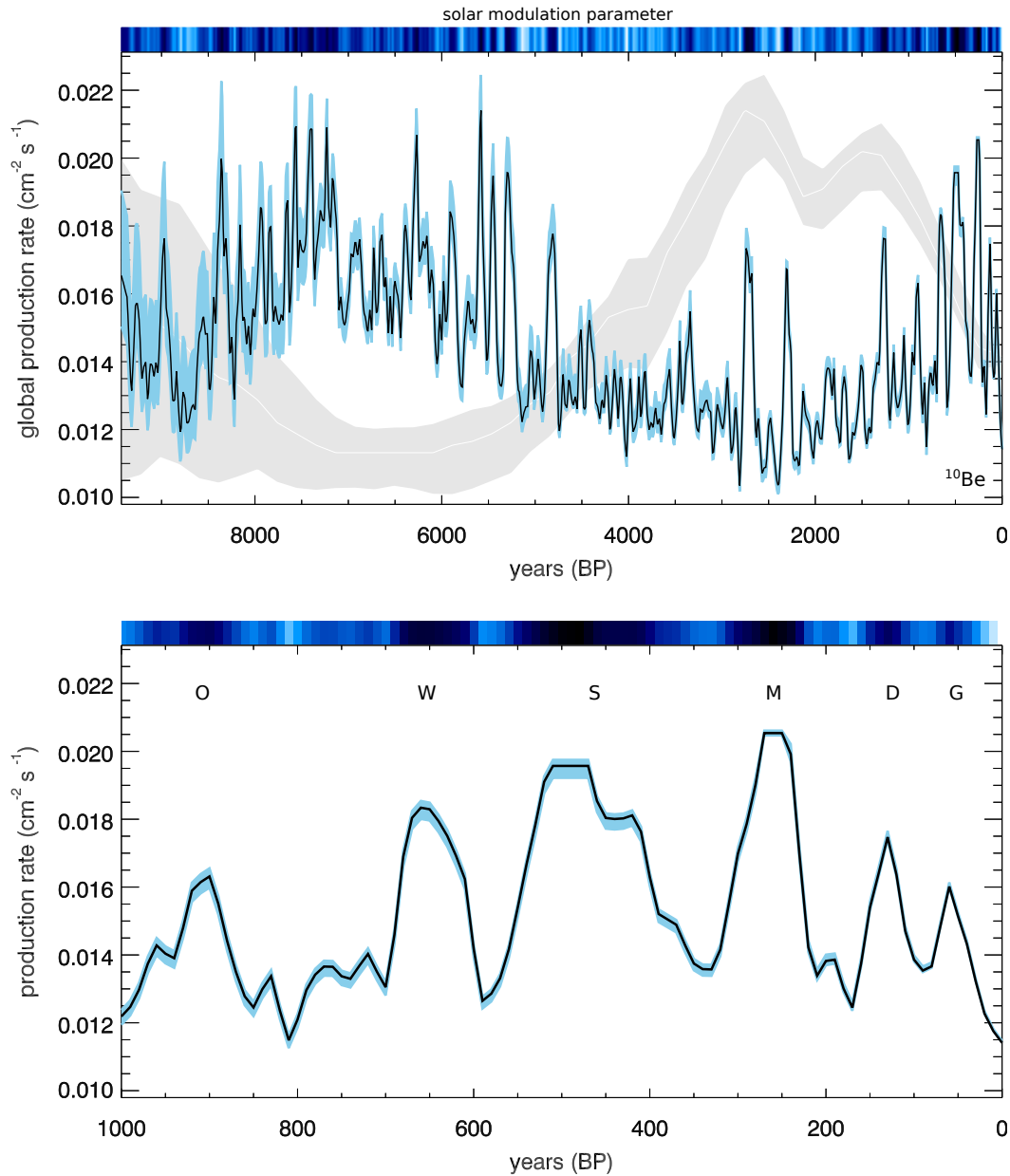


Figure 7.25: *Upper panel: The reconstructed global  $^{10}\text{Be}$  production rate values during the Holocene using the magnetic field reconstruction by Knudsen et al. (2008) (gray shaded area in the background) as well as the solar modulation parameter by Steinhilber et al. (2012) (color bar on top). Lower panel: A zoom into the last millennium showing the six Grand Solar Minima: O = Oort, W = Wolf, S = Spörer, M = Maunder, D = Dalton and G = Gleisberg. In both cases the light blue band corresponds to the magnetic field uncertainties.*



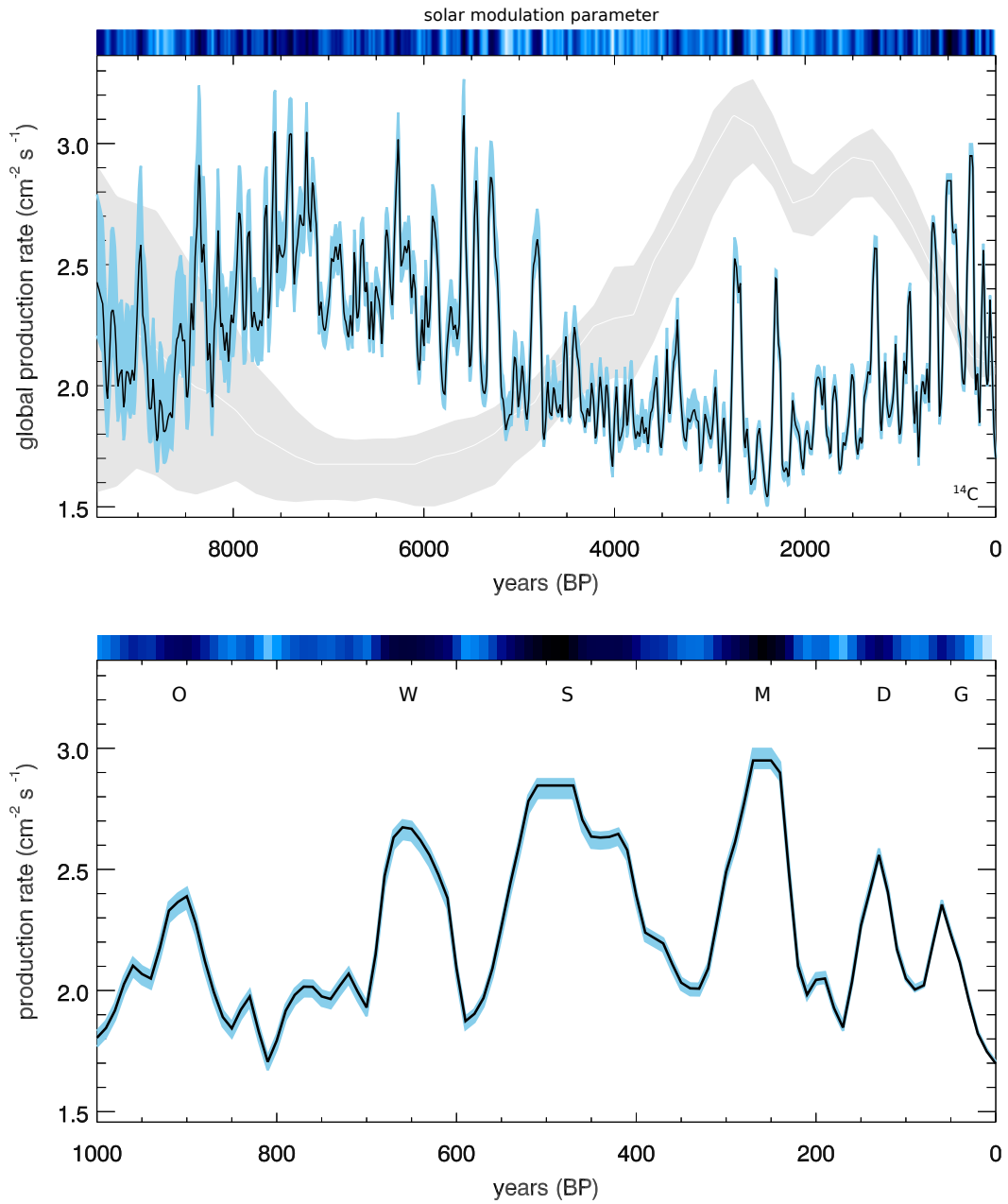


Figure 7.26: Same as Fig. 7.25 for the global  $^{14}\text{C}$  production during the Holocene.

$^{10}\text{Be}$  (upper panel) and  $^{14}\text{C}$  (lower panel) during the Holocene, both radionuclide-dependent data sets (red lines) deviate almost by the same amount from the computations of this work. Thus, because a much wider time period is covered, based on the ocean-atmosphere diffusion box model computations available at <http://www.radiocarbon.org/IntCal09.htm> (see also Reimer et al., 2009), the global  $^{14}\text{C}$  production rate between 10,500 BP and 0 BP is studied in more detail in the following.

### A More Detailed Comparison of the Reconstructed Global $^{14}\text{C}$ Production Rates with $^{14}\text{C}$ computations from a ocean-atmospheric diffusion box model (see e.g. Reimer et al., 2009)

A comparison between the results of the previous investigation (see upper panel of Fig. 7.26) and the simulations from an ocean-atmosphere diffusion box model (see e.g. Reimer et al., 2009) are presented in Fig. 7.28. Here the computations of this work are displayed by the black line and the corresponding light blue error band, while the ocean-atmosphere diffusion box model results are given as red line. The comparison clearly reveals that strong differences between the two computations exist. Assuming a) the ocean-atmosphere diffusion box model results to be valid and b) the production rates computed in this work, and thus the self-consistent chain, to be correct from the modeling point the discrepancies may be caused by either the used reconstructed magnetic field strength values by Knudsen et al. (2008), which may not represent the proper conditions throughout the Holocene or the reconstructed solar modulation parameter used in this work, which may show too low values (see discussion at the beginning of this Section). Both dependencies will be studied in the following.

### Influence of the Used Geomagnetic Field Strength Reconstructions

As mentioned earlier, the geomagnetic field strength reconstructions by Knudsen et al. (2008) are not the only ones available. Concentrating on the time period throughout the Holocene most recent investigations are published by Korte et al. (2011). Using the first time-dependent spherical-harmonic geomagnetic field *CALS10k.1b* model, which can be downloaded at [ftp://ftp.gfz-potsdam.de/home/mag/Download/CALS10k1b/CALS10k\\_1b.zip](ftp://ftp.gfz-potsdam.de/home/mag/Download/CALS10k1b/CALS10k_1b.zip), they calculated the geomagnetic dipole strength for the past 10,000 years.

A comparison of the temporal evolution of the reconstructed magnetic field strengths by Knudsen et al. (2008) and Korte et al. (2011) relative to present values is displayed in Fig. 7.29. Here the black solid line represents the mean values reconstructed by Knudsen et al. (2008) whereas the red dashed one is displaying the results by Korte et al. (2011), revealing differences between the two models to only occur between three time-frames: 8,750 BP and 6,250 BP, 3,500 BP and 1,000 BP as well as . During the other times the mean geomagnetic field strength

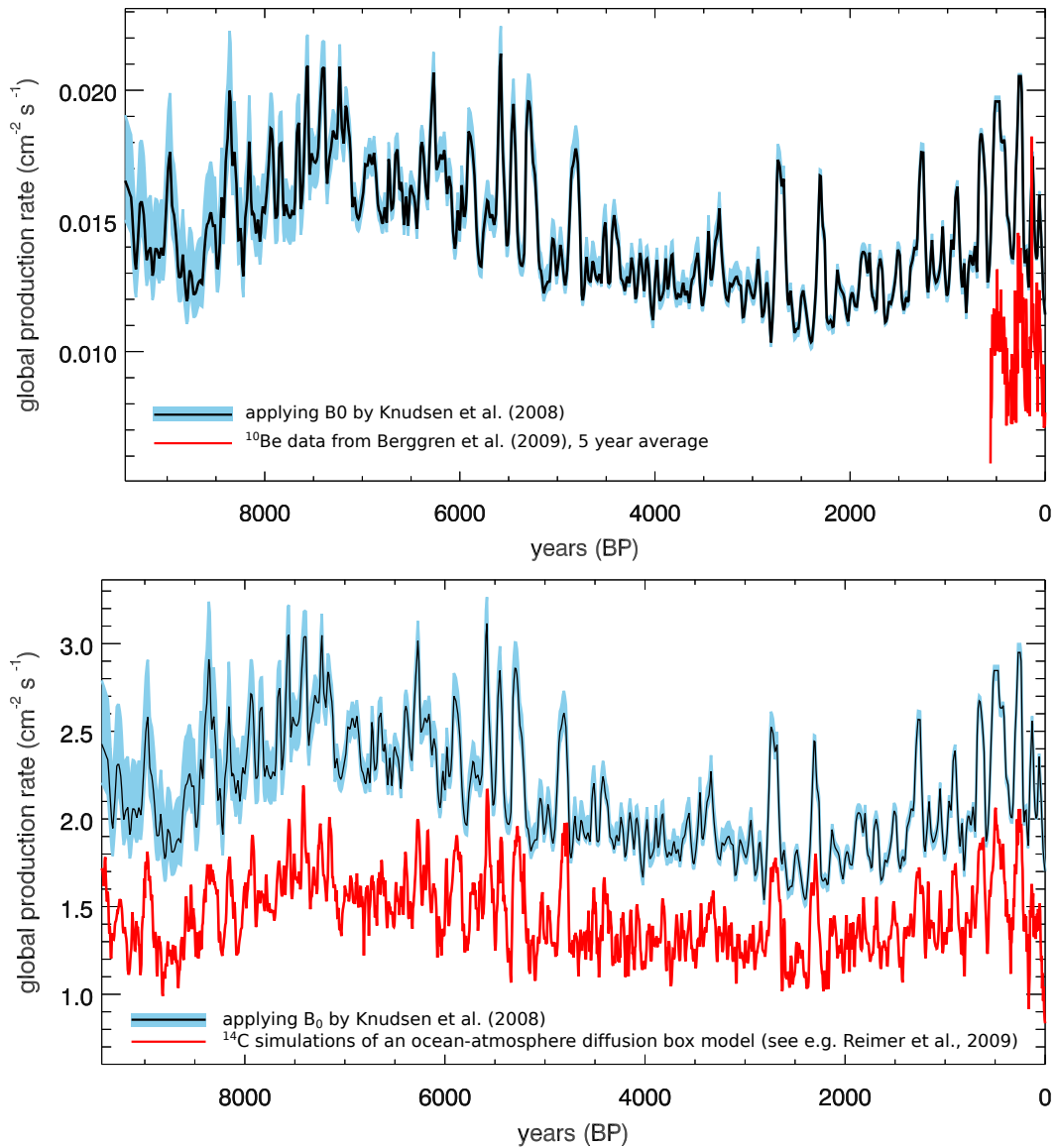


Figure 7.27: Global <sup>10</sup>Be (upper panel) and <sup>14</sup>C production rates (lower panel) during the Holocene in comparison with measurements by Berggren et al. (2009) and ocean-atmosphere diffusion box model data (see e.g. Reimer et al., 2009) given as red curves, respectively.

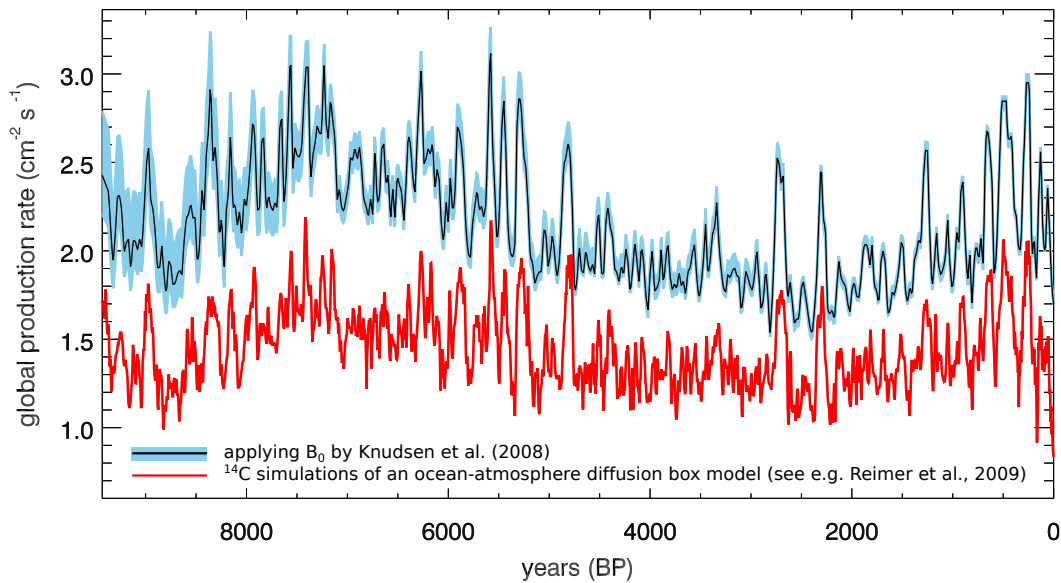


Figure 7.28: Computed global  $^{14}\text{C}$  production rates using  $\phi_{ST12}$  and well as the magnetic field strengths by Knudsen et al. (2008) (black line and corresponding band) during the Holocene. In comparison the ocean-atmosphere diffusion box model data (see e.g. Reimer et al., 2009) are shown as red curve.

values by Korte et al. (2011) are well within the upper and lower magnetic field strength value error estimates by Knudsen et al. (2008). Furthermore, during most of the time the values by Korte et al. (2011) are well below the mean values by Knudsen et al. (2008), revealing that a change to their values will lead to higher production rates within the period of time of major differences. Nevertheless, in order to investigate the strength of this effect the global  $^{14}\text{C}$  production rates using the geomagnetic field strength values by Korte et al. (2011) are computed.

These new results, displayed as black dots, in comparison to the result using the values by Knudsen et al. (2008), black line and corresponding error estimates, are displayed in the upper panel of Fig. 7.30. As expected the production rates taking into account the reconstructions by Korte et al. (2011) only show higher production values during the times of strong differences between the two data sets highlighted as gray shaded areas. Differences, which, however, are not as significant as previously thought. In order to complete the picture, the lower panel in addition displays both computations in comparison to the ocean-atmosphere diffusion box model data (see e.g. Reimer et al., 2009). Unfortunately, the differences between both computations can not be minimized due to the use of another magnetic field strength model. Thus, the differences more likely are caused by the solar modulation parameter applied.

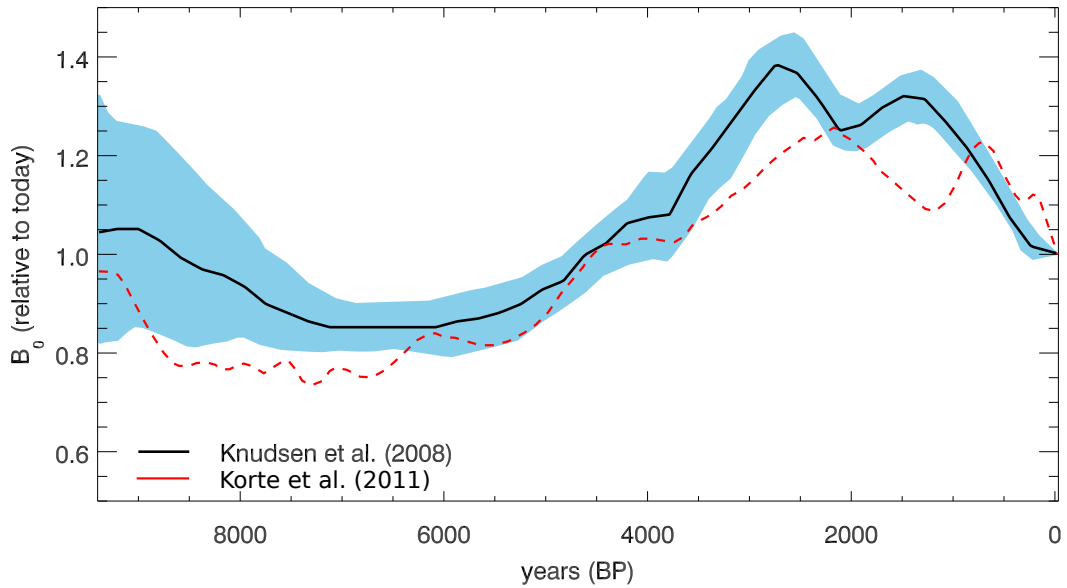


Figure 7.29: The reconstructed magnetic field strengths by *Knudsen et al. (2008)* (black line and band) compared with the most recent ones by *Korte et al. (2011)* (red dashed line) for the time period between 9400 BP to 0 BP.

### On the Influence of the Solar Modulation Parameter

For the computation of global production rates during the Holocene the solar modulation parameter  $\phi_{ST12}$  by *Steinhilber et al. (2012)* was used. For the first time this modulation parameter was derived on the basis of two cosmogenic radionuclides. Using measurements of ice-cores and tree rings as well as the computations of the global  $^{10}\text{Be}$  and  $^{14}\text{C}$  production rates by *Masarik and Beer (2009)* they were able to reconstruct a new modulation parameter set. Unfortunately, as mentioned earlier, there are still negative, and therefore non-physical  $\phi$  values present, which would imply that the spectrum during the Grand Solar Minima would have exceeded the LIS. By now no other reconstruction of a general solar modulation parameter during the Holocene, using both cosmogenic radionuclides, is available, and no other group was able to define a single solar modulation parameter which can represent both  $^{10}\text{Be}$  and  $^{14}\text{C}$  data during the Holocene.

Nevertheless, in order to see whether the computations of this work are able to provide a cosmogenic radionuclides independent solar modulation parameter the following method is applied:

- 1) Taking into account the full interaction chain investigated in this work and the resulting computed three-dimensional data matrix of the global  $^{14}\text{C}$  production rate a synchronization with the data by *Reimer et al. (2009)* can be performed.

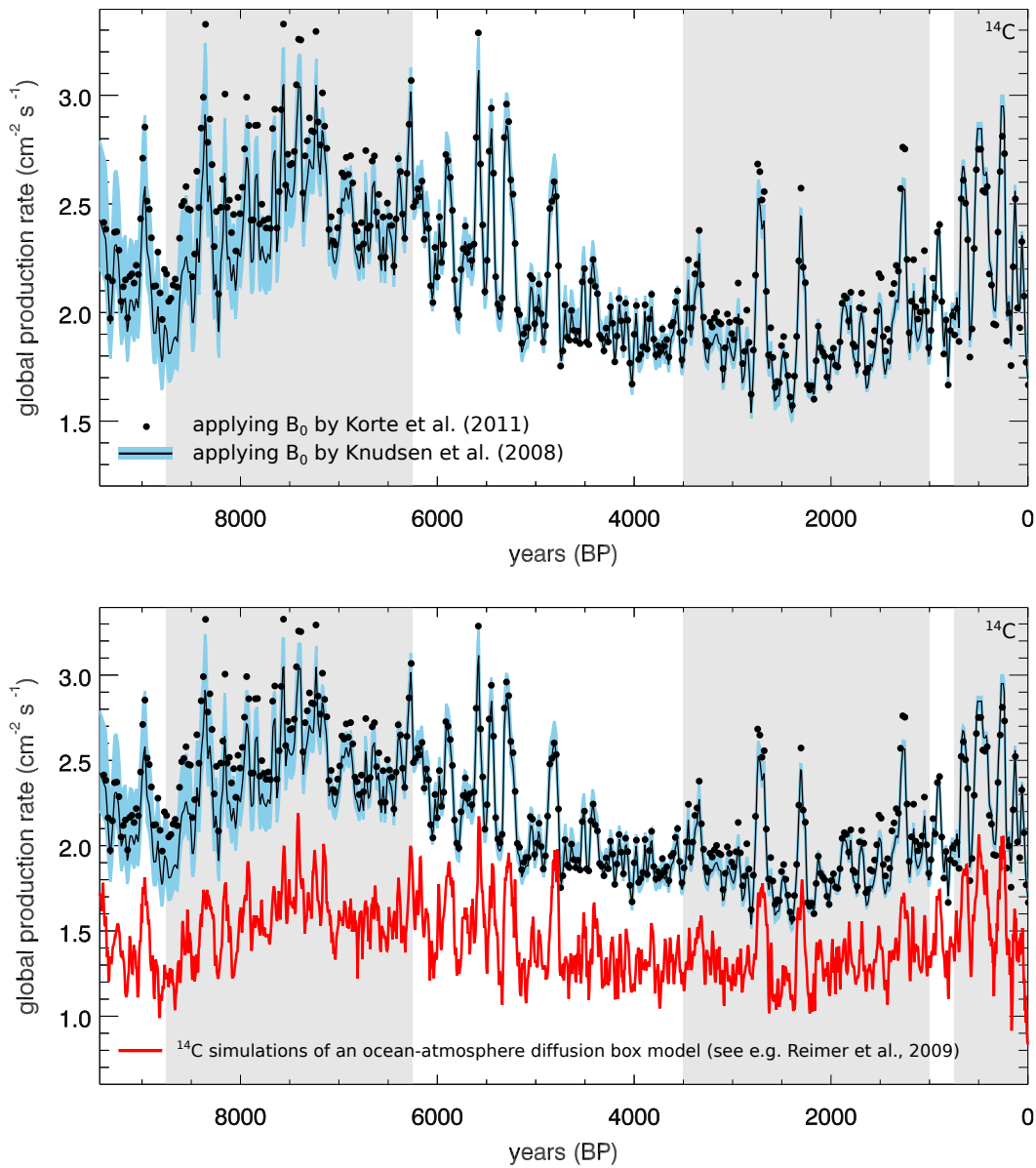


Figure 7.30: *Upper panel: The reconstructed global <sup>14</sup>C production rates for the magnetic field reconstructions by Knudsen et al. (2008) (black line and band) and Korte et al. (2011) (filled black dots). Lower panel: Computations of the upper panel in comparison to the ocean-atmosphere diffusion box model output (red line, see e.g. Reimer et al., 2009)*

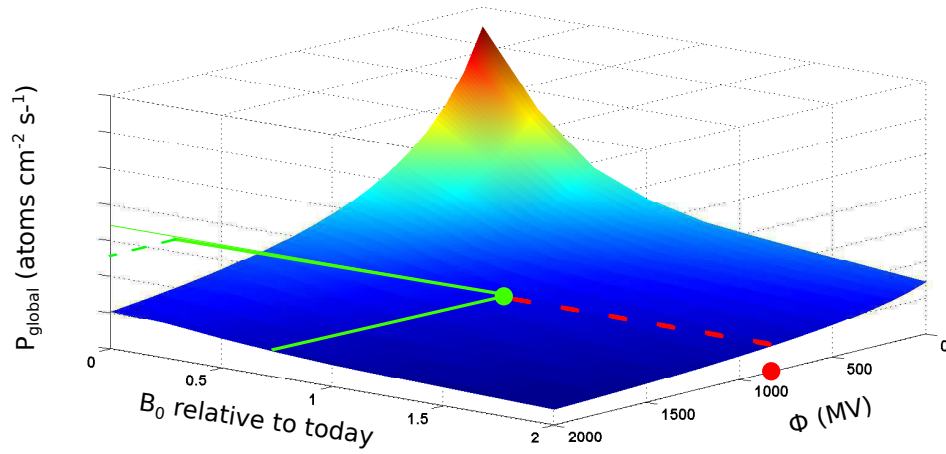


Figure 7.31: *Reconstruction of the solar modulation parameter from the computations of this work: Knowing the global production rates from the measurements (z-axis) and the information on the magnetic field (x-axis), both represented by the green solid lines, it is possible to reconstruct the corresponding solar modulation parameter (red dashed line and red dot).*

- 2) Using the global production rates of the ocean-atmosphere diffusion box model (see e.g. [Reimer et al., 2009](#)) and taking into account the temporal evolution of the geomagnetic field strengths by either [Knudsen et al. \(2008\)](#) or [Korte et al. \(2011\)](#) for each combination a corresponding solar modulation parameter can be reconstructed. An illustration of the procedure is shown in Fig. 7.31, where the green lines show the global production rate value and the geomagnetic field strength, both given values, while red displays the corresponding reconstructed solar modulation value.
- 3) Applying this method a new time-dependent solar modulation parameter, in the following denoted as  $\phi_{HE12}$ , can be reconstructed.
- 4) To test  $\phi_{HE12}$ , and therewith indirectly the computations of this work, afterwards the global  $^{10}\text{Be}$  production rates during the Holocene using the new modulation parameter  $\phi_{HE12}$  are computed, and a comparison with the GRIP ice core data by [Berggren et al. \(2009\)](#) is performed.

The result of the first three steps, the reconstruction of the solar modulation parameter during the Holocene based on the global  $^{14}\text{C}$  production rates, is shown in the upper panel of Fig. 7.32. Here the results based on the use of the geomagnetic field strengths by [Knudsen et al. \(2008\)](#) are displayed as solid red line combined with the light blue band for its upper and lower limits, while those for the reconstructions by [Korte et al. \(2011\)](#) are displayed as filled dots. It shows

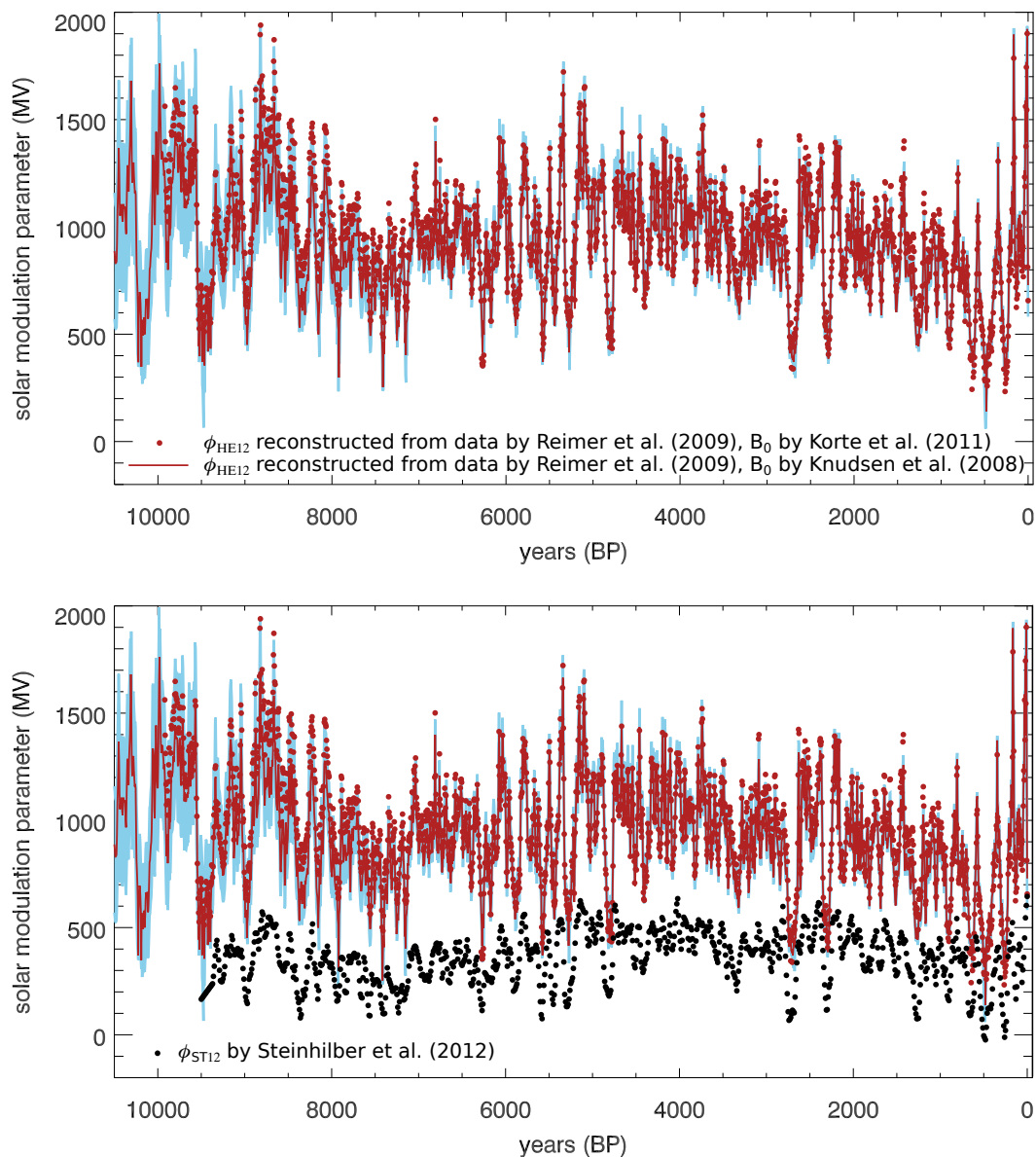


Figure 7.32: *Upper Panel: The reconstructed solar modulation parameter  $\phi_{HE12}$  during the Holocene depending on the geomagnetic field strength reconstruction used. Red line as well as the light blue band correspond to the results applying the reconstructions by Knudsen et al. (2008), filled dots correspond to the computations applying the reconstructions by Korte et al. (2011). Lower panel: Same as in the upper panel but compared with the solar modulation parameter by Steinhilber et al. (2012) (black filled dots).*



that both reconstructed solar modulation parameter do not become negative (i.e. non-physical). However, using the  $B_0$  values of Korte et al. (2011) temporarily shifts the reconstructed values of  $\phi_{HE12}$  towards higher values, in mean by about 120 MV, which is comparable with findings by Vonmoos et al. (2006). In addition the lower panel shows the reconstructed modulation parameter of this work in comparison with  $\phi_{ST12}$  (black dots), where the strong differences become obvious.

However, to see whether or not  $\phi_{HE12}$  has the potential to also be able to reconstruct  $^{10}\text{Be}$  measurements the computations of this work in the following are compared to data provided by Berggren et al. (2009). Thus, applying the geomagnetic field strengths by Knudsen et al. (2008) and Korte et al. (2011) as well as  $\phi_{HE12}$  the new global  $^{10}\text{Be}$  production rates during the Holocene are computed in the next step. The corresponding results for the period between 10,000 BP and -50 BP are displayed in the upper panel of Fig. 7.33. Here the computed  $^{10}\text{Be}$  production rates using the magnetic field strength values by Knudsen et al. (2008) are displayed as black triangles, while those using the data by Korte et al. (2011) are displayed in red. The GRIP ice-core data by Berggren et al. (2009) in addition are given by the gray line. As mentioned before this data set is limited to the last 600 years, thus a zoom into 550 BP to -50 BP is displayed in the lower panel. In summary the results reveal that a) the influence on the used magnetic field reconstructions is of minor importance and b) the computed global  $^{10}\text{Be}$  production rate values are in good agreement with the measurements by Berggren et al. (2009). The differences between both, however, can be explained by the stratospheric and tropospheric mixing processes of  $^{10}\text{Be}$  (see Heikkilä et al., 2008, for further information), which, however, was beyond the scope of this work.

In order to investigate the entire Holocene also more recent investigations from the space era need to be taken into account. On the basis of Ionization Chamber data and Neutron Monitor measurements Usoskin et al. (2011) reconstructed the solar modulation parameter between 1939 and 2010. This reconstruction in the following is added to the investigation, and, furthermore, will be compared to the reconstructed solar modulation  $\phi_{HE12}$ .

The upper panel of Fig. 7.34 shows the solar modulation parameter  $\phi_{HE12}$  and its limits due to the magnetic field strengths by Knudsen et al. (2008) (red line and light blue band) and Korte et al. (2011) (filled dots) in combination with the solar modulation parameter values by Usoskin et al. (2011) ( $\phi_{US11}$ , black line). However, because the period is much too wide in order to compare  $\phi_{HE12}$  and  $\phi_{US11}$  in more detail the lower panel shows both time-dependent parameters between 300 BP and -62 BP corresponding to the time-period between 1650 and 2012. Both values are normalized to the value of 1950. In addition also the sunspot numbers throughout this period is shown in dark blue. As can be seen a) the three Grand Solar Minima are well represented and b) both  $\phi_{US11}$  and  $\phi_{HE12}$  are in good agreement within the limits of the geomagnetic field strength variations

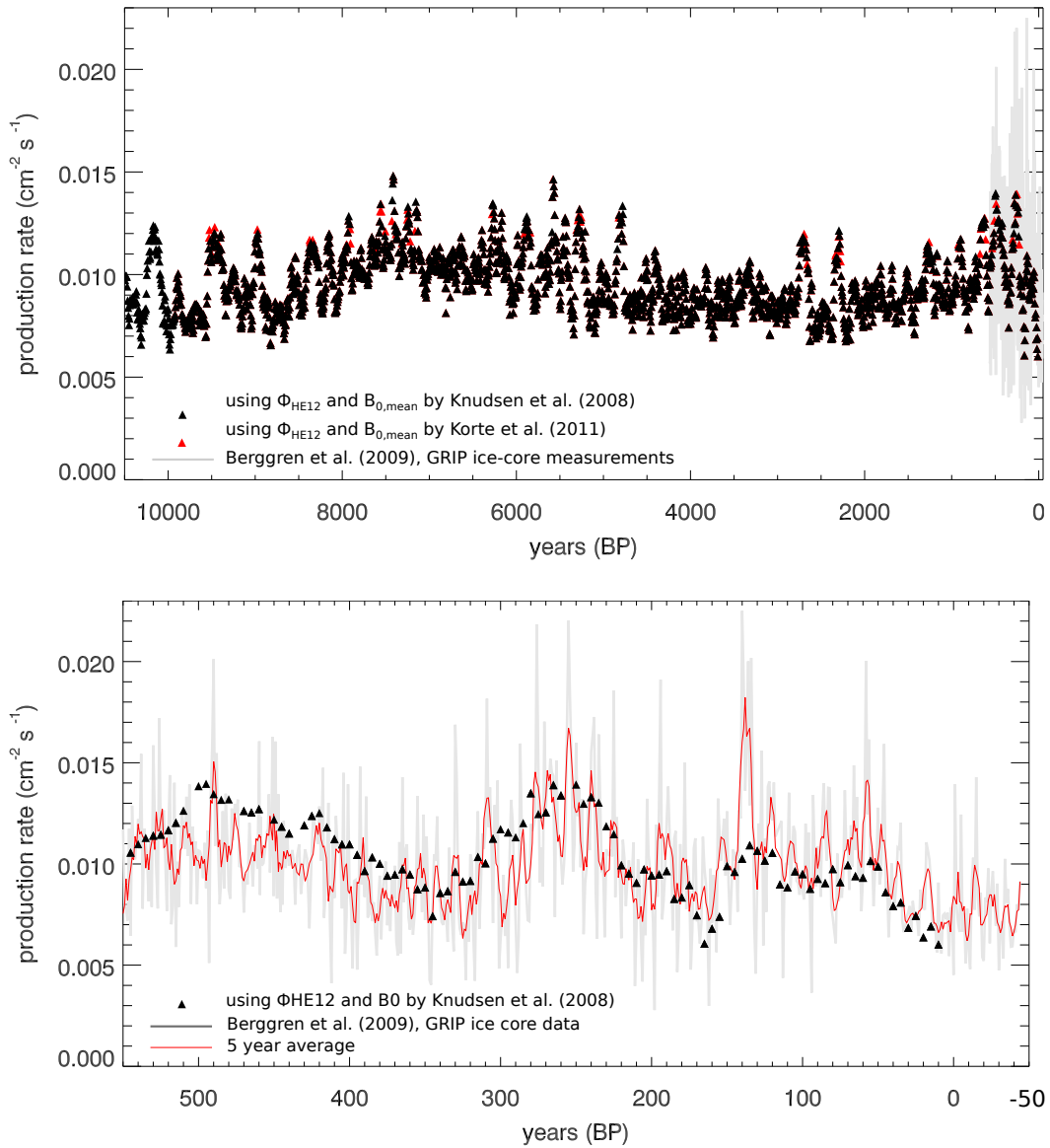


Figure 7.33: *Upper panel: The global  $^{10}\text{Be}$  production rates using  $\phi_{\text{HE12}}$  and the geomagnetic field reconstructions by Knudsen et al. (2008) (black triangles) as well as Korte et al. (2011) (red triangles) in comparison to the GRIP ice-core data by Berggren et al. (2009) (gray line) between 10,000 BP and -50 BP. Lower panel: Same as upper panel but zoomed into times between 550 BP and -50 BP.*

investigated in this work.

Note, however, that further investigations on the reconstruction of the solar modulation parameter during 2006 and 2008 using proton measurements from the PAMELA instrument were performed in this work as well. As displayed in Fig. 7.35 the solar modulation parameter values reconstructed from the PAMELA measurements in mean are about 160 MV above those reconstructed by [Usoskin et al. \(2011\)](#), findings which seem to indicate that  $\phi_{US11}$  is computed systematically too low.

## Conclusions

Taking into account the full interaction chain the global production rates of  $^{10}\text{Be}$ ,  $^7\text{Be}$ ,  $^3\text{H}$ ,  $^{36}\text{Cl}$ ,  $^{26}\text{Al}$  as well as  $^{14}\text{C}$  could be computed self-consistently. For the first time in this work it was possible to reconstruct a solar modulation parameter throughout the Holocene, which

- a) never becomes negative (i.e. non-physical)
- b) leads to a reasonably well description of the  $^{10}\text{Be}$  measurements by [Berggren et al. \(2009\)](#) as well as the ocean-atmosphere diffusion box model  $^{14}\text{C}$  data ([Reimer et al., 2009](#)) during the Holocene.

Unfortunately, therewith the conclusions by [Herbst et al. \(2010\)](#), which, at the time of their publication, could only be based on the solar modulation by [Steinhilber et al. \(2008\)](#), need to be reinvestigated. Thus, by using the conversion equations determined in Section 3.5 and the solar modulation parameter reconstructed in this work, the LIS-dependent modulation-parameters during the Holocene are re-calculated in the following. The results for the models by [Garcia-Munoz et al. \(1975\)](#), [Webber and Higbie \(2003\)](#) and [Webber and Higbie \(2009\)](#) are displayed in the three panels of Fig. 7.36. Note that a conversion to the LIS model by [Langner et al. \(2003\)](#) would lead to even higher modulation values as those given by  $\phi_{HE12}$ , thus they here are not investigated further.

It shows that the LIS-dependent modulation parameters by [Garcia-Munoz et al. \(1975\)](#) (upper panel) and [Webber and Higbie \(2003\)](#) (middle panel) represented by the black lines still show positive (i.e. physical) values over the entire period. The conversion to the model by [Webber and Higbie \(2009\)](#) (lower panel), however, shows a different picture. Here during two of the six Grand Solar Minima between 1000 BP and 0 BP, in particular the Wolf minimum around 640 BP as well as the Maunder Minimum around 240 BP, negative (i.e. non-physical) solar modulation parameter values occur. As discussed in Section 3.5 this leads to the conclusion that the spectrum by [Webber and Higbie \(2009\)](#) may not be a proper LIS model.

Weakening the conclusions by [Herbst et al. \(2010\)](#), this new investigation,

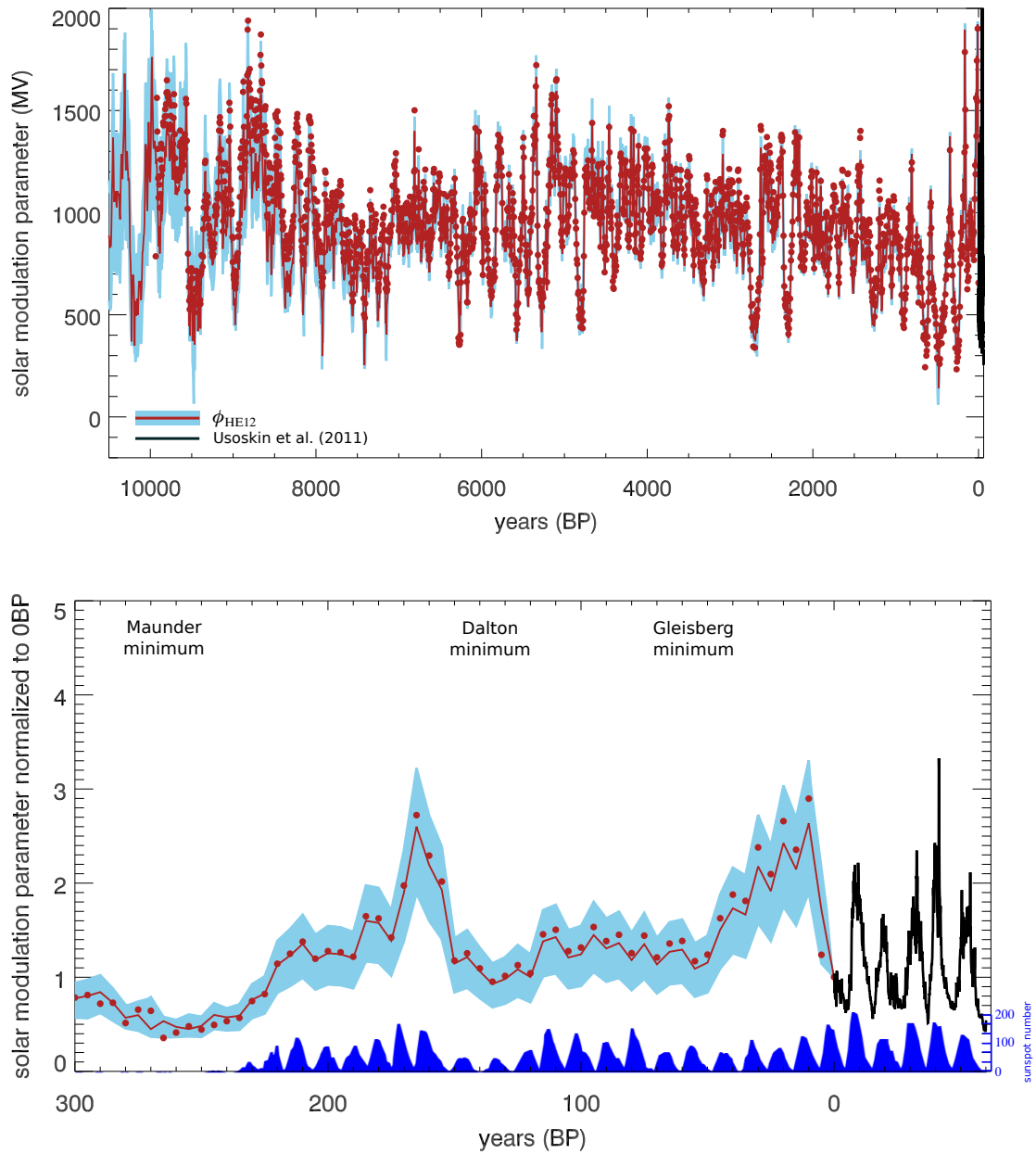


Figure 7.34: Upper panel: The solar modulation parameter reconstructed in this work (red line/dots, light blue band) in comparison with the values by *Usoskin et al. (2011)* (black line). Lower panel: Zoom into the years 1650 to 2012, showing in addition the observed sunspot numbers in dark blue.

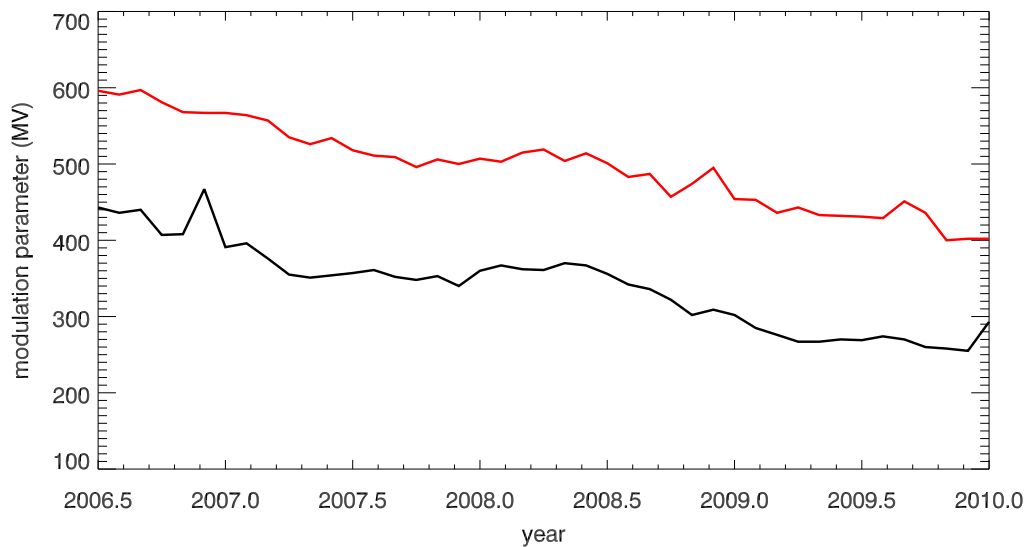


Figure 7.35: Solar modulation parameter by *Usoskin et al. (2011)* (black line) in comparison with parameter values determined from PAMELA proton measurements using the method described in Section 3.4 (red line).

however, supports the findings discussed in Section 3.2. Consequently, neither from the Voyager measurements nor the cosmogenic radionuclides preserved in ice sheets, tree rings or sediments it is possible to reveal information on the "true" LIS. However, the models by *Garcia-Munoz et al. (1975)*, *Webber and Higbie (2003)*, *Langner et al. (2003)* as well as *Usoskin et al. (2005)* are able to fit the measurements reasonably well and thus all may be proper LIS models, findings which are consistent with recent Voyager data (see discussion in Section 3.2).

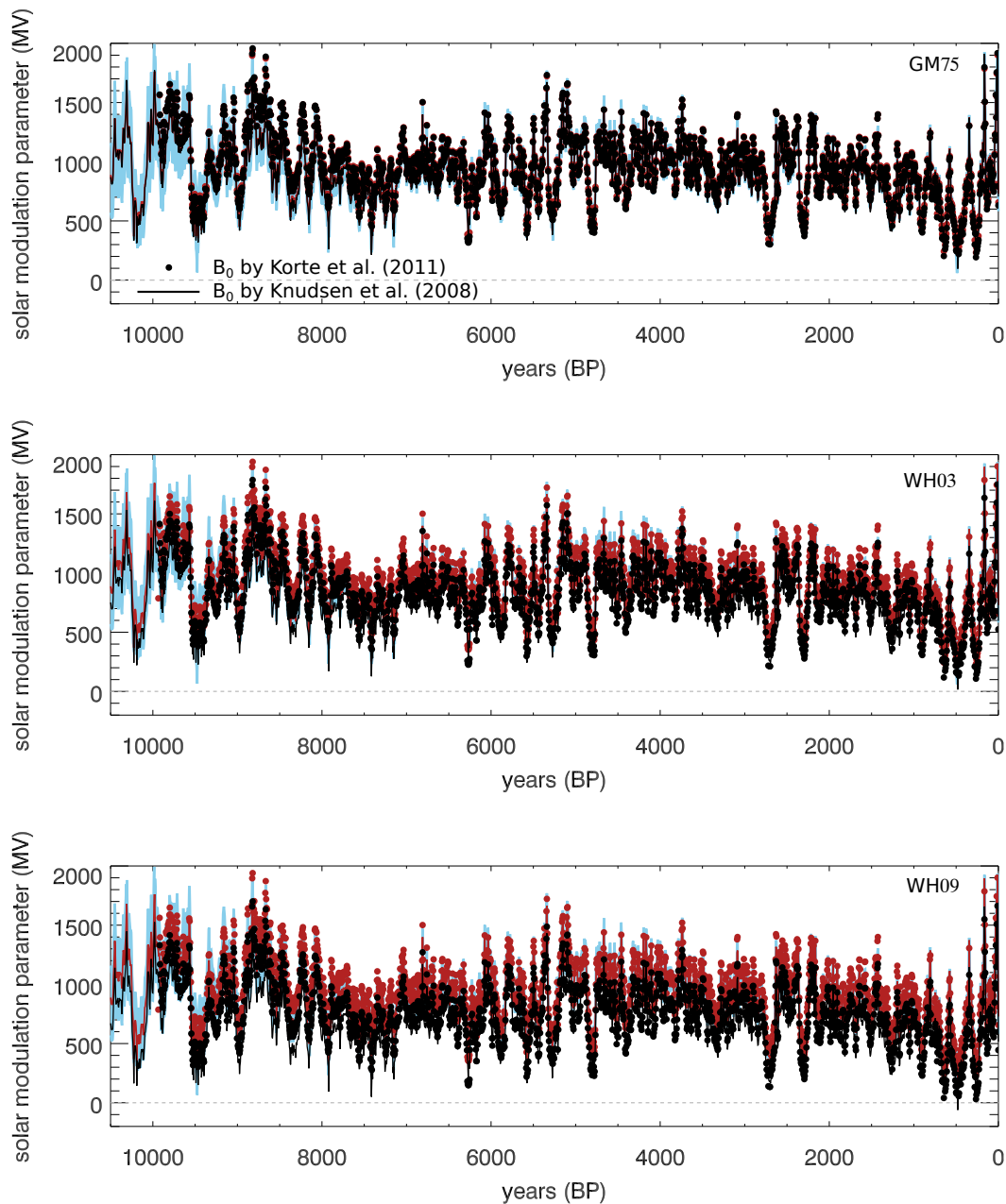


Figure 7.36: Influence of the LIS model on the reconstructed solar modulation parameter applying the conversion equations by *Herbst et al. (2010)*. Upper panel: LIS model by *Garcia-Munoz et al. (1975)*. Middle panel: LIS model by *Webber and Higbie (2003)*. Lower panel: LIS by *Webber and Higbie (2009)*. Here the reconstructed modulation parameter for the magnetic field variations by *Knudsen et al. (2008)* and its limits are given as red line and light blue band, while those for the magnetic field variations by *Korte et al. (2011)* are displayed as filled red dots. The LIS-dependent solar modulation parameter values are given as black lines and dots, respectively.

# Summary

---

One of the main goals of this work was the self-consistent modeling of the production of cosmogenic radionuclides being consistent with both  $^{10}\text{Be}$  and  $^{14}\text{C}$  measurements, by taking into account the full simulation chain starting with different local interstellar spectrum (LIS) models and their modulation outside as well as within the heliosphere and ending with the deposition of the cosmogenic radionuclides in natural archives like trees, ice sheets or sediments.

Starting with the investigation of the different LIS models used in the literature, this work investigated whether or not the Voyager spacecraft will be able to measure the LIS in the near future. Furthermore, a method to convert the LIS-dependent solar modulation parameters into each other was presented. Although being only a rough approximation of the particle transport, for the purpose of this work to provide solar-activity reconstructions over thousands of years the Force Field solution, leading to the solar modulation parameter  $\phi$  (Caballero-Lopez and Moraal, 2004) was used. In addition, the influence of the Earth's magnetic field variation as well as the importance of its geometry on the vertical cutoff rigidity were studied. The atmospheric production of secondary particles was investigated depending on the LIS model and the hadronic interaction model. Furthermore, in order to identify the most suitable hadronic model the galactic CR-induced ionization of the atmosphere was studied, favoring the Bertini model rather than the BIC model. Using this full chain, the local and global cosmogenic radionuclides production rates were computed for the first time self-consistently.

The main results of this work can be summarized as follows:

- a) On the basis of the finding by Scherer et al. (2011) that modulation takes place already in the outer heliosheath, this work proposes that i) all LIS models are consistent with the HPS and ii) non of the above LIS models can be excluded to be the proper LIS as well as that the Voyager spacecraft will not be able to measure the LIS in the near future.
- b) The various LIS models can be converted into each other by energy-dependent conversion equations. On the basis of the modulation parameters by Steinhilber et al. (2008) (however, note point f) below) this leads to the conclusion that not all of these models, especially not the ones by Webber and Higbie (2003, 2009) as well as Garcia-Munoz et al. (1975), may be proper LIS models.

- c) Based on the studies by [Pilchowski et al. \(2010\)](#), the influence of the geometry of the geomagnetic field is studied further. Following their discussion this work could show that the geometry of the magnetic field, represented by the introduced measure  $\delta B$  given as the difference of vertical and horizontal components, is a sufficiently good proxy for the cutoff rigidity. Both measures reflect, consistent with each other, the magnetic-field variations over the time-period from 1900 to 2010, thus the magnetic field variations cannot be neglected for e.g. the local production of  $^{10}\text{Be}$  and  $^{14}\text{C}$ .
- d) Beyond the investigations by [Matthiä \(2009\)](#) this work investigates the influence of the two hadronic interaction models BIC and Bertini on the galactic CR-induced ionization, confirming the findings by [Matthiä \(2009\)](#) by means of ridges investigations.
- e) Only by taking into account the complete chain, starting with the LIS and ending with the deposition of cosmogenic radionuclides into terrestrial archives, it was possible to compute new self-consistent local and global production rates of cosmogenic radionuclides.
- f) By taking into account the interaction chain on the basis of global  $^{14}\text{C}$  data derived from an ocean-atmosphere diffusion box model [Oeschger et al. \(1975\)](#); [Hughen et al. \(2004\)](#); [Reimer et al. \(2009\)](#) the new solar modulation parameter  $\phi_{HE12}$  is computed for the entire Holocene, which, for the first time, is
- compatible with both  $^{10}\text{Be}$  and  $^{14}\text{C}$  data
  - does not become negative (i.e. non-physical) independent of the LIS model during the Grand Solar Minima, with the exception of the heliopause spectrum by [Webber and Higbie \(2009\)](#), which still shows non-physical values.



# Outlook

---

Further improvements of the simulation chain will briefly be discussed in the following.

a) Modulation of the LIS

In this work the solar modulation parameter  $\phi$  has been used in order to reconstruct the solar activity throughout the Holocene. However, as discussed in Chapter 3, the Force Field solution is just a rough first order approximation of the particle transport inside the heliosphere. As shown in Section 3.2 time-consuming numerical simulations are necessary in order to model the particle transport in a more realistic way.

b) Solar Energetic Particles

Solar energetic particles events, mainly consisting of protons and alpha particles in the energy range of several MeV up to a few hundred MeV, and, in particular, so-called ground level events which can be detected at sea-level, may also contribute significantly to the production of cosmogenic radionuclides. The question arises to what amount such strong solar events contribute to the global production rates preserved in tree rings, ice sheets or sediments. By now this is a controversially discussed topic, however, the investigation of Section 7.2 indicate that such events are more likely visible in high-resolution  $^{36}\text{Cl}$  data rather than in those of  $^{10}\text{Be}$ , supporting the investigations by e.g. [Webber et al. \(2007\)](#).

c) Geomagnetic Field

As shown in Section 7.6, the reconstruction of the geomagnetic field strength has a non-negligible influence on the global cosmogenic radionuclides production rates. Earlier reconstructions by e.g. [Yang et al. \(2000\)](#) show much higher geomagnetic field strength values than those by [Knudsen et al. \(2008\)](#) or [Korte et al. \(2011\)](#), used in this work, which would influence the computations of the cosmogenic radionuclides as well as the reconstruction of the solar modulation parameter.

d) Atmospheric Mixing

The production of the cosmogenic radionuclide  $^{10}\text{Be}$  strongly depends

on latitude and altitude, and thus the signal stored in ice sheets contains information from different locations. As shown by Heikkilä et al. (2008), in addition  $^{10}\text{Be}$  is in contrary to  $^{14}\text{C}$  not fully globally mixed because stratospheric and tropospheric mixing have to be treated differently. In order to take into account these mixing processes global circulation models like e.g. the ECHAM5-HAM climate model (see e.g. Roeckner et al., 2003; Stier et al., 2005), a state-of-the-art climate model developed at the Max-Planck-Institut für Meteorologie in Hamburg, are necessary.

## On the Influence of Galactic and Heliospheric Variations

Despite the investigations outlined in this work, also other factors like, e.g., galactic variations due to the passage of a spiral arm, heliospheric variations or the influence of geomagnetic field reversals need to be studied more closely in the future. As a first step into this direction in the following first results of the influences of galactic and heliospheric variations on the production of the cosmogenic radionuclide  $^{10}\text{Be}$  are presented.

Due to the combination of several observations it is commonly known today that our solar system is located inside one out of the four spiral arms of our Galaxy. Inside these spiral arms a huge amount of new stars are formed while others end their shell-burning with a supernova explosion. As mentioned in Section 2.2, Supernova remnants (SNRs) are a possible source of cosmic rays (CRs) measured in our heliosphere. At first, however, galactic magnetic fields attach the CRs to the spiral arms they are produced in, but on long time scales the particles are able to diffuse into the surrounding space (see e.g. Büsching and Potgieter, 2008). Furthermore, the position of our solar system inside the Milky Way varies. Thus, every 70 to 100 million years it passes through one of the four arms (Beer et al., 2012). Because SNRs occur more frequently inside galactic arms the GCR flux beyond the solar system is believed to vary over large time-scales. In addition, localized regions of extremely high GCR fluxes due to multiple SNRs may exist within a spiral arm, as e.g. in the Gould's belt a region of star-forming clouds inside the Milky Way (Büsching et al., 2005, see e.g.). Both facts would lead to dramatic increases of the primary particle flux inside the heliosphere. Moreover, the shape and the structure of the heliosphere itself, but also the GCR flux within it, are also strongly influenced by the interstellar environment (see e.g. Scherer et al., 2006, and references therein).

The local and global  $^{10}\text{Be}$  production rates for selected scenarios are shown in the following.

### Galactic Variations

The scale on top of Fig. 9.1 (adopted from Shaviv, 2003) shows the simulated galaxy arm passages (upper scale) as well as the corresponding cosmic ray fluxes with re-

spect to present-day LIS values (lower scale, black solid line) over the past 1,000 Myr. Note that the flux around the time of a spiral arm passage is lagging behind the spiral arm crossing itself (see [Shaviv, 2003](#), for further information). The lower panel shows the LIS by [Usoskin et al. \(2005\)](#) and its maximum variations according to [Shaviv \(2003\)](#) (black lines) as well as computations of possible galaxy arm spectra by [Büsching and Potgieter \(2008\)](#) (colored lines), corresponding to the locations of the blue stars in the implemented figure in the upper right corner. The corresponding computations of the local and global  $^{10}\text{Be}$  production rates are given in Fig 9.2. From the left, showing the local  $^{10}\text{Be}$  production rates, it becomes obvious that much higher local production rates occur at mid and equatorial regions.

### Heliospheric Variations

Using the BoPo model (see [Scherer and Ferreira, 2005](#), for a model description), [Scherer et al. \(2008\)](#) investigated the influence of variations of the LISM conditions on the heliospheric environment, concentrating on stable phases of the local interstellar medium (LISM), like a hot, a warm and a cold LISM ([Frisch and Slavin, 2006](#)). Among others, the following two scenarios were investigated:

- model b) A low density ISM with a proton density  $n_p=0.04\text{ cm}^{-3}$ , a hydrogen density of  $n_H=0.04\text{ cm}^{-3}$ , a relative LISM inflow speed of 26 km/s and a LIS temperature of  $T_{\text{LISM}}=7000\text{ K}$ . Additionally the termination shock (TS) is assumed to be at 126 AU, the heliopause (HP) to be located at 180 AU while a possible bow shock (BS) is set at 290 AU.
- model d) A perturbed interstellar medium due to, e.g., SNs close to the solar system ([Frisch, 1997](#)) with a proton density of  $n_p=0.04\text{ cm}^{-3}$ , a hydrogen density of  $n_H=0.04\text{ cm}^{-3}$ , a relative LISM inflow speed of 100 km/s, and a LIS temperature of  $T_{\text{LISM}}=8000\text{ K}$ . Additionally, the TS is assumed to be at 11 AU, and the HPS to be located at 16 AU, while a possible BS is set at only 22 AU.

The present heliosphere is assumed to have a proton density of  $n_p=0.1\text{ cm}^{-3}$ , a hydrogen density of  $n_H=0.1\text{ cm}^{-3}$ , a relative LISM inflow speed of 25 km/s, and a LIS temperature of  $T_{\text{LISM}}=6500\text{--}8000\text{ K}$ . Additionally the TS is assumed to be at 80 AU while the HPS may be located at 130 AU. Thus the upper two cases can be seen as important extreme cases which may have a strong influence on the local as well as global cosmogenic radionuclide production rates.

The corresponding local and global  $^{10}\text{Be}$  production rates are displayed in the left and right panels of Fig. 9.4.

The spectra by [Scherer et al. \(2008\)](#) are modeled for typical solar minimum conditions in the order of  $\phi = 500\text{ MV}$ . From the left panel, displaying the local  $^{10}\text{Be}$ , it becomes obvious that both hemispherical scenarios would lead to much higher production rate values at polar and mid-latitudes than the typical minimum conditions, given by the dashed-dotted line.

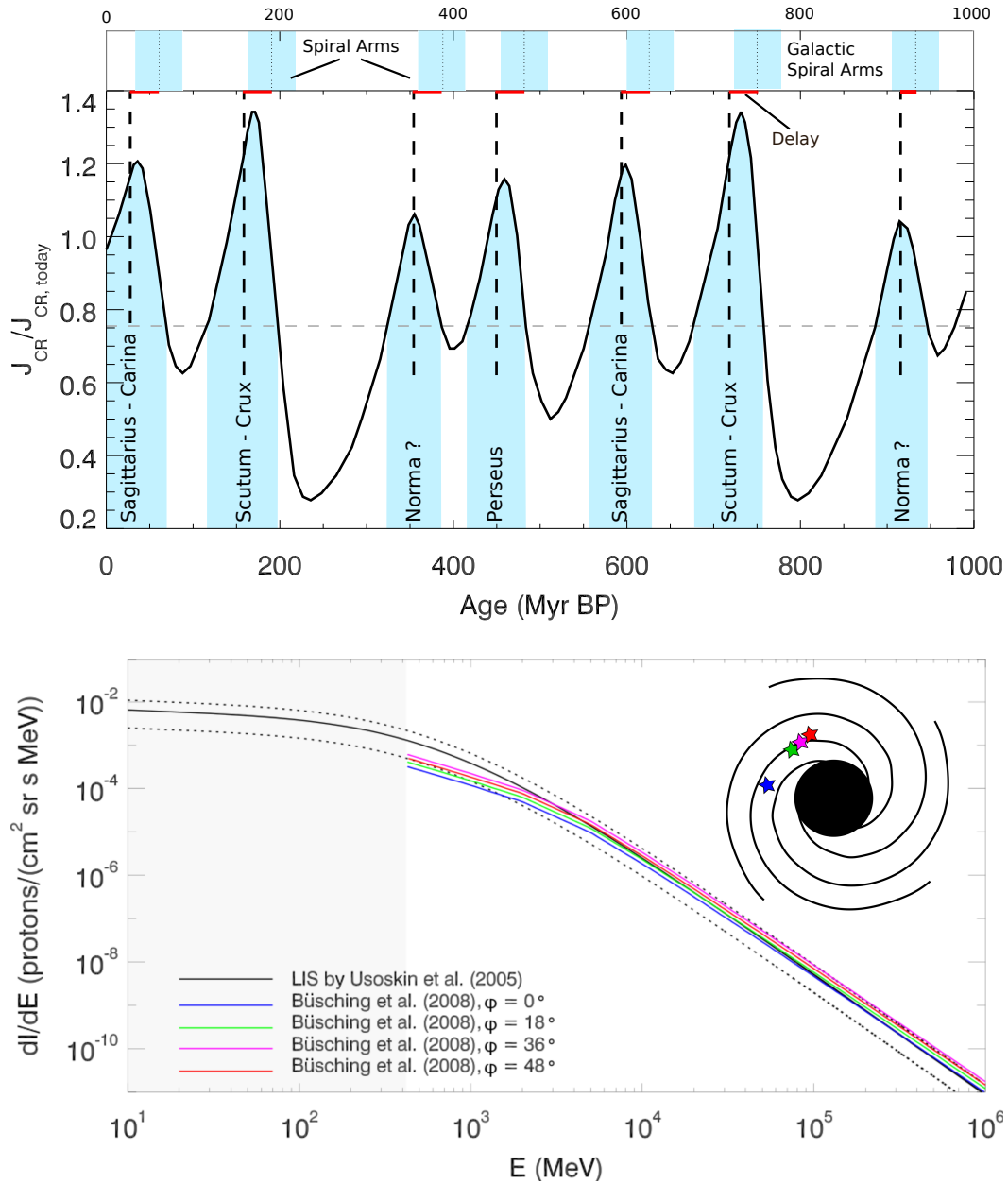


Figure 9.1: *Upper panel: Cosmic ray history adopted from Shaviv (2003). Shown here are the simulated galaxy arm passages (shaded areas in the upper scale) as well as the corresponding cosmic ray fluxes with respect to present LIS values (lower scale, black solid line) as function of time over the past 1,000 Myr as adopted from Shaviv (2003). Lower panel: LIS model by Usoskin et al. (2005) as black solid line, its maximum variations due to Shaviv (2003) as dashed lines and the computed spectra by Büsching and Potgieter (2008) for a spiral arm passage. The sketch of the Galaxy in the upper right panel shows the color code for the angle dependent spectra by Büsching and Potgieter (2008).*

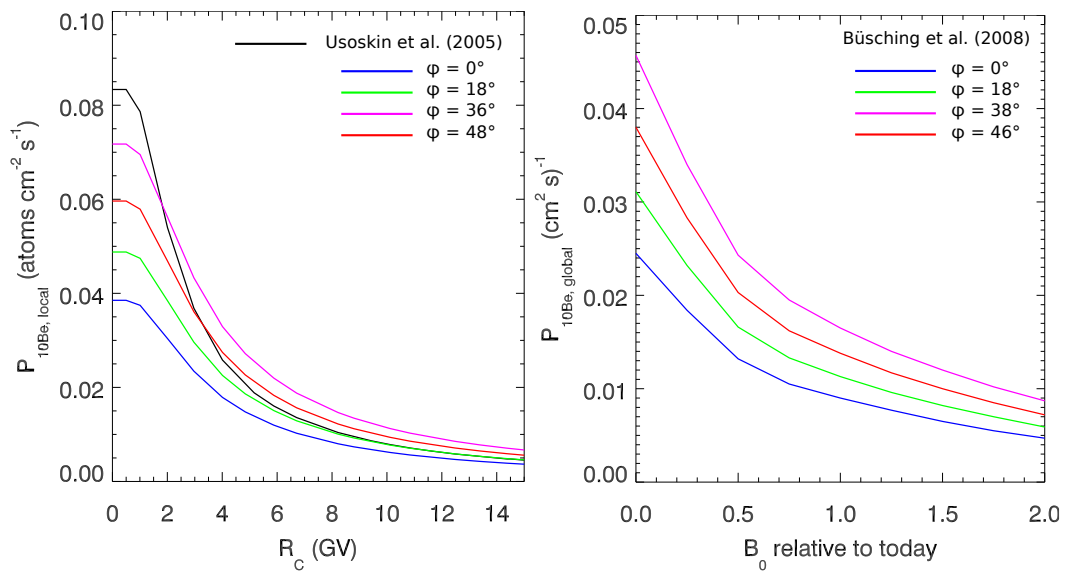


Figure 9.2: *Left panel: Local  $^{10}\text{Be}$  production rates due to primary protons. The black solid line represents the results using the unmodulated LIS by Usoskin et al. (2005), the red curves correspond to the four stages of the galaxy arm passage. Right panel: The corresponding global production rates for geomagnetic field strengths between zero and two times the present value.*

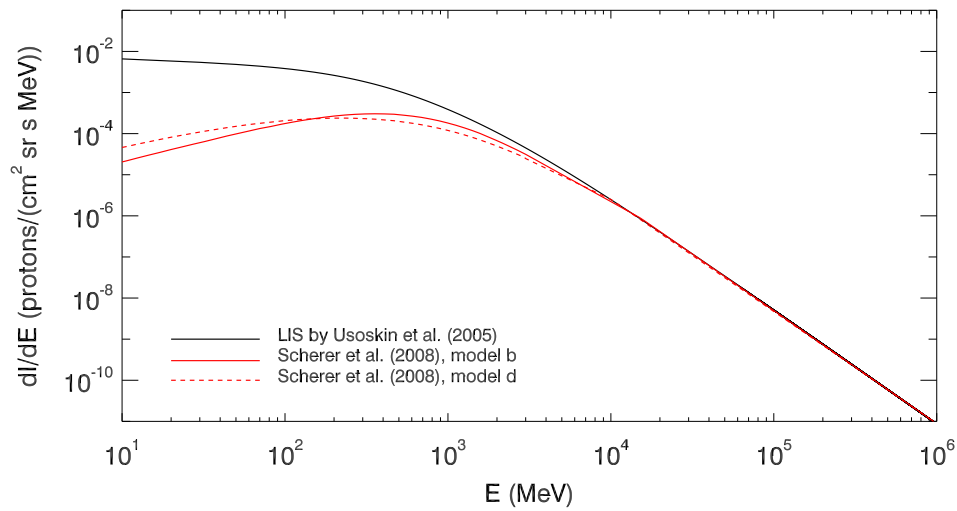


Figure 9.3: *The differential energy spectra of different heliospheric conditions computed by Scherer et al. (2008) at 1 AU (red lines) in comparison to the unmodulated LIS by Usoskin et al. (2005) (black line).*

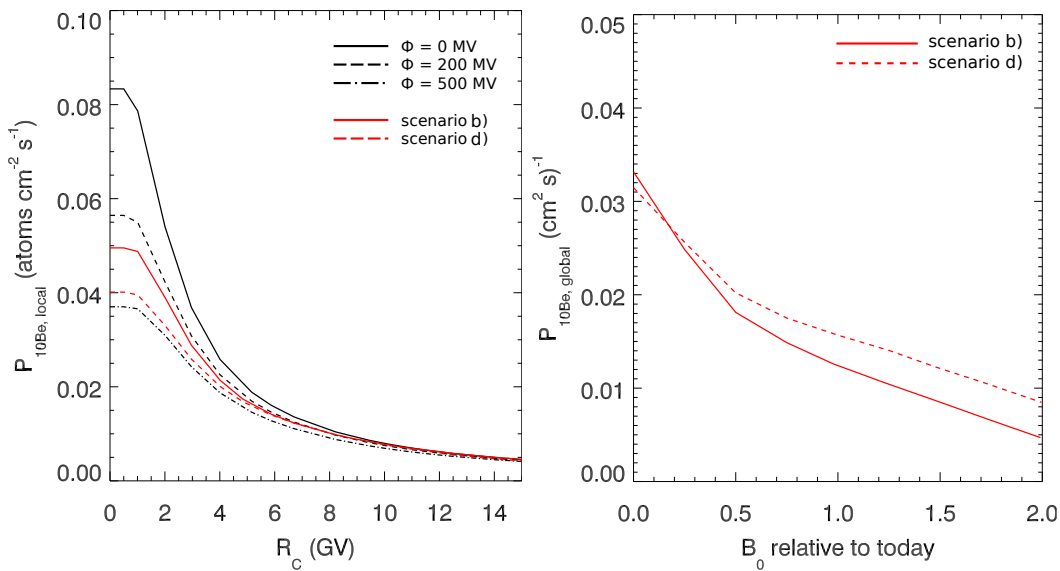


Figure 9.4: *The local and global  $^{10}\text{Be}$  production rates for different heliospheric conditions (red lines) in comparison to the computations of present heliospheric conditions (black lines). In this study only primary protons are investigated.*

# List of Figures

1.1	Sketch of the processes involved in order to model the atmospheric ionization as well as the production of the cosmogenic radionuclides .	4
2.1	The yearly average sunspot number between 1610–2010 . . . . .	8
2.2	The eleven year solar activity cycle . . . . .	9
2.3	The relative chemical abundances . . . . .	11
2.4	Galactic cosmic ray intensity variation in comparison to the sunspot number . . . . .	12
2.5	The two different drift cycles, $A>0$ and $A<0$ . . . . .	13
2.6	Sketch of the external terrestrial magnetic field. . . . .	15
2.7	The atmospheric temperature profile . . . . .	19
2.8	The atmospheric energy loss of primary protons . . . . .	22
2.9	The evolution of an extensive air shower . . . . .	23
3.1	Ratio of the different proton and alpha particle LIS spectra with respect to the model by Usoskin et al. (2005) . . . . .	31
3.2	The proton and alpha LIS spectra . . . . .	32
3.3	Projection of the heliosphere onto the equatorial plane . . . . .	34
3.4	Relative intensities of the different LIS models with respect to the spectrum by Webber and Higbie (2003) . . . . .	35
3.5	Sample trajectories of protons illustrating the OHS modulation due to adiabatic cooling within the TS . . . . .	37
3.6	Modulated spectra for a constant diffusion coefficient . . . . .	38
3.7	Modulated spectra for an energy-dependent diffusion coefficient . . . . .	39
3.8	Combination of simulations for a constant (left panel) and rigidity-dependent (right panel) diffusion coefficient . . . . .	39
3.9	Diffusion coefficient bands for $\kappa=10^{26}$ cm <sup>2</sup> s <sup>-1</sup> and $\kappa=10^{27}$ cm <sup>2</sup> in comparison with the HPS . . . . .	40
3.10	Diffusion tensor in comparison with the solar modulation parameter . . . . .	42
3.11	Ratio of the modulated proton LIS models to PAMELA measurements . . . . .	44
3.12	LIS dependent linear regressions corresponding to the energy range investigated in this work and the one used by Usoskin et al. (2005) . . . . .	45
3.13	Influence of the used energy ranges on the linear relations . . . . .	46
3.14	Deviations of the proton LIS dependent linear relations between the three energy ranges investigated . . . . .	47
3.15	Proton LIS and modulation dependent error in $\phi_{\text{LIS}}$ . . . . .	48
3.16	Comparison of the $\Delta\phi_{\text{LIS}}$ corrected primary proton spectra with the PAMELA measurements . . . . .	49
3.17	Best fit of the investigated alpha LIS models to measurements by the PAMELA instrument . . . . .	51

3.18	Deviations of the alpha LIS dependent linear relations between the three energy ranges investigated and the resulting modulation dependent errors . . . . .	52
3.19	The converted reconstructed modulation parameters for the different proton LIS models . . . . .	53
4.1	Geometric visualization of the three subspaces for particles with given rigidities . . . . .	56
4.2	The backward-trajectory-tracing method . . . . .	59
4.3	The vertical cutoff rigidity at 20 km . . . . .	60
4.4	Computed global vertical cutoff rigidity distributions for varying altitudes . . . . .	61
4.5	Magnitude and geometry of the magnetic field in comparison with the cutoff rigidity . . . . .	62
4.6	Temporal evolution of the magnetic field measures $R_C$ , $\delta B$ and $ B $ . . . . .	64
4.7	Absolute differences of $R_C$ and $\delta B$ between 1900 and 1955 as well as 1955 and 2010 . . . . .	65
4.8	Absolute differences of $R_C$ and $\delta B$ for the time intervals between 1900 and 1955 as well as 1955 and 2010 . . . . .	66
4.9	Neutron Monitor stations . . . . .	67
4.10	Vertical cutoff rigidities as well as $\delta B$ values between 1900 and 2010 at selected locations . . . . .	68
4.11	NM latitude scan by Villorosi et al. (1997) and the counting rate variations at Kiel, Moscow, Mexico and the BVIs . . . . .	70
4.12	Sketch of the angular connection of incidenting particles . . . . .	73
4.13	Global cutoff rigidity distributions for three different zenithal angles . . . . .	74
5.1	Omnidirectional differential secondary neutron intensities at an atmospheric depth of $1030 \text{ g/cm}^2$ and $R_C = 2.7 \text{ GV}$ computed with different LIS models . . . . .	79
5.2	Omnidirectional differential secondary proton intensities at an atmospheric depth of $1030 \text{ g/cm}^2$ and $R_C = 2.7 \text{ GV}$ computed with different LIS models . . . . .	83
5.3	Hadronic model dependent differential neutron intensities in comparison with the measurements by Goldhagen et al. (2003) . . . . .	84
5.4	Hadronic model dependent differential proton intensities in comparison to the measurements by Sanuki et al. (2003) and Diggory et al. (1974) . . . . .	85
6.1	Influence of the Secondary cascade branches on the cosmic ray induced ionization (taken from Usoskin et al. (2006)) . . . . .	91
6.2	Ionization Yield $Y_i$ of primary protons with an energy of 1 GeV and 100 GeV. . . . .	92
6.3	CR proton induced ionization yield $Y_{\text{protons}}$ . . . . .	94



6.4	$Y$ at different atmospheric depths . . . . .	95
6.5	$F_p$ as function of atmospheric depth . . . . .	96
6.6	Total ionization function as function of atmospheric depth . . . . .	97
6.7	Polar ionization during solar minimum and maximum conditions in comparison to the measurements by Neher (1971) as well as computations by Usoskin et al. (2006) . . . . .	100
6.8	Equatorial ionization during solar minimum conditions . . . . .	101
6.9	Local ionization during solar minimum at an atmospheric depth of 140 g/cm <sup>2</sup> . . . . .	103
6.10	Latitude survey at 140 g/cm <sup>2</sup> , 200 g/cm <sup>2</sup> and 280 g/cm <sup>2</sup> in comparison with the measurements by Neher (1967) . . . . .	104
6.11	Latitude survey . . . . .	105
6.12	Shifted latitude survey at 140 g/cm <sup>2</sup> , 200 g/cm <sup>2</sup> and 280 g/cm <sup>2</sup> using the magnetic field parameters of 1900 and 2010 . . . . .	105
6.13	Shifted latitude survey . . . . .	106
6.14	Shifted latitude survey at 140 g/cm <sup>2</sup> , 200 g/cm <sup>2</sup> and 280 g/cm <sup>2</sup> using the magnetic field parameters of 1900 and 2010 . . . . .	107
6.15	Influence of the solar modulation on the local ionization rates at 700 g/cm <sup>2</sup> (left) and 1000 g/cm <sup>2</sup> (right) . . . . .	108
6.16	Solar modulation and depth dependent atmospheric ionization at polar regions . . . . .	109
6.17	Solar modulation and depth dependent atmospheric ionization at equatorial regions . . . . .	110
7.1	Cross sections for the production of the cosmogenic radionuclides <sup>10</sup> Be, <sup>7</sup> Be, <sup>3</sup> H, <sup>26</sup> Al, <sup>36</sup> Cl and <sup>14</sup> C . . . . .	116
7.2	The processes involved in the production of cosmogenic radionuclides . . . . .	118
7.3	Production of <sup>10</sup> Be produced by primary hydrogen . . . . .	122
7.4	Production of <sup>10</sup> Be produced by primary helium . . . . .	123
7.5	Yield functions of the cosmogenic radionuclides <sup>10</sup> Be, <sup>36</sup> Cl and <sup>14</sup> C . . . . .	124
7.6	Response function of <sup>10</sup> Be, <sup>14</sup> C and <sup>36</sup> Cl . . . . .	125
7.7	Local production rates of <sup>10</sup> Be, <sup>7</sup> Be, <sup>36</sup> Cl, <sup>3</sup> H, <sup>26</sup> Al as well as <sup>14</sup> C as function of the cutoff rigidity . . . . .	127
7.8	Local production rates of <sup>10</sup> Be as function of latitude . . . . .	128
7.9	Contour plot of the local <sup>10</sup> Be production rate using a non-tilted dipole field as well as the IGRF parameter of 2010 . . . . .	129
7.10	Cross section sets for the production of <sup>10</sup> Be and <sup>7</sup> Be . . . . .	130
7.11	Local production rates of <sup>10</sup> Be and <sup>7</sup> Be depending on the used cross sections . . . . .	131
7.12	Method to calculate the global cosmogenic radionuclides production rates . . . . .	132
7.13	Global production rates of <sup>10</sup> Be, <sup>7</sup> Be, <sup>3</sup> H and <sup>14</sup> C as function of the solar modulation parameter . . . . .	133
7.14	Local production rates of <sup>10</sup> Be depending on the applied LIS model . . . . .	135

7.15	Global production rates of $^{10}\text{Be}$ and $^7\text{Be}$ depending on the used cross sections . . . . .	136
7.16	Computed cutoff rigidities in comparison to the results using the approximation by Elsasser et al. (1956) . . . . .	137
7.17	Global $^{14}\text{C}$ production rates and their dependence on the used cutoff rigidity calculation method . . . . .	138
7.18	Global $^{10}\text{Be}$ and $^{14}\text{C}$ production variations between 1940 and 2010 .	139
7.19	The influence of the magnetic field on the global production rates of $^{10}\text{Be}$ . . . . .	140
7.20	Influence of the cross sections on the global production rates of $^{10}\text{Be}$	141
7.21	Solar modulation during the Holocene by Steinhilber et al. (2012) . .	142
7.22	The magnetic dipole strength during the Holocene reconstructed by Knudsen et al. (2008) . . . . .	143
7.23	Sketch of the method used to reconstruct the global production rates during the Holocene . . . . .	144
7.24	Dependence of the global $^{10}\text{Be}$ production rates on the strength of the magnetic field as well as the solar modulation . . . . .	145
7.25	The global $^{10}\text{Be}$ production rate during the Holocene . . . . .	146
7.26	Global $^{14}\text{C}$ production rate during the Holocene . . . . .	147
7.27	Global $^{10}\text{Be}$ and $^{14}\text{C}$ production rates during the Holocene in comparison with measurements by Berggren et al. (2009) and ocean-atmosphere diffusion box model data, respectively . . . . .	149
7.28	Computed global $^{14}\text{C}$ production rates during the Holocene compared to calibrated $^{14}\text{C}$ data by Reimer et al. (2009) . . . . .	150
7.29	Reconstructed magnetic field strength by Knudsen et al. (2008) and Korte et al. (2011) . . . . .	151
7.30	Global $^{14}\text{C}$ production rates for the magnetic field reconstructions by Knudsen et al. (2008) and Korte et al. (2011) . . . . .	152
7.31	Reconstructing the solar modulation parameter from the computations	153
7.32	Reconstructed solar modulation parameter $\phi_{HE12}$ for different magnetic field strength reconstructions . . . . .	154
7.33	Global $^{10}\text{Be}$ production rates using $\phi_{HE12}$ in comparison to the GRIP ice-core data by Berggren et al. (2009) . . . . .	156
7.34	$\phi_{HE12}$ in comparison with the solar modulation parameter by Usoskin et al. (2011) . . . . .	158
7.35	Solar modulation parameter by Usoskin et al. (2011) during recent times in comparison with parameter values determined from PAMELA proton measurements . . . . .	159
7.36	Influence of the LIS model on the reconstructed solar modulation parameter . . . . .	160
9.1	Cosmic ray history adopted from Shaviv (2003) . . . . .	166
9.2	Local and global $^{10}\text{Be}$ production rates during the passage of a galactic spiral arm . . . . .	167

---

9.3	Differential energy spectra of different heliospheric conditions in comparison to the LIS by Usoskin et al. (2005) . . . . .	168
9.4	Local and global $^{10}\text{Be}$ production rates for different heliospheric conditions . . . . .	168
C.1	Number of events computed within selected energy bins . . . . .	207
C.2	Computation time needed in order to simulate $10^5$ events . . . . .	208



# List of Tables

3.1	The model-dependent modulation parameters $\phi_i$ adapted by the best-fit method . . . . .	43
4.1	Vertical cutoff rigidities for Kiel, Moscow, Mexico and the British Virgin Islands in 1910, 1955 and 1997 . . . . .	69
4.2	Measured normalized counting rates for Kiel, Moscow, Mexico and the British Virgin Islands in 1910, 1955 and 1997 . . . . .	70
6.1	Locations of the latitude survey measurements performed by Neher (1967). . . . .	102
7.1	Characteristics of different cosmogenic (radio)nuclides . . . . .	114
7.2	Production reactions of the CNs investigated . . . . .	115
E.2	The total local cosmogenic radionuclides production rate for cutoff rigidities between 0 and 16 GV for different solar modulation phases . . . . .	212
E.3	The total global cosmogenic radionuclides production rate for different solar modulation phases . . . . .	213



# Bibliography

- Adriani, O. et al. *PAMELA Measurements of Cosmic-Ray Proton and Helium spectra*. *Science*, 332, 69–72, 2011. [50](#), [51](#)
- Agostinelli, S. et al. *Geant4 - a simulation toolkit*. *Nuc. Instr. Meth. Phys. Res.*, 506, 250–303, 2003. [119](#), [193](#)
- Allison, J. et al. *Geant4 developments and applications*. *IEEE Trans. Nucl. Sci.*, 53, 270–278, 2006. [193](#)
- Amako, K. et al. *Comparison of Geant4 electromagnetic physics models against the NIST reference data*. *IEEE Trans. Nucl. Sci.*, 52, 910–918, 2005. [193](#), [194](#)
- Amsler, C. et al. *Review of Particle Physics*. *Phys. Lett. B*, 667, 1–5, 1–6, 2008. [10](#)
- Aplin, K. L., R. G. Harrison and M. J. Rycroft. *Investigating Earth's Atmospheric Electricity: a Role Model for Planetary Studies*. *Space Sci. Rev.*, 137, 11–27, 2008. [87](#)
- Apostolakis, J. et al. *The implementation of ionization energy loss in very thin absorbers for the Geant4 simulation package*. *Nucl. Instrum. Meth.*, A453, 597, 2000. [194](#)
- Apostolakis, J., M. Asai, A.G. Bogdanov et al. *Geometry and physics of the Geant4 toolkit for high and medium energy applications*. *Radiation Physics and Chemistry*, 78, 859–873, 2009. [193](#), [194](#), [195](#)
- Baumjohann, W. and R. A. Treumann. *Advanced Space Plasma Physics*. Imperial College Press, 1997. [16](#)
- Bard, E., G. M. Raisbeck, F. Yiou and J. Jonzel. *Solar modulation of cosmogenic nuclides production over the last millennium: Comparison between  $^{14}\text{C}$  and  $^{10}\text{Be}$  records*. *Sci. Lett.*, 150, 453–462, 1997. [112](#)
- Bazilevskaya, G. A. and A. K. Svirzhevskaya. *On the stratospheric measurements of cosmic rays*. *Space Sci. Rev.*, 85, 431–521, 1998. [88](#)
- Bazilevskaya, G. A. et al. *Cosmic Ray Induced Ion Production in the Atmosphere*. *Space Sci. Rev.*, 137, 149–173, 2008. [87](#), [88](#), [99](#)
- Beer, J. et al. *Informations on past solar activity and geomagnetism from  $^{10}\text{Be}$  in the Camp Century ice core* *Nature*, 331, 675–679, 1988. [112](#)
- Beer, J., A. Blinov, G. Bonani, H. J. Hofmann and R. C. Finkel. *Use of  $^{10}\text{Be}$  in polar ice to trace the 11-year cycle of solar activity*. *Nature*, 347, 164–166, 1990. [112](#)

- Beer, J. et al.  $^{10}\text{Be}$  as an indicator of solar variability and climate. Springer, In: The Solar Engine and Its Influence on Terrestrial Atmosphere and Climate, edited by E. Nesme-Ribes, 221–233, 1994.
- Beer, J. *Long-term indirect indices of solar variability*. Space Sci. Rev., 94, 53–66, 2000. [112](#)
- Beer, J., W. Mende and R. Stellmacher. *The role of the sun in climate forcing*. Quaternary Sci. Rev., 19, 403–415, 2000. [112](#)
- Beer, J., K. McCracken and R. von Steiger. *Cosmogenic Radionuclides - Theory and Applications in the Terrestrial and Space Environment*. Springer, 2012 [115](#), [117](#), [119](#), [123](#), [141](#), [164](#)
- Belov, A. V., L. I. Dorman and V. A. Oleneva. *Determination of the north-south asymmetry of cosmic rays from ground-based observations*. Kosmicheskie Luchi, 25, 5–23, 1988.
- Belov, A. V., E. A. Eroshenko, O. N. Kryakunovay, V. G. Kurtz and V. G. Yanke. *GLEs in the last three solar cycles*. Proceedings of the 31st ICRC, 2009. [10](#)
- Berberan-Santos, M. N., E. N. Bodunov and L. Pogliani. *On the barometric formula*. Am. J. Phys., 65, 404–412, 1997. [21](#)
- Berggren, A. M. et al. *A 600-year annual  $^{10}\text{Be}$  record from the NGRIP ice core*. Geophys. Res. Lett., 36, L11801, 2009. [1](#), [113](#), [145](#), [149](#), [153](#), [155](#), [156](#), [157](#), [172](#)
- Bertini, H. W., M. P. Guthrie. *News item results from medium-energy intranuclear-cascade calculation*. Nucl. Phys. A, 169, 1971. [120](#), [195](#)
- Binder, K. and D. W. Heermann. *Monte Carlo Simulation in Statistical Physics: An Introduction*. Springer, 2010. [89](#), [193](#)
- Boezio, M. et al. *Energy spectra of atmospheric muons measured with the CAPRICE98 balloon experiment*. Astroparticle Phys., 19, 583–604, 2003. [77](#), [80](#)
- Brüggemann M. *Determination of an arrival time cut for the separation of electrons and muons in extensive air showers*. PhD thesis, Universität Siegen, Germany, 2006. [24](#)
- Burger, R. A., M. S. Potgieter and B. Heber. *Rigidity dependence of cosmic ray proton latitudinal gradients measured by the Ulysses spacecraft: Implications for the diffusion tensor*. J. Geophys. Res., 105, 447–456, 2000. [28](#), [29](#)
- Büsching, I., A. Kopp, M. Pohl, R. Schlickeiser, C. Perrot and I. Grenier. *Cosmic-Ray Propagation Properties for an Origin in Supernova Remnants*. Astrophys. J., 619, 314–326, 2005. [10](#), [164](#)



- Büsching, I. and M. S. Potgieter. *The variability of the proton cosmic ray flux on the Sun's way around the galactic center*. Adv. Space Res., 42, 504–509, 2008. [36](#), [164](#), [165](#), [166](#)
- Caballero-Lopez, R. A. and H. Moraal. *Limitations of the force field equation to describe cosmic ray modulation*. J. Geophys. Res., 109, A12102, 2004. [27](#), [28](#), [161](#)
- Capella, A. and A. Krzywicki. *Unitarity corrections to short-range order: Long-range rapidity correlations*. Phys. Rev. D, 18, 4120–4133, 1978 [195](#)
- Casolino, M. et al. *Cosmic ray measurements with Pamela experiment*. Nuc. Phys. B (Proc. Suppl.), 190, 293–299, 2009. [43](#), [48](#)
- Chauvie, S. et al. *Geant4 low energy electromagnetic physics*. IEEE NSS 2004 Conference Record, Rome, 2004. [194](#)
- Chauvie, S., P. Nieminen and M. G. Pia. *Geant4 Model for the Stopping Power of Low Energy Negatively Charged Hadrons*. Nucl. Sci., 54, 578–584, 2007. [194](#)
- Chemeleff, J., F. Blanckenburg, K. Kossert and D. Jakob. *Determination of the  $^{10}\text{Be}$  half-life by Multi Collector ICP-Mass Spectrometry and Liquid Scintillation Counting*. Geochim. Cosmochim. Acta, 73, A221, 2009. [114](#)
- Choudhuri, A. R. *How far are we from a standard model of the solar dynamo?*. Adv. Space Res., 41, 868–873, 2008. [7](#)
- Clem, J. M. and L. I. Dorman. *Neutron Monitor Response Functions*. Adv. Space Res., 93, 335–359, 2000. [69](#), [124](#)
- Compton, H. and N. Turner. *Cosmic Rays on the Pacific Ocean*. Phys. Rev., 52, 799–814, 1937. [103](#)
- Connerney, J. E. P. *Magnetic fields of the outer planets*. J. Geophys. Res., 98, 18659–18679, 1993. [17](#)
- Cooke, D. J., J. E. Humble, M. A. Shea, D. F. Smart and N. Lund. *On cosmic-ray cut-off terminology*. Nuovo Cimento C Geophys. Space Phys. C, 14, 213–234, 1991. [56](#), [57](#), [58](#)
- Desorgher, L. *The PLANETOCOSMICS code, Tech. rep., <http://cosray.unibe.ch/laurent/planetocosmics>, 2006. [119](#), [195](#)*
- Diehl, R., M. Lang, K. Kretschmer and W. Wang.  *$^{26}\text{Al}$  emission throughout the Galaxy*. New Astron. Rev., 52, 440–444, 2006. [10](#)
- Diggory, I. S., J. R. Hook, I. A. Jenkins, and K. E. Turver. *The momentum spectra of nuclear active particles in the cosmic radiation at sea level - I. Experimental data*. J. Phys., 7, 741–764, 1974. [81](#), [82](#), [85](#), [170](#)

- Dorman, L. I., R. T. Guschina, M. A. Shea and D. F. Smart. *Cosmic Ray Effective Cut-off Rigidities*. Nauka, Moscow, 1972. 58
- Dorman, L. I. et al. *Monitoring and Forecasting of Great Solar Proton Events Using the Neutron Monitor Network in Real Time*. IEEE Trans. on Plasma Sci., 32, 1478–1488, 2004. 88
- Dorman, L. I. *Cosmic rays and space weather: effects on global climate change*. Annales Geophys., 30, 9–19, 2012. 103
- Dunai, T., F. M. Smart, R. Pik, P. Bunard and E. Gayer. *Production of  $^3\text{He}$  in crustal rocks by cosmogenic thermal neutrons*. Earth and Planet. Sci. Lett., 258, 228–236, 2007. 113
- Dunai, T. *Cosmogenic Nuclides*. Cambridge University Press, 2010. 77, 113, 117
- Dunzlaff, P. et al. *Observations of recurrent cosmic ray decreases during solar cycles 22 and 23*. Annales Geophys., 26, 3127–3138, 2006. 13
- Eidelman, A., T. Elperin, N. Kleecoin, I. Rogachevskii, J. Buchholz and G. Grünfeld. *Turbulent thermal diffusion of aerosols in geophysics and in laboratory experiments*. Nonlin. Proc. Geophys., 11, 343–350, 2004. 113
- Elsasser, W., E. Nay and J. Winkler. *Cosmic-ray intensity and geomagnetism*. Nature, 178, 1226–1227, 1956. 136, 137, 138, 172
- Ermakov, V. I., G. A. Bazilevskaya, P. E. Pokrevsky and Y. I. Stozhkov. *Ion balance equation in the atmosphere*. J. Geophys. Res., 102, 23413–23420, 1997. 88
- Ferreira, S. E. S., M. S. Potgieter and K. Scherer. *Transport and acceleration of anomalous cosmic rays in the inner heliosheath*. J. Geophys. Res., 112, 11101, 2007. 14
- Fichtner, H. and K. Scherer. *The heliosphere: a brief overview*. In: Scherer, K., Fichtner, H., Marsch, E. (Eds.), *The Outer Heliosphere: Beyond the Planets*, 1–11, 2000. 34
- Fichtner, H. *Anomalous Cosmic Rays: Messengers from the Outer Heliosphere*. Space Sci. Rev., 65, 639–754, 2001. 9
- Fichtner, H., B. Heber, K. Herbst, A. Kopp, K. Scherer. *Solar Activity, the Heliosphere, Cosmic Rays and Their Impact on the Earth's Atmosphere*. In: *Climate And Weather of the Sun-Earth System (CAWSES): Highlights from a priority program*, Springer, Ed.: F.-J. Lübken, Dordrecht, The Netherlands, 55–78, 2012. 55, 61, 87, 111
- Finlay, C. C. and the Working Group V-MOD. *International Geomagnetic Reference Field: the eleventh generation*. Geophys. J. Int., 183, 1216–1230, 2010. 18, 61, 197

- Fisk, L. A. and G. Gloeckler. *The acceleration of Anomalous Cosmic Rays by stochastic acceleration in the heliosheath*. Adv. Space Res., 43, 1471–1478, 2009. [9](#)
- Florinski, V., R. B. Decker and J. A. Le Roux. *Low-energy particle acceleration and compression at the termination shock and in the heliosheath*. In: American Institute of Physics Conference Series, volume 1039 of American Institute of Physics Conference Series, 361–366, 2008. [14](#)
- Folger, G., V. N. Ivanchenko and J. P. Wellisch. *The Binary Cascade - Nucleon nuclear reactions*. The Europ. Phys. J. A, 21, 407–417, 2004. [195](#)
- Forsyth, S. E. *On world-wide changes in cosmic-ray variations*. Phys. Rev., 54, 975–988, 1938. [122](#)
- Forsyth, R. J. *Ulysses and the Reversal of the Solar Magnetic Field*. [http : //www.sp.ph.ic.ac.uk/ forsyth/reversal/](http://www.sp.ph.ic.ac.uk/forsyth/reversal/). [9](#)
- Frisch, P. C. *The interstellar cloud surrounding the solar system*. In: Jokipii, J.R., Sonett, C.P., Giampapa, M.S. (Eds.), Cosmic Winds and the Heliosphere, University of Arizona Press, 733–758, 1997. [165](#)
- Frisch, P. C. and J. D., Slavin. *The Sun's journey through the local interstellar medium: the paleoLISM and paleoheliosphere*. Astrophys. and Space Sci. Trans., 2, 53–61, 2006. [165](#)
- Gaisser, T. K. and T. Stanev. *High-energy cosmic rays*. Nuc. Phys. A, 777, 98–110, 2006. [29](#)
- Garcia-Munoz, M., G. M. Mason and J. A. Simpson. *The anomalous  $^4\text{He}$  component in the cosmic-ray spectrum at  $\leq 50$  MeV per nucleon during 1972-1974*. Astrophys. J., 202, 265–275, 1975. [28](#), [29](#), [31](#), [32](#), [34](#), [41](#), [45](#), [47](#), [48](#), [49](#), [54](#), [75](#), [78](#), [134](#), [135](#), [136](#), [138](#), [142](#), [157](#), [159](#), [160](#), [161](#), [196](#)
- Gauß, C. F. *Allgemeine Theorie des Erdmagnetismus: Resultate aus den Beobachtungen des magnetischen Vereins im Jahre 1836*. Göttinger Magnetischer Verein, Leipzig, 1–52, 1863. [17](#), [197](#)
- Gleeson, L. J. and W. I. Axford. *Solar Modulation of Galactic Cosmic Rays*. Astrophys. J., 154, 1011–1026, 1968. [27](#)
- Goldhagen, P., J. M. Clem and J. W. Wilson. *Recent results from measurements of the energy spectrum of cosmic-ray induced neutrons aboard an ER-2 airplane and on the ground*. Adv. in Space Res., 32, 35–40, 2003. [77](#), [78](#), [79](#), [81](#), [82](#), [83](#), [84](#), [170](#)
- Griffin, J.J. and M. Dworzecka. *Classical wall formula and quantal one-body dissipation*. Nucl. Phys. A, 455, 61–99, 1986. [195](#)
- Grosse, A. *An unknown activity*. J. Am. Chem. Soc., 56, 1922–1924, 1934. [111](#)

- Harrison, R. G., K. L. Aplin and Y. Yair. *Planetary Atmospheric Electricity*. Space Sci. Rev., 125, 81–93, 2004. [87](#)
- Heber, B. et al. *Spatial variation of  $> 40$  MeV/n nuclei fluxes observed during the Ulysses rapid latitude scan*. Astron. Astrophys., 316, 538–546, 1996. [28](#)
- Heber, B. et al. *Modulation of Galactic Cosmic Ray Protons and Electrons During an Unusual Solar Minimum*. Astrophys. J., 699, 1956–1963, 2009. [12](#)
- Hedin, A. E. . *Extension of the MSIS thermosphere model into the middle and lower atmosphere*. J. Geophys. Res., 96, 1159–1172, 1991. [18](#), [199](#)
- Heikkilä, U., J. Beer and J. Feichter. *Modeling cosmogenic radionuclides  $^{10}\text{Be}$  and  $^7\text{Be}$  during the Maunder Minimum using the ECHAM5-HAM General Circulation Model*. Atmos. Chem. Phys., 8, 2797–2809, 2008. [117](#), [155](#), [164](#)
- Herbst, K. *Wechselwirkung der kosmischen Strahlung mit Erdatmosphäre, Marsatmosphäre und Marsboden*. Diploma thesis, 2007. [22](#)
- Herbst, K. et al. *On the importance of the Local Interstellar Spectrum for the Solar Modulation Parameter*. J. Geophys. Res., 115, D00I20, 2010. [11](#), [27](#), [30](#), [40](#), [41](#), [42](#), [43](#), [112](#), [142](#), [157](#), [160](#)
- Herbst, K., B. Heber, A. Kopp, O. Sternal and F. Steinhilber. *The Local Interstellar Spectrum Beyond the Heliopause: What can be Learned from Voyager in the Inner Heliosheath?*. Astrophys. J., 761, 17, 2012. [27](#), [33](#)
- Herbst, K., A. Kopp, B. Heber. *On the Influence of the Geomagnetic Field Geometry on the Propagation of Charged Energetic Particles*. to be submitted to Annales Geophys., 2012. [55](#)
- Herbst, K., B. Heber and J. Beer. *Modeling Global  $^{10}\text{Be}$  and  $^{14}\text{C}$  Production Rates During the Holocene*. in prep., 2012. [111](#)
- Hofmann, H. J. et al.  *$^{10}\text{Be}$ : half-life and AMS standards*. Nucl. Inst. Meth. Rhys. Res. B, 29, 32–36, 1987. [114](#)
- Hugen, K. A. et al. *MARINE04 marine radiocarbon age calibration, 0–26 CAL KYR BP*. Radiocarbon, 46, 1059–1086, 2004. [145](#), [162](#)
- Ivanchenko, V. N. et al. *Detector and event simulation in high energy physics*. Proc. of Int. Conf., 79–85, 1991. [194](#)
- Jacklyn, R. M. and A. G. Fenton. *Changes in the High-latitude East-West Asymmetry of Cosmic Rays*. Phys. Rev., 106, 1957. [72](#)
- Jan, S. et al. *GATE: a simulation toolkit for PET and SPECT*. Phys. Med. Biol., 49, 4543–4561, 2004. [193](#)

- Jiang, J., P. Chatterjee and A. R. Choudhuri. *Solar activity forecast with a dynamo model*. Mon. Not. R. Astron., 381, 1527–1542, 2007. [7](#)
- Jokipii, J. R., E. H. Levy and W. B. Hubbard. *Effects of particle drift on cosmic-ray transport. I. General properties, application to solar modulation*. Astrophys. J., 213, 861–868, 1977. [13](#), [14](#)
- Kaidalov, A. B., K. A. Ter-Martirosyan. *Pomeron as quark-gluon strings and multiple hadron production at SPS-Collider energies*. Phys. Lett. B, 117, 247–251, 1982. [195](#)
- Kallenrode, M. B. *Space Physics - An Introduction to Plasma and Particles in the Heliosphere and Magnetosphere*. Springer, Third Edition, 2004. [21](#)
- Kavaltsov, G. A. and I. G. Usoskin. *A new 3D numerical model of cosmogenic nuclide  $^{10}\text{Be}$  production in the atmosphere*. Earth and Planet. Sci. Lett., 291, 182–188, 2010. [119](#)
- Kavaltsov, G. A., A. Mishev and I. G. Usoskin. *A new model of cosmogenic production of radiocarbon  $^{14}\text{C}$  in the atmosphere*. Earth and Planet. Sci. Lett., 337–338, 114–120, 2012. [4](#), [113](#), [119](#), [134](#), [136](#), [137](#)
- Knudsen, M. F. et al. *Variations in the geomagnetic dipole moment during the Holocene and the past 50 kyr*. Earth and Planet. Sci. Lett., 272, 319–329, 2008. [113](#), [141](#), [142](#), [143](#), [144](#), [146](#), [148](#), [150](#), [151](#), [152](#), [153](#), [154](#), [155](#), [156](#), [160](#), [163](#), [172](#)
- Konradi, A., A. C. Hardy and W. Atwell. *Radiation environment models and the atmospheric cutoff*. J. Spacecraft and Rockets, 24, 284–285, 1987. [20](#)
- Koi, T. et al. *Interfacing the JQMD and JAM nuclear reaction codes to Geant4*. SLAC-PUB 9978, SLAC, 2008. [120](#), [135](#), [203](#)
- Kopp, A., I. Büsching, R. D. Strauss, and M. S. Potgieter. *A stochastic differential equation code for multidimensional Fokker-Planck type problems*. Comp. Phys. Comm., 183, 530–542, 2012. [36](#), [41](#), [209](#)
- Korschinek, G. et al. *A new value for the half-life of  $^{10}\text{Be}$  by heavy-ion elastic recoil detection and liquid scintillation counting*. Nucl Instrum Meth B, 268, 187–191, 2010. [114](#)
- Korschinek, G., C. Constable, F. Donadini and R. Holme. *Reconstructing the Holocene geomagnetic field*. Earth and Planet. Sci. Lett., 312, 497–505, 2011. [113](#), [148](#), [150](#), [151](#), [152](#), [153](#), [154](#), [155](#), [156](#), [160](#), [163](#), [172](#)
- Lal, D. and B. Peters. *Cosmic rays produced radioactivity on the Earth*. Handbuch der Physik, Springer, 551–612, 1967. [119](#), [134](#)
- Langel, R. A. *The main field*. Geomagnetism, 1, 249–512, 1987.

- Langner, U. W., M. S. Potgieter and W. R. Webber. *Modulation of cosmic ray protons in the heliosheath*. J. Geophys. Res., 108, A108039, 2003. [28](#), [29](#), [34](#), [41](#), [43](#), [45](#), [47](#), [48](#), [49](#), [78](#), [157](#), [159](#)
- Lassila-Perini, K. and L. Urban. *Energy loss in thin layers in GEANT*. Nucl. Instrum. Meth., A362, 416–422, 1995. [194](#)
- Leo, W. R. *Techniques for Nuclear and Particle Physics Experiments*. Springer, ISBN 3-540-57280-5, 1994. [21](#)
- Libby, W. *Atmospheric helium three and radiocarbon from cosmic radiation*. Phys. Rev., 69, 671–672, 1946. [111](#)
- Libby, W., E. C. Anderson, J. R. Arnold. *Age determination by radiocarbon content - world wide essay of natural radiocarbon*. Science, 109, 227–228, 1949. [111](#)
- Liu, Z. et al. *Measurement of Change of  $^7\text{Be}$  Decay Rate in Be and Au*. Chin. Phys. Lett., 30, 1–5, 2003. [114](#)
- Lowder, W. M., P. D. Raft and H. L. Beck. *Experimental determination of cosmic-ray charged particle intensity profiles in the atmosphere*. in Proceedings of the National Symposium on Natural and Manmade Radiation in Space, 908–913, 1972. [88](#), [90](#), [98](#), [99](#), [100](#)
- Marsh, N. D. and H. Svensmark. *Low Cloud Properties Influenced by Cosmic Rays*. Phys. Rev. Lett., 85, 23, 2000. [88](#)
- Masarik, J. and R. C. Reedy. *Terrestrial cosmogenic-nuclide production systematic calculated from numerical simulations*. Earth Planet. Sci. Lett., 136, 381–395, 1995.
- Masarik, J. and J. Beer. *Simulation of particle fluxes and cosmogenic nuclide production in the Earth's atmosphere*. J. Geophys. Res., 104, 12009–12111, 1999. [4](#), [24](#), [51](#), [113](#), [115](#), [119](#), [128](#), [130](#), [131](#), [134](#), [135](#), [136](#), [140](#), [141](#)
- Masarik, J. and J. Beer. *An updated simulation of particle fluxes and cosmogenic nuclide production in the Earth's atmosphere*. J. Geophys. Res., 114, D11103, 2009. [4](#), [43](#), [113](#), [119](#), [136](#), [142](#), [151](#)
- Matthiä, D., L. Sihver and M. Meier. *Monte-Carlo calculations of particle fluences and neutron effective dose rates in the atmosphere*. Radiation Protection Dosimetry, 131, 222–228, 2008. [75](#)
- Matthiä, D. *The Radiation Environment in the Lower Atmosphere - A Numerical Approach*. PhD thesis, Christian-Albrechts-Universität zu Kiel, Germany, 2009. [5](#), [75](#), [77](#), [78](#), [81](#), [82](#), [120](#), [162](#), [196](#)
- Matthiä, D., K. Herbst, B. Heber, T. Berger and G. Reitz.  *$^{10}\text{Be}$  Production in the Atmosphere by Galactic Cosmic Rays*. Space Sci Rev, DOI 10.1007/s11214-011-9817-5, 2011. [111](#), [119](#), [120](#), [122](#)

- McComas, D. J. et al. *Global Observations of the Interstellar Interaction from the Interstellar Boundary Explorer (IBEX)*. *Science*, 326, 959–962, 2009. 34
- McComas, D. J. et al. *The Heliosphere's Interstellar Interaction: No Bow Shock*. *Science*, 336, 1291–1293, 2012. 33, 34
- McCracken, K. G. and A. Fréon. *Asymptotic Directions and Cut-Off Rigidities in the Geomagnetic Field*. *J. Phys. Soc. of Japan Suppl.*, 17, 455–456, 1962. 58
- McCracken, K. G. *Geomagnetic and atmospheric effects upon the cosmogenic  $^{10}\text{Be}$  observed in polar ice*. *J. Geophys. Res.*, 109, A04101, 2004. 43
- McCracken, K. G., F. B. McDonald, J. Beer, G. Raisbeck and F. Yiou. *A phenomenological study of long-term cosmic ray modulation 850–1958 AD*. *J. Geophys. Res.*, 109, A12103, 2004. 112
- McCracken, K. G. and J. Beer. *Long-term changes in the cosmic ray intensity at Earth, 1428–2005*. *J. Geophys. Res.*, 112, A10101, 2007. 41
- McDonald, F. B. *Cosmic-Ray Modulation in the Heliosphere A Phenomenological Study*. *Space Sci. Rev.*, 83, 33–50, 1998. 34
- McPherson, G. J., G. R. Huss and A. M. Davis. *Extinct  $^{10}\text{Be}$  in Type A calcium-aluminium-rich inclusions from CV chondrites*. *Geochim. Cosmochim. Acta*, 67, 3165–3179, 2003. 114
- Michaelsen, J. *Geog.* 266, Spring 2010, Michaelsen Lectures. <http://www.geog.ucsb.edu/~joel>. 73
- Moraal, H., M. S. Potgieter, P. H. Stoker and A. J. van der Walt. *Neutron monitor latitude survey of cosmic ray intensity during the 1986/1987 solar minimum*. *J. Geophys. Res.*, 94, 1459–1464, 1989. 69
- Moraal, H. *Cosmic-Ray Modulation Equations*. *Space Sci. Rev.*, DOI 10.1007/s11214-011-9819-3, 2011. 27, 28
- Moskalenko, I. V., A. W. Strong, J. F. Ormes and M. S. Potgieter. *Secondary Antiprotons and Propagation of Cosmic Rays in the Galaxy and Heliosphere*. *Astrophys. J.*, 565, 280–296, 2002. 29
- Muller, R. A. *Radioisotope dating with a cyclotron*. *Science*, 196, 489, 489–494, 1977. 111
- Müller, D., S. P. Swordy, P. Meyer, J. L. L'Heureux and J. M. Grunsfeld. *Energy Spectra and Composition of Primary Cosmic Rays*. *Astrophys. J.*, 374, 356–365, 1991. 11
- Neher, H. V. *Cosmic-Ray Particles That Changed from 1954 to 1958 to 1965*. *J. Geophys. Res.*, 72, 1527–1539, 1967. 88, 90, 101, 102, 103, 104, 171, 175

- Neher, H. V. *Cosmic rays at high latitudes and altitudes covering four solar maxima*. J. Geophys. Res., 76, 1637–1651, 1971. [88](#), [90](#), [98](#), [99](#), [100](#), [101](#), [171](#)
- Nelson, W. R., H. Hirayama and D. W. Rogers. *The egs4 code system*. SLAC-PUB, Stanford Linear Accelerator Center, 1985. [89](#), [193](#)
- Nir, A., S. T. Kruger, R. E. Lingenfelder and E. J. Flamm. *Natural tritium*. Rev. Geophys., 4, 441–456, 1966. [113](#), [117](#)
- Nishiizumi, K., M. Imamura, M. W. Caffee, J. R. Southon, R. C. Finkel and J. McAninch. *Absolute calibration of Be-10 AMS standards*. Nucl. Instr. Meth. Phys. Res. B, 358, 403–414, 2007. [114](#)
- O'Brien, K. *Secular variations in the production of cosmogenic isotopes in the Earth's atmosphere*. J. Geophys. Res., 84, 423–431, 1979. [135](#)
- Oeschger, H., J. Houtermann, H. Loosli, and M. Wahlen. *The constancy of cosmic radiation from isotope studies in meteorites and on the Earth*. In: Radiocarbon Variations and Absolute Chronology: Proceedings of the Twelfth Nobel Symposium Held at the Institute of Physics at Uppsala University, edited by I. U. Olsen, Wiley-Interscience, 64–78, 1970. [135](#)
- Oeschger, H., U. Siegenthaler, U. Schotterer, and A. Gugelmann. *A box diffusion model to study the carbon dioxide exchange in nature*. Tellus, 27, 168–192, 1975. [1](#), [145](#), [162](#)
- Parker, E. N. *The passage of energetic charged particles through interplanetary space*. Planet. Space Sci., 13, 9–49, 1965. [13](#), [34](#), [36](#)
- Phillips, F. M., W. D. Stone, J. T. Fabryka-Martin. *An improved approach calculating low-energetic cosmic ray neutron fluxes near the land/atmospheric interface*. Chem. Geol., 175, 689–701, 2001. [113](#)
- Picone, J. M., A. E. Hedin, D. P. Drob and A. C. Aikin. *NRLMSISE-00 empirical model of the atmosphere: Statistical comparisons and scientific issues*. J. Geophys. Res., 107, A12, 2002. [18](#), [199](#)
- Pilchowski, J., A. Kopp, K. Herbst, and B. Heber. *On the definition and calculation of a generalised McIlwain parameter*. Astrophys. and Space Science Trans., 6, 9–17, 2010. [17](#), [58](#), [60](#), [61](#), [136](#), [162](#)
- Porter, H. S., C. H. Jackman and A. E. S. Green. *Efficiencies for production of atomic nitrogen and oxygen by relativistic proton impact in air*. J. Chem. Phys., 167, 154–167, 1976. [89](#)
- Potgieter, M. S. and H. Moraal. *A drift model for the modulation of galactic cosmic rays*. Astrophys. J., 294, 425–440, 1985. [13](#)



- Potgieter, M. S. and J. A. le Roux. *The simulated features of heliospheric cosmic-ray modulation with a time-dependent drift model. I - General effects of the changing neutral sheet over the period 1985-1990.* *Astrophys. J.*, 386, 336–346, February 1992. [13](#)
- Potgieter, M. S. *Heliospheric modulation of galactic electrons: Consequences of new calculations for the mean free path of electrons between 1 MeV and  $\sim 10$  GeV.* *J. Geophys. Res.*, 101, 24411–24422, 1996. [36](#), [209](#)
- Potgieter, M. S. and S. E. S. Ferreira. *Modulation of cosmic rays in the heliosphere over 11 and 22 year cycles: a modelling perspective.* *Adv. Space Res.*, 27, 3, 481–492, 2001. [13](#)
- Potgieter, M. S. *Cosmic Rays in the Inner Heliosphere: Insights from Observations, Theory and Models.* *Adv. Space Res.*, 22, 2011. [34](#)
- Prentice, I. C. et al. *The carbon cycle and atmospheric carbon dioxide.* In: *Climate change 2001: the scientific basis: contribution of Working Group I to the Third Assessment Report of the Intergovernmental Panel on Climate Change / Houghton, J.T. [edit.]*, Cambridge: Cambridge University Press, 183–237, 2001. [117](#)
- Regener, E. R. A. and J. G. Pfozter. *Vertical Intensity of Cosmic Rays by Threefold Coincidences in the Stratosphere.* *Nature*, 136, 718–719, 1935. [88](#)
- Reimer, P. J. et al. *INTCAL09 and MARINE09 Radiocarbon age Calibration Curves, 0–50,000 YEARS CAL BP.* *Radiocarbon*, 51, 4, 1111–1150, 2009. [1](#), [113](#), [145](#), [148](#), [149](#), [150](#), [151](#), [152](#), [153](#), [157](#), [162](#), [172](#)
- Roeckner, E. et al. *The atmospheric general circulation model ECHAM5 - Part 1: Model description.* *Reports of the Max-Planck-Institute for Meteorology*, 349, 1, 2003. [164](#)
- Rosen, J. M., D. J. Hofmann and W. Gringel. *Measurements of ion mobility to 30 km.* *J. Geophys. Res.*, 90, 5876–5884, 1985. [88](#)
- Russell, C. T. and J. G. Luhmann. *EARTH: MAGNETIC FIELD AND MAGNETOSPHERE.* In: *Encyclopedia of Planetary Science*, Chapman and Hall, Ed.: J. H. Sirely and R. W. Fainbridge, New York, 208–211, 1997. [15](#)
- Sanuki, T. et al. *Measurement of cosmic-ray proton and antiproton spectra at mountain altitude.* *Phys. Letters B*, 577, 10–17, 2003. [81](#), [82](#), [85](#), [170](#)
- Scherer, K. and S. E. S. Ferreira. *A heliospheric hybrid model: hydrodynamic plasma flow and kinetic cosmic ray transport.* *Astrophys. Space Sci. Trans.*, 1, 17–27, 2005. [14](#), [165](#)

- Scherer, K. et al. *Interstellar-Terrestrial Relations: Variable Cosmic Environments, the Dynamic Heliosphere, and Their Imprints on Terrestrial Archives and Climate*. *Space Sci. Rev.*, 127, 327–465, 2006. [34](#), [41](#), [58](#), [164](#)
- Scherer, K., H. Fichtner, S. E. S. Ferreira, I. Büsching and M. S Potgieter. *Are Anomalous Cosmic Rays the Main Contribution to the Low-Energy Galactic Cosmic Ray Spectrum?*. *Astrophys. J. Lett.*, 680, 105–108, 2008. [165](#), [168](#)
- Scherer, K., H. Fichtner, R. D. Strauss, S. E. S. Ferreira, M. S Potgieter and H. J. Fahr. *On Cosmic Ray Modulation Beyond the Heliopause: Where is the Modulation Boundary?*. *Astrophys. J.*, 735, 128–133, 2011. [30](#), [33](#), [35](#), [36](#), [41](#), [161](#), [209](#)
- Shaviv, N. J. *The spiral structure of the Milky Way, cosmic rays, and ice age epochs on Earth*. *New Astron.*, 8, 39–77, 2003. [164](#), [165](#), [166](#), [172](#)
- Shea, M. A. and D. F. Smart. *On the application of trajectory-derived cutoff rigidities to cosmic ray intensity variations*. *Acta Physica*, 29, 533–537, 1970 [58](#)
- Simpson, J. A. *Elemental and Isotopic Composition of the Galactic Cosmic Rays*. *Annual Rev. of Nucl. and Particle Sci.*, 33, 323–382, 1983. [10](#)
- Simpson, J. A. *The Cosmic Ray Nucleonic Component: The Invention and Scientific Uses of the Neutron Monitor*. *Space Sci. Rev.*, 93, 11–32, 2000. [10](#), [23](#), [65](#)
- Sinnhuber, M., N. Wieters and H. Winkler. *The impact of energetic particle precipitation on the chemical composition of the middle atmosphere: measurements and model predictions*. In: *Climate And Weather of the Sun-Earth System (CAWSES): Highlights from a priority program*, Springer, Ed.: F.-J. Lübken, Dordrecht, The Netherlands, 275–299, 2012. [10](#)
- Smart, D. F. and M. A. Shea. *A review of geomagnetic cutoff rigidities for earth-orbiting spacecraft*. *Adv. Space Res.*, 36, 2012–2020, 2005. [56](#), [59](#)
- Smart, D. F. and M. A. Shea. *Fifty years of progress in geomagnetic cutoff rigidity determinations*. *Adv. Space Res.*, 44, 1107–1123, 2009. [57](#)
- Snowball, I. and R. Muscheler. *Paleomagnetic intensity data: an Achilles heel of solar activity reconstructions*. *The Holocene*, 17, 851–859, 2007. [52](#)
- Steinhilber, F., J. A. Abreu and J. Beer. *Solar modulation during the Holocene*. *Astrophys. Space Sci. Trans.*, 4, 1–6, 2008. [3](#), [50](#), [51](#), [53](#), [54](#), [112](#), [157](#), [161](#)
- Steinhilber, F., J. A. Abreu, J. Beer and K. G. McCracken. *Interplanetary magnetic field during the past 9300 years inferred from cosmogenic radionuclides*. *J. Geophys. Res.*, 115, A01104, 2010. [112](#)
- Steinhilber, F. *Reconstruction of Solar Activity during the Holocene using the Cosmogenic Radionuclide Beryllium-10*. PhD thesis, ETH Zürich, Switzerland, 2010. [114](#)

- Steinhilber et al. *9,400 years of cosmogenic radiation and solar activity from ice cores and tree rings*. *Earth, Atm. and Planet. Sci.*, 109, 5967–5971, 2012. [141](#), [142](#), [143](#), [144](#), [146](#), [151](#), [154](#), [172](#)
- Sternal et al. *Possible Evidence for a Fisk-type Heliospheric Magnetic Field. I. Analyzing Ulysses/KET Electron Observations*. *Astrophys. J.*, 741, 23, 2011. [36](#)
- Stier, P., J. Feichter and S. Kinne. *The evolution of the global aerosol system in a transient climate simulation from 1860 to 2100*. *Atmosph. Chem. and Phys.*, 5, 1125, 2005. [164](#)
- Stone, E. C., A. C. Cummings, F. B. McDonald, B. C. Heikkila, N. Lal and W. R. Webber. *Voyager 1 Explores the Termination Shock Region and the Heliosheath Beyond*. *Science*, 309, 2017–2020, 2005. [35](#)
- Stone, E. C., A. C. Cummings, F. B. McDonald, B. C. Heikkila, N. Lal and W. R. Webber. *An asymmetric solar wind termination shock*. *Nature*, 454, 71–74, 2008. [35](#)
- Størmer, C. *The Polar Aurora*. Clarendon Press, Oxford, 1955. [56](#)
- Strauss, R. D., M. S. Potgieter, A. Kopp and I. Büsching. *On the propagation times and energy losses of cosmic rays in the heliosphere*. *J. Geophys. Res.*, 116, 12105, 2011. [36](#), [41](#), [209](#)
- Stuiver, M. and T. F. Braziunas. *Modeling atmospheric  $^{14}\text{C}$  influences and  $^{14}\text{C}$  ages of marine samples to 10,000 BC*. *Radiocarbon*, 35, 137–189, 1993. [1](#), [145](#)
- Suess, H. E. *Radiocarbon Concentration in Modern Wood*. *Science*, 122, 415–417, 1955. [141](#)
- Sugiura, M. and T. Kamei. *IAGA Bulletin*, 40, 1991. [198](#)
- Urban, L. *Multiple scattering model in Geant4*. CERN-OPEN-2002-070, 2002. [194](#)
- Usoskin, I. G., K. Mursula, S. K. Solanki, M. Schüssler and K. Alanko. *Reconstruction of solar activity for the last millennium using  $^{10}\text{Be}$  data*. *Astron. and Astrophys.*, 413, 745–751, 2004. [119](#)
- Usoskin, I. G. and B. Kromer. *Reconstruction of the  $^{14}\text{C}$  Production Rate From Measured Relative Abundance*. *Radiocarbon*, 47, 31–37, 2005. [3](#)
- Usoskin, I. G., K. Alanko-Huotari, G. A. Kovaltsov and K. Mursula. *Heliospheric modulation of cosmic rays: Monthly reconstruction for 1951-2004*. *J. Geophys. Res.*, 110, A12108, 2005. [28](#), [29](#), [30](#), [31](#), [32](#), [34](#), [41](#), [42](#), [43](#), [44](#), [45](#), [50](#), [78](#), [81](#), [95](#), [102](#), [124](#), [126](#), [134](#), [135](#), [136](#), [137](#), [138](#), [142](#), [159](#), [165](#), [166](#), [167](#), [168](#), [169](#), [173](#)
- Usoskin, I. G. and G. A. Kovaltsov. *Cosmic ray induced ionization in the atmosphere: Full modeling and practical applications*. *J. Geophys. Res.*, 111, D21206, 2006. [87](#), [88](#), [89](#), [90](#), [91](#), [92](#), [93](#), [94](#), [99](#), [100](#), [101](#), [170](#), [171](#)

- Usoskin, I. G., G. A. Kovaltsov and I. A. Mironova. *Cosmic ray induced ionization model CRAC:CRII: An extension to the upper atmosphere*. J. Geophys. Res., 115, D10302, 2010 [88](#), [89](#), [93](#), [95](#), [97](#)
- Usoskin, I. G., G. A. Brazlevskaia and G. A. Kovaltsov. *Solar modulation parameter for cosmic rays since 1936 reconstructed from ground-based neutron monitors and ionization chambers*. J. Geophys. Res., 116, A02104, 2011 [69](#), [78](#), [80](#), [95](#), [102](#), [107](#), [109](#), [110](#), [138](#), [155](#), [157](#), [158](#), [159](#), [172](#)
- Velinov, P. I. Y and L. N. Mateev. *Analytical approach for cosmic ray proton ionization in the lower ionosphere and middle atmosphere*. C. r. Acad. bulg. Sci., 58, 511–516, 2005. [89](#)
- Velinov, P. I. Y and L. N. Mateev. *Improved cosmic ray ionization model for the system ionosphere-atmosphere. Calculation of electron production rate profiles*. J. Atmos. Solar-Terr. Phys., DOI:10.1016/j.jastp.2007.08.049, 2007. [89](#)
- Velinov, P. I. Y, A. Mishev and L. Mateev. *Model for induced ionization by galactic cosmic rays in the Earth atmosphere and ionosphere*. Adv. Space Res., 44, 1002–1007, 2009. [89](#), [90](#), [91](#), [92](#), [93](#)
- Villoresi G. et al. *Latitude Survey of Cosmic Ray Nucleonic Component (Italy-Antarctic, 1996-1997)*. Proc. 25th Int. Cosmic Ray Conf., Durban 2, 421, 1997. [69](#), [70](#), [170](#)
- Vitt, F. M. and C. H. Jackman. *A comparison of sources of odd nitrogen production from 1974 through 1993 in the Earth's middle atmosphere as calculated using a two-dimensional model*. J. Geophys. Res., 101, 6729–6740, 1996. [88](#)
- Vonmoos, M., J. Beer and R. Muscheler. *Large variations in Holocene solar activity: Constraints from  $^{10}\text{Be}$  in the Greenland Ice Core Project ice core*. J. Geophys. Res., 111, A10105, 2006. [50](#), [52](#), [53](#), [54](#), [112](#), [155](#)
- Vonmoos, M. *Rekonstruktion der solaren Aktivität im Holozän mittels Beryllium-10 im GRIP Eisbohrkern*. PhD thesis, ETH Zürich, Switzerland, 2005. [115](#)
- Wagner, G. et al. *Reconstruction of the geomagnetic field between 20 and 60 kyr BP from cosmogenic radionuclides in the GRIP ice core*. Nuc. Instr. Methods in Phys. Res. B, 172, 597–604, 2000. [112](#)
- Webber, W. R. and J. A. Lockwood. *Voyager and Pioneer spacecraft measurements of cosmic ray intensities in the outer heliosphere: Toward a new paradigm for understanding the global solar modulation process: 1. Minimum solar modulation (1987 and 1997)*. J. Geophys. Res., 106, 29323-29332, 2001. [29](#)
- Webber, W. R. and J. A. Lockwood. *Voyager and Pioneer spacecraft measurements of cosmic ray intensities in the outer heliosphere: Toward a new paradigm for understanding the global modulation process: 2. Maximum solar modulation (1990-1991)* J. Geophys. Res., 106, 29333-29340, 2001. [29](#)

- Webber, W. R. and P. R. Higbie. *Production of cosmogenic Be nuclei in the Earth's atmosphere by cosmic rays: Its dependence on solar modulation and the interstellar cosmic ray spectrum*. J. Geophys. Res., 108, A91355, 2003. [28](#), [29](#), [31](#), [32](#), [34](#), [35](#), [41](#), [45](#), [47](#), [48](#), [50](#), [78](#), [113](#), [115](#), [119](#), [128](#), [130](#), [131](#), [134](#), [135](#), [136](#), [140](#), [141](#), [157](#), [159](#), [160](#), [161](#), [169](#)
- Webber, W. R., P. R. Higbie and K. G. McCracken. *Production of the cosmogenic isotopes  $^3\text{H}$ ,  $^7\text{Be}$ ,  $^{10}\text{Be}$ , and  $^{36}\text{Cl}$  in the Earth's atmosphere by solar and galactic cosmic rays*. J. Geophys. Res., 112, A10106, 2007. [4](#), [163](#)
- Webber, W. R. and P. R. Higbie. *Galactic propagation of cosmic ray nuclei in a model with an increasing diffusion coefficient at low rigidities: A comparison of the new interstellar spectra with Voyager data in the outer heliosphere*. J. Geophys. Res., 114, A02103, 2009. [28](#), [30](#), [31](#), [32](#), [33](#), [35](#), [38](#), [39](#), [40](#), [41](#), [45](#), [47](#), [48](#), [50](#), [78](#), [81](#), [134](#), [135](#), [157](#), [160](#), [161](#), [162](#)
- Webber, W. R. and P. R. Higbie. *What Voyager cosmic ray data in the outer heliosphere tells us about  $^{10}\text{Be}$  production in the Earth's polar atmosphere in the recent past*. J. Geophys. Res., 115, A05102, 2010. [30](#), [119](#)
- Wefel, F. *Cosmic rays, supernovae and the interstellar medium*. NATO ASIC Series, 337, 1991. [10](#), [11](#)
- Wicht, J., S. Stellmach, and H. Harder. *Numerical models of the geodynamo: From fundamental Cartesian models to 3D simulations of field reversals*. In: Geomagnetic Variations, Springer, 107–158, 2009. [14](#)
- Wiebel-Sooth, B., P. L. Biermann, and H. Meyer. *Cosmic Rays VII. Individual element spectra: prediction and data*. Astron. Astrophys., 330, 389–398, 1998. [10](#)
- Yang, S., H. Odah, and J. Shaw. *Variations in the geomagnetic dipole moment over the last 12000 years*. Geophys. J. Int., 140, 158–162, 2000. [163](#)



# GEANT4 and PLANETOCOSMICS

---

## A.1 The GEANT4 toolkit

GEANT4 is a C<sup>++</sup>-based Monte Carlo simulation toolkit (see e.g. [Agostinelli et al., 2003](#); [Allison et al., 2006](#); [Apostolakis et al., 2009](#)) which can be implemented in multiple settings and simulation codes like e.g. that used in this work, PLANETOCOSMICS. For further information on the Monte Carlo Method (see e.g. [Nelson et al., 1985](#); [Binder and Heermann, 2010](#)).

The GEANT4 toolkit provides the possibility to simulate the transport of particles through as well as their interaction within a certain medium such as the Earth's atmosphere (see e.g. [Apostolakis et al., 2009](#)). Because of its numerous applications GEANT4 has been established in multiple communities such as the large hadron collider community, in high-energy physics as well as in the medical physics branch (see e.g. [Jan et al., 2004](#); [Amko et al., 2005](#); [Allison et al., 2006](#)).

The main applications of GEANT4 are:

1. the description of an experimental setup by user-defined geometrical volumes
2. the transport of particles through this setup
3. the simulation of particle interaction and events by Monte-Carlo based generators
4. the visualization of the user-defined setup as well as the particle trajectories through the setup

In order to compute the interaction of primary particles with the Earth's atmosphere PLANETOCOSMICS selects from the physical processes embedded in the GEANT4 toolkit: a) decay processes, b) electromagnetic processes, c) hadronic processes, d) photoelectron-hadron processes, e) optical processes, f) parameterization processes and g) transportation processes. Of great importance for this work are the electromagnetic as well as the hadronic processes, which therefore will be described further. A more detailed investigation of the two electromagnetic sub-packages can be found at <http://GEANT4.web.cern.ch/GEANT4/support/userdocuments.shtml>.

## The Electromagnetic Physics Packages

In order to simulate the electromagnetic (em) interactions of charged particles as well as photons with the surrounding material GEANT4 provides two sub-packages, the standard em package and the low-energy em package.

**The Standard em Package** allows for computations of the atmospheric ionization,  $\gamma$ -conversion, bremsstrahlung etc. due to electromagnetic interactions (see [Lassila-Perini and Urban, 1995](#); [Apostolakis et al., 2000](#); [Urban, 2002](#)). This package, however, merely averages the influences and effects of atomic shell structures, so that the electromagnetic interaction simulations are restricted to particles within the energy range of 1 keV to 10 PeV. Nevertheless, the standard em package nowadays is established especially in high-energy physics as well as space and medical physics.

**The Low Energy em Package** provides alternative models in order to simulate interaction of photons as well as charged particles down to energies of 100 eV (see e.g. [Chauvie et al., 2004](#); [Amko et al., 2005](#)). This package also includes models for the computation of atomic relaxation and other shell effects (see [Chauvie et al., 2007](#)). Because of the additionally implemented features one of the disadvantages of this package is the strong increase in CPU time.

However, the most important development to former GEANT versions is the implementation of an integral sampling approach in order to compute the particle interaction length. To take into account the energy dependence of electromagnetic cross sections the probability  $p$  for an interaction is sampled and is given by

$$p = 1 - \exp\left(-\int \sigma(E)n dx\right), \quad (\text{A.1})$$

where  $\sigma(E)$  represents the energy-dependent cross section,  $n$  gives the atomic density and  $x$  describes the arc length along the trajectory (see [Apostolakis et al., 2009](#)). In this process the sampling is performed by using the approach first described by [Ivanchenko et al. \(1991\)](#). According to [Apostolakis et al. \(2009\)](#) before each step the energy range dependent maximum cross section  $\sigma_{\max}$  in the energy range  $(\eta E_0 - E_0)$  is estimated. Thereby the parameter  $\eta = 1 - \alpha$  with a default value of 0.8 while  $E_0$  represents the energy at the beginning of the step. After the first step the energy has changed, thus the energy-dependent cross section  $\sigma(E_1)$  has to be calculated. The sampling of the final state of the first step therewith is performed randomly with a certain probability given by

$$p_s = \frac{\sigma(E_1)}{\sigma_{\max}}. \quad (\text{A.2})$$

Unfortunately, due to the increase of computation time this method is not performed for every step along the trajectory of the investigated particle.



## The Hadronic Physics Packages

The GEANT4 toolkit provides several packages to simulate hadronic interaction, which strongly depend on the energy range of interest. In order to compute highly energetic particle interaction, which are of great importance for this work, the GEANT4 collaboration offers a standard set of models including

- a) **The quark-gluon string (QGS) model:** This model provides the possibility to simulate the interaction of protons, neutrons, pions as well as kaons in the energy range of 20–50 TeV. The QGS model is able to provide the physical necessities to a) compute the splitting of nucleons into quarks as well as di-quarks and b) the formation and excitation of quark-gluon strings. In order to take into account the formation of strings the model uses the approach by [Capella and Krzywicki \(1978\)](#) and [Kaidalov and Ter-Martirosyan \(1982\)](#). According to [Apostolakis et al. \(2009\)](#) the simulations using this model are in good agreement to the available experimental data.
- b) **The Bertini-style cascade model:** The Bertini model describes hadronic interaction using the standard intra-nuclear cascade application by [Bertini and Guthrie \(1971\)](#), covering the simulation of hadronic interaction for protons, neutrons, pions, kaons and hyperons with energies up to 10 GeV. In case of a collision an excited residual nucleus is built by creating multiple particle-hole states. In order to destroy them and to de-excite the residual nucleus afterwards the [Griffin and Dworzecka \(1986\)](#) approach is applied.
- c) **The Binary cascade (BIC) model:** The BIC model is a combination of a classical cascade model and a full quantum-molecular dynamics model, which is able to cover particle energies up to 10 GeV (see [Folger et al., 2004](#)). Note that thereby only incident protons and neutrons in the energy range below 3 GeV are simulated so that incident particles and the resulting subsequent secondaries for particles with higher energy are propagated by a numerical integration of the equation of motion in a potential. The cascade stops when the mean energy of all scattered particles is below an energy between 18 – 90 MeV (see [Apostolakis et al., 2009](#)).

The latter two hadronic cascade models, the BIC and the Bertini model are used to estimate the uncertainties of the processes involved, when calculating the production of secondary particles (see Chapter 5) as well as the atmospheric ionization (see Chapter 6). Note, however, that the GEANT4 collaboration proposes the usage of the Bertini-style cascade for high energetic particle interactions while the BIC model should be used for particles with energies below 1 GeV.

## A.2 The PLANETOCOSMICS Code

The PLANETOCOSMICS simulation code (see e.g. [Desorgher, 2006](#)), a GEANT4-based Monte-Carlo package which also can be found at

<http://cosray.unibe.ch/~laurent/planetocosmics/>, was developed by combining and upgrading the two already existing codes MAGNETOCOSMICS and ATMOCOSMICS, providing the possibility to

- a. Compute the cut-off rigidity as function of position, direction, and time (see Section 4.1).
- b. Compute asymptotic directions (see Section 4.3).
- c. Visualize particle trajectories and magnetic field lines.
- d. Compute the resulting flux of atmospheric-shower particles at user-defined altitudes and/or depths (see Section 5) and therewith e.g. the production of cosmogenic radionuclides (see Chapter 7).
- e. Simulate the energy being deposited in the atmosphere vs altitude and/or depth (see Section 6).

In the following, a short overview of the magnetospheric and atmospheric models, which are available in the PLANETOCOSMICS code, is given together with details of the configurations used in order to provide the results of this work will be presented in addition.

### The Primary Particle Spectra

In order to compute the secondary particle production in the Earth's atmosphere it is necessary to define a primary particle spectrum at 1 AU. This can either be done by choosing the built-in modulated galactic cosmic ray spectrum by [Garcia-Munoz et al. \(1975\)](#), by defining an arbitrary galactic cosmic ray spectrum as well as a solar energetic particle spectrum as input files or by simulating mono-energetic primary particles and their contribution to the interaction with the magnetosphere as well as the atmosphere and convolve the results with a certain local interstellar spectrum afterwards. The latter method is employed in this work and will be discussed in more detail in Section 5.

### The Geometry of the Simulation Volume

The user can select between a spherical shell structure or a flat geometry arranged in layers of equal pressure, temperature and composition in order to set the simulation environment. However, a comparison of the model results using a spherical geometry and a flat geometry shows that there are only small variations between the two models. As pointed out by [Matthiä \(2009\)](#), these variations occur due to differences in the particles path lengths, showing the variation to be in the order of 1% for particles with a zenith incidence angle of  $40^\circ$  and of about 4% for particles with zenith incidence angle around  $70^\circ$ , respectively. The influence of this effect was shown to be negligible for the secondary particle intensities produced in the Earth's atmosphere ([Matthiä, 2009](#)). For all investigations of this work, thus a flat geometry is adopted.

## The Magnetospheric Models

PLANETOCOSMICS provides different models to describe the internal terrestrial magnetic field as well as the influence of the external magnetic field. For both magnetic field configurations three models are available.

### 1. The Internal Magnetic Field

#### a) Dipole field

Using this magnetic field model the user is able to vary the strength of the dipole field  $B_0$ , the tilt angle of the dipole field  $\varphi$  and the position of the center of the dipole with respect to the center of the Earth.

#### b) Eccentric tilted dipole

In contrast to the simple dipole model the eccentric tilted dipole model includes the temporal evolution of the magnetic field while neglecting higher moments.

#### c) IGRF field

As mentioned in Section 2.3 the IGRF is a geomagnetic field model provided by the International Association of Geomagnetism and Aeronomy (IAGA). The IGRF is a series of mathematical models which describe the Earth's internal field and its secular variation (see e.g. [Gauß, 1863](#); [?](#)). According to Eq.(2.3) the internal magnetic field can be described as the negative gradient of the scalar potential  $V(r, \vartheta, \varphi, t)$  given by

$$V(r, \vartheta, \varphi, t) = r_0 \sum_{n=1}^{\infty} \sum_{m=0}^n \left(\frac{r_0}{r}\right)^{n+1} (g_n^m(t) \cos m\varphi + h_n^m(t) \sin m\varphi) P_n^m(\cos \vartheta), \quad (\text{A.3})$$

with  $r$  representing the Earth's radius,  $\vartheta$  the zenith angle,  $\varphi$  the azimuthal angle,  $g_n^m(t), h_n^m(t)$  the Gauss spherical harmonic coefficients and their linear interpolation as well as  $P_n^m$  the Legendre Polynomials. Every five years a new set of Gauss parameters is released. By now the eleventh generation of the IGRF is available ([Finlay et al., 2010](#)), providing the opportunity to reconstruct the magnetic field variations from 1900 to 2011.

If not stated otherwise this work utilizes the IGRF model in order to compute the internal magnetic field.

### 2. The External Magnetic Field

While the internal magnetic field represents the undisturbed isolated magnetic field within the first six Earth radii the external magnetic field is disturbed by the

interaction with the solar wind.

Here the user has the possibility to choose between three models developed by Nicolai Tsyganenko (*Tsy89*, *Tsy96* and *Tsy2001*, see <http://geo.phys.spbu.ru/~tsyganenko/modeling.html> which are based on a large number of satellite observations (e.g. IMP, POLAR and GOES). These models are semi-empirical best-fit representations of the Earth's magnetic field, including contributions of the ring current system, magnetotail current system, magnetopause current system and the large-scale system of field-aligned currents.

a) *Tsy89*

The *Tsy89* model was primarily developed as a simple empirical approximation for the global magnetosphere, binned into several intervals of the disturbance index Kp. Variations of the Kp index are only due to disturbances of the geomagnetic field caused by the solar wind within a three hour interval. The geomagnetic disturbances are monitored by at least thirteen satellite stations at an altitude of 70  $R_E$ . Thus, the global Kp index can be obtained as the mean value of the disturbance levels in the two horizontal field components measured at these stations. For further information see <http://wwwuser.gwdg.de/~rhennin/kp.html>.

b) *Tsy96*

The *Tsy96* model includes magnetopause, large-scale Birkeland current systems, and heliospheric magnetic field reconnection across the boundary. The model is parameterized by the solar wind pressure  $P_{dyn} = \frac{1}{2}n \cdot v^2$  with  $n$  the solar wind particle number density and  $v$  the solar wind speed. An additional parameter introduced in this model is the so-called Disturbance storm time (Dst) index, defined as the disturbance field axially symmetric with respect to the dipole axis as a function of storm-time (see e.g. Sugiura and Kamei, 1991), which shows negative values caused by the ring current, while positive variations are mostly caused by the compression of the magnetosphere from a solar wind pressure increase and the transverse components of the heliospheric magnetic field (see Sugiura and Kamei, 1991).

c) *Tsy2001*

The *Tsy2001* model represents the mathematical form of a variable configuration of individual inner and near magnetosphere current systems for different interplanetary conditions and ground disturbance levels. This model was adjusted by the observed dawn-dusk asymmetry of the inner magnetosphere due to the partial ring current that develops during magnetospheric disturbances. Therefore data from a large number of spacecraft have been used to define the new parameters of the model. In general the *Tsy2001* model, like the *Tsy96* model is defined by the input parameters a) solar wind dynamic pressure, b) solar wind speed and c) Dst index. Additionally this model also takes into account the interplanetary magnetic field.

### Atmospheric Models

Implemented in PLANETOCOSMICS are three different possibilities to define the terrestrial atmosphere. While the two empirical atmospheric models, the MSISE90 model (see [Hedin, 1991](#)) and the upgraded version NRLMSISE00 (see [Picone et al., 2002](#)) are fully implemented, a user-defined atmosphere can be put into the PLANETOCOSMICS code as well.

If not stated otherwise the NRLMSISE00 model is used to define the atmospheric conditions.

### Hadronic Interaction

In order to simulate the hadronic interactions of primary particles with the ambient atmospheric matter PLANETOCOSMIC provides multiple GEANT4 models (see [Section A.1](#)). For the purpose of this work the GEANT4 collaboration suggests either to use the QGSP\_BIC\_HP model or the QGSP\_BERT\_HP model.

For the investigation of the secondary particle environment (see [Chapter 5](#)) as well as the cosmic ray induced ionization (see [Chapter 6](#)) the BIC and Bertini model are used which reveal that the Bertini model is the better choice in order to compute the production of the cosmogenic radionuclides (see [Chapter 7](#)).

### Electromagnetic Interaction

The electromagnetic interactions can either be calculated by using the GEANT4 low energy em model or the GEANT4 standard em model.

In this work the GEANT4 standard em model is applied.

### Composition of the Soil

PLANETOCOSMICS provides the possibility to define composition and thickness of the Earth's soil, where the composition of the soil plays an important role, due to albedo particles a) produced by the interaction of produced secondary particles with the soil itself or b) by back-scattered incoming particles.



# PLANETOCOSMICS - Macro File Examples

---

## B.1 Computation of the Vertical Cutoff Rigidity Distribution

An exemplary macro of the computation of vertical cutoff rigidities at an altitude of 200 km on March 15<sup>th</sup> 2005. The computations are performed for the IGRF field.

```
/tracking/verbose 0
/tracking/storeTrajectory 0
/control/verbose 1
/run/verbose 0
/control/verbose 1

#
# Geometry and physics
#

/PLANETOCOS/SPACECOORDINATE/UseSpice true
/PLANETOCOS/GEOMETRY/SetConsiderAtmosphere false

/PLANETOCOS/PHYSICS/SelectTypeOfEMPhysics NONE
/PLANETOCOS/PHYSICS/SelectTypeOfHadronicPhysics NOHADRONIC
/PLANETOCOS/Initialise

/PLANETOCOS/USERLIMIT/SetMagnetoMaxStepLength .1 rplanet
/PLANETOCOS/STOPCONDITION/SetMaxTrackLength 70. rplanet

#
# Step length definition
#

/PLANETOCOS/INTEGRATION/SetStepperModel CashKarpRKF45
/PLANETOCOS/INTEGRATION/SetPrecision 1e-6
/PLANETOCOS/INTEGRATION/SetG4MaxStep 5e-2 rplanet
/PLANETOCOS/INTEGRATION/SetDeltaIntersection 1e-2 km

#
# Set year, date and time
```

```

#

/PLANETOCOS/BFIELD/SetStartDate 2005 03 15 10 0 0

#
# Set magnetic field model
#

/PLANETOCOS/BFIELD/SetInternalFieldModel IGRF

#
# Set coordinate system and direction of incidence
#
/PLANETOCOS/SOURCE/SetDirection GEO 0. 0. degree
/PLANETOCOS/SOURCE/verbose 1

#
# Compute and save the cutoff rigidities in a user defined grid
# here at an altitude of 200 km, resulting in a 5°x5° grid
#
/PLANETOCOS/MAGNETIC/RCutoffVsPosition GEO 200 km -90 5 37 -180 5 74 0 0
degree 2005Alt200km.out

```

## B.2 Computation of the Secondary Particle flux and the Atmospheric Ionization

An exemplary macro file for the computation of the specific energy loss as well as the production of secondary particles inside the Earth's atmosphere. As explained in Section 5 the secondary particle environment was computed for logarithmical equally binned mono-energetic primary particles. Here the macro for primary protons with energies between 926 GeV and 1 TeV is presented.

```

/control/verbose 1

#
# Atmospheric definitions
#

/PLANETOCOS/SPACECOORDINATE/UseSpice true
/PLANETOCOS/GEOMETRY/SetType Flat
/PLANETOCOS/GEOMETRY/SetConsiderAtmosphere true
/PLANETOCOS/GEOMETRY/SetPlanetCoreThickness 10 km
/PLANETOCOS/GEOMETRY/SetHeightOfWorldAboveAtmosphere 150 km
/PLANETOCOS/GEOMETRY/SetMaxLayerThickness 5. km
/PLANETOCOS/GEOMETRY/SetMinLayerThickness .01 km
/PLANETOCOS/GEOMETRY/SetHeightOfWorldAboveAtmosphere 10 km
/PLANETOCOS/GEOMETRY/SetAtmosphereTop 200. km
/PLANETOCOS/GEOMETRY/SetGroundAltitude 0. km

```



## B.2. Computation of the Secondary Particle flux and the Atmospheric Ionization

203

```
/PLANETOCOS/GEOMETRY/SetAtmosphereModel NRLMSISE00
/PLANETOCOS/GEOMETRY/SetAp 10.
/PLANETOCOS/GEOMETRY/SetF107 100.
/PLANETOCOS/GEOMETRY/SetF107A 100.

/PLANETOCOS/GEOMETRY/SetGroundAltitude 0 km
/PLANETOCOS/GEOMETRY/verbose 1

#
# Set reference date
#

/PLANETOCOS/GEOMETRY/SetReferenceDate 2004 5 5 10 0 0

#
# Set physics models including the PHITS model by Koi et al. (2008)
#

/PLANETOCOS/PHYSICS/SelectTypeOfEMPhysics STANDARD
/PLANETOCOS/PHYSICS/SelectTypeOfHadronicPhysics QGSP_BERT_HP
/PLANETOCOS/PHYSICS/SelectTypeOfIonHadronicPhysics PHITS

#
# Soil definitions
#

/PLANETOCOS/SOIL/ResetLayers
/PLANETOCOS/SOIL/AddLayer 2 1 g/cm3 10 m
/PLANETOCOS/SOIL/AddElementToLayer Hydrogen 0.111894
/PLANETOCOS/SOIL/AddElementToLayer Oxygen 0.888106

#
# Define detector altitude
#

/PLANETOCOS/GEOMETRY/DetectorAtAltitude 0.001 km
/PLANETOCOS/GEOMETRY/DetectorAtAltitude 0.01 km
/PLANETOCOS/GEOMETRY/DetectorAtAltitude 0.05 km
/PLANETOCOS/GEOMETRY/DetectorAtAltitude 0.1 km
/PLANETOCOS/GEOMETRY/DetectorAtAltitude 0.3 km
/PLANETOCOS/GEOMETRY/DetectorAtAltitude 0.6 km
/PLANETOCOS/GEOMETRY/DetectorAtAltitude 1 km
/PLANETOCOS/GEOMETRY/DetectorAtAltitude 2 km
/PLANETOCOS/GEOMETRY/DetectorAtAltitude 3 km
/PLANETOCOS/GEOMETRY/DetectorAtAltitude 4 km
/PLANETOCOS/GEOMETRY/DetectorAtAltitude 5 km
/PLANETOCOS/GEOMETRY/DetectorAtAltitude 6 km
```

```
/PLANETOCOS/GEOMETRY/DetectorAtAltitude 7 km
/PLANETOCOS/GEOMETRY/DetectorAtAltitude 8 km
/PLANETOCOS/GEOMETRY/DetectorAtAltitude 9 km
/PLANETOCOS/GEOMETRY/DetectorAtAltitude 10 km
/PLANETOCOS/GEOMETRY/DetectorAtAltitude 11 km
/PLANETOCOS/GEOMETRY/DetectorAtAltitude 12 km
/PLANETOCOS/GEOMETRY/DetectorAtAltitude 13 km
/PLANETOCOS/GEOMETRY/DetectorAtAltitude 14 km
/PLANETOCOS/GEOMETRY/DetectorAtAltitude 15 km
/PLANETOCOS/GEOMETRY/DetectorAtAltitude 16 km
/PLANETOCOS/GEOMETRY/DetectorAtAltitude 17 km
/PLANETOCOS/GEOMETRY/DetectorAtAltitude 18 km
/PLANETOCOS/GEOMETRY/DetectorAtAltitude 19 km
/PLANETOCOS/GEOMETRY/DetectorAtAltitude 20 km
/PLANETOCOS/GEOMETRY/DetectorAtAltitude 30 km
/PLANETOCOS/GEOMETRY/DetectorAtAltitude 50 km
/PLANETOCOS/GEOMETRY/DetectorAtAltitude 70 km
/PLANETOCOS/GEOMETRY/DetectorAtAltitude 90 km
/PLANETOCOS/GEOMETRY/DetectorAtAltitude 100 km
```

```
#
# Initialise
#
```

```
/PLANETOCOS/Initialise
```

```
#
# Switch of the magnetic field
#
```

```
/PLANETOCOS/BFIELD/SwitchOff
#
# Informations on the primary particles
#
```

```
/PLANETOCOS/ANALYSIS/PRIMARY/FluxHisto proton 1 100 10 4e6 MeV log
/PLANETOCOS/ANALYSIS/PRIMARY/CosZenithHisto proton 2 100 0. 1.
/PLANETOCOS/ANALYSIS/PRIMARY/CosZenVsEnergyHisto proton 3 200 0.0001 200 GeV log 100 0. 1.
```

```
#
# Computing the secondary particle flux for given secondary energy ranges
#
```

```
/PLANETOCOS/ANALYSIS/SECONDARY/SelectAllDetectors
/PLANETOCOS/ANALYSIS/SECONDARY/SetTypeOfWeight INVERSE_COSTH
```

```
/PLANETOCOS/ANALYSIS/SECONDARY/DownwardFluxHisto proton 1 200 1.e-8 1e6 MeV log
/PLANETOCOS/ANALYSIS/SECONDARY/DownwardFluxHisto e- 1 200 1.e-8 1e6 MeV log
/PLANETOCOS/ANALYSIS/SECONDARY/DownwardFluxHisto gamma 1 200 1.e-8 1e6 MeV log
```

## B.2. Computation of the Secondary Particle flux and the Atmospheric Ionization

205

```
/PLANETOCOS/ANALYSIS/SECONDARY/DownwardFluxHisto neutron 1 200 1.e-8 1e6 MeV log

/PLANETOCOS/ANALYSIS/SECONDARY/UpwardFluxHisto proton 2 200 1.e-8 1e6 MeV log
/PLANETOCOS/ANALYSIS/SECONDARY/UpwardFluxHisto e- 2 200 1.e-8 1e6 MeV log
/PLANETOCOS/ANALYSIS/SECONDARY/UpwardFluxHisto gamma 2 200 1.e-8 1e6 MeV log
/PLANETOCOS/ANALYSIS/SECONDARY/UpwardFluxHisto neutron 2 200 1.e-8 1e6 MeV log

/PLANETOCOS/ANALYSIS/SECONDARY/CosZenithHisto proton 3 200 -1. 1.
/PLANETOCOS/ANALYSIS/SECONDARY/CosZenithHisto e- 3 200 -1. 1.
/PLANETOCOS/ANALYSIS/SECONDARY/CosZenithHisto gamma 3 200 -1. 1.
/PLANETOCOS/ANALYSIS/SECONDARY/CosZenithHisto neutron 3 200 -1. 1.

/PLANETOCOS/ANALYSIS/SECONDARY/CosZenithVsEkinHisto proton 4 200 1.e-08 1.e6 MeV log 200 -1. 1.
/PLANETOCOS/ANALYSIS/SECONDARY/CosZenithVsEkinHisto alpha 4 200 1.e-08 1.e6 MeV log 200 -1. 1.
/PLANETOCOS/ANALYSIS/SECONDARY/CosZenithVsEkinHisto e- 4 200 1.e-08 1.e6 MeV log 200 -1. 1.
/PLANETOCOS/ANALYSIS/SECONDARY/CosZenithVsEkinHisto e+ 4 200 1.e-08 1.e6 MeV log 200 -1. 1.
/PLANETOCOS/ANALYSIS/SECONDARY/CosZenithVsEkinHisto mu- 4 200 1.e-08 1.e6 MeV log 200 -1. 1.
/PLANETOCOS/ANALYSIS/SECONDARY/CosZenithVsEkinHisto mu+ 4 200 1.e-08 1.e6 MeV log 200 -1. 1.
/PLANETOCOS/ANALYSIS/SECONDARY/CosZenithVsEkinHisto pi- 4 200 1.e-08 1.e6 MeV log 200 -1. 1.
/PLANETOCOS/ANALYSIS/SECONDARY/CosZenithVsEkinHisto pi+ 4 200 1.e-08 1.e6 MeV log 200 -1. 1.
/PLANETOCOS/ANALYSIS/SECONDARY/CosZenithVsEkinHisto kaon- 4 200 1.e-08 1.e6 MeV log 200 -1. 1.
/PLANETOCOS/ANALYSIS/SECONDARY/CosZenithVsEkinHisto kaon+ 4 200 1.e-08 1.e6 MeV log 200 -1. 1.
/PLANETOCOS/ANALYSIS/SECONDARY/CosZenithVsEkinHisto gamma 4 200 1.e-08 1.e6 MeV log 200 -1. 1.
/PLANETOCOS/ANALYSIS/SECONDARY/CosZenithVsEkinHisto neutron 4 200 1.e-08 1.e6 MeV log 200 -1. 1.

# Deposited energy

/PLANETOCOS/ANALYSIS/EDEP/AtmoEdepVsAltitudeHisto 1 1000
/PLANETOCOS/ANALYSIS/EDEP/AtmoEdepVsDepthHisto 1 1000

#
# Cut in range definition
#

/PLANETOCOS/CUT/SetCutInDepthForAllAtmosphericLayers 2. g/cm2
/run/setCut 1. m
/run/particle/applyCuts true e-
/run/particle/applyCuts true gamma
/run/particle/applyCuts true e+
/run/particle/dumpCutValues

#
# Stopping conditions
#

/PLANETOCOS/STOPCONDITION/SetStoppingEnergy e- 1.e-8 MeV
/PLANETOCOS/STOPCONDITION/SetStoppingEnergy gamma 1.e-8 MeV
/PLANETOCOS/STOPCONDITION/SetStoppingEnergy proton 1.e-8 MeV
/PLANETOCOS/STOPCONDITION/SetStoppingEnergy alpha 1.e-8 MeV
```

```
/PLANETOCOS/STOPCONDITION/SetStoppingEnergy neutron 1.e-8 MeV
```

```
#  
# Set maximum computation time for this particular energy  
#
```

```
/PLANETOCOS/DURATION/SetMaxTotalDuration 24.0 hour
```

```
#  
# No visualisation  
#
```

```
/vis/enable false  
/tracking/storeTrajectory 0  
/PLANETOCOS/DRAW/DrawTrajectory false
```

```
#  
# Define the characteristics of the primary particle (GEANT4-style)  
#
```

```
/PLANETOCOS/RANDOM/SetRandomSeedAtRunStart true  
/PLANETOCOS/ANALYSIS/ResetHistograms
```

```
/PLANETOCOS/SOURCE/ConsiderCutoff false
```

```
/gps/particle proton  
/gps/pos/centre 0 0 180 km  
/gps/direction 0 0 -1  
/gps/ang/rot1 1 0 0  
/gps/ang/rot2 0 1 0  
/gps/ang/type cos  
/gps/ang/mintheta 0 deg  
/gps/ang/maxtheta 90 deg
```

```
/gps/ene/min 9261187.28129 MeV  
/gps/ene/max 10000000.0 MeV  
/gps/ene/type Pow  
/gps/ene/alpha 0.
```

```
/tracking/verbose 0
```

```
#  
# Set number of events and save results in an output file  
#
```

```
/run/beamOn 100000  
/PLANETOCOS/ANALYSIS/SaveTree 9.261e+06_1.0e+07.ascii ascii
```

# On the Computation Time

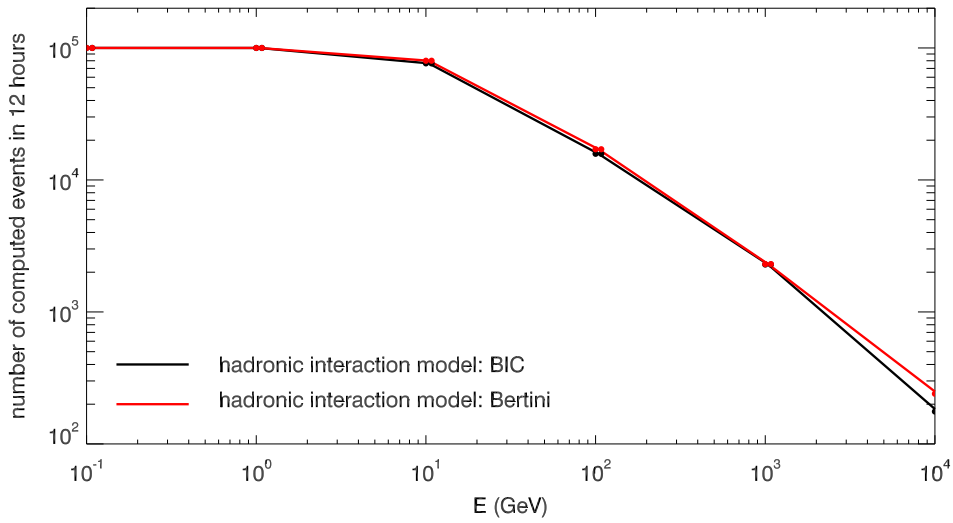


Figure C.1: *Number of events computed within selected energy bins using the BIC (black dots and line) and Bertini (red dots and line) interaction model.*

As mentioned in Chapter 5 the mono-energetic computation-method used in this work is very time consuming, thus the computation time per primary energy bin was restricted to a computation time of 12 hours. Because of the fact that the higher the number of computed events the better the statistics, this, however, downgrades the statistics in the high energy range, as shown in Fig. C.1. Here the number of computed events within the 12 hour simulation window as function of selected primary particle bins (filled dots) for the hadronic BIC (black) and Bertini (red) models is displayed. It shows that energy bins between 0.1 GeV up to 1 GeV are only minor influenced by the 12 hour limitation, while in the high energy range significant event number decreases can be observed. Starting with  $10^5$  events at energies between 0.1 GeV up to 1 GeV only 176 and 240 events using the BIC and Bertini model are computed at around 10 TeV, respectively. Nevertheless, the Bertini model possesses better statistics in the high energy range.

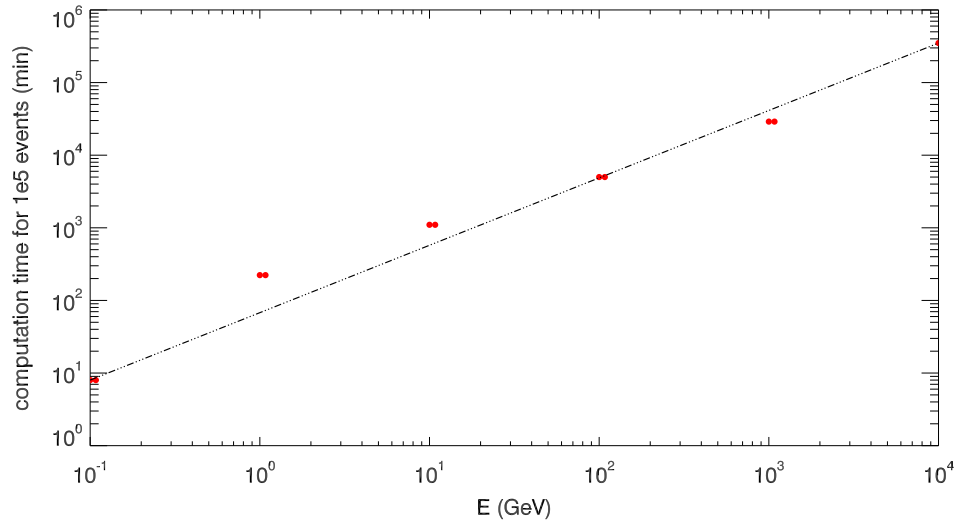


Figure C.2: *Computation time needed in order to simulate  $10^5$  events.*

Furthermore, Fig. C.2 shows the amount of time needed in order to compute  $10^5$  events for the selected primary particle energy bins (red dots). It becomes obvious that only a computation time of 8 minutes is needed in order to simulate the secondary particle interactions for an energy bin of 0.1 to 0.107 GeV while the computations for the energy bin of 10 TeV to 10.8 TeV would need at least 35 weeks.

This study reveals that it is indeed of importance to limit the computation time of the mono-energetic primary particle bins. Moreover, due to the fact that high energy primary particles statistically are rare a time limitation as applied in this work is adequate.

# Information on the SDE model

---

The SED model by [Strauss et al. \(2011\)](#) and [Kopp et al. \(2012\)](#) is essentially based on [Potgieter \(1996\)](#), the values are the same as in [Scherer et al. \(2011\)](#). The TS is located at 100 AU, the HP at 130 AU, a possible BS forms the outer boundary of the simulation volume at 250 AU. Within the HP the solar wind speed is assumed to be directed radially outwards with a constant value of 400 km/s, beyond the solar wind speed is assumed to vanish. The adiabatic energy change due to the factor  $\vec{\nabla} \cdot \vec{v}_{sw} = 2 \frac{v_{sw}}{r}$  is taken into account only for  $r \leq r_{TS}$  and is set to zero elsewhere. The mean free path is given by

$$\lambda_{\parallel} = \lambda_0 \cdot (1 + r) \cdot P, \quad (\text{D.1})$$

with  $\lambda_0 = 0.1$  for distances between  $r \leq r_{TS}$  and 0.01 beyond. Within the HP the diffusion tensor is

$$\mathbf{K}_S = \begin{pmatrix} \kappa_{rr} & 0 & \kappa_{r\varphi} \\ 0 & \kappa_{\vartheta\vartheta} & 0 \\ \kappa_{\varphi r} & 0 & \kappa_{\varphi\varphi} \end{pmatrix} \quad (\text{D.2})$$

with the components

$$\begin{aligned} \kappa_{rr} &= \kappa_{\parallel} \cdot \cos^2 \psi + \kappa_{\perp,r} \cdot \sin^2 \psi \\ \kappa_{r\varphi} &= (\kappa_{\perp,r} - \kappa_{\parallel}) \cdot \sin \psi \cdot \cos \psi = \kappa_{\varphi r} \\ \kappa_{\vartheta\vartheta} &= \kappa_{\perp,\vartheta} \\ \kappa_{\varphi\varphi} &= \kappa_{\parallel} \cdot \sin^2 \psi + \kappa_{\perp,r} \cdot \cos^2 \psi, \end{aligned} \quad (\text{D.3})$$

where  $\psi$  represents the Parker angle between the radial direction and that of the averaged HMF at the actual position of the particle, and the components are related to the mean free path by

$$\begin{aligned} \kappa_{\parallel} &= \frac{1}{3} \lambda_{\parallel} v \\ \kappa_{\perp,r} &= \kappa_{\perp,\vartheta} = \kappa_0 \cdot \kappa_{\parallel}, \end{aligned} \quad (\text{D.4})$$

with  $v$  representing the speed of the particle and  $\kappa_0 = 0.1$ . Note the change of  $\lambda_{\parallel}$  beyond the TS according to Eq. (D.1).

Beyond the HP the diffusion tensor is replaced by a scalar value, which is varied between  $10^{25}$  and  $10^{28}$  cm<sup>2</sup>/s, and is either constant or proportional to the rigidity  $P$ . This model neglects drift effects and, moreover, does not take into account the heliospheric current sheet, for the inclusion of these effects we refer to [Strauss et al. \(2011\)](#).





APPENDIX E

# The Cosmogenic Radionuclide Production Rates

---

CN	Local Production Rate ( $\text{cm}^{-2} \text{s}^{-1}$ ) as Function of $R_C$ (GV)															
	0	1	2	3	4	5	6	7	8	9	10	12	16			
$^{10}\text{Be}$	0.0476	0.0472	0.0413	0.0332	0.0267	0.0221	0.0180	0.0155	0.0136	0.0120	0.0103	0.0081	0.0055			
$^7\text{Be}$	0.1001	0.0983	0.0844	0.0676	0.0543	0.0449	0.0366	0.0315	0.0276	0.0242	0.0209	0.0165	0.0113			
$^{36}\text{Cl}$	0.0099	0.0098	0.0087	0.0070	0.0057	0.0047	0.0038	0.0033	0.0029	0.0025	0.0022	0.0017	0.0012			
$^3\text{H}$	0.4986	0.4941	0.4340	0.3517	0.2846	0.2366	0.1935	0.1668	0.1464	0.1287	0.1113	0.0882	0.0605			
$^{26}\text{Al}$	5.4e-5	5.3e-5	4.7e-5	3.8e-5	3.0e-5	2.5e-5	2.0e-5	1.8e-5	1.6e-5	1.4e-5	1.2e-5	9.3e-6	6.4e-6			
$^{14}\text{C}$	8.0423	7.9805	7.0736	5.7499	4.6573	3.8734	3.1616	2.7244	2.3904	2.1004	1.8128	1.4327	0.9822			
$^{10}\text{Be}$	0.0298	0.0297	0.0277	0.0239	0.0203	0.0175	0.0147	0.0129	0.0115	0.0103	0.0090	0.0073	0.0051			
$^7\text{Be}$	0.0617	0.0613	0.0565	0.0487	0.0414	0.0356	0.0300	0.0264	0.0235	0.0209	0.0183	0.0148	0.0104			
$^{36}\text{Cl}$	0.0063	0.0062	0.0058	0.0051	0.0043	0.0037	0.0031	0.0027	0.0024	0.0022	0.0019	0.0015	0.0011			
$^3\text{H}$	0.3145	0.3135	0.2926	0.2544	0.2173	0.1874	0.1587	0.1397	0.1247	0.1113	0.0977	0.0789	0.0556			
$^{26}\text{Al}$	3.4e-5	3.4e-5	3.1e-5	2.7e-5	2.3e-5	2.0e-5	1.7e-5	1.5e-5	1.3e-5	1.2e-5	1.0e-5	8.4e-6	5.9e-6			
$^{14}\text{C}$	5.1036	5.0890	4.7734	4.1583	3.5541	3.0668	2.5930	2.2816	2.0352	1.8147	1.5904	1.2830	0.9030			
$^{10}\text{Be}$	0.0211	0.0210	0.0201	0.0182	0.0161	0.0142	0.0123	0.0110	0.0099	0.0090	0.0080	0.0065	0.0047			
$^7\text{Be}$	0.0433	0.0431	0.0411	0.0370	0.0327	0.0289	0.0251	0.0224	0.0202	0.0182	0.0162	0.0133	0.0096			
$^{36}\text{Cl}$	0.0044	0.0044	0.0042	0.0038	0.0034	0.0030	0.0026	0.0023	0.0021	0.0019	0.0017	0.0014	0.0010			
$^3\text{H}$	0.2231	0.2228	0.2138	0.1938	0.1718	0.1524	0.1326	0.1188	0.1075	0.0971	0.0864	0.0711	0.0645			
$^{26}\text{Al}$	2.4e-5	2.4e-5	2.3e-5	2.1e-5	1.8e-5	1.6e-5	1.4e-5	1.3e-5	1.1e-5	1.0e-5	9.2e-6	7.5e-6	5.4e-6			
$^{14}\text{C}$	3.6298	3.6248	3.4888	3.1676	2.8094	2.4924	2.1660	1.9390	1.7538	1.5834	1.4064	1.1554	0.8329			

Table E.2: The total local cosmogenic radionuclides production rate due to primary protons for cutoff rigidities between 0 and 16 GV. The results are given for solar minimum conditions ( $\phi=500$  MV, dark gray shading), for conditions in the transition between solar minimum and maximum ( $\phi=1000$  MV, light gray shading) as well as solar maximum ( $\phi=1500$  MV, no shading).

---

$\phi$ (MV)	$^{10}\text{Be}$	$^{14}\text{C}$
0	0.0304	3.1124
200	0.0238	2.4853
400	0.0197	2.0868
600	0.0167	1.8043
800	0.0146	1.5912
1000	0.0129	1.4237
1200	0.0115	1.2880
1400	0.0104	1.1756
1600	0.0094	1.0807
1800	0.0086	0.9994
2000	0.0079	0.9290

Table E.3: The total global cosmogenic radionuclides production rate in units of  $(\text{cm}^2 \text{ s})^{-1}$  for different solar modulation phases with  $\phi$  varying between 0 and 2000 MV.



# Lebenslauf

## Persönliche Daten

Klaudia Herbst

E-Mail: herbst@physik.uni-kiel.de  
Geboren am: 19. Mai 1982 in Leipzig  
Nationalität: Deutsch

## Berufserfahrung

seit 03/2007 Wissenschaftliche Mitarbeiterin in der Abteilung für Extraterrestrische Physik am Institut für Experimentelle und Angewandte Physik der Christian-Albrechts-Universität zu Kiel  
03/2006 - 03/2007 Studentische Hilfskraft

## Promotion

seit 04/2007 Promotion in der Abteilung für Extraterrestrische Physik am Institut für Experimentelle und Angewandte Physik der Christian-Albrechts-Universität zu Kiel

Thema der Promotion: *Interaction of Cosmic Rays with the Earth's Magnetosphere and Atmosphere - Modeling the Cosmic Ray Induced Ionization and the Production of Cosmogenic Radionuclides*

## Studium

10/2001 - 03/2007 Studium der Physik an der Christian-Albrechts-Universität zu Kiel

Thema der Diplomarbeit: *Wechselwirkung der kosmischen Strahlung mit Erdatmosphäre, Marsatmosphäre und Marsboden*



# Danksagung

*"...jedes Problem wird wie Luft sein,  
bis ich wieder atmen kann,  
ich seh' klar was übrig bleibt,  
für eine kleine Ewigkeit..."*

Bosse

An dieser Stelle möchte ich all jenen Menschen danken, die mich auf diesem manchmal steinigen Weg begleitet und tatkräftig unterstützt haben. Mein besonderer Dank gilt dabei...

- ... Herrn Prof. Dr. Bernd Heber, der mir die Möglichkeit gab mich in das spannende Thema der Kosmogenen Radionuklide einzuarbeiten und mir jeder Zeit mit Rat und Tat zur Seite stand. Des Weiteren bin ich ihm sehr dankbar, dass ich auf zahlreichen Dienstreisen meinen Horizont erweitern durfte.
- ... Herrn Prof. Dr. Jürg Beer, der mir stets ein Ansprechpartner in der interessanten Welt der Kosmogenen Radionuklidmessungen und deren Geheimnissen war. Ich danke ihm weiterhin dafür, dass ich jederzeit im Schweizer Land willkommen und gern gesehen war.
- ... dem zweiten, wenn auch Wahl-Schweizer, Herrn Dr. Friedhelm Steinhilber, der in einer sehr schweren Zeit in mein Leben trat und mir mit seiner enthusiastischen, ansteckenden Art im Athener Sommer des Jahres 2010 die Augen und das Herz für die Kosmogenen Radionuklide öffnete.
- ... den Herren Dr. Andreas Kopp und Dr. Oliver Sternal, die bestimmt hunderte *informations* korrigieren mussten und trotz allem immer ein Lächeln, ein paar herzliche Worte und ein paar Minuten für ein Kännchen hatten.
- ... meinen Leipzigern, ohne deren Zuspruch und Unterstützung ich diese Arbeit nie begonnen, geschweige denn beendet hätte. Schön, dass es Euch gibt.
- ... den Preetzern, die stets ein offenes Ohr, viel Geduld und einen freien Liegestuhl auf der Terasse mit *George-Beschallung* für mich hatten.
- ... Frau Dominique Gloe. Du hast, vor allem in der Endphase, von allen die mir lieb und teuer sind am meisten Verzicht üben und einstecken müssen.
- ... und nicht zuletzt allen Mitgliedern des vierten und fünften Stockes.





# Eidesstattliche Erklärung

Hiermit erkläre ich, dass

- die vorliegende Arbeit, abgesehen von der Beratung durch den Betreuer, nach Inhalt und Form meine eigene Arbeit ist
- die Arbeit noch nicht an anderer Stelle im Rahmen eines Prüfungsverfahrens vorgelegen hat
- die vorliegende Arbeit unter Einhaltung der Regeln guter wissenschaftlicher Praxis entstanden sowie selbstständig verfasst wurde und keine anderen als die angegebenen Quellen verwendet wurden.

Wie im Text verwiesen, sind Teile der Arbeit in folgenden wissenschaftlichen Zeitschriften veröffentlicht:

Herbst, K., A. Kopp, B. Heber, F. Steinhilber, H. Fichtner, K. Scherer and D. Matthiä, *On the Importance of the Local Interstellar Spectrum for the Solar Modulation Parameter*, J. Geophys. Res., 115, A14, 2010

Matthiä, D., Herbst, K., B. Heber, T. Berger and G. Reitz,  *$^{10}\text{Be}$  production in the atmosphere by galactic cosmic rays*, Space Sci. Rev., 2011

Fichtner, H., B. Heber, Herbst, K., A. Kopp and K. Scherer, *Solar Activity, the Heliosphere, Cosmic Rays and Their Impact on the Earth's Atmosphere*, in: Climate And Weather of the Sun-Earth System (CAWSES): Highlights from a priority program, Springer, Ed.: F.-J. Lübken, Dordrecht, The Netherlands, 2012

Herbst, K., A. Kopp, B. Heber, F. Steinhilber, and O. Sternal, *The Local Interstellar Spectrum Beyond the Heliopause: What can be Learned from Voyager in the Inner Heliosheath?*, Astrophys. J., 761, 17, 2012

Des Weiteren werden die folgenden Manuskripte demnächst eingereicht:

Herbst, K., A. Kopp, B. Heber and J. Pilchowski, *The Influence of the Geometry of the Earth's Magnetic Field on the Vertical Cutoff Rigidity of Cosmic Ray Particles*, to be submitted to Annales Geophys.

Herbst, K., B. Heber and J. Beer, *Modeling Global  $^{10}\text{Be}$  and  $^{14}\text{C}$  Production Rates During the Holocene*, in prep.

Kiel, den \_\_\_\_\_

\_\_\_\_\_